

UNCLASSIFIED

AD 413932

DEFENSE DOCUMENTATION CENTER

FOR

SCIENTIFIC AND TECHNICAL INFORMATION

CAMERON STATION, ALEXANDRIA, VIRGINIA



UNCLASSIFIED

NOTICE: When government or other drawings, specifications or other data are used for any purpose other than in connection with a definitely related government procurement operation, the U. S. Government thereby incurs no responsibility, nor any obligation whatsoever; and the fact that the Government may have formulated, furnished, or in any way supplied the said drawings, specifications, or other data is not to be regarded by implication or otherwise as in any manner licensing the holder or any other person or corporation, or conveying any rights or permission to manufacture, use or sell any patented invention that may in any way be related thereto.

63-4-4

413932 ASD-TR-61-181
Part III

413932

CATALOGED BY DDC
AS AD No. _____

SUBSTRUCTURE AND MECHANICAL PROPERTIES OF REFRACTORY METALS

TECHNICAL DOCUMENTARY REPORT NO. ASD-TR-61-181, Part III
April 1963

Directorate of Materials and Processes
Aeronautical Systems Division
Air Force Systems Command
Wright-Patterson Air Force Base, Ohio

Project No. 7351, Task No. 735101

(Prepared under Contract No. AF33(657)-8424 by ManLabs, Inc.,
Cambridge, Massachusetts; B. S. Lement, D. A. Thomas,
S. Weissmann, W. S. Owen, P. B. Hirsch, authors)

DDC
RECEIVED
AUG 2 1963
TASK 2

FOR ERRATA

AD _____

413932

THE FOLLOWING PAGES ARE CHANGES

TO BASIC DOCUMENT

AD 413932

ASD-TR-61-181
Part III

April 1963

ERRATA - August 1963

The following correction is applicable to ASD-TR-61-181, Part III, entitled "Substructure and Mechanical Properties of Refractory Metals", and dated April 1963:

Front Cover

Change report number to WADD-TR-61-181, Part III.

Aeronautical Systems Division
Air Force Systems Command
United States Air Force
Wright-Patterson Air Force Base, Ohio

413932

NOTICES

When Government drawings, specifications, or other data are used for any purpose other than in connection with a definitely related Government procurement operation, the United States Government thereby incurs no responsibility nor any obligation whatsoever; and the fact that the Government may have formulated, furnished, or in any way supplied the said drawings, specifications, or other data, is not to be regarded by implication or otherwise as in any manner licensing the holder or any other person or corporation, or conveying any rights or permission to manufacture, use, or sell any patented invention that may in any way be related thereto.

Qualified requesters may obtain copies of this report from the Armed Services Technical Information Agency, (ASTIA), Arlington Hall Station, Arlington 12, Virginia.

This report has been released to the Office of Technical Services, U. S. Department of Commerce, Washington 25, D.C., in stock quantities for sale to the general public.

Copies of this report should not be returned to the Aeronautical Systems Division unless return is required by security considerations, contractual obligations, or notice on a specific document.

Aeronautical Systems Division, Dir/Materials
And Processes, Metals & Ceramics Lab,
Wright-Patterson AFB, Ohio
Rpt No ASD-TR-61-181, Part III. SUB-
STRUCTURE AND MECHANICAL PROPER-
TIES OF REFRACTORY METALS. Final
report, Apr 63, 220 p. incl. illus., tables,
refs.

Unclassified Report

Coordinated program on W, Mo, Ta and Cb
was carried out by ManLabs, M.I.T.,
Rutgers, U. Liverpool (Eng.) and U. Cam-
bridge (Eng.) by means of advanced micro-
scopic, x-ray diffraction, and mechanical
testing techniques. The effective surface
energy for fracture of molybdenum strip was

(over)

found to be about 3000 ergs/cm². The tensile
ductility transition in molybdenum is asso-
ciated with the occurrence of necking. Fiber-
like grains containing a dislocation cell struc-
ture in which fine platelets occur. Discon-
tinuous yielding in tantalum single crystals
is correlated with a decrease in the shearing
strain in the principal slip system to zero
while that in the secondary system continues
to increase. The binding energy between
oxygen atoms and dislocations in tantalum is
about 0.54 e.v. Dissociation of screw dis-
locations along three interesting symmetri-
cally located planes may account for the
strong lattice friction stress in b.c.c.
metals.

1. Refractory metals
2. X-ray diffraction analysis
3. Electron micro-
scopy
- I. AFSC Project 7351,
Task 735101
- II. Contract AF33(657)-
8424

III. ManLabs, Inc.
Cambridge, Mass.
IV. Lement, B.S. et al.
V. Aval fr OTS
VI. In ASTIA collection

Aeronautical Systems Division, Dir/Materials
And Processes, Metals & Ceramics Lab,
Wright-Patterson AFB, Ohio
Rpt No ASD-TR-61-181, Part III. SUB-
STRUCTURE AND MECHANICAL PROPER-
TIES OF REFRACTORY METALS. Final
report, Apr 63, 220 p. incl. illus., tables,
refs.

Unclassified Report

Coordinated program on W, Mo, Ta and Cb
was carried out by ManLabs, M.I.T.,
Rutgers, U. Liverpool (Eng.) and U. Cam-
bridge (Eng.) by means of advanced micro-
scopic, x-ray diffraction, and mechanical
testing techniques. The effective surface
energy for fracture of molybdenum strip was

(over)

found to be about 3000 ergs/cm². The tensile
ductility transition in molybdenum is asso-
ciated with the occurrence of necking. Fiber-
like grains containing a dislocation cell struc-
ture in which fine platelets occur. Discon-
tinuous yielding in tantalum single crystals
is correlated with a decrease in the shearing
strain in the principal slip system to zero
while that in the secondary system continues
to increase. The binding energy between
oxygen atoms and dislocations in tantalum is
about 0.54 e.v. Dissociation of screw dis-
locations along three interesting symmetri-
cally located planes may account for the
strong lattice friction stress in b.c.c.
metals.

1. Refractory metals
2. X-ray diffraction analysis
3. Electron micro-
scopy
- I. AFSC Project 7351,
Task 735101
- II. Contract AF33(657)-
8424

III. ManLabs, Inc.
Cambridge, Mass.
IV. Lement, B.S. et al.
V. Aval fr OTS
VI. In ASTIA collection

Aeronautical Systems Division, Dir/Materials And Processes, Metals & Ceramics Lab, Wright-Patterson AFB, Ohio
Rpt No ASD-TR-61-181, Part III. SUB-STRUCTURE AND MECHANICAL PROPERTIES OF REFRACTORY METALS. Final report, Apr 63, 220 p. incl. illus., tables, refs.

Unclassified Report

Coordinated program on W, Mo, Ta and Nb was carried out by ManLabs, M.I.T., Rutgers, U. Liverpool (Eng.) and U. Cambridge (Eng.) by means of advanced microscopic, x-ray diffraction, and mechanical testing techniques. The effective surface energy for fracture of molybdenum strip was

(over)

1. Refractory metals
 2. X-ray diffraction analysis
 3. Electron microscopy
- I. AFSC Project 7351, Task 735101
 - II. Contract AF33(657)-8424

- III. ManLabs, Inc. Cambridge, Mass.
- IV. Lement, B.S. et al.
- V. Aval fr OTS
- VI. In ASTIA collection

Aeronautical Systems Division, Dir/Materials And Processes, Metals & Ceramics Lab, Wright-Patterson AFB, Ohio
Rpt No ASD-TR-61-181, Part III. SUB-STRUCTURE AND MECHANICAL PROPERTIES OF REFRACTORY METALS. Final report, Apr 63, 220 p. incl. illus., tables, refs.

Unclassified Report

Coordinated program on W, Mo, Ta and Nb was carried out by ManLabs, M.I.T., Rutgers, U. Liverpool (Eng.) and U. Cambridge (Eng.) by means of advanced microscopic, x-ray diffraction, and mechanical testing techniques. The effective surface energy for fracture of molybdenum strip was

(over)

1. Refractory metals
 2. X-ray diffraction analysis
 3. Electron microscopy
- I. AFSC Project 7351, Task 735101
 - II. Contract AF33(657)-8424

- III. ManLabs, Inc. Cambridge, Mass.
- IV. Lement, B.S. et al.
- V. Aval fr OTS
- VI. In ASTIA collection

found to be about 3000 ergs/cm². The tensile ductility transition in molybdenum is associated with the occurrence of necking. Fiber- ing in tungsten involves formation of ribbon- like grains containing a dislocation cell structure in which fine platelets occur. Discon- tinuous yielding in tantalum single crystals is correlated with a decrease in the shearing strain in the principal slip system to zero while that in the secondary system continues to increase. The binding energy between oxygen atoms and dislocations in tantalum is about 0.54 e.v. Dissociation of screw dis- locations along three interesting symmetri- cally located planes may account for the strong lattice friction stress in b. c. c. metals.

found to be about 3000 ergs/cm². The tensile ductility transition in molybdenum is asso- ciated with the occurrence of necking. Fiber- ing in tungsten involves formation of ribbon- like grains containing a dislocation cell struc- ture in which fine platelets occur. Discon- tinuous yielding in tantalum single crystals is correlated with a decrease in the shearing strain in the principal slip system to zero while that in the secondary system continues to increase. The binding energy between oxygen atoms and dislocations in tantalum is about 0.54 e.v. Dissociation of screw dis- locations along three interesting symmetri- cally located planes may account for the strong lattice friction stress in b. c. c. metals.

Aeronautical Systems Division, Dir/Materials
And Processes, Metals & Ceramics Lab,
Wright-Patterson AFB, Ohio
Rpt No ASD-TR-61-181, Part III. SUB-
STRUCTURE AND MECHANICAL PROPER-
TIES OF REFRACTORY METALS. Final
report, Apr 63, 220 p. incl. illus., tables,
refs.

Unclassified Report

Coordinated program on W, Mo, Ta and Nb
was carried out by ManLabs, M.I.T.,
Rutgers, U. Liverpool (Eng.) and U. Cam-
bridge (Eng.) by means of advanced micro-
scopic, x-ray diffraction, and mechanical
testing techniques. The effective surface
energy for fracture of molybdenum strip was

(over)

found to be about 3000 ergs/cm². The tensile
ductility transition in molybdenum is asso-
ciated with the occurrence of necking. Fiber-
ing in tungsten involves formation of ribbon-
like grains containing a dislocation cell struc-
ture in which fine platelets occur. Discon-
tinuous yielding in tantalum single crystals
is correlated with a decrease in the shearing
strain in the principal slip system to zero
while that in the secondary system continues
to increase. The binding energy between
oxygen atoms and dislocations in tantalum is
about 0.54 e.v. Dissociation of screw dis-
locations along three interesting symmetri-
cally located planes may account for the
strong lattice friction stress in b.c.c.
metals.

1. Refractory metals
 2. X-ray diffraction analysis
 3. Electron microscopy
- I. AFSC Project 7351, Task 735101
 - II. Contract AF33(657)-8424
 - III. ManLabs, Inc. Cambridge, Mass.
 - IV. Lement, B.S. et al.
 - V. Aval fr OTS
 - VI. In ASTIA collection

Unclassified Report

Coordinated program on W, Mo, Ta and Nb
was carried out by ManLabs, M.I.T.,
Rutgers, U. Liverpool (Eng.) and U. Cam-
bridge (Eng.) by means of advanced micro-
scopic, x-ray diffraction, and mechanical
testing techniques. The effective surface
energy for fracture of molybdenum strip was

(over)

found to be about 3000 ergs/cm². The tensile
ductility transition in molybdenum is asso-
ciated with the occurrence of necking. Fiber-
ing in tungsten involves formation of ribbon-
like grains containing a dislocation cell struc-
ture in which fine platelets occur. Discon-
tinuous yielding in tantalum single crystals
is correlated with a decrease in the shearing
strain in the principal slip system to zero
while that in the secondary system continues
to increase. The binding energy between
oxygen atoms and dislocations in tantalum is
about 0.54 e.v. Dissociation of screw dis-
locations along three interesting symmetri-
cally located planes may account for the
strong lattice friction stress in b.c.c.
metals.

Aeronautical Systems Division, Dir/Materials
And Processes, Metals & Ceramics Lab,
Wright-Patterson AFB, Ohio
Rpt No ASD-TR-61-181, Part III. SUB-
STRUCTURE AND MECHANICAL PROPER-
TIES OF REFRACTORY METALS. Final
report, Apr 63, 220 p. incl. illus., tables,
refs.

Unclassified Report

Coordinated program on W, Mo, Ta and Nb
was carried out by ManLabs, M.I.T.,
Rutgers, U. Liverpool (Eng.) and U. Cam-
bridge (Eng.) by means of advanced micro-
scopic, x-ray diffraction, and mechanical
testing techniques. The effective surface
energy for fracture of molybdenum strip was

(over)

found to be about 3000 ergs/cm². The tensile
ductility transition in molybdenum is asso-
ciated with the occurrence of necking. Fiber-
ing in tungsten involves formation of ribbon-
like grains containing a dislocation cell struc-
ture in which fine platelets occur. Discon-
tinuous yielding in tantalum single crystals
is correlated with a decrease in the shearing
strain in the principal slip system to zero
while that in the secondary system continues
to increase. The binding energy between
oxygen atoms and dislocations in tantalum is
about 0.54 e.v. Dissociation of screw dis-
locations along three interesting symmetri-
cally located planes may account for the
strong lattice friction stress in b.c.c.
metals.

1. Refractory metals
 2. X-ray diffraction analysis
 3. Electron microscopy
- I. AFSC Project 7351, Task 735101
 - II. Contract AF33(657)-8424
 - III. ManLabs, Inc. Cambridge, Mass.
 - IV. Lement, B.S. et al.
 - V. Aval fr OTS
 - VI. In ASTIA collection

Unclassified Report

Coordinated program on W, Mo, Ta and Nb
was carried out by ManLabs, M.I.T.,
Rutgers, U. Liverpool (Eng.) and U. Cam-
bridge (Eng.) by means of advanced micro-
scopic, x-ray diffraction, and mechanical
testing techniques. The effective surface
energy for fracture of molybdenum strip was

(over)

found to be about 3000 ergs/cm². The tensile
ductility transition in molybdenum is asso-
ciated with the occurrence of necking. Fiber-
ing in tungsten involves formation of ribbon-
like grains containing a dislocation cell struc-
ture in which fine platelets occur. Discon-
tinuous yielding in tantalum single crystals
is correlated with a decrease in the shearing
strain in the principal slip system to zero
while that in the secondary system continues
to increase. The binding energy between
oxygen atoms and dislocations in tantalum is
about 0.54 e.v. Dissociation of screw dis-
locations along three interesting symmetri-
cally located planes may account for the
strong lattice friction stress in b.c.c.
metals.

<p>Aeronautical Systems Division, Dir./Materials And Processes, Metals & Ceramics Lab, Wright-Patterson AFB, Ohio Rpt No ASD-TR-61-181, Part III. SUB-STRUCTURE AND MECHANICAL PROPERTIES OF REFRACTORY METALS. Final report, Apr 63, 220 p. incl. illus., tables, refs.</p> <p style="text-align: center;">Unclassified Report</p> <p>Coordinated program on W, Mo, Ta and Cb was carried out by ManLabs, M.I.T., Rutgers, U. Liverpool (Eng.) and U. Cambridge (Eng.) by means of advanced microscopic, x-ray diffraction, and mechanical testing techniques. The effective surface energy for fracture of molybdenum strip was</p> <p style="text-align: center;">(over)</p>	<p>1. Refractory metals 2. X-ray diffraction analysis 3. Electron microscopy</p> <p>I. AFSC Project 7351, Task 735101 II. Contract AF33(657)-8424</p> <p>III. ManLabs, Inc. Cambridge, Mass. IV. Lement, B.S. et al. V. Aval fr OTS VI. In ASTIA collection</p>	<p>Aeronautical Systems Division, Dir./Materials And Processes, Metals & Ceramics Lab, Wright-Patterson AFB, Ohio Rpt No ASD-TR-61-181, Part III. SUB-STRUCTURE AND MECHANICAL PROPERTIES OF REFRACTORY METALS. Final report, Apr 63, 220 p. incl. illus., tables, refs.</p> <p style="text-align: center;">Unclassified Report</p> <p>Coordinated program on W, Mo, Ta and Cb was carried out by ManLabs, M.I.T., Rutgers, U. Liverpool (Eng.) and U. Cambridge (Eng.) by means of advanced microscopic, x-ray diffraction, and mechanical testing techniques. The effective surface energy for fracture of molybdenum strip was</p> <p style="text-align: center;">(over)</p>	<p>1. Refractory metals 2. X-ray diffraction analysis 3. Electron microscopy</p> <p>I. AFSC Project 7351, Task 735101 II. Contract AF33(657)-8424</p> <p>III. ManLabs, Inc. Cambridge, Mass. IV. Lement, B.S. et al. V. Aval fr OTS VI. In ASTIA collection</p>
<p>found to be about 3000 ergs/cm². The tensile ductility transition in molybdenum is associated with the occurrence of necking. Fiber-like grains containing a dislocation cell structure in which fine platelets occur. Discontinuous yielding in tantalum single crystals is correlated with a decrease in the shearing strain in the principal slip system to zero while that in the secondary system continues to increase. The binding energy between oxygen atoms and dislocations in tantalum is about 0.54 e.v. Dissociation of screw dislocations along three interesting symmetrically located planes may account for the strong lattice friction stress in b.c.c. metals.</p> <p style="text-align: center;">(over)</p>		<p>found to be about 3000 ergs/cm². The tensile ductility transition in molybdenum is associated with the occurrence of necking. Fiber-like grains containing a dislocation cell structure in which fine platelets occur. Discontinuous yielding in tantalum single crystals is correlated with a decrease in the shearing strain in the principal slip system to zero while that in the secondary system continues to increase. The binding energy between oxygen atoms and dislocations in tantalum is about 0.54 e.v. Dissociation of screw dislocations along three interesting symmetrically located planes may account for the strong lattice friction stress in b.c.c. metals.</p> <p style="text-align: center;">(over)</p>	

FOREWORD

This report was prepared by ManLabs, Inc., Cambridge, Mass., under USAF Contract No. AF33(657)-8424. This contract was initiated under Project No. 7351, "Metallic Materials," Task No. 735101, "Refractory Metals." The work was administered under the direction of the Directorate of Materials and Processes, Deputy for Technology, Aeronautical Systems Division, with Lt. J. Bitzer acting as project engineer (succeeded by J. K. Elbaum).

The period covered by this report is 1 April 1962 to 31 March 1963.

The following research investigators participated in this program:

<u>Laboratory</u>	<u>Research Personnel</u>
ManLabs, Inc.	B. S. Lement, Morris Cohen, E. M. Passmore, K. Kreder and I. Vilks
Massachusetts Institute of Technology	D. A. Thomas, M. F. Comerford, E. S. Meieran and J. F. Peck
Rutgers, the State University	S. Weissman, N. Hosokawa and G. Padower
University of Liverpool	W. S. Owen, D. Hull, J. D. McIvor, I. McIvor and A. R. Rosenfield
University of Cambridge	P. B. Hirsch, T. E. Mitchell and R. A. Foxall

ABSTRACT

In addition to covering the results obtained on this program during 1962-63, the main accomplishments since 1959 and their implications with respect to mechanical properties of refractory metals are discussed in this report.

During 1962-63, ManLabs has investigated the relation between microstructural features and the ductile-brittle transition behavior of recrystallized, worked, and annealed molybdenum strip. Starting with the recrystallized condition, the following microstructural changes occur as a result of rolling deformation: a) flattening and elongation of the primary grains, b) formation of additional primary grain boundaries, c) formation of a first-order substructure consisting of elongated bands, and d) formation of a second-order substructure consisting of cells surrounded by dislocation entanglements. On subsequent annealing, recovery is manifested by polygonization of the cells without affecting the tensile transition behavior. However, a marked rise in transition temperature occurs during the early stages of recrystallization and is associated with the emergence of equiaxed, cell-free regions within the deformed primary grains. The effective surface energy of the molybdenum strip calculated on the basis of the Cottrell-Petch fracture relation is about 3000 ergs/cm²; and the critical crack size as calculated on the basis of the Griffith-Orowan relation is approximately equal to the first-order subgrain size. It is proposed that the tensile ductility transition is mainly associated with the occurrence of strengthening effects due to necking, and that T_d is determined by the intersection of the fracture stress and the necking stress vs. temperature curves.

M.I.T. has demonstrated that fibering in tungsten wire involves the formation of ribbon-like grains containing a dislocation cell structure. The previously hypothesized crystallographic mechanism of fibering has been confirmed. In many of the cells, "striation" and "check mark" patterns were observed, which are interpreted as fine platelets with slight misorientations resulting from bending and twisting of the ribbon-like grains. Drawn iron-3.2% silicon wires recover extensively prior to recrystallization, with an activation energy varying from about 54 kcal/mol at 10% recovery to 83 kcal/mol at 50% recovery. For wire-drawn columbium, the textural and microstructural changes as well as the work-hardening characteristics are not affected by substantial differences in impurity content. A nearly random texture can be produced in columbium, initially possessing a strong $\langle 110 \rangle$ fiber texture, by wire drawing followed by recrystallization - annealing.

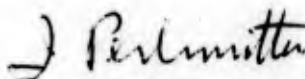
Rutgers has shown that pre-yielding of zone-refined single crystal tantalum is associated with slip primarily in the (101) [111] and the (101)[111] systems in which the shearing strains increase. When discontinuous yielding occurs, the shearing strain in the principal slip system decreases to zero, while that of the secondary system continues to increase. The initial build-up of microstrains is associated with mutual interactions of long-range stress fields, whereas discontinuous yielding is attributed to relaxation in the principal system due to dislocation movement on the secondary slip system. For single crystal tungsten,

the lattice distortion produced by deformation at 185°C is distributed over many slip systems, but over only a few systems at -195°C.

Liverpool has found that the dislocation distributions developed by deformation of tantalum at room temperature are similar to those in iron deformed at a lower temperature. The number of dislocations generated is proportional to the plastic strain raised to an exponent that is dependent on test temperature, grain size and initial structure; moreover, the Keh-Weissmann square-root relation for the flow stress does not hold. The binding energy between oxygen atoms and dislocations in tantalum is about 0.54 e.v. and there is some evidence that electrostatic repulsion is involved. On strain aging at 100°C, the kinetics of the increase in the locking parameter and in the lattice friction stress are not the same.

The work at Cambridge indicates that the thermally activated component of the flow stress in columbium and tantalum single crystals is approximately independent of shear strain and has about the same temperature dependence as the strain-rate sensitivity of the flow stress. For tantalum, the activation energy corresponding to the temperature dependence of the strain rate reaches a constant value of about 1.5 e.v. above 500°K. A hypothesis involving the dissociation of screw dislocations along three intersecting symmetrically located planes has been advanced to account for the temperature-dependent lattice friction stress of b.c.c. metals.

This technical documentary report has been reviewed and is approved.



I. Perlmutter
Chief, Physical Metallurgy Branch
Metals and Ceramics Division
AF Materials Laboratory

TABLE OF CONTENTS

Part and Section	Page
I. SUMMARY OF RESULTS	1
A. <u>ManLabs, Inc.</u> - Ductile-Brittle Transition in Refractory Metals	1
B. <u>Massachusetts Institute of Technology</u> - Fiberling in Refrac- tory Metals	2
C. <u>Rutgers, the State University</u> - X-ray Back Reflection Diver- gent Beam Strain Analyses of Tantalum and Tungsten Single Crystals	3
D. <u>University of Liverpool</u> - Yield Phenomena in Refractory Metals	4
E. <u>University of Cambridge</u> - A Transmission Electron Micros- copy Study of Defects in Columbium and Tantalum.	5
F. Summary of Practical Implications	5
II. DISCUSSION OF ACCOMPLISHMENTS SINCE 1959	6
A. <u>ManLabs, Inc.</u>	6
B. <u>Massachusetts Institute of Technology</u> - Fiberling in Refrac- tory Metals	7
C. <u>Rutgers, the State University</u>	8
D. <u>University of Liverpool</u>	10
E. <u>University of Cambridge</u>	11
III. INTRODUCTION	12
A. Scope	12
B. Experimental Materials	12
IV. DUCTILE-BRITTLE TRANSITION IN REFRACTORY METALS	13
A. Introduction	13
B. Experimental Procedures	13

TABLE OF CONTENTS (Cont.)

Part and Section	Page
C. Effect of Rolling Deformation and Subsequent Annealing on Substructure of Molybdenum Strip	15
D. Effect of Recrystallized Grain Size on the Fracture of Molybdenum Strip	40
E. Effect of Plastic Deformation and Annealing on the Tensile Ductility Transition	46
F. Calculation of Effective Surface Energy for Fracture	54
G. Calculation of Critical Crack Length	59
H. Calculation of Change in Fracture Stress at T_d	59
I. Criterion for Occurrence of Tensile Ductility Transition	67
REFERENCES	72
V. FIBERING IN REFRACTORY METALS	74
A. Scope	74
B. Transmission Electron Microscope Study of Substructure in Tungsten Wire	74
C. Substructure and Mechanical Properties of an Fe-Si Alloy	94
D. Structures and Properties of Columbium Wires	107
REFERENCES	122
VI. X-RAY BACK-REFLECTION DIVERGENT BEAM STRAIN ANALYSES OF TANTALUM AND TUNGSTEN SINGLE CRYSTALS	124
A. Yielding of Tantalum Single Crystals	124
B. Strain Analysis Associated with Ductile-Brittle Transition of Tungsten Crystals	136
C. Improvement of the Precision of the Strain Analysis	137
REFERENCES	142

TABLE OF CONTENTS (Cont.)

Part and Section	Page
VII. YIELD PHENOMENA IN REFRACTORY METALS	143
A. Scope	143
B. Dislocation-Interstitial Binding Energies	143
C. The Strain-Aging of a Dilute Tantalum-Oxygen Alloy	148
D. The Variation of Flow Stress with Substructure in Tantalum	161
REFERENCES	180
VIII. A TRANSMISSION ELECTRON MICROSCOPY STUDY OF DEFECTS IN COLUMBIUM AND TANTALUM	182
A. Introduction	182
B. Experimental Techniques	182
C. Mechanical Test Results	182
D. Peierls force in b.c.c. metals	190
E. Electron microscopy	192
REFERENCES	194
APPENDIX A	195
APPENDIX B	198
APPENDIX C	219

LIST OF FIGURES

Figure		Page
1	Thin-film electron micrographs of recrystallized molybdenum (Mo-E2) strip	17
2	Thin-film electron micrographs of slightly worked molybdenum (Mo-E1) strip	17
3	Thin-film electron micrographs of molybdenum strip, rolling plane sections, showing cell structure development upon progressive deformation	18
4	Substructure in moderately worked molybdenum strip, rolling plane section	20
5	Substructure in moderately worked, 46% reduction, molybdenum (Mo-E1) strip, longitudinal section	22
6	Thin-film electron micrograph of moderately worked, 46% reduction, molybdenum (Mo-E1) strip, longitudinal section	23
7	(a) Thin-film electron micrograph of moderately worked (46% reduction) molybdenum (Mo-E1) strip, longitudinal section, showing a broad band. (b), (c) and (d) are consecutive selected area diffraction patterns, $\{211\}$, taken by traversing broad band in (a) from top to bottom. These show a variation in misorientation along the length of the band	25
8	(a) Thin-film electron micrograph of moderately worked, 46% reduction, molybdenum (Mo-E1) strip, longitudinal section. (b), (c) and (d) consecutive selected area diffraction patterns taken by traversing several bands in (a) going from top to bottom. A change in orientation from (311) to (211) was found	26
9	(a) Thin-film electron micrograph of moderately worked, 46% reduction, molybdenum (Mo-E1) strip, longitudinal section, showing a high-angle grain boundary. (b), (c) and (d) are selected area diffraction patterns taken in area above the boundary, at the boundary, and below the boundary. Changes in orientation from (311) to (111) to (100) were found	28
10	Substructure in moderately worked, 46% reduction, molybdenum (Mo-E1) strip, transverse section	29
11	Substructure in heavily worked (88% reduction) molybdenum (Mo-E1) strip, rolling plane sections	31
12	Substructure in heavily worked, 88% reduction, molybdenum (Mo-E1) strip, longitudinal section	32

LIST OF FIGURES (Cont.)

Figure		Page
13	Light micrographs of moderately worked (46% reduction) and annealed (1 hour at 1000°C) molybdenum (Mo-E1) strip, showing recrystallized regions	34
14	Thin-film electron micrographs of moderately worked, 46% reduction, and annealed (1 hour at 1000°C) molybdenum (Mo-E1) strip	36
15	Substructure in heavily worked, 88% reduction, and annealed (1 hour at 900°C) molybdenum (Mo-E1) strip rolling plane section	37
16	Thin-film electron micrograph of heavily worked and annealed (1 hour at 900°C) molybdenum (Mo-E1) strip, rolling plane section, showing clearly defined cell boundaries (arrow A) and cell coalescence (arrow B)	38
17	Effect of the test temperature on the tensile properties of high purity molybdenum (Mo-E2) strip in the as-recrystallized condition ($l^{-1/2} = 6.2 \text{ mm}^{-1/2}$)	41
18	Observed and predicted effects of grain size on yield stress, fracture stress, and fracture strain of molybdenum (Mo-E2) strip in the as-recrystallized condition tested at -40°C	43
19	Log-log true stress - true strain curve of molybdenum (Mo-E2) strip in the as-recrystallized condition ($l^{-1/2} = 6.2 \text{ mm}^{-1/2}$) tested at -40°C	45
20	Effect of the test temperature on the tensile properties of molybdenum (Mo-E1) strip in the slightly worked condition (5% reduction)	47
21	Effect of the test temperature on the tensile properties of molybdenum (Mo-E1) strip in the moderately worked condition (46% reduction)	48
22	Effect of the test temperature on the tensile properties of high purity molybdenum (Mo-E1) strip in the heavily worked condition (88% reduction)	49
23	Light micrographs of high purity molybdenum (Mo-E1) strip, tensile specimen after testing at -70°C, showing transgranular cleavage fracture	51
24	Light micrographs of high purity molybdenum (Mo-E1) strip tensile specimen after testing at -50°C, showing transgranular cleavage fracture	52

LIST OF FIGURES (Cont.)

Figure		Page
25	Effect of recovery-annealing (1 hour at 1000°C) on the tensile properties of moderately worked (46% reduction) molybdenum (Mo-E1) strip	53
26	Effect of recovery-annealing (1 hour at 900°C) on the tensile properties of heavily worked (88% reduction) molybdenum (Mo-E1) strip	55
27	Correction factor ($1/q_p$) for reducing applied tensile stress to effective flow stress (Bridgman)	65
28	Schematic variation of the yield stress (σ_y), necking stress (σ_n), fracture stress (σ_F) for the unnecked condition, and fracture stress (σ_{Fn}) for the necked condition vs. test temperature	69
29	Light micrographs of as-drawn tungsten wire	75
30	Transmission electron micrograph of longitudinal section of as-drawn tungsten wire	76
31	As-drawn tungsten wire, second area	76
32	As-drawn tungsten wire, third area	77
33	As-drawn tungsten wire, electron micrograph	79
34	Tungsten wire annealed at 900°C for 10 min.	79
35	Schematic diagram of bent and twisted fiber containing cell structure	80
36	As-drawn tungsten wire	81
37	As-drawn tungsten wire	81
38	Crystal UC-34, transverse sections	82
39	Crystal UC-34, longitudinal section, electron micrograph with corresponding electron diffraction pattern	82
40	Crystal UC-34, 45° section: (a) electron micrograph, (b) electron diffraction pattern	84
41	Geometry of streaks in reciprocal space, showing intersection of streaks with $(\bar{1}11)$ plane and (110) plane	85
42	Crystal UC-44, transverse section, electron micrograph with corresponding electron diffraction pattern	86

LIST OF FIGURES (Cont.)

Figure		Page
43	Crystal UC-34, 45° section. The specimen was tilted about 2° in the microscope between (a) and (b), resulting in changes in striation contrast	86
44	Tungsten wire annealed at 1000°C for 10 min	89
45	Tungsten wire annealed at 1200°C for 10 min	89
46	Fiber width vs. annealing temperature for 10 and 30-minute anneals	90
47	Fiber widths vs. annealing time at constant temperature	91
48	Tungsten wire annealed at 1500°C for 30 min	92
49	Tungsten wire annealed at 900°C for 10 min.	93
50	Optical micrograph of tungsten wire annealed at 1200°C for 10 min.	93
51	Flow stress vs. inverse square root of fiber widths	95
52	Representative engineering stress-strain relationships for Fe-Si wire cold drawn 31% and annealed for 30 minutes at temperatures indicated	96
53	Diamond pyramid hardness as a function of annealing time for Fe-Si wire cold drawn 66%	98
54	Residual fraction of hardness, (1-f), of cold drawn Fe-Si wire as a function of annealing time	99
55	Fe-3.2% Si, drawn 66% reduction in area	104
56	Fe-3.2% Si, drawn 66%	104
57	Fe-3.2% Si, drawn 66% and annealed at 600°C	105
58	Fe-3.2% Si, drawn 66% and annealed at 600°C	106
59	Fe-3.2% Si, drawn 66% and annealed at 700°C for 30 sec	108
60	Fe-3.2% Si, drawn 66% and annealed at 700°C for 1 min	108
61	Drawing texture of Cb-E1 wires with initial <110> fiber texture	109
62	Drawing texture of Cb-E1 wires with random texture	111
63	Microhardness of drawn Ni and Cb	112

LIST OF FIGURES (Cont.)

Figure		Page
64	Microhardness of drawn Cb and Ni	114
65	Microhardness of drawn and rolled Cb	115
66	Columbium wire Cb-E1	116
67	Columbium wire Cb-E1	116
68	Columbium wire Cb-E1	117
69	Columbium wire Cb-E1	117
70	Columbium wire Cb-E1	118
71	Columbium wire Cb-E1	118
72	Columbium wire Cb-E4	120
73	Columbium wire Cb-E4	120
74	Stress-Strain curve of Ta crystal	126
75	Effect of compression on the principal strains in zone-refined tantalum crystal	128
76	Dependence of shear strain upon direction on (101) slip plane	132
77	Dependence of shear strain upon direction on (10 $\bar{1}$) slip plane	134
78	Dislocation structure in tantalum after yielding	135
79	Divergent beam pattern of tungsten crystal compressed at -195°C ($\epsilon = 0.48\%$)	138
80	Divergent beam pattern of tungsten crystal compressed at 185°C ($\epsilon = 7.8\%$)	139
81	Schematic representation of the generation of pseudo-kossel patterns by the divergent beam method	140
82	Ta-E2 annealed 1300°K	146
83	Schematic stress-strain curve for a prestrain, age and retest sequence	149
84	Strain-hardening index as a function of aging time	152
85	$\Delta\bar{\sigma}_f$ and k_y as a function of aging time at 100°C	154

LIST OF FIGURES (Cont.)

Figure		Page
86	σ_f and k_y as a function of aging time at 100°C	155
87	$\Delta\sigma_f$ and k_y as a function of aging time at 100°C	156
88	σ_f and k_y as a function of aging time at 100°C	157
89	$\Delta\sigma_f$ and k_y as a function of aging time at 100°C	158
90a	Tantalum-oxygen alloy (Ta-E4) annealed 1750°C, deformed 7.5 percent at 293°K	159
90b	Tantalum-oxygen alloy (Ta-E4) annealed 1750°C, deformed 7.0 percent at 240°K	159
91	Ta(1) strained 4.3% at 293°K	165
92	Ta(1) strained 6.2% at 293°K	165
93	Ta(1) strained 9.9% at 293°K	165
94	Ta(1) strained 6.9% at 240°K	165
95	Initial substructure in Ta(2)	166
96	Ta(2) after Lüder's strain	166
97	Ta(2) strained at 293°K	166
98	Initial substructure in Ta(3)	166
99	Experimental stress-strain curves	168
100	Dislocation density as a function of flow stress according to equation (8)	169
101	Variation of dislocation density with strain	171
102	Variation of dislocation density with strain	172
103	Variation of dislocation density with strain according to equation 9	173
104a	Definition of σ_{fo} according to equations 6 and 12	178
104b	Definition of σ_{fo} taking account of Peierls stress and initial dislocation density	178
105	Temperature dependence of T_o for single crystals of tantalum and columbium	184

LIST OF FIGURES (Cont.)

Figure		Page
106	Temperature cycling experiment on a Tantalum crystal	186
107	Temperature dependence of flow stress for tantalum single crystals	187
108	ΔT vs. τ curves for tantalum single crystals	188
109	Temperature dependence of term indicative of strain-rate sensitivity of flow stress for tantalum single crystals	189
110	Activation energy vs. temperature for tantalum single crystals . .	191
C-1	Effect of prior recovery annealing (for 16 hours) on subsequent recrystallization (900°C , 1/4 hour) on microhardness of columbium (Cb-E1 and Cb-E4) wire	220

LIST OF TABLES

Table	Page
1 Conditions and Interstitial Contents of Materials	14
2 Average Substructure Dimensions* in Mo-E1 and Mo-E2 Strip Materials	35
3 Procedures and Materials Used to Determine the Effect of Grain Size on Yield Stress, Fracture Stress, and Fracture Strain	42
4 Calculated Effective Surface Energy of Molybdenum Strip Just Below Transition Temperature Based on Primary Grain Size	57
5 Calculated Effective Surface Energy of Molybdenum Strip Just Below Transition Temperature Based on Subgrain Size	58
6 Calculated Critical Crack Length of Molybdenum Strip Based on Primary Grain Size	60
7 Calculated Critical Crack Length of Molybdenum Strip Based on Subgrain Size	60
8 Comparison of Calculated and Measured Values of Fracture Stress Ratio at T_d	62
9 Comparison of Round and Flat Tensile Tests of Steel	66
10 Comparison of Calculated Values of n and Measured Values of ϵ_u	71
11 Activation Energies for Recovery in Fe-Si Based on Equal Fractions of Recovered Hardness.	101
12 Effect of Compression on the Principal Strains in Zone Refined Tantalum Crystal	127
13 Computation of Maximum Resolved Shear Stress of Zone-Refined Ta Single Crystal Deformed by Compression	129
14 Computation of Shear Strains in (101) Slip Plane of Zone-Refined Tantalum Crystal from Principal Strains.	131
15 Computation of Shear Strain in (10 $\bar{1}$) Slip Plane of Zone-Refined Tantalum Crystal From Principal Strains	133

LIST OF TABLES (Cont.)

Table		Page
16	Measured and Calculated Binding Energies	145
17	Details of Specimen Preparation, Grain Size, Dislocation Density and Distribution	163
18	Flow Stress and Work Hardening Parameters	175
19	Calculated Parameters (c.g.s. units).	177
B-1	Interstitial Contents of Fabricated Experimental Materials	199
B-2	Results of Fabrication of Tantalum and Columbium Experi- mental Materials to 30-mil Wire	201
B-3	Results of Fabrication of Tungsten and Molybdenum Experi- mental Materials to Wire	202
B-4	Results of Fabrication of Tantalum and Columbium Experi- mental Materials to Strip	203
B-5	Results of Fabrication of Tungsten and Molybdenum Experi- mental Materials to Strip	204
B-6	Fabrication Schedule of Single Crystal Molybdenum Experi- mental Materials to Wire and Strip	206
B-7	Fabrication Schedule for Single Crystal Tungsten Experi- mental Materials to Wire	208
B-8	Fabrication Schedule for Mo-E4 Strip Bar	209
B-9	Fabrication Schedule for Mo-E4 Strip	209
B-10	Fabrication Schedule for W-E1, W-E2, and W-E4 Wire and Strip Bars	210
B-10-A	Conditioning of Extruded Bars	213
B-10-B	Swaging Sequence	214
B-10-C	Conditioning of Swaged Bars	215
B-11	Fabrication Schedule for W-E1 and W-E2 Strip	216

I. SUMMARY OF RESULTS

The results obtained during 1962-63 by the five research participants* listed below are presented in Sections IV to VII in the following order:

<u>Section</u>	<u>Research Participant</u>	<u>In Charge</u>
IV	ManLabs, Inc.	Dr. B.S. Lement
V	Massachusetts Institute of Technology	Dr. D.A. Thomas
VI	Rutgers, the State University	Dr. S. Weissmann
VII	University of Liverpool	Dr. W.S. Owen
VIII	University of Cambridge	Dr. P.B. Hirsch

The main findings of each participant are summarized in this section.

A. ManLabs, Inc. - Ductile-Brittle Transition in Refractory Metals

1. As observed by light microscopy, thin-film electron microscopy and selected area electron diffraction, deformation of molybdenum strip (Mo-E1 and Mo-E2) by rolling results in a structure of flattened and elongated primary grains. A first-order substructure consisting of elongated bands is present within these grains. The planes on which the band boundaries occur appear to coincide with {110}, {112} or {123} slip planes.

1.1 In strip rolled to about 50% reduction, the bands (about 1.5 microns in width) contain a second-order of substructure that consists of approximately equiaxed cells (about 0.5 micron in size).

1.2 In strip rolled to about 90% reduction, additional elongated primary grain boundaries form, the band boundaries straighten with an orientation approximately parallel to the rolling plane, and the cells become indistinguishable from the bands.

2. The average thickness (about 0.3 micron) of the bands measured perpendicularly to the rolling plane of the heavily worked strip is of the same order of magnitude as the coherently reflecting lattice domain size calculated from x-ray line broadening measurements.

3. Moderate and heavy plastic deformation of molybdenum strip by rolling results in marked decreases in the tensile ductility transition temperature (T_d). Although the formation of polygonized cells by the rearrangement of tangled dislocations into clearly defined boundaries and an increase in cell size of about 50% were found to occur during recovery-annealing of the deformed molybdenum strip, such substructural changes do not appear to have any significant effect on the transition behavior. On the other hand, a definite rise in transition temperature occurs during the early stages of recrystallization. This is attributed to the formation of equiaxed cell-free regions intermediate in size between the polygonized cells and the elongated primary grains.

4. For recrystallized molybdenum strip, it was found that the observed fracture stress and strain values as determined at constant test

*Manuscript released by the authors, 5 April 1963, for publication as an ASD Technical Documentary Report.

temperature (-40°C) as a function of grain size are higher than predicted on the basis of their measured temperature dependence at constant grain size.

5. For recrystallized molybdenum strip tested at -40°C, the yield parameter (k_y) was found to be 2.5×10^8 cgs as determined by the Petch method (lower yield stress vs. square root of mean grain diameter) and 1.3×10^8 cgs as determined by the extrapolation method. These values are in relatively good agreement with k_y as predicted on the basis of the Rosenfield relation (1.7×10^8 cgs).

6. Using the Cottrell-Petch fracture relation, as modified for the effect of plastic straining during the tensile test, the effective surface energy (γ') for the as-recrystallized as well as the as-worked conditions is calculated to be about 3000 ergs/cm² at T_d . Based on the Griffith-Orowan fracture relation, the calculated critical crack size is approximately equal to the first-order subgrain size.

7. The discontinuous change in both ductility and fracture stress that occurs at T_d does not correlate with changes in fracture mode, mechanical twinning, or the occurrence of nil-ductility. Rather the tensile ductility transition appears to be related to the occurrence of necking as the temperature is raised just above T_d .

8. Calculations were made of the change in fracture stress at T_d based on the concept that necking results in strengthening contributions such as a) increased local strain rate, b) plastic constraint, and c) decrease in effective grain size; good agreement (within 10%) was obtained between the calculated and the observed values for the various conditions of molybdenum strip studied. Accordingly, a suggested criterion for the tensile ductility transition is the intersection of the fracture stress (σ_F) and the necking stress (σ_n) vs. temperature curves, i. e. $\sigma_F = \sigma_n$ at T_d .

B. Massachusetts Institute of Technology - Fiberling in Refractory Metals

1. Based on transmission electron microscopy of thin films, fiberling in 30-mil tungsten wire (W-P4) involves the formation of ribbon-like grains about 0.3 micron thick and up to 10 microns wide. Most of these grains contain a cell structure of size 0.1 to 1 micron. The previously proposed crystallographic mechanism of the formation of the ribbon-like grains has been confirmed by electron diffraction.

2. Unusual "striation" and "check mark" patterns were found in many of the cells present in both W-P4 wire and in groove-rolled W-P5 tungsten single crystals. These patterns are interpreted as a fine substructure consisting of 150Å thick platelets which are parallel to $\langle 110 \rangle$ and misoriented with respect to neighboring platelets by a twist of 1.8 minutes of arc about a $\langle 110 \rangle$ axis.

The platelets are believed to be a consequence of the bending and twisting of the ribbon-like grains in the heavily drawn specimens.

3. Annealing of W-P4 wire up to 1500°C results in dislocation annihilation and rearrangement, polygonization, and migration of existing boundaries without major textural change. Conventional recrystallization involving the formation of new grains does not occur.

4. A Petch-type relationship exists between the flow stress and the fiber width of annealed W-P4 wire.

5. Drawn iron - 3.2% silicon wires recover extensively prior to recrystallization. The activation energy for the process ranges from 54,000 cal/mol at 10% recovery to 83,000 cal/mol at 50% recovery.

6. Softening of iron - 3.2% silicon is accompanied by substructural changes which are readily detectable by dislocation etch-pit techniques. Recrystallization starts at deformation bands within the primary grains and subsequently occurs at grain boundaries.

7. Despite varying interstitial contents, columbium wires undergo similar changes in texture, microstructure, and work-hardening characteristics during wire drawing to 98% reduction. The marked increase in work hardening observed at high deformation appears to be characteristic of b.c.c. metals.

8. Annealed columbium wire with an initial $\langle 110 \rangle$ fiber texture achieves a random texture after wire drawing approximately 25 to 75% reduction followed by recrystallization-annealing. This is associated with the occurrence of inhomogeneous lattice rotations (deformation bands).

C. Rutgers, the State University - X-ray Back Reflection Divergent Beam Strain Analyses of Tantalum and Tungsten Single Crystals.

1. Based on the x-ray back-reflection divergent beam method, complete strain analyses were obtained of zone-refined tantalum (Ta-E5) single crystals with an (012) orientation as a function of amount of deformation in compression.

1.1 In the pre-yield (microstrain) region, yielding is associated with accumulation of shearing strains, principally in the (101) $[11\bar{1}]$ and the (10 $\bar{1}$) $[111]$ slip systems. Increased compression in the pre-yield region from 0.077% to 0.097% results in increased shearing strain on both active slip planes.

1.2 On further compression to 1.44%, discontinuous yielding occurs and the shearing strain in the principal slip system decreases to zero, whereas that in the secondary slip system continues to increase and attains a value of 0.45%.

1.3 The build-up of microstrains in the pre-yield region is explained in terms of mutual interactions of long-range stress fields created by

the active slip systems. Subsequent discontinuous yielding is attributed to the relaxation of strains in the principal slip system due to the movement of dislocations on the secondary slip system.

1.4 Dislocation pinning by impurities is not considered to be a primary cause of discontinuous yielding. In some cases, however, impurities may significantly affect the strain distribution on the active slip systems and thereby indirectly affect the yield behavior.

2. Strain analyses of tungsten single crystals (W-E5) compressed various amounts at 185°C, room temperature and -195°C were carried out in an exploratory study of the ductile-brittle transition.

2.1 For specimens deformed at 185°C, the lattice distortions introduced affect virtually all lattice planes and the strains are distributed over many slip planes.

2.2 For specimens deformed at -195°C, the lattice distortions introduced appear to affect only a few sets of lattice planes over which the strains are mainly distributed.

3. Two methods were developed to improve the precision of the x-ray measurements on which the strain analyses are based.

3.1 One method utilizes a quartz crystal for internal calibration in order to determine the specimen-to-film distance. The precision of strain measurement by this method is ± 0.0002 (strain units).

3.2 The other method involves multiple exposures at different specimen-to-film distances. Direct measurement of the specimen-to-film distance is eliminated and the precision of strain measurement is also ± 0.0002 .

D. University of Liverpool - Yield Phenomena in Refractory Metals

1. Based on thin-film electron microscopy of deformed tantalum-oxygen (Ta-E4), it was found that the dislocation distributions developed by deformation of tantalum at room temperature are similar to those in iron deformed at lower temperatures. The distribution and density of dislocations after a given amount of strain is dependent on the initial arrangement of the dislocations; and there is also some evidence that subboundary dislocation networks present in the as-annealed material persist after extensive deformation.

2. If the initial substructure consists of randomly arranged dislocations, the rate of increase of dislocation density with plastic strain is independent of the initial dislocation density; whereas the density increases more rapidly if the initial substructure is in the form of hexagonal networks. The increase of dislocation density (N) with plastic strain (ϵ) at room temperature can be represented by $N = C\epsilon^a$ where C is a constant and the exponent a is dependent upon testing temperature, grain size and initial substructure.

3. The Keh-Weissmann square root relationship does not satisfactorily represent the actual relationship between flow stress and dislocation density in tantalum.

4. By quenching experiments conducted on tantalum-oxygen alloys, it was found that a) discontinuous yielding can be completely suppressed by quenching from a sufficiently high annealing temperature; b) the binding energy between oxygen atoms and dislocations in tantalum is 0.54 ± 0.1 e.v. independent of impurity concentration; and c) there is some evidence of an electronic contribution to the dislocation-solute interaction energy.

5. For tantalum-oxygen alloys strain aged at 100°C , a) the value of k_y and the time at which it becomes positive are independent of the prestraining temperature; b) the maximum value of k_y developed is about 15% of the as-annealed value; and c) the aging time at which the lattice friction stress starts to increase is dependent on both the prestraining and final test temperatures, but does not appear to be related to the time that k_y starts to increase.

E. University of Cambridge - A Transmission Electron Microscopy Study of Defects in Columbium and Tantalum.

1. The temperature dependence of the flow stress in shear (τ) of tantalum and columbium single crystals was determined over the range of 77° to 477°K .

2. The thermally activated component of the flow stress (τ_s) is approximately independent of the shear strain, which indicates that the movement of dislocations are controlled by the same frictional mechanism over the entire strain range.

3. The strain-rate sensitivity of the flow stress, as expressed by $1/T \left(\frac{\partial \tau}{\partial \ln \dot{\epsilon}} \right)_T$ where $\dot{\epsilon}$ is the strain rate, has about the same temperature dependence as τ_s .

4. For tantalum, the activation energy corresponding to the temperature dependence of the strain rate increases with temperature and reaches a constant value of about 1.5 e.v. above 500°K where $\tau_s = 0$, which is interpreted as the energy required to overcome a dislocation barrier without the aid of stress.

5. It is tentatively suggested that the large Peierls stress in b.c.c. metals is at least partly due to the dissociation of screw dislocations along three intersecting symmetrically-placed planes. This requires that constriction of the dislocations take place before they can move, and leads to a temperature-dependent frictional stress.

II. DISCUSSION OF ACCOMPLISHMENTS SINCE 1959

From November 1959 to March 1963, this program has been conducted as a joint effort of five research participants. The main accomplishments over this period and the implications with respect to improvement of mechanical properties of refractory metals are discussed below. As listed in Appendix A, 34 reports and papers have resulted from the work accomplished on this program.

A. ManLabs, Inc.

The main accomplishments here have been to elucidate the ductile-brittle transition behavior of tungsten and molybdenum based on tensile testing, light microscopy, thin-film electron microscopy, and x-ray diffraction measurements.

It was shown that during recovery of heavily deformed tungsten wire there is an initial increase in room-temperature strength accompanied by increased delineation of etch-pit subboundaries. This is apparently associated with a process of segregation of interstitials to dislocations, which corresponds to an activation energy of about 35 kcal/mol; however, as indicated by a decrease in the effective x-ray particle size, microtwinning may also contribute to the initial strengthening.

The initial increase in strength observed during recovery was more marked in the tungsten wire than in any of the other refractory metals (wire or strip) studied. This correlates with the fact that prior recovery-annealing was found to inhibit subsequent recrystallization of the tungsten wire, although this phenomenon does not occur in any of the other refractory metals studied. For the tungsten wire, the retarding effect on recrystallization is more marked the lower the recovery-annealing temperature. As for the initial strengthening effect, this behavior suggests that some type of relatively stable substructure is formed due to segregation of interstitials. From the standpoint of enhancement of elevated-temperature strength, prior recovery-annealing may prove advantageous for worked tungsten alloys.

In the past, the sharp drop in room-temperature ductility on annealing the heavily deformed tungsten wire above about 1100°C has been attributed to a discontinuous microstructural change such as extensive polygonization and subgrain growth. In the present study, the drop in ductility was correlated with a continuous rise of the ductility transition temperature (T_d) to above room temperature. Since the effective surface energy (γ') as calculated by the Cottrell-Petch fracture relationship on the basis of fiber width does not change with increase in recovery-annealing temperature, the observed rise of T_d is mainly attributed to a continuous increase in fiber width.

Based on fiber width, the value of γ' as calculated using fracture stress values just below T_d is about 7000 ergs/cm² for the tungsten wire studied. Since much smaller values of γ' were calculated on the basis of subgrain size (about 200 ergs/cm²) and values of surface energy are generally believed to be about 2000-3000 ergs/cm², it appears that fiber width

plays a more important role in fracture than does subgrain size. On the other hand, the critical crack size as calculated from the Griffith-Orowan relation appears to correspond more closely to the first-order subgrain size. From the standpoint of ductile-brittle behavior, achievement of as small a fiber width as possible during processing appears to be a worthwhile objective.

For molybdenum strip in the as recrystallized, worked, and recovered conditions, the calculated values of γ' based on primary grain size is about 3000 ergs/cm² just below T_d ; and the critical crack size again corresponds closely to the first-order subgrain size. Deformation by rolling results in a decrease in the effective primary grain size and thereby in T_d . On subsequent annealing of worked molybdenum strip, recovery is manifested by polygonization of the cells without affecting the ductility transition behavior. A marked rise in transition temperature occurs during the early stages of recrystallization and is associated with the emergence of equiaxed, cell-free regions within the deformed primary grains.

The occurrence of the tensile ductility transition in molybdenum strip appears to be mainly associated with the intersection of the fracture stress and necking stress vs. temperature curves. As compared to the tensile behavior below T_d , the occurrence of necking above T_d results in higher fracture stress and strain values because of such factors as increased local strain rate, increased plastic constraint, and smaller effective grain size. In order to lower T_d , it is necessary to raise the fracture stress vs. temperature curve relative to the necking stress vs. temperature curve.

Based on x-ray measurements of lattice domain size and lattice strain, the recovery ranges of tungsten, molybdenum, tantalum and columbium strip materials were determined. It was found that the lattice strains do not change as much as the particle size, which indicates that most of the lattice imperfections are not eliminated during recovery but rather are incorporated into arrays or boundaries. For molybdenum strip, the size of the cells formed by dislocation tangles was found to be of the same magnitude as the x-ray lattice domain size.

B. Massachusetts Institute of Technology - Fiberizing in Refractory Metals.

The main accomplishments have been advances in knowledge of microstructures, substructures, textures, and mechanical properties of b. c. c. metals such as tungsten, columbium, and iron - 3.2% silicon in wire form.

Wires drawn more than about 50% reduction in area develop ribbon-like rather than true fiber-like grains. This finding is explained by a simple crystallographic mechanism based on the $\langle 110 \rangle$ fiber texture formed in b. c. c. wires. Although past experience has indicated that the $\langle 110 \rangle$ texture of drawn b. c. c. wires is retained upon recrystallization, such a texture in columbium can be converted to a nearly random texture by drawing 25 to 75% and recrystallizing. It is known that texture control as obtained by recrystallizing cold worked

wires can enhance torsional strength, which is important for an application such as coil springs. However, even greater enhancement may result from texture control in as-worked wires, which are much stronger than after recrystallization.

In contrast to the work-hardening saturation that occurs in f. c. c. metals, wire drawing more than about 50% results in substantial hardening in b. c. c. metals. Although the basic mechanism involved has not been understood, this effect has been commercially exploited for a long time in making high-strength tungsten wire and high-strength music-wire (heavily drawn pearlitic steel). Based on the present work as carried out on columbium wire, it appears that the marked work hardening does not depend on interstitial content (from 50 to 450 ppm) or initial texture but rather is characteristic of b. c. c. metals. However, the actual strength level obtained by wire drawing depends on the particular metal and its purity, and a higher strength would be expected if one metal is stronger than another prior to drawing.

The tensile ductility transition temperature of 30 mil tungsten wire drawn at about 800°C was found to be lowered about 100°C by subsequent drawing to 20 mils at 150°C. This large reduction in transition temperature indicates the advantage of using relatively low drawing temperatures.

Complex substructures and substructural changes during annealing were observed in tungsten and iron - 3.2% silicon by transmission electron microscopy and dislocation etch-pit techniques, respectively. A fine substructure has been found in tungsten wire, which is interpreted as twist-misoriented platelets about 150 Å thick. These exist within many of the cells present in both the commercial tungsten wire and groove-rolled tungsten single crystals studied. The twist-misorientation apparently results from bending and twisting of the ribbon-like grains, and therefore appears unique to wire drawing.

In confirmation of previous work based on microscopic and x-ray results, transmission electron microscopy shows that the migration of existing boundaries is the principal mechanism of structural change during annealing of commercial tungsten wire. The texture is little changed and conventional recrystallization does not occur. In contrast, columbium and iron - 3.2% silicon recrystallize in a conventional manner. Since these materials were not cold drawn as severely as the tungsten wire, they may possess regions of sufficiently differing orientations to facilitate nucleation of recrystallized grains.

C. Rutgers, the State University

The main accomplishments have been a) determination of dislocation substructure in tungsten and tantalum by means of x-ray reflection microscopy, double crystal x-ray diffraction, and thin-film electron microscopy; and b) strain analyses of tantalum single crystals deformed in compression based on the x-ray divergent beam method.

Three orders of substructure were detected in a tungsten single crystal. Information on dislocations at subboundaries was obtained from the disorientation angles between adjacent subgrains, and on dislocations within subgrains from measurements of lattice misalignment.

Studies of the deformation substructure of polycrystalline tungsten and tantalum has revealed structural features similar to those in other b.c.c. metals. Starting with the annealed condition, progressive deformation results in such dislocation features as superjogs, dipoles, tangles, and cell structures. For a sufficiently high concentration of impurities, precipitation of a second phase may occur in the form of clusters. It was shown that such clusters can function as barriers to dislocation movement and it is possible to compute the internal stresses in their vicinity from the radii of curvature of the dislocation segments bowed out between the clusters. Stacking faults were observed in impure tungsten specimens annealed above 2000°C, as well as in those quenched from above 2500°C with or without prior deformation. The formation of stacking faults in tungsten appears to be associated with impurity segregation.

The observations made suggest that enhanced strength can be obtained by the following types of barriers to dislocation movement: a) dense dislocation tangles, b) pinning by impurities, c) interspersed small particles of a second phase, and d) stacking faults. The ability of impurity atoms to facilitate the formation of stacking faults is of particular interest since these impart strong work-hardening characteristics. When dislocations meet due to intersecting slip planes, interaction occurs and subsequent motion is obstructed to varying degrees. The obstruction is most intense if the dislocation split apart to form wide stacking faults that provide virtually impenetrable plane barriers with respect to the passage of dislocations gliding on other planes. It is possible that enhanced strength can be developed in this way without making the material excessively brittle. Furthermore, materials with broad stacking fault ribbons may possess enhanced elevated temperature strength; for it is difficult to move such ribbons in any direction other than in their own plane regardless of the temperature. Since the movement of stacking fault ribbons is also obstructed by the presence of fine second phase particles, the elevated temperature strength can be further enhanced. It seems likely that alloying elements could be utilized for the purpose of either widening stacking fault ribbons or stabilizing them by the formation of fine second phase particles.

By means of strain analyses, it has been shown that pre-yielding of tantalum single crystals is primarily associated with plastic strain accumulation on two (101) [111] slip systems; and that discontinuous yielding is accompanied by release of strain to zero in the principal slip system concurrent with an increase of strain in the secondary slip system. Based on these results, it may be advantageous to provide b.c.c. materials with a special texture such that plastic strains introduced by deformation can be distributed over many rather than a few slip systems. Under such conditions, it is conceivable that continuous instead of discontinuous yielding would occur.

A preliminary study of the ductile-brittle transition in single crystal tungsten utilizing strain analyses has been carried out. It was found that straining well above the transition temperature results in distortion of virtually all the lattice planes and that many slip planes are activated, whereas straining well below the transition temperature affects only a few sets of lattice planes. Further utilization of this approach may ascertain whether the effects of plastic deformation change continuously or discontinuously at the transition temperature.

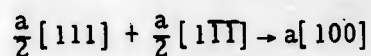
D. University of Liverpool

The major accomplishments have been more accurate determinations of the yield parameters of tantalum, as well as a more basic understanding of how these parameters are influenced by such variables as interstitial content, dislocation substructure, plastic strain, and thermal treatments.

It was shown that the empirical Petch relationship is satisfied only when the grain size differences are achieved without a variation in the substructure. More reliable values of k_y and σ_i are obtained by analysis of the stress-strain curve corresponding to a known grain size. The initial substructure has a marked effect upon k_y in very dilute alloys; however, k_y does not vary with substructure if the total interstitial content is greater than 150 ppm. This effect has been satisfactorily explained in terms of Cottrell interaction concepts. Dislocation pinning can occur when a small fraction of the available dislocation sites are occupied by interstitial atoms. In accordance with the theory of Lothe, weak pinning of this type is only slightly temperature dependent.

Maximum values of k_y are obtained by slow cooling from the annealing temperature. These values are a measure of the local stress necessary to generate dislocations from virgin crystal at or near a grain boundary. The maximum values of k_y for a number of b. c. c. metals were found to be proportional to the shear modulus. During strain aging, the rate controlling step of the process that results in an increase in σ_i is either the diffusion of the slowest moving interstitial atom or the migration of vacancies. The major part of the interaction energy between oxygen atoms and dislocations in dilute tantalum-oxygen alloys is due to elastic interaction, but there is probably also a small electronic interaction contribution.

During cold work the dislocation density increases with plastic strain in accordance with a simple power relationship. However, theories of strain hardening that predict a square-root relationship between dislocation density and flow stress are not applicable to polycrystalline tantalum. On subsequent recovery of cold worked tantalum, the rearrangement of dislocations appears to be the same as in other b. c. c. metals. Low-angle dislocation boundary networks form by the reactions of the type:



E. University of Cambridge

The main accomplishments have been thin-film electron microscopic observations on dislocation substructures in tantalum and columbium, as well as the determination of the strain-rate and temperature dependence of the flow stress of these metals.

For both tantalum and columbium, slip traces on several (110) planes were observed with frequent cross-slip, and studies on annealing twins and stacking-faults were made. Based on the annealing-out of dislocation loops produced by fatigue, an activation energy for self-diffusion of $3.0 + 0.5$ e. v. was obtained. Since this value is significantly less than that obtained by regular methods, it appears that the recovery process may involve conservative climb controlled by pipe diffusion rather than the usually assumed volume diffusion controlled climb process.

Studies of the strain-rate and temperature dependence of the flow stress of tantalum and columbium single crystals indicate that the large temperature dependent part of the flow stress is governed by the Peierls force. A mechanism involving the three-fold dissociation of screw dislocations has been advanced to explain the occurrence of a large Peierls force in b. c. c. metals. The work carried out so far is not sufficiently extensive to allow any practical suggestions to be made regarding the improvement of the mechanical properties of b. c. c. metals; however, it is quite clear that purification results in improvement of ductility, particularly at ordinary temperatures.

F. Summary of Practical Implications

Based on the results of this program, the following suggestions are offered to producers and users of refractory metals and alloys as potentially practical ways of improving the processing and mechanical properties of these materials.

1. Enhancement of elevated temperature strength of as-worked tungsten (and possibly tungsten alloys) may result from recovery treatments that inhibit recrystallization.
2. The use of grain growth inhibitors may act to prevent the sharp drop in room temperature ductility that occurs after recovery-annealing heavily worked tungsten wire above 1100°C .
3. Prior warm working at relatively low temperatures lowers the ductility transition temperature of tungsten and molybdenum, and may increase their resistance to cracking on subsequent processing at or near room temperature.
4. Enhanced strength of tungsten and columbium wire may result from texture control as obtained by prior working, recrystallizing and final working under controlled conditions.
5. The elevated temperature strength of tungsten and tantalum depends to some extent on the presence of wide stacking faults which act as barriers to glide dislocations. Alloying elements might be utilized either to widen such faults or stabilize them by the formation of fine second phase particles.

III. INTRODUCTION

A. Scope

This report covers the period of 1 April 1962 to 31 March 1963 on Contract No. AF33(657)-8424 and represents the third summary report on "Substructure and Mechanical Properties of Refractory Metals". The first summary report⁽¹⁾ was issued in August 1961 and the second summary report⁽²⁾ was issued in October 1962. The program which started in November, 1959 was carried out with ManLabs, Inc. as the prime contractor and with four other research participants including Massachusetts Institute of Technology, Rutgers, The State University, University of Liverpool (England), and University of Cambridge (England) as subcontractors.

The individual summary reports of the five research participants are given in Sections IV to VII of this report. A progress report⁽³⁾ covering portions of the work described here was issued on 15 August 1962.

B. Experimental Materials

In the second summary report⁽²⁾, the status of experimental materials was presented as of October, 1962. Information was given on interstitial contents fabrication schedules, annealing schedules, and distribution to research participants. Additional information on materials is given in Appendix B of the present report, which includes the following tables.

Table B-1	Interstitial Contents of Fabricated Experimental Materials.
Table B-2	Results of Fabrication of Tantalum and Columbium Experimental Materials to 30-mil Wire.
Table B-3	Results of Fabrication of Tungsten and Molybdenum Experimental Materials to Wire.
Table B-4	Results of Fabrication of Tantalum and Columbium Experimental Materials to Strip.
Table B-5	Results of Fabrication of Tungsten and Molybdenum Experimental Materials to Strip.
Table B-6	Fabrication Schedule of Single Crystal Molybdenum Experimental Materials to Wire and Strip.
Table B-7	Fabrication Schedule for Single Crystal Tungsten Experimental Materials to Wire.
Table B-8	Fabrication Schedule for Mo-E4 Strip Bar
Table B-9	Fabrication Schedule for Mo-E4 Strip.
Table B-10	Fabrication Schedule for W-E1, W-E2, and W-E4 Wire and Strip Bars
Table B-11	Fabrication Schedule for W-E1 and W-E2 Strip

IV. DUCTILE-BRITTLE TRANSITION IN REFRACTORY METALS - Work

carried out at ManLabs, Inc. by B. S. Lement, E. M. Passmore, K. Kreder and I. Vilks.

A. Introduction

This report covers an investigation of the effects of both primary grain structure and substructure on the ductile-brittle transition behavior of recrystallized, worked, and recovery-annealed molybdenum strip. By means of thin-film electron microscopy, an extensive study was made to elucidate the various types of dislocation substructures found present in the various conditions. An attempt was made to correlate the size of substructural cells composed of tangled dislocations with that of coherently reflecting x-ray domains. Based on determination of tensile properties as a function of test temperature, analyses were made of a) the dependence of the fracture stress of recrystallized material on fracture strain, b) the effective surface energy for the recrystallized and worked materials just below the tensile ductility transition temperature (T_d), and c) the role of necking in causing a discontinuous change in both fracture stress and strain at T_d .

B. Experimental Procedures

1. Materials

The conditions and interstitial contents of the molybdenum strip and columbium wire materials used in this program are listed in Table 1. The fabrication and annealing procedures were described in the previous summary report⁽²⁾.

2. Light Microscopy

Specimens of molybdenum strip were mounted, mechanically polished, and electropolished in a solution of alcohol and H_2SO_4 , as described in the previous summary report⁽²⁾. Following etching in boiling 3% H_2O_2 for about 10 seconds, examination of the specimens was performed using a Leitz metallograph at magnifications up to 1500X.

3. Thin-Film Electron Microscopy

Thin-film specimens of the rolling plane were prepared from the bulk molybdenum strip (30 to 40 mils thick) by a procedure similar to that employed by Thomas⁽²⁾, which consists of the following steps:

a) Chemically thin the strip to about 10 mils using modified CP-4 etchant (25 cc glacial acetic acid, 12 cc HNO_3 , 5 cc HF).

b) Cut a 1/8-inch diameter, disc-shaped specimen from the thinned strip.

c) Electrolytically indent center of the specimen to a depth of 2 to 3 mils on each side, using a mixture of 150 cc methyl alcohol, 50 cc HCl, 20 cc H_2SO_4 as the electrolyte, a stainless steel cathode, and a potential of 150 to 200 volts.

d) Electropolish specimen with a cooled (0-10°C) electrolyte of 25% H_2SO_4 in methyl alcohol, using a circular stainless steel cathode and a current

Table 1
Conditions and Interstitial Contents of Materials

<u>Ingot</u>	<u>Product</u>	<u>Condition</u>	<u>Interstitial Content, ppm</u>			
			<u>C</u>	<u>N</u>	<u>O</u>	<u>H</u>
Mo-E1	M1C	5% reduction	-	-	-	-
	M1D	40% reduction	-	-	-	-
	M1D-RX	as-recrystallized (1200°C, 1 hr.)	-	-	-	-
	M1E	46% reduction	32, 34	-	22, 20	-
	M1E-HT	as-recovered (1000°C, 1 hr.)	-	-	-	-
	M1F	52% reduction	13	4	23	0.8
	M1H	88% reduction	42, 53	-	31, 17	-
	M1H-HT	as-recovered (900°C, 1 hr.)	-	-	-	-
Mo-E2	M2C	as-recrystallized (1200°C, 1 hr.)	44	-	15	-
	M2D	40% reduction	-	-	-	-
	M2D-RX	as-recrystallized (1200°C, 1 hr.)	-	-	-	-
	M2E	46% reduction	75	3	46	0.3
	M2F	52% reduction	-	-	-	-
	M2F-RX	as-recrystallized (1200°C, 1 hr.)	-	-	-	-
	M2H	88% reduction	40, 36	-	13, 65	-
	M2H-RX	as-recrystallized (1200°C, 1/2 hr.)	-	-	-	-
Cb-E1	Wire	40% reduction	12-27	50-80	128-161	4-9
Cb-E4	Wire	40% reduction	16**	76**	628-767	17

* approximate

** ingot analysis

density of approximately 4 amps/cm². The electropolishing should be continued until a small hole appears within the indented area, which indicates that the area around the hole may be sufficiently thin to permit transmission of the electron beam. In order to detect the exact moment at which the hole forms, the specimen is observed through a binocular microscope while being electropolished. To prevent etching, electropolishing is terminated by removing the thin-film specimen from the electrolyte while the current is still on.

e) Thoroughly wash thin-film specimen in distilled water and alcohol, dry and store in a dessicator.

In order to prepare longitudinal and transverse sections of the molybdenum strip, slices were first cut perpendicular to the rolling plane to a thickness of 20 to 25 mils and then ground to about 10 mils. The subsequent electropolishing procedure was essentially the same as that used for rolling plane sections, except that special care was taken to confine the electrolytic indentation to the center of the section.

All the thin-film specimens were examined at magnifications from 5,000X to 25,000X, using a Hitachi HU-11 electron microscope operating at 100 kv. Higher magnifications were obtained by subsequent enlargement of the photographic plates.

4. Selected Area Transmission Electron Diffraction of Thin-Films

Electron diffraction patterns were obtained from selected areas in thin specimens in order to determine:

a) the orientation of the foil plane, using the b. c. c. reciprocal lattice model of molybdenum, as described by Thomas⁽⁴⁾;

b) the misorientation within one selected area diffraction pattern from the shape of the diffraction spots; and

c) the misorientation across a given area by identifying and relating the orientations in a series of selected area diffraction patterns.

Unknown crystal planes making traces on planes of known indices were identified by means of a stereographic projection, as described by Barrett⁽⁵⁾.

5. Mechanical Testing

The procedures used for microhardness and tensile testing were the same as those described in the previous summary report⁽²⁾. Tensile tests were conducted at a strain rate of 2.8×10^{-4} sec⁻¹.

C. Effect of Rolling Deformation and Subsequent Annealing on Substructure of Molybdenum Strip

1. Scope

This part of the investigation dealt with the effect of rolling deformation and subsequent annealing treatments on the substructure of molybdenum strip materials. The principal experimental method used for observing substructure

was electron microscopy of thin films. Correlations were made with light microscopy and selected area diffraction observations, as well as with x-ray line broadening measurements, where possible.

2. As-Recrystallized Condition

Both Mo-E1 and Mo-E2 strips (Products M1D-RX and M2C, see Table 1) were recrystallized at 1200°C, 1 hour, and the grain size obtained was about 0.03 mm. Thin-film electron micrographs show well-defined regions, about 10 to 50 microns in diameter, surrounded by distinct, high-angle boundaries (Fig. 1a). The isolated dislocation lines that were frequently observed in these regions (Fig. 1b) correspond to a relatively low dislocation density of about $10^8/\text{cm}^2$. This indicates that the regions are the primary grains of the recrystallized structure.

Selected area diffraction patterns obtained from various grains in the same specimen show that the difference in orientation between neighboring grains ranges from 25 to 45°, with no preferred orientation evident. Although the Mo-E2 strip is approximately 30 ppm higher in carbon than Mo-E1 strip, this difference does not appear to have an appreciable effect on the dislocation substructure. Certain features were observed which might be interpreted as second phase particles; however, no identifiable electron diffraction pattern was obtained, possibly due to the minute dimensions of the particles. No evidence of similar particles was found in the as-recrystallized Mo-E1 specimens.

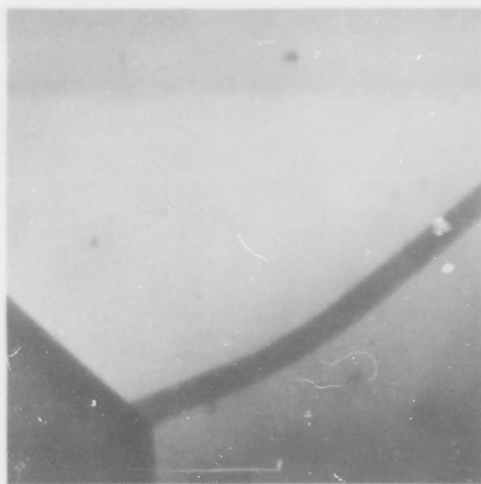
3. Slightly Worked Condition

Although supposedly supplied in the recrystallized condition, the Mo-E1 strip (Product M1C, Table 1) had unintentionally been slightly worked to an extent estimated as about 5% deformation based on observations by light microscopy of the occurrence of slip lines in some grains. Using thin-film electron microscopy, it was found that numerous dislocation lines had been introduced by the working, corresponding to a dislocation density of about $10^{10}/\text{cm}^2$. As shown in Fig. 2a, the distribution of dislocations is quite non-uniform. Instead of straight dislocation segments as observed in the recrystallized material, both jagged and tangled dislocations occur within individual grains. The presence of tangles indicates that the rolling temperature was such to permit easy cross-slip on two or more slip systems and thereby result in interactions between dislocations. In areas containing isolated dislocation clusters (Fig. 2b), evidence was found that dislocation tangles joined together to form distinct boundaries.

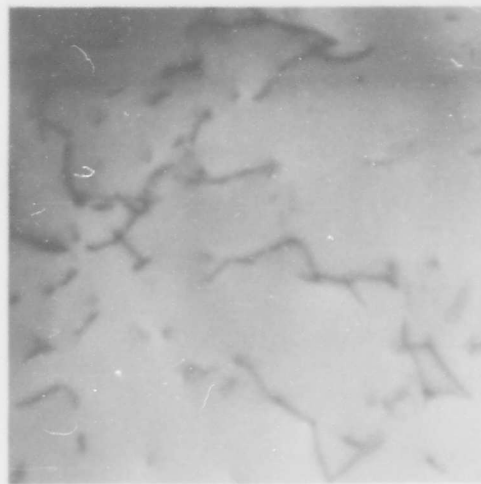
4. Moderately Worked Conditions

4.1 Rolling Plane Sections

For the moderately worked Mo-E1 and Mo-E2 strips subjected to 40 to 52% reduction (Products M1D, M1E, M2E, M1F, Table 1), it was observed that more dislocation tangles are produced as compared to the slightly worked condition. As shown in Figs. 3a, 3b and Table 2, the tangles appear to

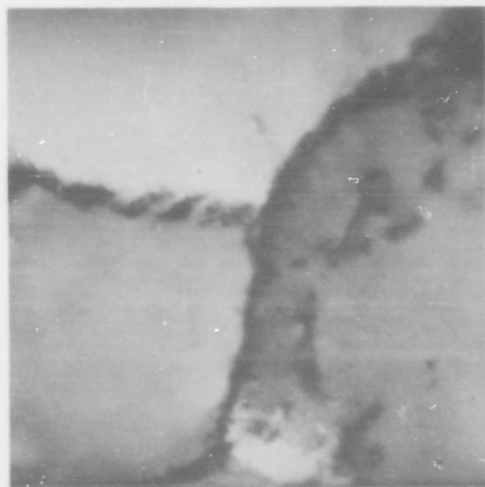


(a) 2112 30,000X

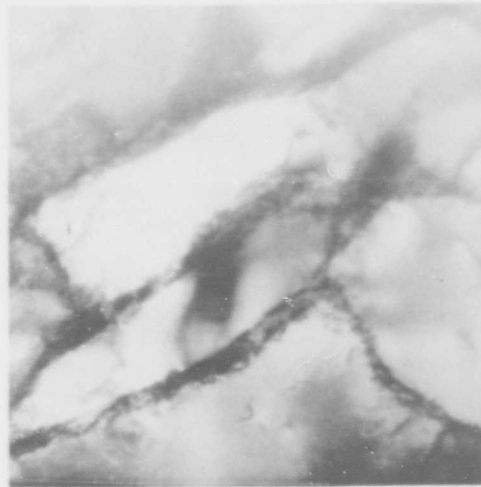


(b) 2560 10,000X

Fig. 1 - Thin-film electron micrographs of recrystallized molybdenum (Mo-E2) strip, showing (a) high-angle boundaries and (b) isolated dislocation lines within grains.

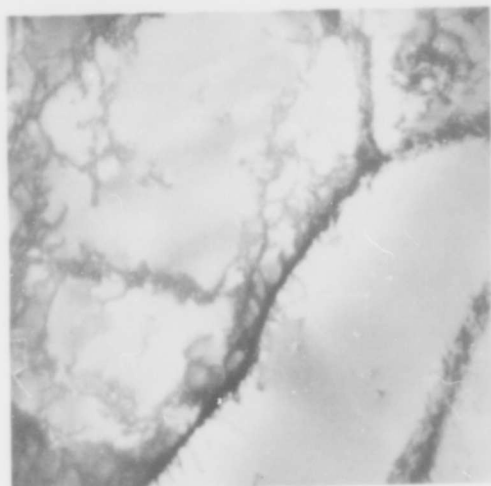


(a) 2088 30,000X



(b) 2089 30,000X

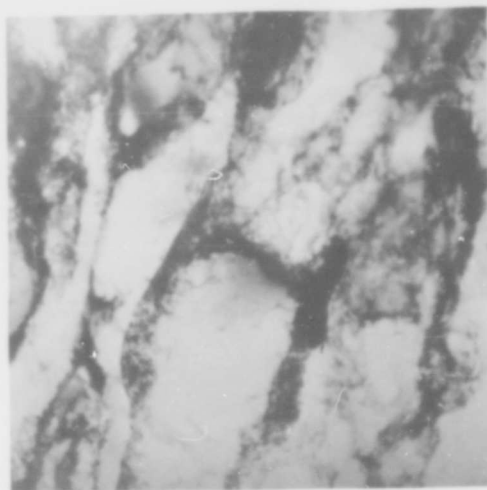
Fig. 2 - Thin film electron micrographs of slightly worked molybdenum (Mo-E1) strip, showing (a), (b) substructural cells surrounded by dislocation tangles.



(a)

2724

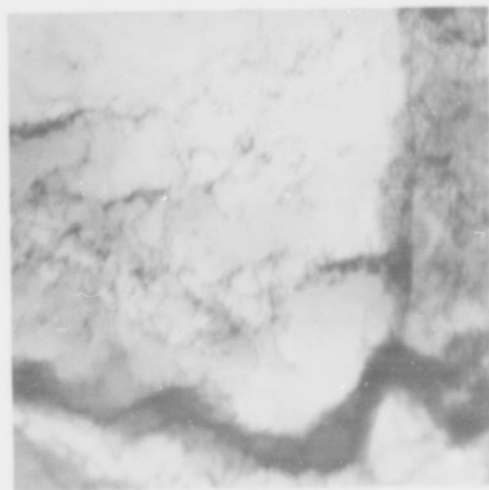
30,000X



(b)

2722

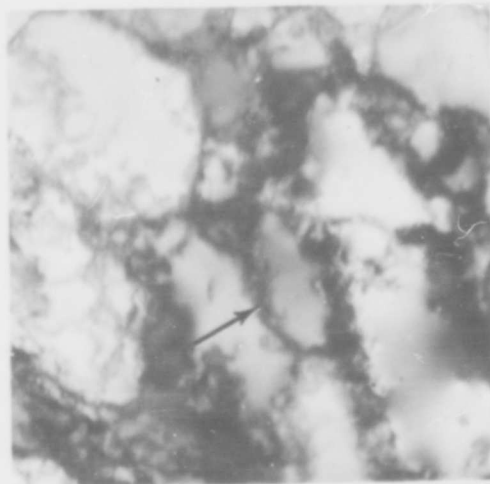
15,000X



(c)

2395

30,000X



(d)

2395

15,000X

Fig. 3 - Thin-film electron micrographs of molybdenum strip, rolling plane sections, showing cell structure development upon progressive deformation: (a) 40% reduction, Mo-E2; (b) 46% reduction, Mo-E1; (c) and (d) 52% reduction, Mo-E1.

have joined together and formed a substructure consisting of elongated subgrains about 2 microns wide and 4-6 microns long that are visible on rolling plane sections. The small difference in carbon content between Mo-E1 and Mo-E2 strips does not seem to have an appreciable effect on the dislocation arrangements.

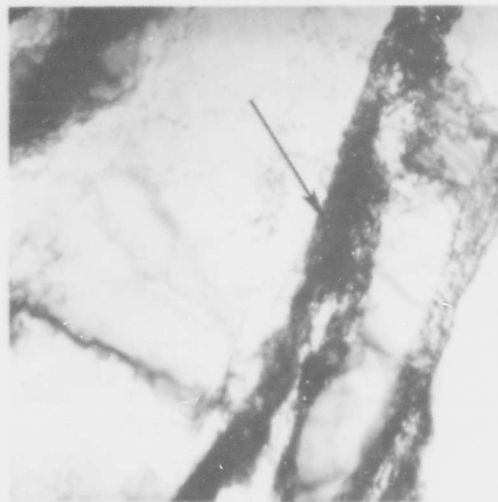
Although after 40% reduction the dislocation density within the subgrains is relatively low compared to that in the subboundaries (Fig. 3a), it increases with higher deformation (Figs. 3b and 3c). Along with the observed occurrence of additional dislocation tangles, new subboundaries (arrow, Fig. 3d) form what is generally termed a cell structure. The individual cells consist of essentially equiaxed areas, about 1-2 microns in diameter, in which the dislocation density is relatively low.

The rolling plane as determined by selected area electron diffraction of individual thin-film specimens is of the $\{111\}$ or $\{100\}$ type in most cases. This is consistent with a weak $(100)[110]$ preferred orientation which has a substantial spread due to rotation about the rolling direction. As pointed out by Semchysheva⁽⁶⁾, even heavily worked molybdenum sheet (93% reduction) exhibits a rotation about the rolling direction as much as 40° , but only up to 7° about the transverse direction. However, a greater spread in orientation would be expected in the moderately worked Mo-E1 and Mo-E2 strip studied here because of less working. This accounts for the occasional observations of the $\{100\}$ orientations. It was also noted that there appears to be a tendency for more substructure to be present with $\{111\}$ grain orientations than with either $\{100\}$ or $\{110\}$.

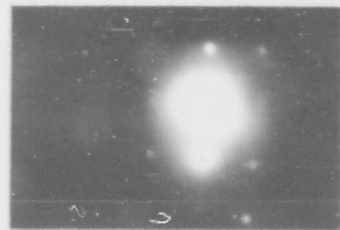
Although primary grain boundaries may be recognized in thin-film electron micrographs as distinct cross boundaries (arrow, Fig. 4a), such boundaries are less clearly evident in the light micrographs of the rolling plane sections (Fig. 4d). Electron diffraction patterns indicate orientation differences across such boundaries of 25 to 45° (Figs. 4b, c).

By means of measurements on a series of extended or split electron diffraction spots (Fig. 4b), the orientation differences between cells within the subgrains were calculated to be in the range 0 to 4° . However, the misorientation between cells is not uniform. Some areas contain 2 to 3 cells (approximately 3 square microns) and yield a single crystal pattern, whereas other areas of about the same size give a pattern indicating several subgrains with a misorientation of a few degrees. If at one of the latter locations, a second pattern is taken which represents an area approximately twice the size of the first, a spotty Debye-Scherrer pattern is usually obtained. This indicates that subgrains with greater differences of orientation were irradiated.

From such "polycrystalline" patterns and from patterns taken from areas containing a single subboundary, it was estimated that misorientations across such subboundaries are in the range of 2 to 6° . It also appears that the misorientation is additive over a distance comprising several subgrains. In other words, the bending of the deformed lattice which is accommodated mainly by the subboundaries appears to be responsible for the observed spotty "polycrystalline" patterns.



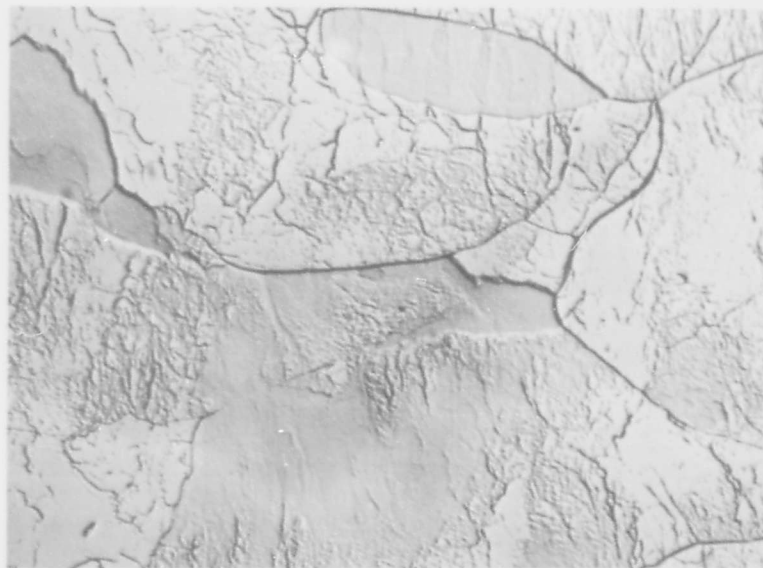
(a) 2721 15,000X



(b) (100)



(c) (111)



(d) H_2O_2 etch 22 1,500X

Fig. 4 - Substructure in moderately worked molybdenum strip, rolling plane section. (a) thin-film electron micrograph of Mo-E2, 40% reduction, showing a grain boundary (arrow); (b) and (c) selected area diffraction patterns on both sides of the boundary; (d) light micrograph of Mo-E1, 46% reduction, showing subgrains delineated by etch pit subboundaries.

4.2 Longitudinal Sections

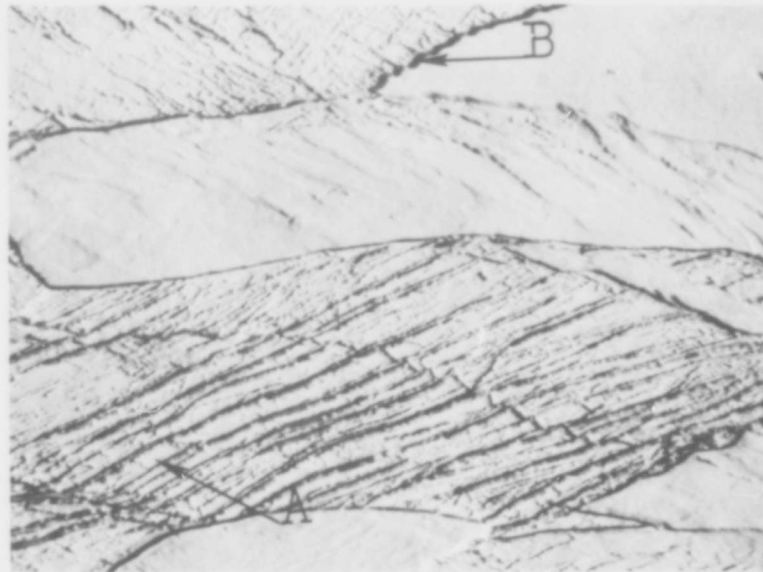
In addition to examination of rolling plane sections of the Mo-E1 strip (46% reduction), observations were also made on longitudinal and transverse sections by light microscopy and thin-film electron microscopy. In light micrographs of longitudinal sections, certain grains show parallel etch pit subboundaries that are spaced about 1 to 3 microns apart and oriented at angles of 20 to 50° with respect to the rolling direction and rolling plane (Fig. 5a). Relatively widely spaced transverse etch pit boundaries divide the bands into approximately rectangular segments (arrow, Fig. 5a).

By thin-film electron microscopy, longitudinal sections were found to exhibit a substructure consisting of distinct parallel bands, ranging from 0.5 to 2 microns in width and about 6 microns and more in length (Fig. 5b). The boundaries of the bands are quite distinct and consist of approximately parallel arrangements of dislocation tangles. Clearly defined primary grain boundaries are occasionally evident as long boundaries either cutting across the band boundaries at an oblique angle or separating areas containing bands of obviously different orientations (arrow, Fig. 5c). In other areas, however, the primary grain boundaries are indistinguishable from the band boundaries and can only be positively identified by an abrupt change in orientation as determined by electron diffraction.

Some of the bands contain clearly defined transverse subboundaries, which form a substructure within the bands that consists of cells about 0.5 to 1 micron in diameter. In other band segments, indications were found of potential subboundaries evolving from dislocation tangles traversing the band (arrow, Fig. 6a), which can be considered as embryonic cell structures.

As determined by electron diffraction, almost all of the thin-film orientations observed in longitudinal sections are in the $[110]$ zone; and, consequently, there is a $\langle 110 \rangle$ direction lying in the plane of the thin film. In the order of decreasing frequency of observation, these orientations are: $\{311\}$, $\{211\}$, $\{111\}$, $\{110\}$ and $\{100\}$. Similar to rolling plane sections, the longitudinal thin-film orientations are generally consistent with the reported (100) $[110]$ rolling texture in molybdenum, in which a substantial spread exists corresponding to a rotation about the rolling direction. However, it should be pointed out that occasional thin-film specimens were observed to have a $\{210\}$ orientation, which is in the $[100]$ zone and is therefore not consistent with the reported rolling texture.

Stereographic analysis was employed in order to determine the relationship between the band boundaries and the slip systems in molybdenum. Slip has been reported by several investigators^(7,8) to occur in $\langle 111 \rangle$ directions on both the $\{110\}$ and $\{112\}$ planes, especially at elevated temperatures. Some observations of slip along $\{123\}$ planes have also been reported⁽¹⁰⁾. However, as pointed out by Greninger⁽⁹⁾, it is possible that traces corresponding approximately with $\{112\}$ or $\{123\}$ are composites of alternate slipping on two or more $\{110\}$ planes. All of these planes contain $\langle 111 \rangle$ directions, and each $\{112\}$ plane bisects the angle between two $\{110\}$ planes. Likewise, each $\{123\}$ plane is located between a $\{110\}$ and a $\{112\}$ plane. Thus, if slip were to proceed by



(a)

61

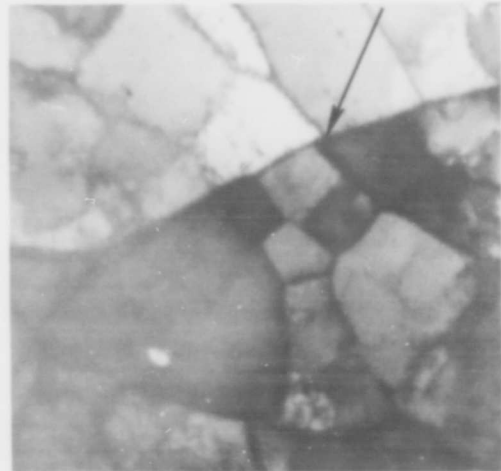
1,500X



(b)

2577

10,000X

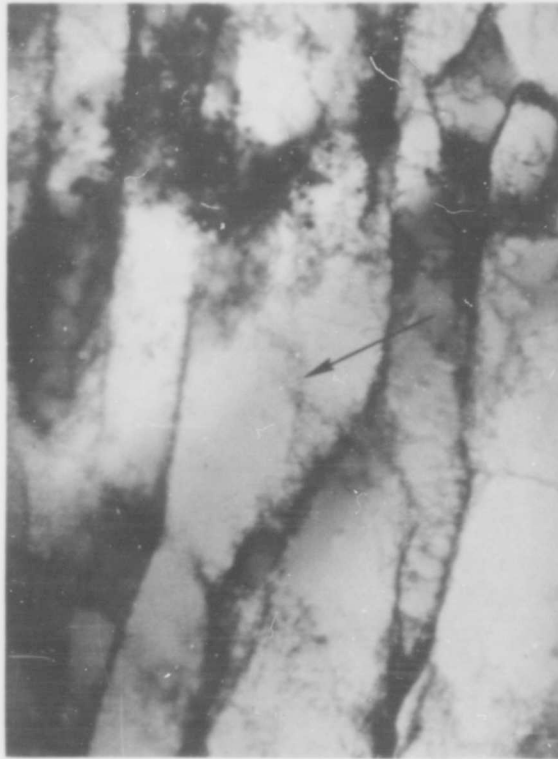


(c)

2587

20,000X

Fig. 5 - Substructure in moderately worked, 46% reduction, molybdenum (Mo-E1) strip, longitudinal section. (a) Light micrograph showing "rectangular" subboundary networks (arrow A) and saw-toothed grain boundary segment (arrow B). (b) and (c) thin-film electron micrographs showing typical microstructure (b), and grain boundary (c).



2728

20,000X

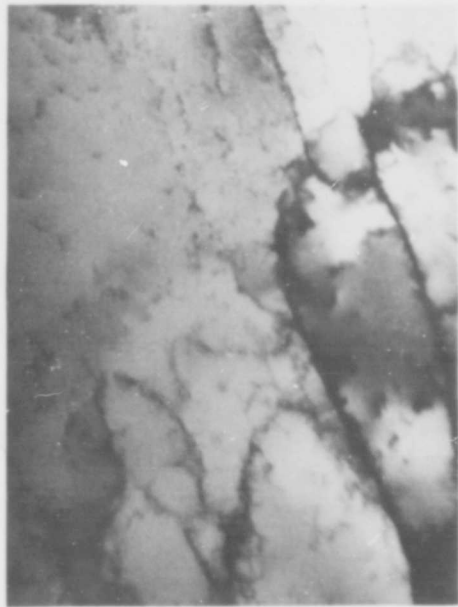
Fig. 6 - Thin-film electron micrograph of moderately worked, 46% reduction, molybdenum (Mo-E1) strip, longitudinal section. Note subboundary formation by dislocation tangles (arrow).

approximately equal minute displacements along both $(1\bar{1}0)$ and $(01\bar{1})$, the slip plane might appear as an approximate $(1\bar{2}1)$; whereas, if the ratio of displacement along $(1\bar{1}0)$ and $(01\bar{1})$ were 4:1, the slip plane would appear as $(2\bar{3}1)$.

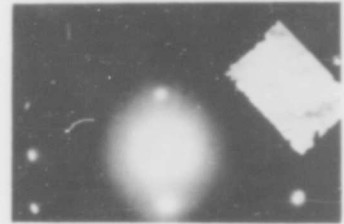
From observations of the trace of a plane (such as the band boundary) on another single plane (the longitudinal section), the crystallographic indices of the former plane cannot be identified conclusively. However, the zone containing the band boundary plane can be identified by stereographic analysis of its trace on the longitudinal section. By determination of the planes in the zone of the band boundary trace for many longitudinal thin films, the possible boundary planes occurring most frequently were found to be the $\{110\}$, $\{112\}$ and $\{123\}$. Thus, the crystallographic structure of the bands is consistent with their boundaries being slip planes, either single slip in the case of $\{110\}$ planes or composite slip when the boundaries are parallel to $\{112\}$ or $\{123\}$ planes.

In order to study in more detail the lattice misorientations characteristic of the various types of boundaries observed, a systematic series of selected area electron diffraction patterns were taken. The locations were: a) along single bands, b) along lines traversing several bands in a direction normal to their axes, and c) in the vicinity of primary grain boundaries. Since the area (3 to 4 square microns) from which a diffraction pattern was obtained usually covered at least two bands, only an occasional selected band was wide enough to permit determination of the misorientations associated with the subboundaries delineating the cell structure within the band. Such misorientations become evident by comparison of a series of electron diffraction patterns. A symmetrical diffraction pattern results only when a lattice plane is exactly perpendicular to the electron beam. When a lattice plane is inclined, corresponding to a rotation about an axis lying in the plane of the thin film, some of the spots do not appear. Thus, when successive patterns from different locations are compared, differences in orientation are manifested by progressive disappearance of old spots on one side of the axis and the appearance of new spots on the other. Such changes in the diffraction patterns were observed on examining areas at different locations along the length of a wide band (using a traverse direction parallel to the band axes). This was considered as evidence that lattice misorientations are associated with the cell boundaries within the band (Figs. 7a, b, c, d).

When the direction traversed was normal to the band axes, most of the individual areas examined were found to contain two or more separate bands. These usually yield single crystal patterns, indicating that each band boundary is associated with a misorientation of only a few degrees, or less. However, extra spots which did not form an identifiable pattern, occasionally appeared at the margins of the fluorescent screen. As indicated by the disappearance and re-appearance of individual spots as the beam was traversed in a direction normal to the band axes, successive patterns taken at different locations revealed relatively small changes in orientation similar to those found by traversal along a single band. However, the presence of a primary grain boundary was revealed by a complete change in the pattern as the beam was traversed from one area to the next (Figs. 8a, b, c, d). adjacent to the grain boundary in which the lattice was inclined far enough so that only the spots belonging to a single zone appeared in the pattern, as compared to the complete patterns observed in the same grain sufficiently far



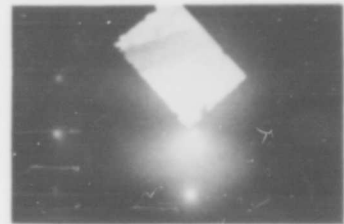
(a) 2888 20,000X



(b)



(c)



(d)

Fig. 7 - (a) Thin-film electron micrograph of moderately worked (46% reduction) molybdenum (Mo-E1) strip, longitudinal section, showing a broad band. (b), (c) and (d) are consecutive selected area diffraction patterns, $\{211\}$, taken by traversing broad band in (a) from top to bottom. These show a variation in misorientation along the length of the band.

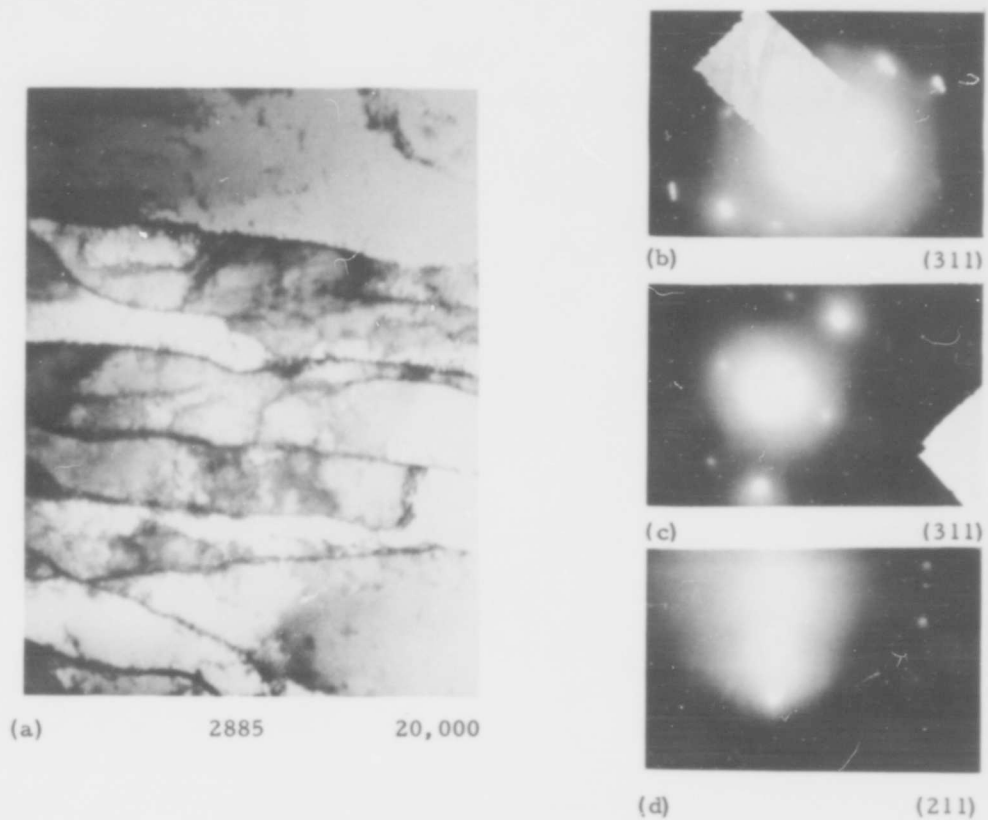


Fig. 8 - (a) Thin film electron micrograph of moderately worked, 46% reduction, molybdenum (Mo-E1) strip, longitudinal section. (b), (c) and (d) consecutive selected area diffraction patterns taken by traversing several bands in (a) going from top to bottom. A change in orientation from (311) to (211) was found.

from the grain boundary. In some areas where distinct but different single crystal patterns were obtained on either side of a primary grain boundary, a pattern from an area comprising the grain boundary and a few bands on either side of it yields a third pattern in addition to the previous ones. For example, Fig. 9 shows the substructure and diffraction patterns in a region in which a $\{311\}$ pattern was found on one side of the grain boundary (arrow) and a $\{100\}$ pattern on the other. In the boundary region itself, however, a $\{111\}$ pattern is present in addition to spots from some zones of both the $\{311\}$ and $\{100\}$ patterns. These observations confirm the conclusions reached by other investigators⁽¹⁰⁾ that there is a region of pronounced lattice distortion in the vicinity of a primary grain boundary in a deformed metal.

4.3 Transverse Section

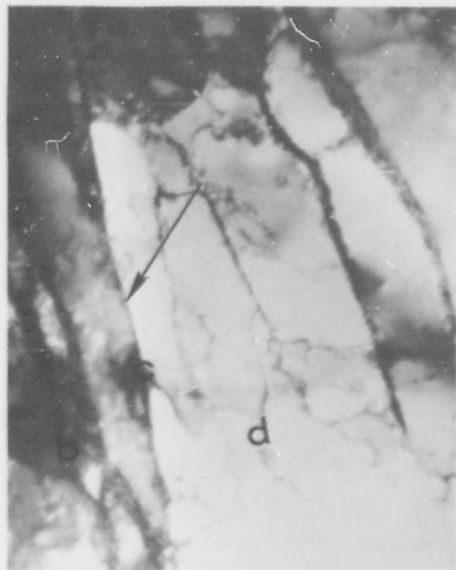
Light micrographs of transverse sections of the Mo-E1 strip reduced 46% (Product M1E, Table 1) show that the deformed grains contain a substructure consisting of poorly defined etch pits (Fig. 10a). There is no well-pronounced etch pit structure as in longitudinal sections, but it appears that there is some alignment of etch pits in the direction of the long axis of the grains (parallel to the rolling plane). On the other hand, corresponding thin-film electron micrographs show a well-defined band structure similar to that observed on longitudinal sections (Fig. 10b). The average width of the bands appears somewhat smaller than observed on longitudinal sections, perhaps because the major boundaries are not as clearly defined. Also, the number of subboundaries, both parallel to the major band boundary and at an angle thereto, is greater on the transverse section. The cell widths within the bands range from 0.2 to 0.7 microns. Some grains were found to exhibit a cell structure that has no preferred direction of alignment.

Most of the observed orientations in the transverse section are in the $[100]$ zone. In the order of decreasing frequency, these are $\{110\}$, $\{210\}$ and $\{100\}$. However, a few thin films were found to have $\{311\}$ and $\{111\}$ orientations, which are in the $[110]$ zone. As for the longitudinal section, stereographic analysis of the band boundary traces in the transverse section showed that in all cases these are consistent with the band boundaries occurring along $\{110\}$, $\{112\}$ or $\{123\}$ slip planes. As pointed out previously, the resultant slip trace may be a result of either a) simple slip on a single plane or b) composite slip on more than one plane.

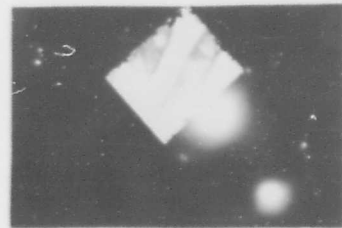
From a misorientation study of transverse sections, it was found that the degree of local misorientation is similar to that observed in longitudinal sections. However, it appears that there is a stronger degree of preferred orientation (distinct majority of $\{110\}$ diffraction patterns).

5. Heavily Worked Condition

For the molybdenum strip rolled to 88% reduction (Products M1H, M2H, Table 1), light micrographs show the occurrence of extensive elongation of the primary grains in the direction of rolling and pronounced flattening normal to the rolling plane. As viewed on the rolling plane, no evidence of grain boundaries was found. However, there appear to be more poorly defined etch



(a) 2881 15,000X



(b) (311)



(c) (111)



(d) (100)

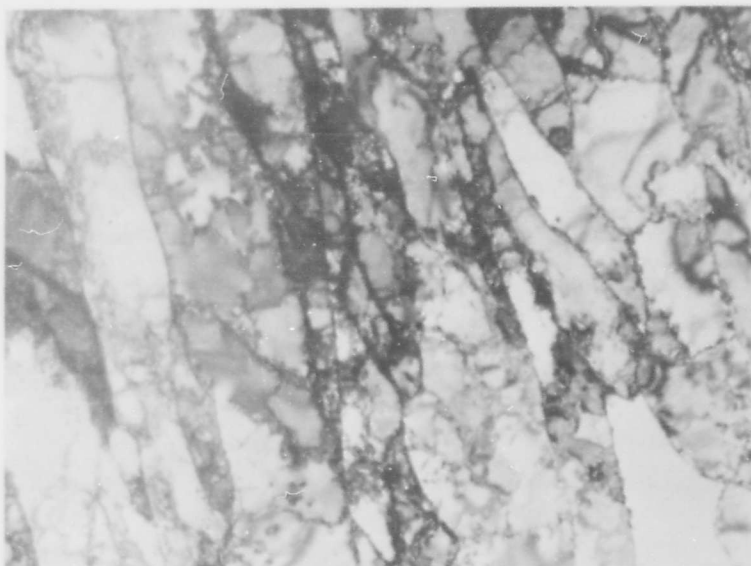
Fig. 9 - (a) Thin-film electron micrograph of moderately worked, 46% reduction, molybdenum (Mo-E1) strip, longitudinal section, showing a high-angle grain boundary (arrow). (b), (c) and (d) are selected area diffraction patterns taken in area above the boundary, at the boundary, and below the boundary. Changes in orientation from (311) to (111) to (100) were found



(a) H_2O_2 etch

20

1,500X



(b)

2738

20,000X

Fig. 10 - Substructure in moderately worked, 46% reduction, molybdenum (Mo-E1) strip, transverse section. (a) Light micrograph. (b) Thin-film electron micrograph.

pits (Fig. 11a) than for the moderately worked strip. Although some etch pit arrays consisting of a few pits each were observed, no preferred orientation of these arrays was found.

Transmission micrographs of rolling plane sections do not show the distinction between the subgrains and cells such as is evident in the moderately worked strip. For the heavily worked condition, the dislocation arrangement is very nonuniform, presumably due to inhomogeneous deformation. Based on examination of various locations in both Mo-E1 and Mo-E2 strips, it appears that the cell sizes are 1 to 2 microns in the moderately worked strip and 0.5 to 1 micron in the heavily worked strip. However, this difference may be misleading in the sense that the cell structure is not uniform over the specimen area. For the heavily worked strip, a higher dislocation density is indicated by the presence of "clouds" of unresolved dislocation-tangles which appear as indistinct dislocation formations, (Fig. 11b). In addition, poorly defined cells tend to be arranged locally in elongated arrays, about 1.5 microns in width, possessing rather distinct and roughly parallel boundaries (Fig. 11c). The substructure within these bands consists of indistinct dislocation line segments along with some well developed cross-boundaries consisting of dislocation tangles.

Similar to observations made on rolling plane sections of the moderately worked strip, the majority of electron diffraction patterns were obtained from $\{111\}$ planes, and the longitudinal direction of the band boundaries was identified in most cases with either the $\langle 110 \rangle$ or $\langle 112 \rangle$ direction. Because of the infrequent occurrence of the bands, the direction of the elongation could not be precisely determined. However, both the $\langle 110 \rangle$ and $\langle 112 \rangle$ directions are compatible with the $\langle 110 \rangle$ rolling direction projected on the $\{111\}$ plane, which implies that the bands are parallel to the rolling direction.

As revealed by light microscopy, longitudinal sections of the heavily worked strip show marked change from the corresponding moderately worked strip (Figs. 12a, 5a, respectively). The primary grains in the heavily worked strip are highly elongated in the rolling direction. Furthermore, it appears that additional boundaries have formed which cannot be distinguished from the original primary grain boundaries prior to working (i. e., the recrystallized condition). In addition to elongated primary grain boundaries, a number of transverse etch pit subboundaries were found to be oriented at about 40° to the rolling direction.

Thin-film micrographs of the longitudinal section of the heavily worked strip show a marked similarity to the corresponding section of the moderately worked strip (Figs. 12b, 5b, respectively). However, most of the elongated subboundaries in the heavily worked strip are relatively straight, and the subboundary width is in the range of about 0.1 to 0.5 micron. The subgrain bands contain relatively few dislocation lines, and cross-boundaries are infrequent.

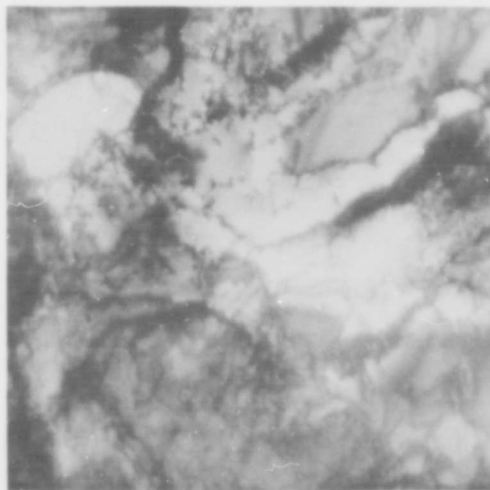
Selected area diffraction patterns of the heavily worked thin film indicate that $\{111\}$ is definitely the preferred orientation with the band direction related to $\langle 110 \rangle$ or $\langle 211 \rangle$ directions. Therefore, the conclusions



(a) H_2O_2 etch

24

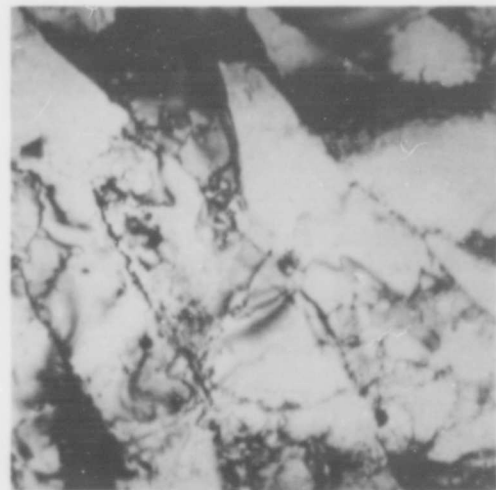
1,500X



(b)

2387

15,000X



(c)

2391

15,000X

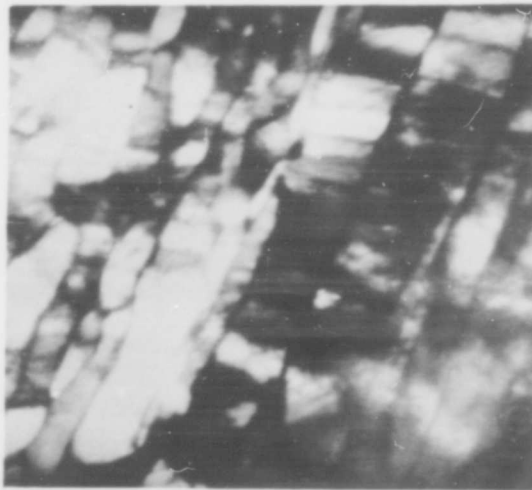
Fig. 11 - Substructure in heavily worked (88% reduction) molybdenum (Mo-E1) strip, rolling plane sections. (a) Light micrograph showing poor definition of grain boundaries and etch-pit subboundaries; (b) and (c) thin-film electron micrographs showing "clouds" of ill-defined dislocations (b) and preferential alignment of cells (c).



(a)

32

1,500X



(b)

2897

25,000X

Fig. 12 - Substructure in heavily worked, 88% reduction, molybdenum (Mo-E1) strip, longitudinal section. (a) Light micrograph showing flattened and highly elongated grains. (b) Thin-film electron micrograph showing small band width.

reached from examination of the crystallographic structure of the moderately worked strip also apply to the heavily worked strip.

6. Effect of Recovery - Annealing on Substructure

As determined by light microscopy, annealing of the moderately worked Mo-E1 strip at 1000°C results in a more distinct etch-pit substructure than observed in the as-rolled condition. In addition, small equiaxed regions form that exhibit little or no evidence of substructure (arrow, Figs. 13a,b). These apparently strain-free regions may be interpreted as the start of recrystallization. Similar dislocation-free regions were found by thin-film electron microscopy of the same material (Fig. 14a). Evidence of dislocation rearrangement and annihilation was found, as indicated by the markedly lower dislocation density and the formation of distinct cell boundaries as compared to the as-rolled condition. The elimination of the dislocation tangles outlining the cells observed in the as-rolled condition apparently results in an increase in cell dimensions due to annealing (see Table 2).

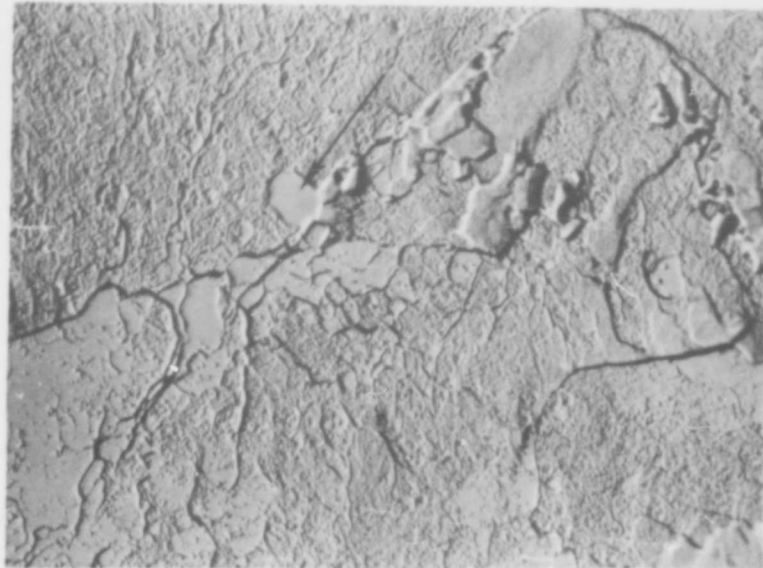
As a result of dislocation movement during annealing of the moderately worked strip at 1000°C, some alignment within the former dislocation tangles takes place, this results in the formation of very fine, quasi-hexagonal dislocation networks (Fig. 14b) made up of distinct low angle boundaries. These networks, which are considered characteristic of polygonization, may result from a simple dislocation rearrangement in accordance with the following reaction:



Although it is believed that only short distances of dislocation climb are involved in the formation of such hexagonal networks, it appears that the annealing temperature is critical, since they were observed in the moderately worked strip annealed at 1000°C and not in the heavily worked strip annealed at 900°C. Where the dislocation density is relatively low in the moderately worked, the distance of climb during annealing is greater than where the dislocation density is relatively high and a parallel arrangement of dislocation lines results (Fig. 14c).

Based on light microscopy, annealing of the heavily worked strip results in the appearance of small, equiaxed subgrains within the highly elongated and flattened primary grains (Fig. 15a). As revealed by thin-film electron microscopy, these subgrains generally contain a mosaic of cells (Figs. 15b,16). This is interpreted as evidence of polygonization without the occurrence of recrystallization, and supports the theory that the formation of recrystallization nuclei involves the coalescence of cells. The latter phenomenon may be due to migration of dislocations from the original low-angle cell boundaries. This is likely to involve dislocation climb along the disappearing cell boundary as well as a rotation of lattice orientation⁽¹¹⁾. It seems reasonable to believe that a subgrain formed by coalescence of cells is a potential nucleus for recrystallization, because the boundaries of this subgrain may be considered as high-angle with respect to its surroundings.

Along with the occurrence of substructural changes during recovery-annealing, the possible re-distribution of interstitial elements is an important consideration. In the previous report⁽²⁾, it was shown that recrystallization of



(a) H_2O_2 etch

52

1,500X



(b) H_2O_2 etch

49

1,500X

Fig. 13 - Light micrographs of moderately worked (46% reduction) and annealed (1 hour at 1000°C) molybdenum (Mo-E1) strip, showing recrystallized regions (arrows). (a) Rolling plane section. (b) Longitudinal section.

Table 2

Average Substructure Dimensions* in Mo-E1 and Mo-E2 Strip Materials

Ingot	Material	Condition	Section or Plane	Primary Grains**	Subgrains or Bands***	Cells***	Tangles***	Lattice Domains
Mo-E2	M2D-RX	as-recryst.	longitudinal	65	---	---	---	---
"	M2H-RX	as-recryst.	longitudinal	26	---	---	---	---
Mo-E1	M1C-AR	5-10% red.	rolling	36	4.5	2.5	none	---
Mo-E2	M2D-AR	40% red.	rolling	--	2.5	1.2	0.2	---
Mo-E1	M1E-AR	46% red.	rolling	--	2.2	1.0 + 0.5	0.3	---
"	M1E-AR	46% red.	longitudinal	15	1.5 + 0.5	0.7 + 0.3	0.1	---
"	M1E-AR	46% red.	transverse	14	0.9	0.4 + 0.2	0.1	0.2
"	M1E-HT	1000°C, 1 hr.	rolling	--	3.5	1.1	none	---
"	M1E-HT	1000°C, 1 hr.	longitudinal	18	---	---	---	---
"	M1H-AR	88% red.	rolling	--	none	0.7 + 0.3	0.3	---
"	M1H-AR	88% red.	longitudinal	6	0.3 + 0.2	---	---	0.11
"	M1H-HT	900°C, 1 hr.	rolling	--	3.0	0.8	none	---
"	M1H-HT	900°C, 1 hr.	longitudinal	9	---	---	---	---
Mo-E2	M2H-AR	88% red.	rolling	--	1.0	0.5	0.4	---
"	M2H-AR	88% red.	longitudinal	6	---	---	---	0.12

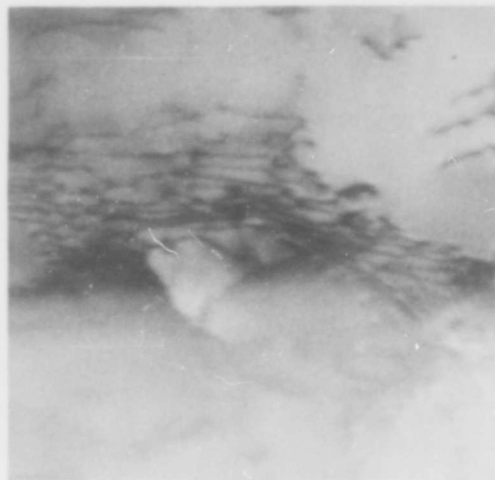
* All dimensions are reported in microns.

** Dimensions were measured on longitudinal sections perpendicular to the rolling direction.

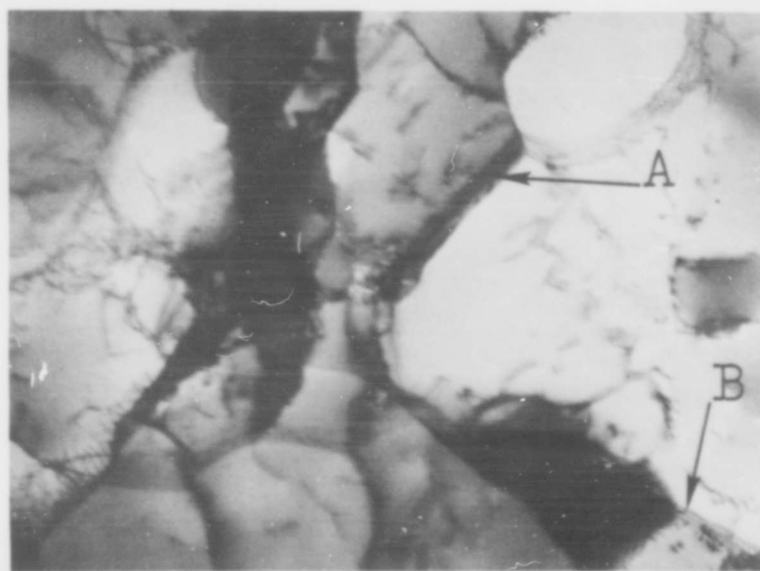
*** Due to the inaccuracies inherent in such measurements, because of ambiguities in definitions, wide local variations in substructure etc., dimensions are rounded off to the nearest one or two significant figures, depending on the estimated accuracy. Ranges are indicated by +.



(a) 2294 40,000X

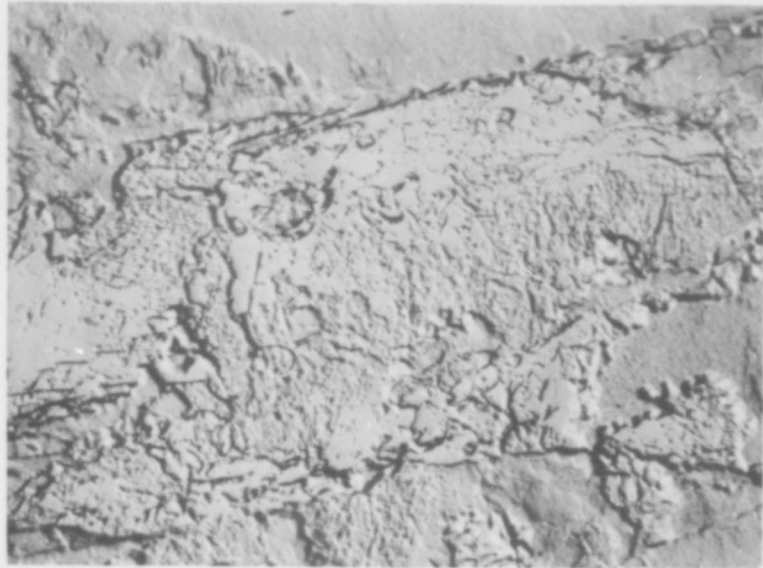


(b) 2592 20,000X



(c) 2532 25,000X

Fig. 14 - Thin-film electron micrographs of moderately worked, 46% reduction, and annealed (1 hour at 1000°C) molybdenum (Mo-E1) strip, rolling plane section, showing (a) recrystallized regions, (b) parallel dislocation arrangement, (c) formation of subgrains (arrow A) and parallel dislocation alignments (arrow B).



(a) H_2O_2 etch

42

1,500X



(b)

2688

40,000X

Fig. 15 - Substructure in heavily worked, 88% reduction, and annealed (1 hour at $900^{\circ}C$) molybdenum (Mo-E1) strip rolling plane section. (a) Light micrograph. (b) Thin-film electron micrograph showing clearly defined subboundaries and a relatively low dislocation density within the subgrains.



2687

40,000X

Fig. 16 - Thin-film electron micrograph of heavily worked and annealed (1 hour at 900°C) molybdenum (Mo-E1) strip, rolling plane section, showing clearly defined cell boundaries (arrow A) and cell coalescence (arrow B).

tungsten wire can be inhibited by prior recovery-annealing. A hypothesis was advanced to explain this phenomenon on the basis that interstitials diffuse to subboundaries and tend to stabilize them. It was decided to check if a similar phenomenon occurs in columbium wire. As shown in Appendix A, recovery-annealing has no effect on subsequent recrystallization. Therefore, the effect seems peculiar to tungsten.

7. Correlation of Observed Dislocation Substructure with X-ray Domain Size

In the previous summary reports^(1,2), calculations were made to determine the size of coherently reflecting lattice domains based on x-ray line broadening measurements as analyzed by means of the Warren-Averbach method. An attempt was made here to correlate lattice domain size with dislocation arrangements as observed by thin-film electron microscopy.

The generally accepted concept of lattice domains is that they consist of blocks of unit cells which are separated by low angle boundaries made up of simple arrays of edge dislocations. However, observations based on thin-film electron microscopy of the molybdenum strip in the deformed condition indicate that the structure on a fine scale consists of complicated dislocation arrays and entanglements.

In Table 2 are given the measured sizes of substructural features as determined by thin-film electron microscopy and the calculated x-ray domain sizes. Since the calculated ratio of domain sizes $D_{\langle 110 \rangle} : D_{\langle 100 \rangle}$ in both the Mo-E1 and Mo-E2 strips is very close to unity, faulting is believed to play a minor role according to Warren⁽¹²⁾. Therefore, the calculated domain size is presumed to accurately represent the length of the column of unit cells perpendicular to the reflecting planes.

One of the main problems in correlating x-ray domain size with substructure involves determining a consistent parameter representing the latter. Based on the variation in dislocation arrangements found depending on the observation plane, it is evident that there is a non-uniform distribution of dislocations with respect to the rolling direction; and this is contrary to the concept of isotropic nature of lattice domains. Since the non-uniformity is extremely noticeable on rolling planes, the error involved in making substructural measurements on this plane is considerable. However, the arrangements of dislocation substructures as bands on planes at right angle to the rolling plane (longitudinal and transverse sections) appear similar and are consistent from specimen to specimen. Although the fine dislocation structure within the bands may vary with specimen orientation with respect to the electron beam, the spacing between clearly defined band boundaries appears to be a parameter that is representative of the amount of deformation. Furthermore, since band boundaries were found to coincide with traces of slip planes in the plane of thin-film specimens, the spacing between bands appears to be inversely related to the amount of deformation, similar to the dependence of domain sizes upon deformation. This is indicated by the

smaller band spacing of heavily worked compared to the moderately worked molybdenum strip (longitudinal section).

For heavily worked Mo-E1 strip (longitudinal section), a small number of the band widths were found to be about the same as the calculated domain size (0.1 micron). However, the average band width is about 0.3 micron, which is three times the value of the domain size.

In line with obtaining a better correlation, small values of domain size have been interpreted⁽¹³⁾ as "some sort of average separation between dislocations". Consequently, the lattice domain size should be inversely proportional to the dislocation density. Direct comparison of these values is seldom possible due to the difficulties encountered in determining dislocation densities of heavily worked specimens. However, based on values of domain sizes and dislocation densities reported by Hu(10) for iron-silicon single crystals, it was calculated that the average distance between dislocations is approximately twice as large as the domain size.

It seems likely that the x-ray domain size and the observed sub-structural size are a function of the number of lattice defects encountered by the x-ray and electron beams, respectively. Therefore, equal volumes of material should be compared. In electron microscopy, the thin-film thickness (about 0.2 micron) is completely penetrated; whereas the depth penetrated by x-rays is a much larger value. Using copper radiation, diffraction occurs from lattice planes over a depth of about 1 micron in molybdenum. If the electron beam could penetrate a comparable thickness of thin-film specimen, then the number of lattice defects encountered would be considerably higher. Presumably, the diffraction contrast effects from additional lattice defects would result in smaller measured values for the size of "dislocation-free" areas. This could account for the apparent discrepancy between the electron microscopic and x-ray measurements.

D. Effect of Recrystallized Grain Size on the Fracture of Molybdenum Strip.

The variations of the observed fracture stress (σ_F), fracture strain (ϵ_F) and lower yield stress (σ_y) with test temperature for recrystallized Mo-E2 strip (Product M2H-RX, Table 1) are shown in Fig. 17. The tensile ductility transition was found to occur over the approximate temperature range of -30°C to -70°C . This resulted in a decrease in true fracture strain from about 0.80 (54% R.A.) at -30°C to about 0.08 (9% R.A.) at -70°C .

Measurements were also made of σ_F , ϵ_F and σ_y at -40°C for the recrystallized grain sizes shown in Table 3. As shown in Fig. 18, a straight line was obtained for the variation of σ_y (normal stress) with the inverse square root of the grain diameter ($d^{-1/2}$) in accordance with the Petch relation^(14, 15). The slope of this line corresponds to a yield stress parameter (k_y) value of 2.5×10^8 cgs. which is somewhat higher than the values reported by other investigators^(16, 17) on the same basis. It is also higher than the value ($k_y = 1.3 \times 10^8$) obtained by extrapolating the

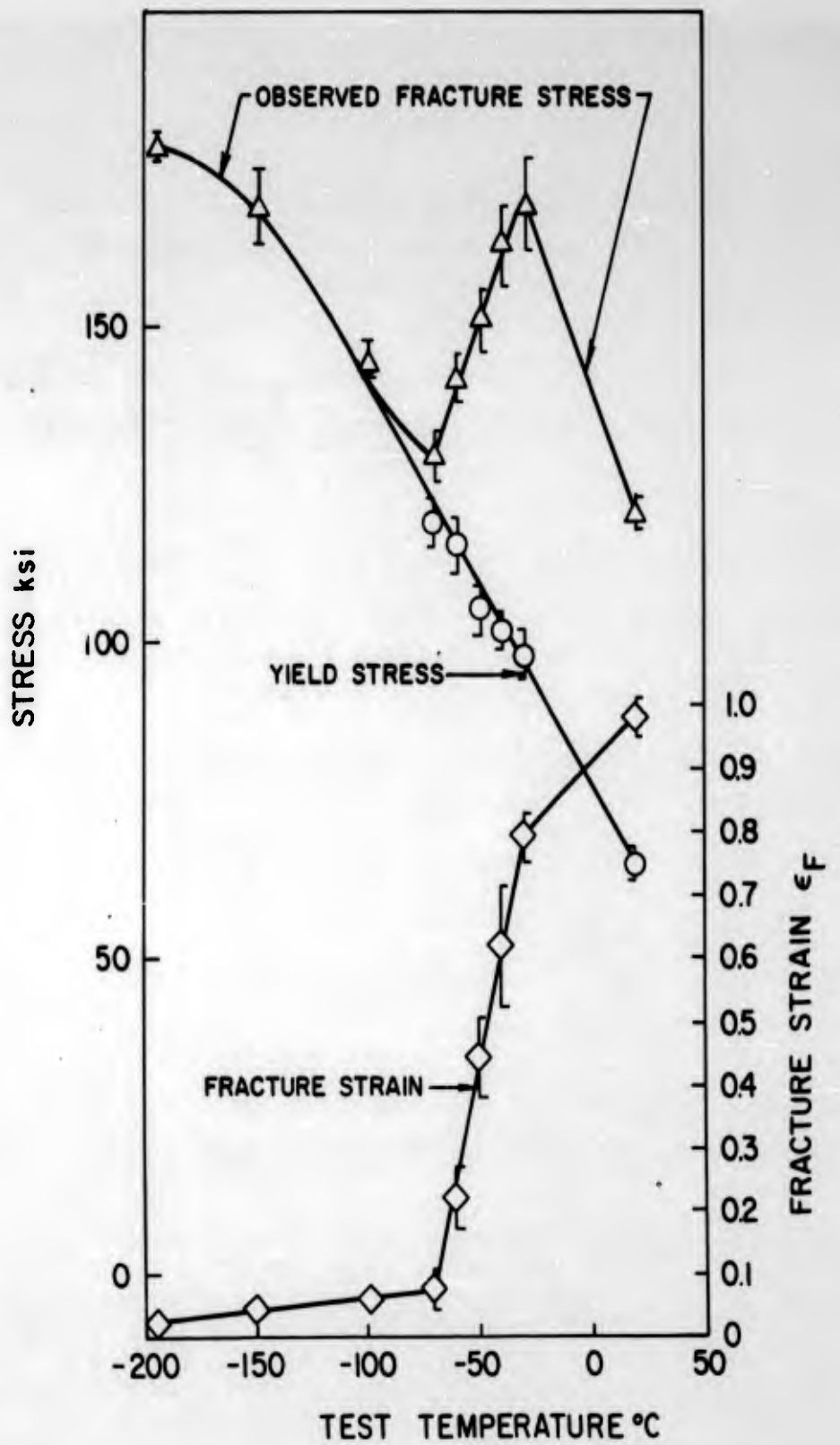


Fig. 17 - Effect of the test temperature on the tensile properties of high purity molybdenum (Mo-E2) strip in the as-recrystallized condition ($l^{-1/2} = 6.2 \text{ mm}^{-1/2}$).

Table 3

Procedures and Materials Used to Determine the Effect of
Grain Size on Yield Stress, Fracture Stress, and
Fracture Strain

<u>Product</u>	<u>Total Deformation</u> <u>Prior to</u> <u>Recrystallization</u>	<u>Final</u> <u>Recrystallization</u> <u>treatment</u>		<u>Approximate</u> <u>Recrystallized</u> <u>grain diameter, l</u> <u>mm</u>	<u>$l^{-1/2}$</u> <u>mm^{-1/2}</u>
		<u>Time</u> <u>mins.</u>	<u>Temp.</u> <u>°C</u>		
M2H-RX	87	30	1200	0.026	6.2
M2D-RX	44	60	1200	0.043	4.8
M2F-RX	15	60	1300	0.173	2.4

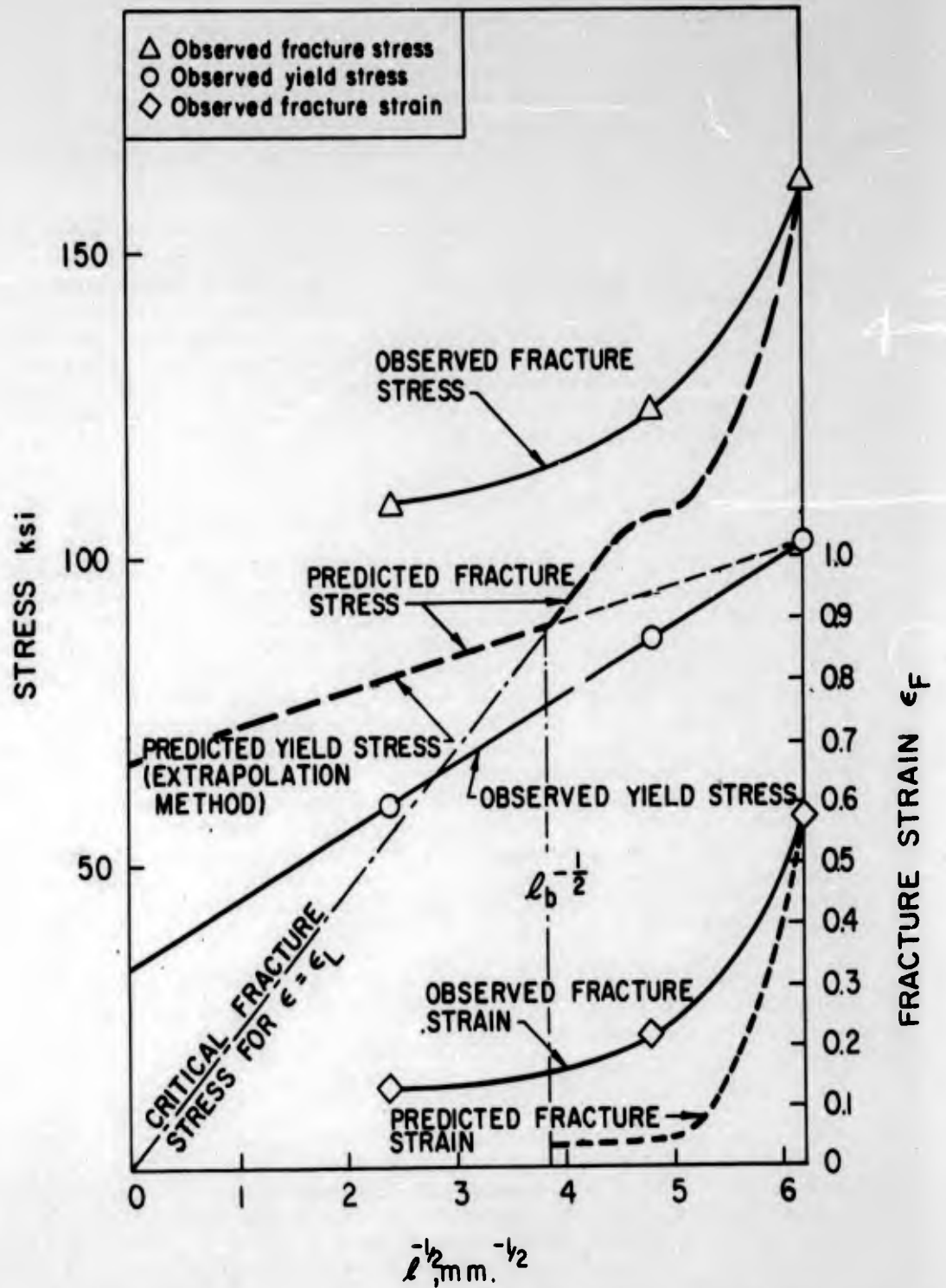


Fig. 18 - Observed and predicted effects of grain size on yield stress, fracture stress, and fracture strain of molybdenum (Mo-E2) strip in the as-crystallized condition tested at -40°C .

stress-strain curve to zero plastic strain, as shown in Fig. 19. Johnson⁽¹⁸⁾ also found that the grain size method gives a higher k_y value than the extrapolation method. It is interesting to note that the value ($k_y = 1.7 \times 10^8$) predicted using the Rosenfield relationship⁽¹⁹⁾ ($k_y = 14 \times 10^{-5} G$, where G is the shear modulus, which is 1.2×10^{12} dynes/cm² for molybdenum) is intermediate between the k_y values found by the grain size and extrapolation methods in the present study.

For the Mo-E2 strip in the as-recrystallized condition, an attempt was made to predict the variations of σ_F and ϵ_F with $l^{-1/2}$ at a test temperature of -40°C based on the assumption of a temperature-independent, strain-dependent critical fracture stress (σ_C). The approach used involved determining the relative positions of the σ_C vs. $l^{-1/2}$ and the flow stress (σ_f) vs. $l^{-1/2}$ plots for a series of increasing strain values. The strain dependence of σ_C was obtained from the data given in Fig. 17 for the fine grain size molybdenum strip ($l^{-1/2} = 6.2 \text{ mm}^{-1/2}$); and in line with the Cottrell⁽²¹⁾ relation as given in the following form:

$$\sigma_C = C_\epsilon l^{-1/2} \quad (1)$$

where the proportionality constant (C_ϵ) is a function of strain (ϵ), a series of σ_C vs. $l^{-1/2}$ straight line plots that pass through the origin were constructed for increasing values of strain. The particular σ_C vs. $l^{-1/2}$ line that corresponds to $\epsilon = \epsilon_L$ at -40°C (where ϵ_L is the Luders strain) intersects the σ_y vs. $l^{-1/2}$ plot (for -40°C) at a grain size which is designated as l_b . Determination of l_b (indicated by the light vertical line in Fig. 18) was based on the σ_y vs. $l^{-1/2}$ plot (indicated by the dashed straight line slightly inclined from the horizontal in Fig. 18) predicted by the extrapolation method (Fig. 19) using data for the fine grain size molybdenum strip ($l^{-1/2} = 6.2 \text{ mm}^{-1/2}$). Thus l_b corresponds to a grain size for which the nil-ductility temperature (T_b) equals -40°C . For $l^{-1/2} < l_b^{-1/2}$, even though $\sigma_y > \sigma_C$ fracture would be expected to occur at σ_y in accordance with Cottrell's⁽²¹⁾ concept that at least a small amount of plastic deformation must take place before a cleavage crack can form. For $l^{-1/2} > l_b^{-1/2}$, σ_y is below σ_C corresponding to $\epsilon = \epsilon_L$ and consequently plastic deformation to $\epsilon_F > \epsilon_L$ should occur prior to fracture.

In order to predict σ_F vs. $l^{-1/2}$ for $l^{-1/2} > l_b^{-1/2}$, it is necessary to determine the flow stress (σ_f) as a function of $l^{-1/2}$ for various values of $\epsilon > \epsilon_L$. According to Armstrong⁽¹⁵⁾,

$$\sigma_f = \sigma_i[\epsilon] + k_f l^{-1/2} \quad (2)$$

where $\sigma_i[\epsilon]$ is constant for a given temperature and strain. Assuming that $k_f \approx 0.3 k_y$ for molybdenum based on data cited by Armstrong⁽¹⁵⁾, the variation of σ_f with $l^{-1/2}$ can be determined by drawing a series of straight parallel lines of slope equal to k_f through points that represent values of flow stress corresponding to increasing strain values (from ϵ_L to ϵ_F) at a constant test temperature ($T > T_b$). This was done using the σ_f vs. ϵ data given in Fig. 19 for the fine grain molybdenum strip of grain size $l^{-1/2} = 6.2 \text{ mm}^{-1/2}$ which is

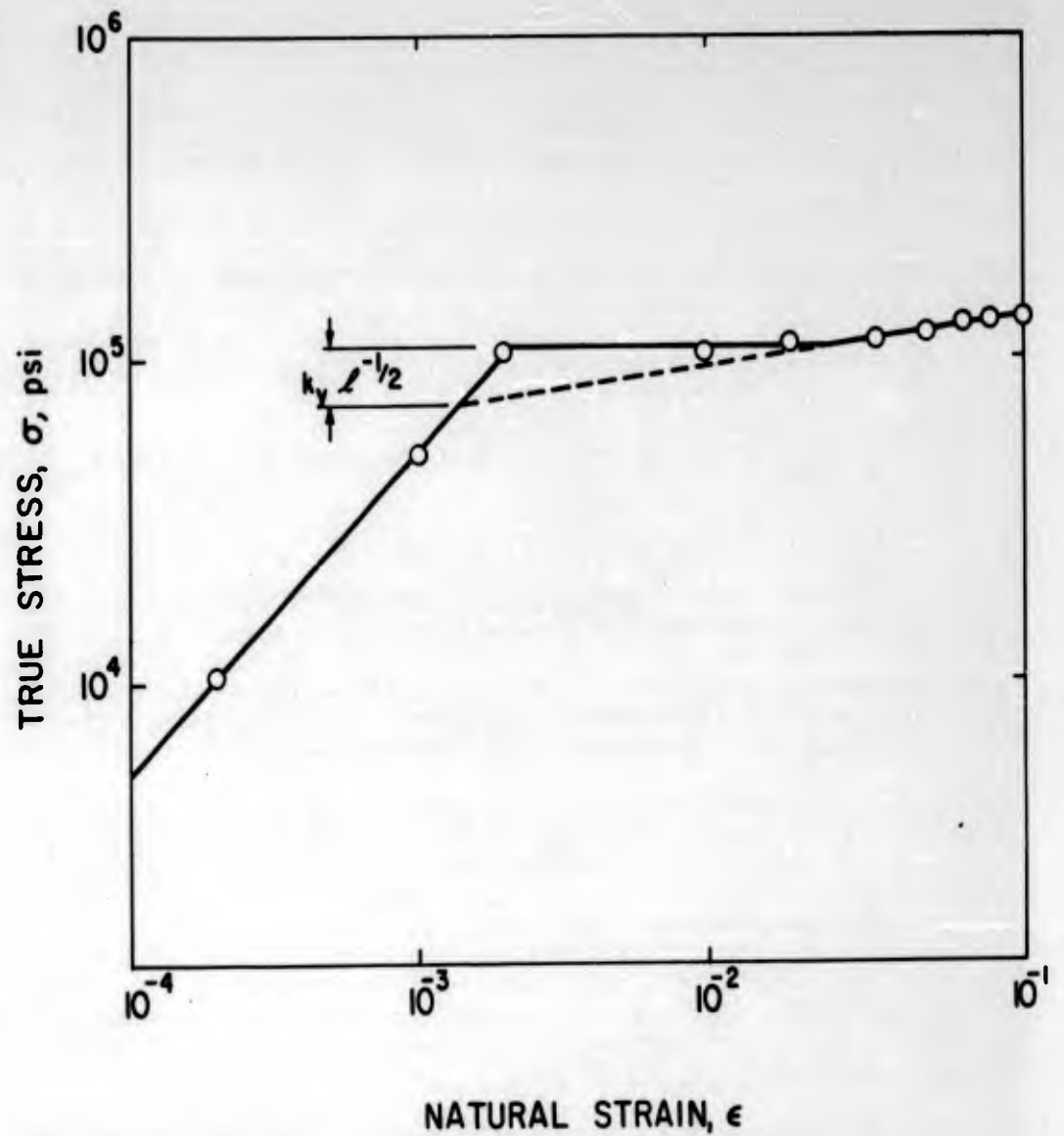


Fig. 19 - Log-log true stress - true strain curve of molybdenum (Mo-E2) strip in the as-recrystallized condition ($l^{-1/2} = 6.2 \text{ mm}^{-1/2}$) tested at -40°C .

greater than $l_b^{-1/2}$. From the σ_E vs. $l^{-1/2}$ and σ_f vs. $l^{-1/2}$ plots for various values of $\epsilon > \epsilon_L$, the variation of σ_F with $l^{-1/2}$ ($> l_b^{-1/2}$) was determined on the basis that σ_F represents the locus of points corresponding to the intersections of the σ_F and σ_f lines for particular values of ϵ . The predicted fracture stress is indicated in Fig. 18 by the dashed curve which lies above the predicted σ_f line for $l^{-1/2} > l_b^{-1/2}$. By plotting the corresponding values of ϵ and $l^{-1/2}$ for each intersection, the predicted curve of ϵ_F vs. $l^{-1/2}$ indicated by a dashed line in the lower portion of Fig. 18 is obtained.

The observed variations of σ_F and ϵ_F with grain size as indicated by the solid curves in Fig. 18 are in fair agreement with the corresponding predicted variations in that the same trends are displayed with increasing $l^{-1/2}$. However, the observed values are somewhat higher than the predicted ones. Although the differences might be explained by an increase in σ_F with increasing test temperature, in contrast to the assumption of a temperature independent σ_F , this does not appear likely.

E. Effect of Plastic Deformation and Annealing on the Tensile Ductility Transition

1. Effect of Deformation by Rolling

The ductile-brittle transition behavior of high purity molybdenum (Mo-E1) strip as determined by uniaxial tension tests parallel to the rolling direction is shown in Figs. 20, 21, and 22. Three conditions of rolling deformation were studied: 5%, 46% and 88% (M1C, M1E-AR, and M1H-AR, respectively, Table 1). Fracture strength, yield strength (0.2% offset), reduction in area, and elongation are plotted against test temperature for each condition.

As shown in Figs. 20, 21, and 22, yield strength decreases continuously with increasing test temperature over the range used (-195°C to +23°C) for the three conditions tested. Fracture strengths also decrease gradually with increasing test temperature except for an abrupt increase at the transition temperature (T_d). Corresponding changes in ductility occur with increasing test temperature. Both elongation to fracture and reduction in area increase gradually up to T_d , at which abrupt increases occur. Above T_d , the elongation remains approximately constant with increasing temperature, whereas the reduction in area increases, especially for the slightly and moderately worked conditions.

Even below T_d , appreciable plastic deformation occurs before fracture. Higher amounts of deformation are found than were previously observed in commercial tungsten (W-P4) wire^(1,2). Whereas elongations and reductions in area of about 1% were found in tungsten below T_d , reductions in area of 8 to 12% are exhibited by the Mo-E1 strip just below T_d . Although the ductility is lowered as the test temperature is decreased, nil-ductility was not attained at the lowest test temperature used.

As shown, increasing amounts of prior plastic deformation raise the level of the yield stress vs. test temperature curve without appreciably

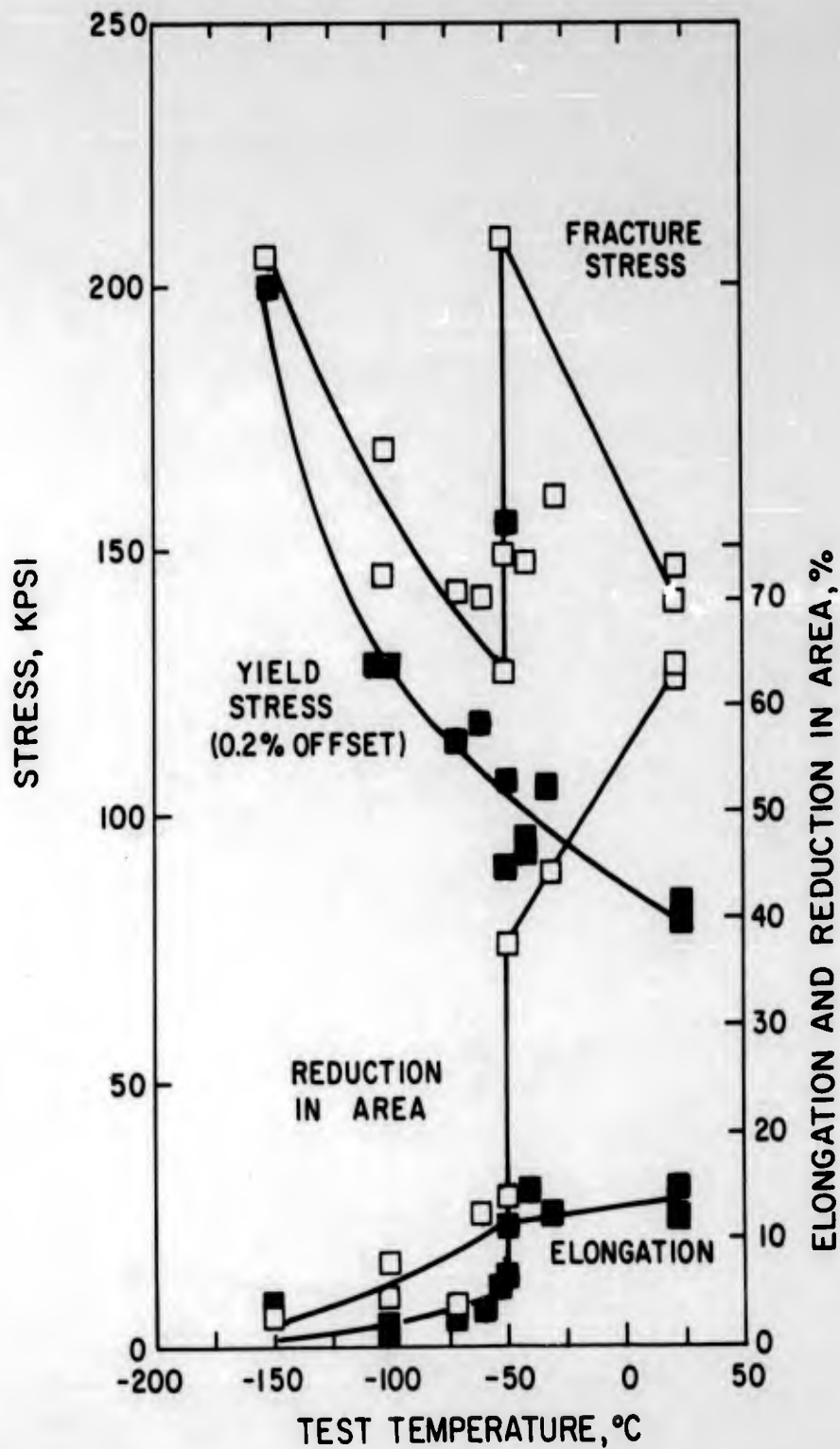


Fig. 20 - Effect of the test temperature on the tensile properties of molybdenum (Mo-E1) strip in the slightly worked condition (5% reduction).

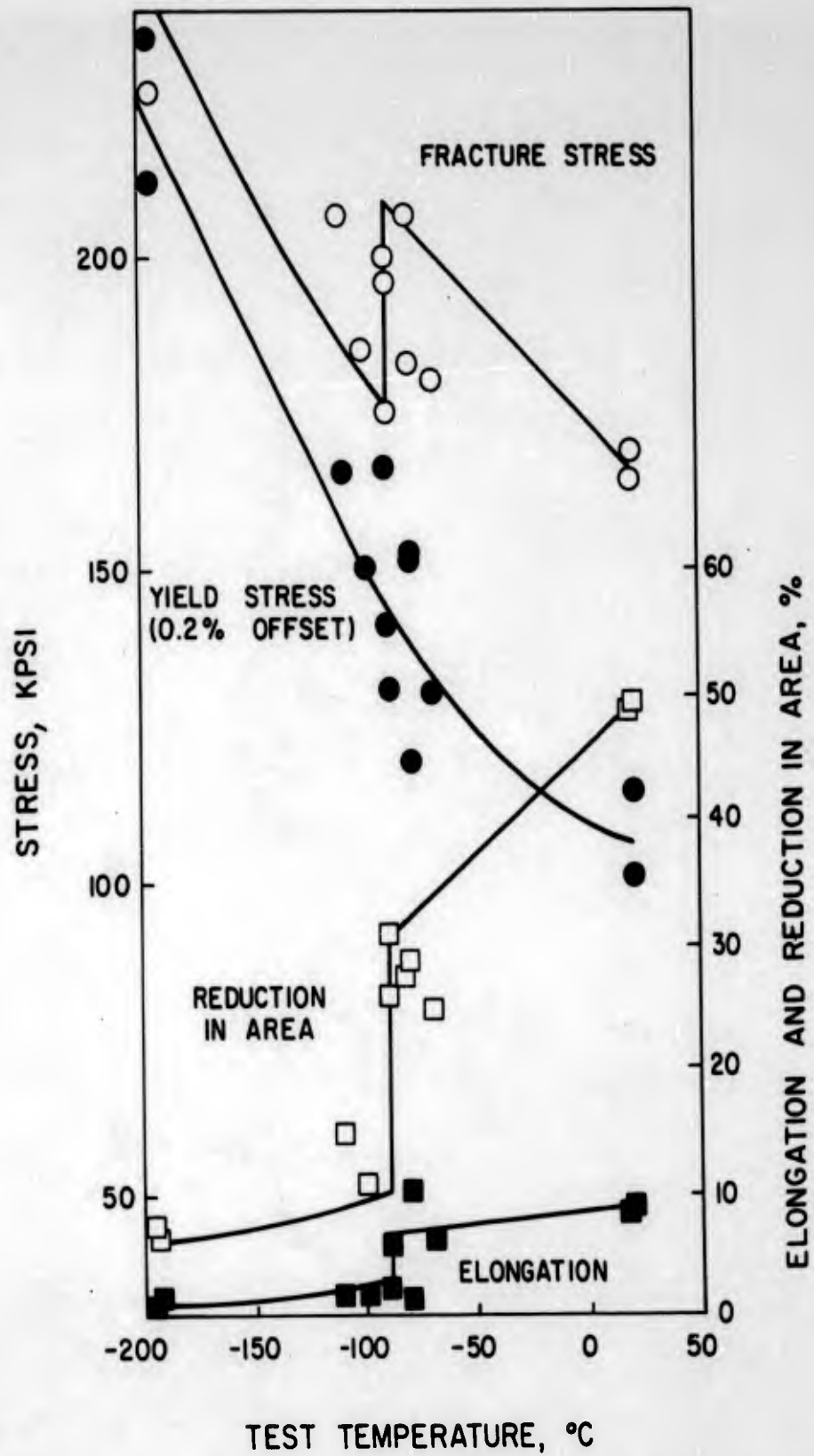


Fig. 21 - Effect of the test temperature on the tensile properties of molybdenum (Mo-E1) strip in the moderately worked condition (46% reduction).

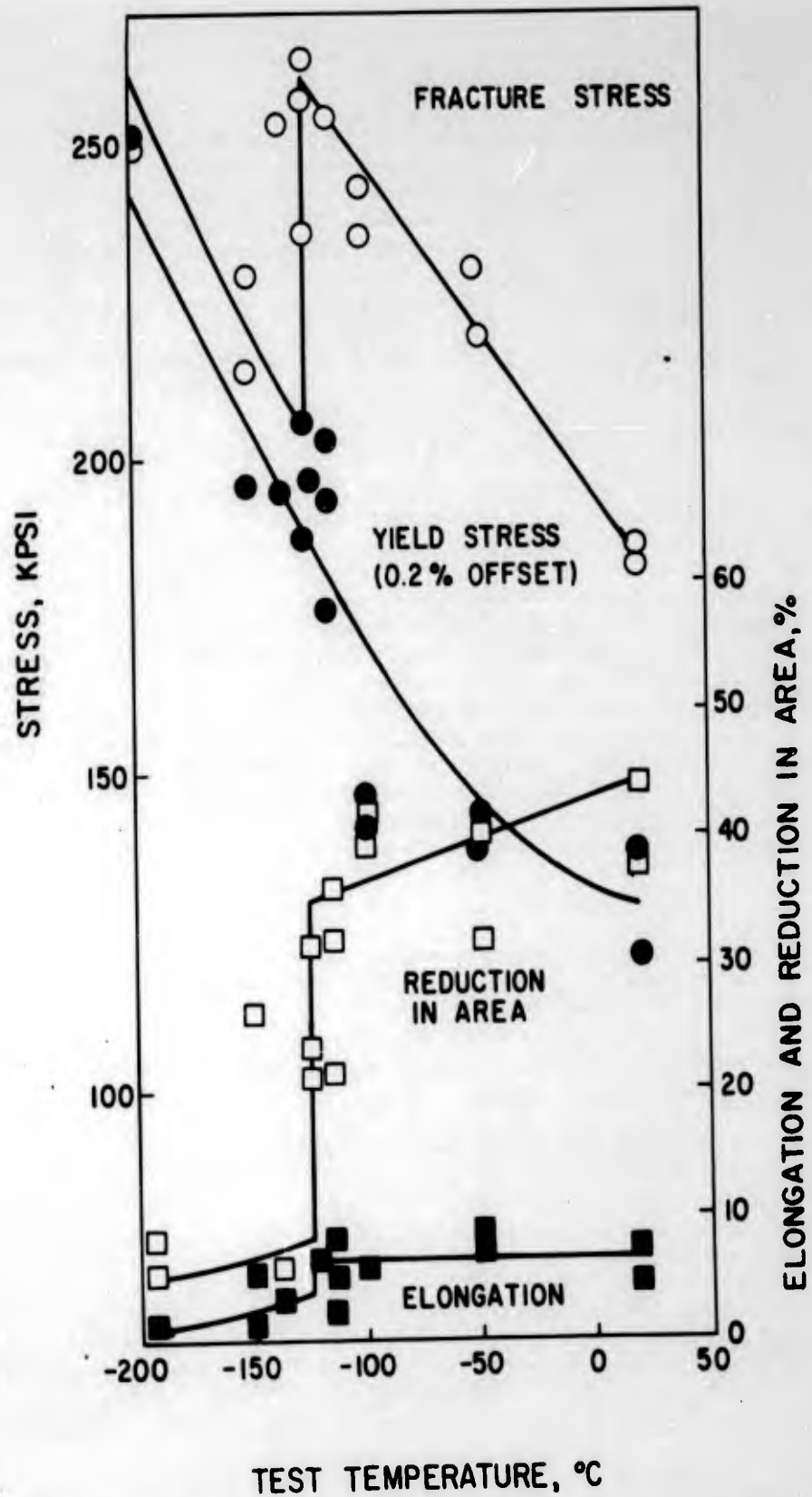


Fig. 22 - Effect of the test temperature on the tensile properties of high purity molybdenum (Mo-E1) strip in the heavily worked condition (88% reduction).

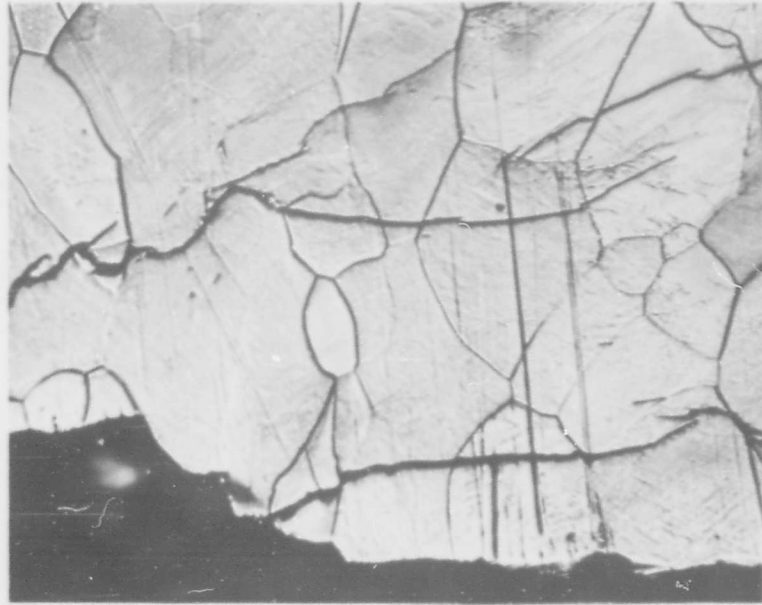
changing its shape. The levels of the fracture stress curves both below and above T_d are also raised with increasing deformation. The ductility transition temperature was found to be lowered from -50°C for the slightly worked condition to -90°C for the moderately worked condition, and to -125°C for the heavily worked condition. As might be expected, continuous decreases in room temperature ductility occur with increasing deformation. At test temperatures just above T_d , however, the reduction in area appears to decrease to a minimum as a result of the moderate deformation (46% reduction) and then increases again as a result of the heavy deformation (88% reduction) to approximately the same level as for the slightly worked condition. Although yield points are not observed, the changes in the shapes of the curves with increasing deformation are consistent with the property changes described above. As expected, the maximum uniform elongation is substantially lower for the moderately worked as compared to the slightly worked condition, although the change as a result of further working is small.

Tensile fractures of the slightly worked strip were found to occur mainly by transgranular cleavage both below and above T_d (Figs. 23 and 24), thus indicating that the observed ductility transition does not correspond to a complete change in the mode of fracture, although the proportion consisting of cleavage facets appears to decrease somewhat with increasing test temperature. However the fractures were still partly cleavage even as high as room temperature (23°C). Microscopic examination of the rolling plane surfaces of both prepolished tensile specimens and of specimens sectioned after testing revealed no conclusive evidence of microcracks, either on the tensile specimen surfaces or in the interiors. Discontinuous cracks up to several grain diameters long are observed, but appear to be associated with secondary cracks branching out from the main fracture, and thus cannot be identified as microcracks. It would appear from these observations that the conditions required to form the first crack are sufficient to propagate it to complete fracture.

2. Effect of Annealing

The effect of annealing on the transition behavior of both moderately and heavily worked Mo-E1 strip products (M1E-HT and M1H-HT, respectively) was investigated for combinations of time and temperature that were expected to produce the maximum changes due to recovery-annealing. By means of preliminary experiments, an attempt was made to select annealing temperatures just below the recrystallization range.

As shown in Fig. 25, annealing of the moderately worked (M1E) strip for 1 hour at 1000°C results in the following changes: a) yield strength was found to decrease compared to the as-rolled state at equivalent test temperatures; b) T_d increases from -90° to -60°C , only 10°C below that of the slightly worked condition; c) elongation and reduction in area also increase above T_d ; and d) fracture strength decreases below T_d , whereas it increases above T_d . These changes in fracture strength are consistent with the decrease in yield strength at all test temperatures and the increase in ductility above T_d . In contrast to the appreciable changes in transition behavior of the moderately worked



(a)

68

500X

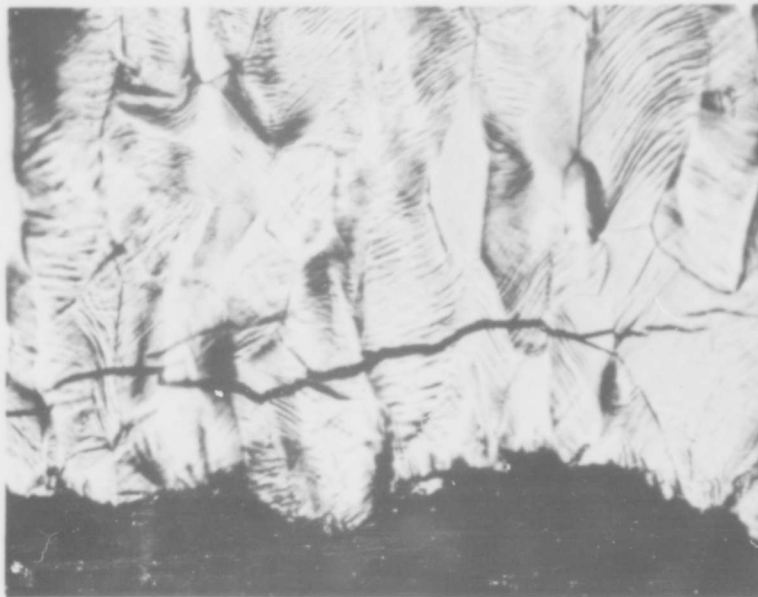


(b)

201

200X

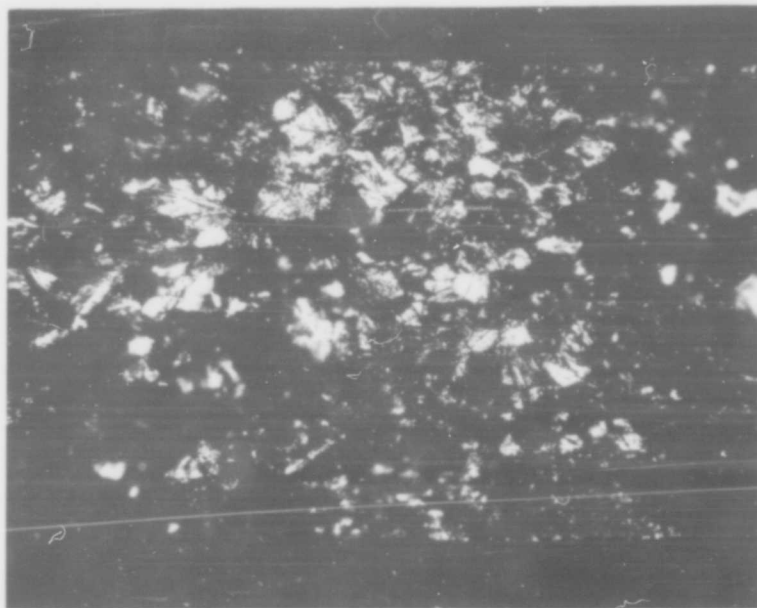
Fig. 23 - Light micrographs of high purity molybdenum (Mo-E1) strip, tensile specimen after testing at -70°C , showing transgranular cleavage fracture. (a) Prepolished rolling plane section, rolling direction and tensile axis vertical, etched lightly after testing; note secondary cracks. (b) Fracture surface, note cleavage facets with river markings.



(a)

69

500X



(b)

205

200X

Fig. 24 - Light micrographs of high purity molybdenum (Mo-E1) strip tensile specimen after testing at -50°C , showing transgranular cleavage fracture. (a) Pre-polished rolling plane section, rolling direction and tensile axis vertical, etched lightly after testing; note secondary cracks. (b) Fracture surface, note cleavage facets with river markings.

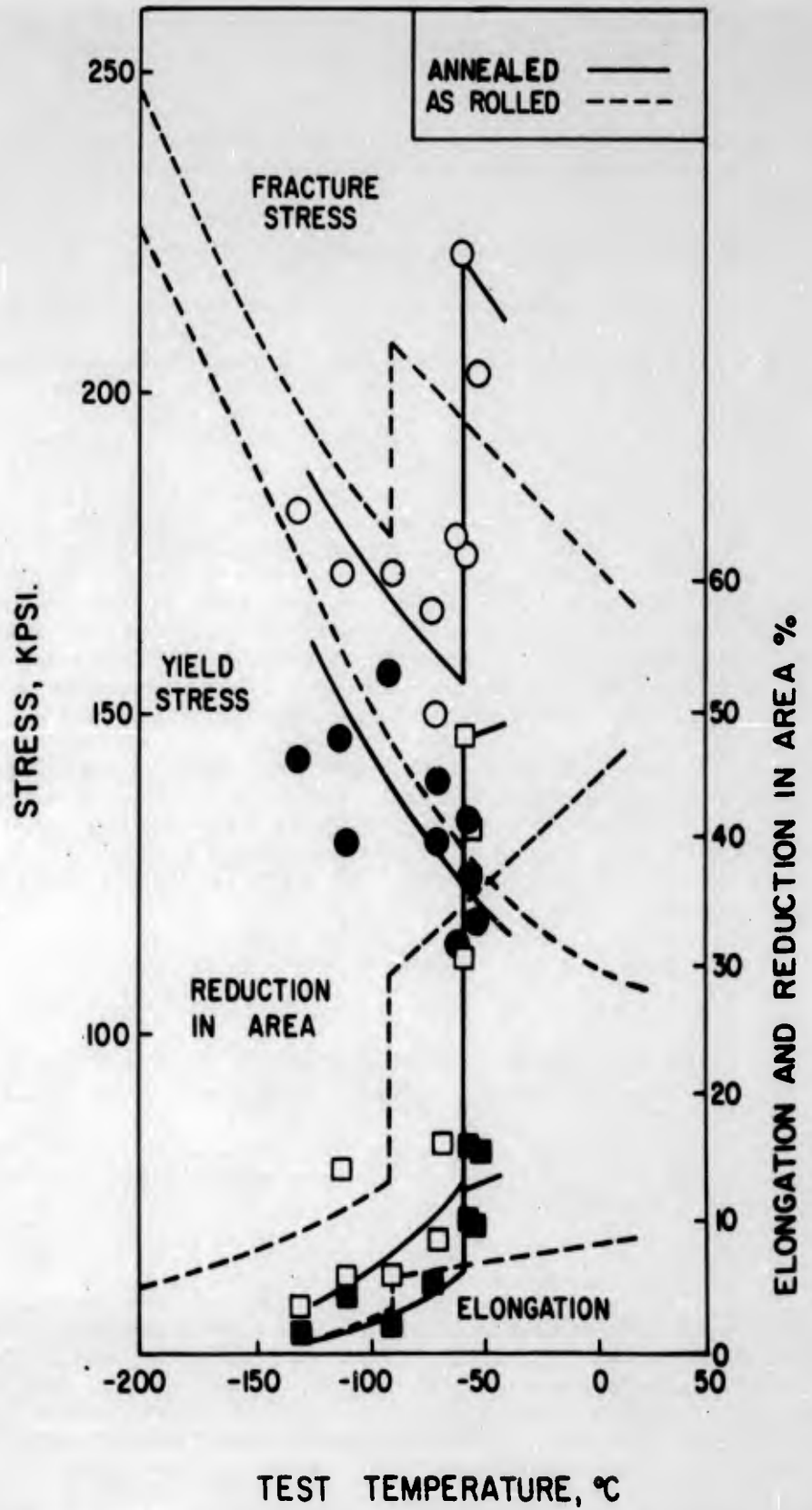


Fig. 25 - Effect of recovery-annealing (1 hour at 1000°C) on the tensile properties of moderately worked (46% reduction) molybdenum (Mo-E1) strip.

strip, Fig. 26 shows that no appreciable changes occur in the heavily worked strip after annealing for 1 hour at 900°C, except for an increase in elongation above T_d .

F. Calculation of Effective Surface Energy for Fracture

Based on the results of fracture stress measurements made on molybdenum strip in the as-recrystallized condition (Fig. 17) and after various amounts of rolling deformation (Figs. 20, 21 and 22), it is possible to calculate the effective surface energy for fracture using the Cottrell fracture relation⁽²¹⁾. This type of calculation is simplified if fracture stress data corresponding to just below T_d are utilized. It was observed that essentially no necking occurs at test temperatures up to T_d , whereas considerable necking occurs above T_d . Just below T_d , appreciable uniform elongation corresponding to about 8-12% reduction in area was found to occur prior to fracture of the four conditions of molybdenum strip studied. Thus calculating the effective surface energy (γ') for the case of fracture just below T_d has the advantage that a) fracture stresses at approximately equivalent plastic strains are utilized and b) plastic constraint associated with necking does not have to be taken into account i. e. Cottrell's plastic constraint factor (β) equals unity. However, it should be pointed out that higher calculated values of γ' are obtained if based on smaller values of plastic strain corresponding to fracture data obtained at lower test temperatures.

It is believed that the Cottrell fracture relation for calculating the effective surface energy (γ'), which applies to fracture taking place at the yield stress, should be modified by substituting the flow stress parameter (k_f) for the yield stress parameter (k_y), if appreciable strain hardening occurs prior to fracture. For the case of molybdenum strip tested just below T_d , the following relation therefore applies:

$$\gamma' = \frac{k_f \sigma_F (D_p)^{1/2}}{2G} \quad (3)$$

where σ_F = fracture stress
 $2D_p$ = average distance between dislocation obstacles
 G = shear modulus (1.2×10^{12} dynes/cm² for molybdenum).

Assuming that $k_f = 0.3 k_y$ for molybdenum⁽¹⁵⁾ and that $k_y/G = 5 \times 10^{-5}$ (based on shear stress and semi-grain size) in accordance with the correlation found by Rosenfield⁽¹⁹⁾, equation (3) becomes:

$$\gamma' = 7.5 \times 10^{-6} \sigma_F (D_p)^{1/2} \quad (4)$$

For deformed materials, it seems more correct to use the average slip distance between obstacles to dislocation movement ($2D_p$) prior to fracture instead of the original primary grain size ($2d_p$). For molybdenum strip in either the annealed or slightly worked condition, essentially equiaxed primary grains are present; and it is therefore believed that the slip distance is approximately equal to the grain diameter corrected for the reduction in area preceding fracture.

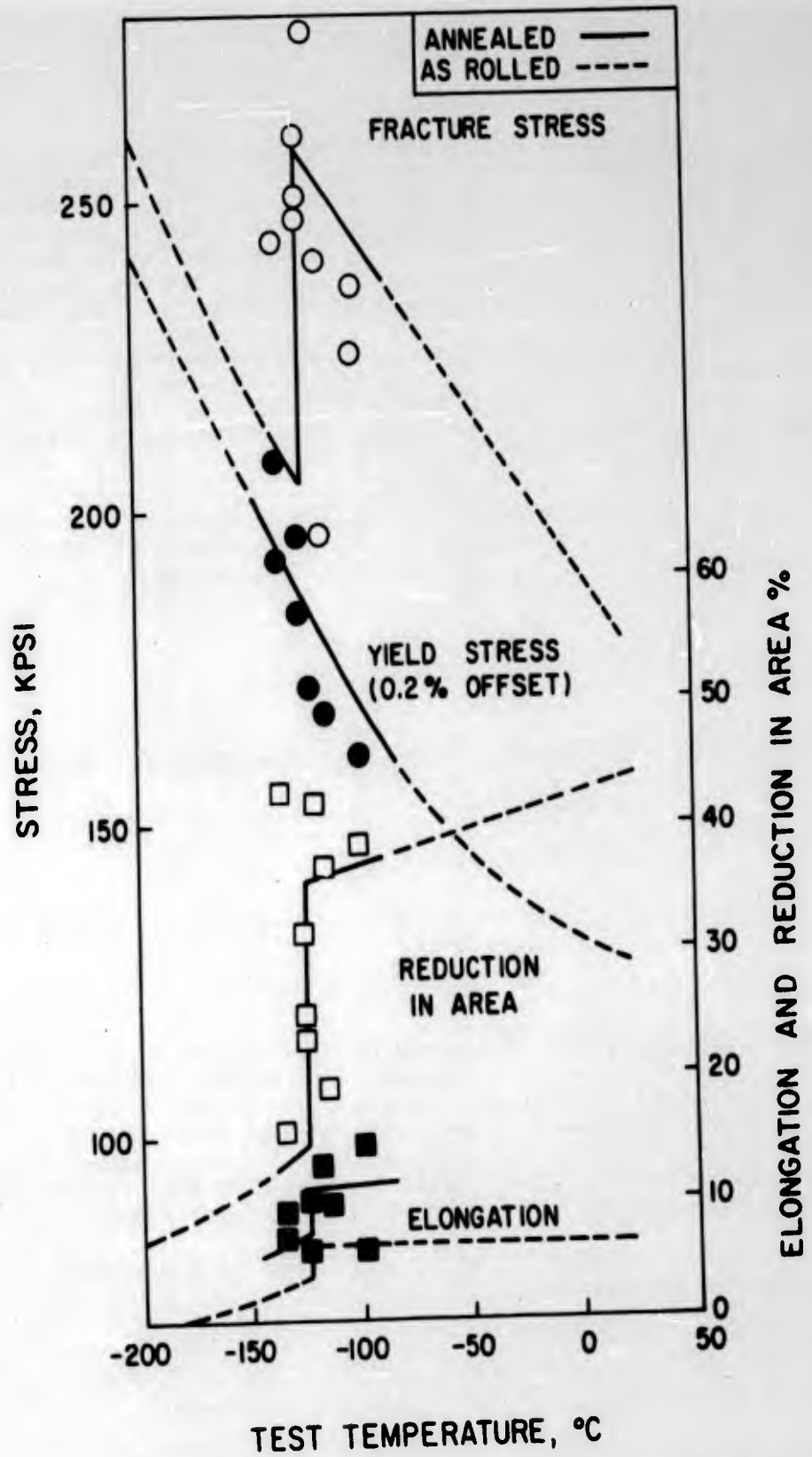


Fig. 26 - Effect of recovery-annealing (1 hour at 900°C) on the tensile properties of heavily worked (88% reduction) molybdenum (Mo-E1) strip.

However, for the more heavily worked conditions, consideration was given to the fact that elongated primary grains of a particular texture (001)[110] are developed. The slip system for molybdenum is along (110)[111], which in a textured condition corresponds to a direction that makes an angle of about 35° with respect to the rolling direction. It can be shown that for this case the slip distance ($2D_p$) may be taken as approximately equal to 1.8 times the width of the elongated grains (corrected for the reduction in area preceding fracture).

Based on the measured values of primary grain size given in Table 2 and of fracture stress just below the transition temperature, the effective surface energy (γ') was calculated for the four conditions of molybdenum strip studied. As shown in Table 4, the average value of γ' based on primary grain size was found to be about 3000 ergs/cm².

Equation (4) should be modified in order to calculate γ' based on the size of the substructure revealed by transmission electron microscopy. Assuming that the ratio $D_p:D_s$ is constant, it can be shown that

$$\frac{k_{fs}}{k_{fp}} = \left(\frac{D_s}{D_p} \right)^{1/2} \quad (5)$$

where k_{fs} = flow stress parameter based on effective subgrain size
 k_{fp} = flow stress parameter based on effective primary grain size
 D_s = effective subgrain size

In order to calculate γ' based on subgrain size, equation (4) can be modified as follows:

$$\gamma' = 7.5 \times 10^{-6} \sigma_F D_s (D_p)^{1/2} \quad (6)$$

In Table 5, the effective slip distance ($2D_s$) based on subgrain size (average first order subgrains, see Table 2) and the corresponding calculated values of γ' are given for the four material conditions. The average value of γ' based on subgrain size was found to be about 200 ergs/cm², which is only about 7% of that calculated on the basis of primary grain size. Considering that the generally accepted surface energy value for molybdenum is 2000-3000 ergs/cm², the low value of γ' calculated on the basis of subgrain size does not seem correct.

A comparison of γ' values reported by various investigators for molybdenum is given below:

Reference	γ' in ergs/cm ²
present work	3000
Owen ⁽²⁰⁾	9000
Ault ⁽¹⁶⁾	3000
Cottrell ⁽²¹⁾	8000
Johnson ⁽¹⁷⁾	12,000

Table 4

Calculated Effective Surface Energy of Molybdenum Strip Just Below Transition Temperature Based on Primary Grain Size

Condition	Transition Temperature °C	Tensile Test % R.A.	Fracture Stress σ_F dynes/cm ²	Slip Distance $2D_p$ cm	Effective Surface Energy** γ' ergs/cm ²
recrystallized	-70	9	9.5×10^9	2.5×10^{-3}	2.5×10^3
5% reduction	-50	12	9.4×10^9	3.4×10^{-3}	2.9×10^3
46% reduction	-90	10	1.2×10^{10}	2.5×10^{-3}	3.2×10^3
88% reduction	-125	8	1.4×10^{10}	1.0×10^{-3}	2.3×10^3

* Corrected for slip direction and reduction in area prior to fracture: $D_p = 1.8 d_p \left[\frac{100 - (1/2) \% R.A.}{100} \right]$ except that 1.8 factor not used for the recrystallized and the slightly worked conditions.

** Calculated on the basis that $\gamma' = 7.5 \times 10^{-6} \sigma_F (D_p)^{1/2}$ just below the transition temperature (T_d).

Table 5

Calculated Effective Surface Energy of Molybdenum Strip Just Below
Transition Temperature Based on Subgrain Size

Condition	Transition Temperature °C	Tensile Test % R.A.	Fracture Stress σ_F dynes/cm ²	Measured Subgrain Size 2 d _s cm	Slip Distance* 2 D _s cm	Effective Surface Energy** γ' ergs/cm ²
recrystallized	-40	9	9.5 x 10 ⁹	3.5 x 10 ⁻⁴	3.3 x 10 ⁻⁴	340
5% reduction	-50	12	9.4 x 10 ⁹	3.5 x 10 ⁻⁴	3.2 x 10 ⁻⁴	270
46% reduction	-90	10	1.2 x 10 ¹⁰	1.1 x 10 ⁻⁴	1.0 x 10 ⁻⁴	130
88% reduction	-125	8	1.4 x 10 ¹⁰	0.25 x 10 ⁻⁴	0.24 x 10 ⁻⁴	60

* Corrected for reduction in area during tensile test: $D_s = d_s \left[\frac{100 - (1/2) \% R.A.}{100} \right]$

** Calculated on the basis that $\gamma' = 7.5 \times 10^{-6} \sigma_F D_s (D_p)^{1/2}$ just below the transition temperature (T_d).

The γ' value (based on primary grain size) obtained in the present work is at the low end of the range of those previously reported.

G. Calculation of Critical Crack Length

The critical crack length ($2c$) corresponding to each of the three conditions of the Mo-E1 strip was calculated by the Griffith-Orowan equation using the γ' values given in Tables 6 and 7:

$$c = \frac{2\gamma' E}{\pi\sigma_F^2} \quad (7)$$

where E is Young's modulus (3.2×10^{12} dynes/cm² for molybdenum). Calculations were made of c based on primary and subgrain size. As shown in Table 6, the average value of the ratio of the critical crack length to the effective grain size (c/D_p) was found to be about 0.04; and as shown in Table 7, the average value of the ratio of the critical crack length to the effective subgrain size (c/D_s) was also found to be about 0.04. Since for the four conditions studied D_s/D_p was found to be in the range of 0.03 to 0.13, it appears that the critical crack size as calculated on the basis of the primary grain size is about the same as the subgrain size. This is considered to be an indication that subgrain size may influence the magnitude of the critical crack size. On the other hand, the critical crack size as calculated on the basis of subgrain size is a very low value. This is attributed to the very low γ' value as calculated on the basis of subgrain size, which is considered fallacious.

H. Calculation of Change in Fracture Stress at T_d

In tensile tests of the molybdenum specimens, it was observed a) that on increasing the test temperature (T) essentially no necking occurs for $T < T_d$ but necking occurs for $T > T_d$ and b) that there is no change in the mode of fracture at T_d i. e. transcrystalline cleavage just below and just above T_d . It therefore appears likely that the sharp increase in fracture stress at T_d is associated with the occurrence of necking. It seems likely that this strengthening phenomenon may involve three factors associated with necking:

- a) increased strain rate due to the fact that necking occurs in a localized region,
- b) plastic constraint due to the geometry of the neck,
- c) decreased grain size due to the occurrence of plastic deformation during the tensile test.

Defining the over-all strengthening factor due to necking (q_n) as the ratio of the observed fracture stress just above T_d to that just below T_d , q_n can be considered as equal to the product of three factors:

$$q_n = q_\epsilon \times q_p \times q_d \quad (8)$$

where q_ϵ = strain rate factor

q_p = plastic constraint factor

q_d = grain size factor.

Table 6

Calculated Critical Crack Length of Molybdenum
Strip Based on Primary Grain Size

<u>Condition</u>	Effective Surface Energy γ' ergs/cm ²	$\frac{\sigma_F^2}{2}$ dynes ² /cm ⁴	Critical Crack Length $2c^*$ cm	c/D_p
annealed	2.5×10^3	9.0×10^{19}	1.1×10^{-4}	0.04
5% reduction	2.9×10^3	8.0×10^{19}	1.3×10^{-4}	0.04
46% reduction	3.2×10^3	1.4×10^{20}	0.9×10^{-4}	0.04
88% reduction	2.3×10^3	2.0×10^{20}	0.5×10^{-4}	0.05

Table 7

Calculated Critical Crack Length of Molybdenum
Strip Based on Subgrain Size

<u>Condition</u>	Effective Surface Energy γ' ergs/cm ²	$\frac{\sigma_F^2}{2}$ dynes ² /cm ⁴	Critical Crack Length $2c^*$ cm	c/D_s
annealed	340	9.0×10^{19}	1.5×10^{-5}	0.05
5% reduction	270	8.9×10^{19}	1.2×10^{-5}	0.03
46% reduction	130	1.4×10^{20}	3.7×10^{-6}	0.04
88% reduction	60	2.0×10^{20}	1.2×10^{-6}	0.05

$$* c = \frac{2.0 \times 10^{12} \gamma'}{\sigma_F^2}$$

Methods of determining the various strengthening factors are described in the following sections. Comparisons of the calculated and measured q_n values for the four molybdenum strip conditions studied in this investigation are given in Table 8, which shows that good agreement was obtained. The difference between the calculated and measured values of q_n is only about 10% for the recrystallized condition and within about 5% for the three worked conditions.

Bechtold⁽²²⁾ in an investigation of flow and fracture of annealed molybdenum bars used a similar approach to explain the difference between the observed fracture stress value (average true stress) and that obtained by extrapolating the initial portion of the true stress-true strain curve. The extrapolation was started at the maximum uniform strain (ϵ_u) and carried up to the fracture strain (ϵ_n). He reported that by subtracting the effects of both increased strain rate and plastic constraint as associated with necking from the observed fracture stress, the corrected flow stress value obtained coincides with that obtained by extrapolation. It should be pointed out that by making a further correction for the decrease in grain size due to about 50% reduction in area that occurred during necking, the stress value obtained coincides with the necking stress i. e. true stress corresponding to maximum load. This confirms the validity of equation (8).

1. Strain Rate Factor

The strain rate factor (q_ϵ) can be determined from the Zener-Hollomon relation⁽²³⁾ for the flow stress (σ_f) as a function of the applied strain rate ($\dot{\epsilon}_a$) at a given temperature in terms of the constants σ_o'' and r :

$$\sigma_f = \sigma_o'' (\dot{\epsilon}_a)^r \quad (9)$$

Due to localized necking and a consequently higher strain rate in the necked region ($\dot{\epsilon}_n$), the flow stress required to produce a given strain is increased by a factor (q_ϵ) where

$$q_\epsilon = \left(\frac{\dot{\epsilon}_n}{\dot{\epsilon}_a} \right)^r \quad (10)$$

In terms of the gage length (L_g) and the length over which necking effectively occurs (L_n), the average strain rate in the necked region $\dot{\epsilon}_n$ of a round tensile specimen is given by

$$\dot{\epsilon}_n = \frac{L_g}{L_n} \dot{\epsilon}_a \quad (11)$$

and assuming $\dot{\epsilon}_n = \frac{\bar{a}_n}{a_n} \dot{\epsilon}_n$ where a_n and \bar{a}_n are the minimum radius and mean radius respectively of the necked region (assuming a circular cross section):

$$\dot{\epsilon}_n = \left(\frac{L_g}{L_n} \right) \left(\frac{\bar{a}_n}{a_n} \right)^r \dot{\epsilon}_a \quad (12)$$

Table 8

Comparison of Calculated and Measured Values of Fracture Stress Ratio at T_d

Condition	% R. A.		Strengthening Factors			Over-All	
	b*	a*	$q_{\dot{\epsilon}}$	q_p	q_d	Calculated	Measured
						q_n	q_n
recrystallized	9	54	1.12	1.10	1.11	1.37	1.23
5% reduction	12	45	1.11	1.08	1.08	1.28	1.27
46% reduction	10	32	1.09	1.05	1.05	1.20	1.25
88% reduction	8	36	1.10	1.06	1.06	1.23	1.29

where q_n = over-all necking factor

$q_{\dot{\epsilon}}$ = strain rate factor

q_p = plastic constraint factor

q_d = grain size factor

* b - just below T_d

a - just above T_d

From geometrical considerations, L_n is given in terms of the radius of curvature at the neck (R), and the radius of the round test section corresponding to maximum uniform elongation (a_u):

$$L_n = 2[2R(a_u - a_n) - (a_u - a_n)^2]^{1/2} \quad (13)$$

Therefore for a round test bar, the strain rate factor is

$$q_\epsilon^* = \left[\frac{a_n L_g}{2a_n [2R(a_u - a_n) - (a_u - a_n)^2]^{1/2}} \right]^r \quad (14)$$

Based on Bridgeman's data⁽²⁴⁾, the following relation given in terms of the total strain at the neck (ϵ_n) and the maximum uniform strain (ϵ_u) appears to hold for round steel tensile specimens:

$$\frac{a_n}{R} = (\epsilon_n - \epsilon_u)^{1/2} \quad (15)$$

It is assumed that equation (15) holds approximately for flat molybdenum tensile specimens with a w/t ratio as large as 4:1. For such a case, the semi-width at the neck ($w_n/2$) is considered equal to a_n and the following approximation which involves the initial (gage) radius a_o should also hold:

$$\epsilon_n \cong \ln \left(\frac{a_o}{a_n} \right) \quad (16)$$

Noting that $(\bar{a}_n/a_n)^r \cong 1$ when $r \ll 1$ as is usually the case, equation (14) can be expressed in terms of ϵ_n by substituting in equations (15) and (16):

$$q_\epsilon^* = \left[\frac{L_g (\epsilon_n - \epsilon_u)^{1/4}}{[8 a_o a_u \exp^{-\epsilon_n} - 8 a_o^2 \exp^{-2\epsilon_n} - 4(\epsilon_n - \epsilon_u)^{1/2} (a_u - a_o \exp^{-\epsilon_n})^2]^{1/2}} \right]^r \quad (17)$$

Using equation (17), calculations were made of q_ϵ^* for the slightly worked condition which gave a uniform reduction of area of about 9% ($\epsilon_u = 0.087$) just below T_d . The initial test specimen dimensions were $L_g = 0.5$ inch and $a_o = 0.033$, and r is considered equal to 0.05 as reported by Bechtold⁽²²⁾ for molybdenum strained to $\epsilon = 0.1$. The results of these calculations are as follows:

ϵ_n	$\epsilon_n - \epsilon_u$	q_ϵ^*
0.1200	0.0000	1.00
0.1201	0.0001	1.03
0.1210	0.0010	1.06
0.1300	0.0100	1.09
0.2200	0.1000	1.11
0.6000	0.4800	1.11

Based on these calculations, it appears that a marked strengthening effect becomes operative right from the start of necking i. e. $q_p^* = 1.03$ for a strain only 0.0001 due to necking alone. This is not the case for the other strengthening factors (increased plastic constraint and decreased grain size), since a considerable amount of necking must occur before their effects became appreciable. As given in Table 8, similar calculations were carried out to determine the values of q_p^* corresponding to the fracture strains of the other three conditions.

2. Plastic Constraint Factor

The plastic constraint factor (q_p) is defined by the following ratio:

$$q_p = \frac{\sigma_a}{2\tau} \quad (18)$$

where σ_a = average true stress and τ = octahedral shear stress. According to Bridgeman⁽²⁴⁾, $1/q_p$ for round steel tensile specimens is related to the true strain (ϵ_n) at the neck as shown in Fig. 27. Although the relation in Fig. 27 is based on results for steel, it seems reasonable to expect that it holds approximately for other b. c. c. metals such as molybdenum. In the present investigation, the molybdenum strip was tested in the form of flat tensile specimens of gage width (w) 0.065 inch and gage thickness (t) 0.017 inch, i. e. $w/t=4$. In order to utilize Fig. 27 for determining q_p in this case, a correction should be made for the difference in plastic constraint behavior between round and flat test specimens.

For the case of a flat tensile specimen, Aronofsky⁽²⁵⁾ reported that the plastic constraint factor is less than for a round tensile specimen of the same steel. Some of Aronofsky's data are shown in Table 9. For the flat specimen ($w/t = 6$), it was found that ϵ_n and $(q_p - 1)$ are respectively 10% and 50% lower than the corresponding values for the round specimen. This information permits an approximate calculation of q_p for the flat molybdenum specimens since their w/t ratio is which is close to $w/t=6$ for Aronofsky's flat specimens. Thus, knowing that $\epsilon_n = 0.78$ (54% R. A.) for a flat recrystallized molybdenum specimen tested at -40°C , the ϵ_n value for a round specimen is estimated to be 10% higher or 0.87. From Fig. 27, the corresponding round tensile value of q_p is 1.20. Converting back to a flat tensile specimen by a decrease of 50% in $(q_p - 1)$ gives $q_p = 1.10$ for the recrystallized condition. Similarly, values of q_p were calculated for the three other conditions as given in Table 8.

3. Reduction in Effective Grain Size

The decrease in effective grain size that accompanies the reduction in area associated with necking is another effect that should be taken into account. According to the Cottrell-Petch fracture theory, the d -parameter represents half the average distance between obstacles to dislocation movement. Since it is generally assumed that the main obstacles are grain boundaries, $2d$ is usually taken as equal to the average original grain size. However, during a tensile test, the grain dimensions are decreased in directions perpendicular to that of the applied tensile stress. This tends to result in a lower

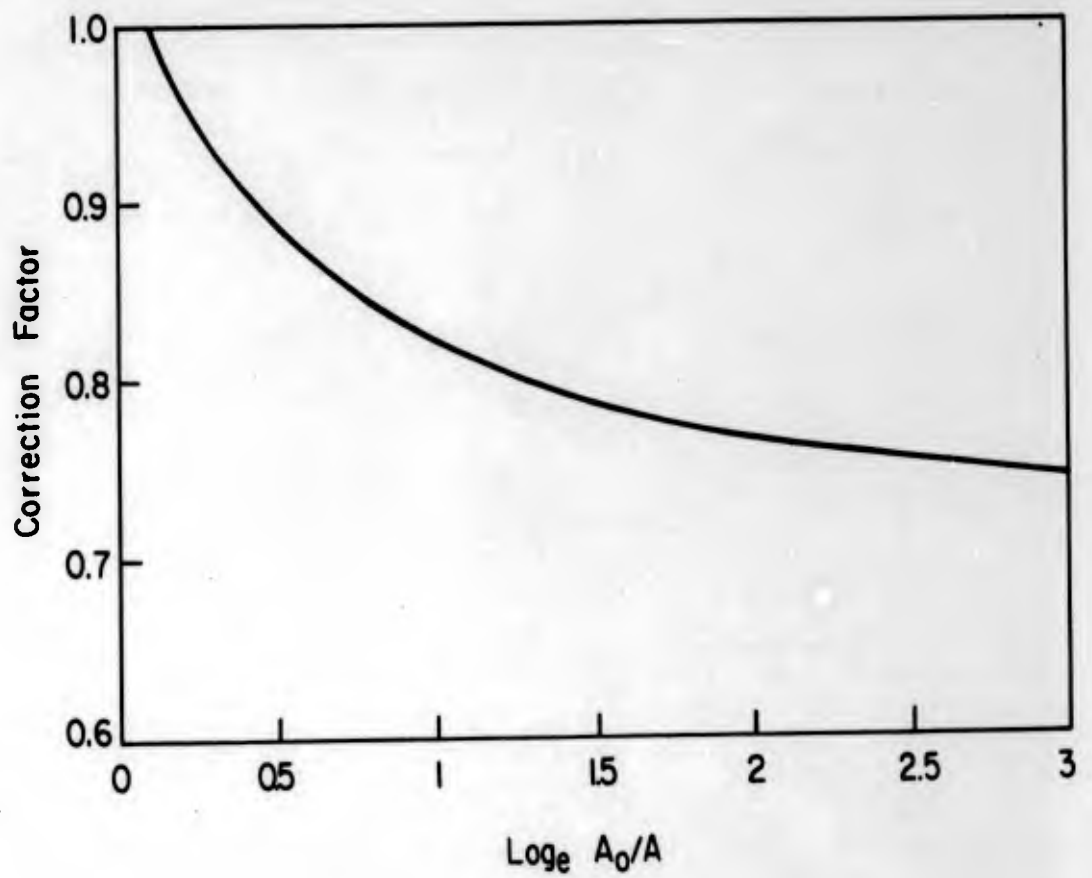


Fig. 27 - Correction factor ($1/q_p$) for reducing applied tensile stress to effective flow stress (Bridgman).

Table 9

Comparison of Round and Flat Tensile Tests of Steel

<u>Initial Test Dimensions</u>	<u>Round Specimen</u>	<u>Flat Specimen</u>
gage length	_____	22.5 inches
gage section	3-inch diameter	0.75 by 4.50 inch
Width: thickness	_____	6:1
gage area	7.1 sq. inches	3.4 sq. inches
<u>Measured Values</u>	<u>Round Specimen</u>	<u>Flat Specimen</u>
fracture strain (ϵ_n)	0.82	0.72**
octohedral shear stress (τ_F)	51.6 ksi	45**ksi
average fracture stress (σ_F)	133 ksi	105 ksi
plastic constraint factor (q_p)	1.29	1.17
$q_p - 1$	0.29	0.17

* Aronofsky⁽²⁵⁾

**Average value (both ϵ_n and τ_F varied from minimum at edge to maximum at center of specimen)

value of d and thereby an increase in the fracture stress (σ_F). Since the fractional decrease in effective grain size equals one-half the fractional reduction in area $(\Delta A/A)_n$ due to necking alone, and σ_F is considered to be proportional to $d^{-1/2}$, the grain size factor q_d is given by the following:

$$q_d = 1 + \frac{\Delta \sigma_F}{\sigma_F} = 1 - \frac{\Delta d}{2d} = 1 - \left(\frac{\Delta A}{4A} \right)_n \quad (19)$$

For the recrystallized condition, 45% R. A. occurred due to necking alone; and q_d equals 1.11 because of this grain size effect. Similarly, q_d values were calculated for the other three molybdenum conditions as given in Table 8.

For recrystallized or slightly worked material, a preferred orientation may develop as a result of the plastic deformation during the tensile test and result in alignment of the slip direction closer to the direction of stress application. In such a case, the effective distance between obstacles would be expected to increase, which contributes to a decrease in fracture stress. On the other hand, additional boundaries (i. e. deformation bands) are observed to form during plastic deformation, which tends to increase the fracture stress. As a rough approximation, the preferred orientation effect may be considered as compensated for by the formation of additional boundaries. Thus, although the grain size factor as given by equation (19) represents the reduction in area effect alone, it is believed to be a fair approximation. For heavily worked materials, the preferred orientation effect is probably present prior to the tensile test and the formation of a significant amount of additional boundaries would not be expected. Thus, equation (19) should also hold in this case as a fair approximation.

I. Criterion for Occurrence of Tensile Ductility Transition

In general, the ductile-brittle behavior of b. c. c. metals as determined by tensile testing is considered to involve the following types of transitions as the test temperature (T) is lowered:

- a) a relatively sharp decrease in both fracture stress and ductility at T_d ,
- b) a change in crystallographic mode of fracture from shear to cleavage at T_m ,
- c) occurrence of fracture induced by mechanical twinning at T_t .
- d) occurrence of fracture just at the lower yield stress which results in nil-ductility at T_b ,

As previously pointed out, the discontinuous change in ductility and fracture strength of the molybdenum studied does not correspond to a change in fracture mode since fracturing occurs by cleavage both just below and just above T_d (i. e. $T_m > T_d$). Furthermore, no evidence of the occurrence of fracture induced by mechanical twinning was found (i. e. $T_t < T_d$); and nil-ductility which corresponds to the original Cottrell-Petch criterion ($\sigma_F = \sigma_y$) occurs at a much lower test temperature (i. e. $T_b < T_d$). It therefore appears that the tensile ductility phenomenon at T_d is different from the other types of ductile-brittle

transitions at least in the molybdenum materials studied in this investigation. The distinctive feature of the tensile ductility phenomenon seems to be the occurrence of necking at test temperatures just above T_d (and higher) in contrast to uniform elongations just below T_d (and lower).

Based on the fairly accurate predictions of the change in fracture stress of molybdenum strip at T_d , the tensile ductility transition can be considered as the consequence of how the relative tendencies with respect to both necking and fracturing vary with test temperature. According to this hypothesis, the condition for a tensile ductility transition is the intersection of the fracture stress and the necking stress vs. temperature curves. On this basis, lowering of T_d can be achieved if by some means the fracture stress curve is raised relative to the necking stress curve; or conversely, if the necking stress curve is lowered relative to the fracture stress curve.

A schematic plot illustrating a ductility transition is shown in Fig. 28. The yield stress (σ_y), necking stress (σ_n), uniform strain fracture stress (σ_F), and observed fracture stress when necking occurs (σ_{Fn}) are plotted vs. test temperature (T). The variation of σ_n with T is shown by a curve which is above and is roughly similar to the σ_y curve. This is justified since σ_n is equal to the ultimate tensile stress (expressed as a true stress). It is assumed that with decreasing test temperature σ_n intersects σ_F at T_d , the extrapolated σ_n curve lies above σ_F ; whereas above T_d , the extrapolated σ_F curve lies between the σ_n and σ_{Fn} curves.

In order to illustrate the concepts involved in Fig. 28, examples of stressing a tensile specimen both below and above T_d are given. On stressing at T_1 which is below T_d , the yield stress (σ_{y1}) is reached first and this is followed by uniform plastic straining until fracture takes place at σ_{F1} . On stressing at T_2 which is above T_d , uniform plastic straining starts at σ_{y2} and continues until the necking stress σ_{n2} is reached. The specimen then necks continuously until it fractures at σ_{F2} . This happens because the strengthening factors associated with necking effectively raise σ_{F2} to σ_{Fn2} .

The condition for T_d is that

$$\sigma_F = \sigma_n \quad (20)$$

Equation(20) holds just below T_d whereas just above T_d the fracture stress depends on the necking factor (q_n):

$$\sigma_{Fn} = q_n \sigma_F \quad (21)$$

It is generally assumed that a flow stress (σ_f) depends on the true plastic strain (ϵ) in accordance with the following relation, which includes the strain hardening coefficient (K) and the strain hardening exponent (n):

$$\sigma_f = K\epsilon^n \quad (22)$$

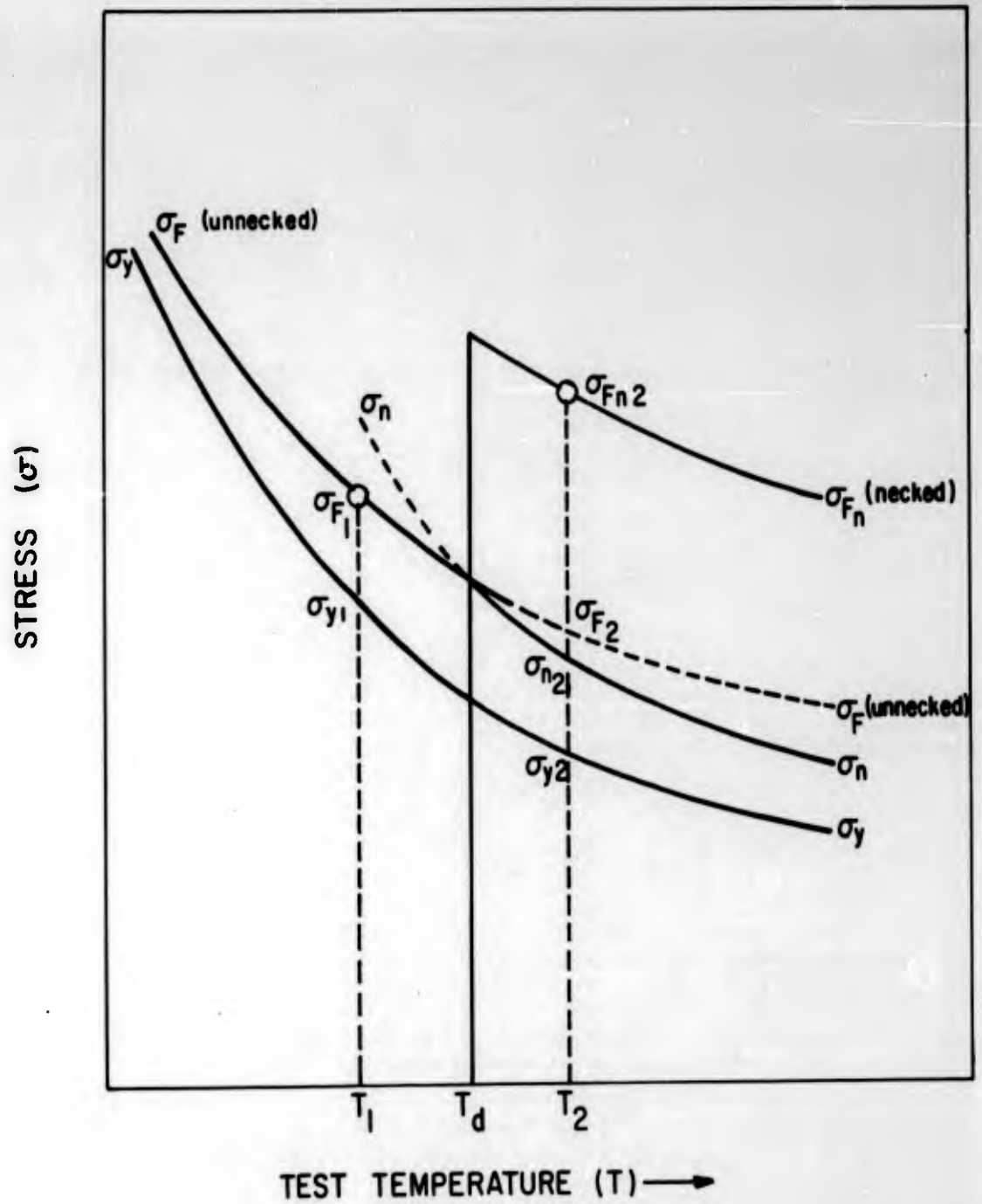


Fig. 28 - Schematic variation of the yield stress (σ_y), necking stress (σ_n), fracture stress (σ_F) for the unnecked condition, and fracture stress (σ_{Fn}) for the necked condition vs. test temperature.

Since when $\sigma_f = \sigma_n$, $\epsilon = n$

$$\sigma_n = K n^n \quad (23)$$

Based on (23), the strain hardening coefficient (K) can be obtained in terms of the yield stress (σ_y) and the yield strain (ϵ_y):

$$K = \frac{\sigma_y}{(\epsilon_y)^n} \quad (24)$$

Therefore the necking stress is related to the yield stress as defined by an arbitrary constant yield strain value (ϵ_y):

$$\sigma_n = \left(\frac{n}{\epsilon_y} \right)^n \sigma_y \quad (25A)$$

Since for the case of discontinuous yielding at the lower yield stress σ_{lys} , ϵ_y equals the Luders strain (ϵ_L), an alternate equation is

$$\sigma_n = \left(\frac{n}{\epsilon_L} \right)^n \sigma_{lys} \quad (25B)$$

Based on equations (1), (6A) and (6B), the ratio of the fracture to the yield stress at T_d is given by

$$\frac{\sigma_F}{\sigma_y} = \left(\frac{n}{\epsilon_y} \right)^n \quad \text{or} \quad \frac{\sigma_F}{\sigma_{lys}} = \left(\frac{n}{\epsilon_L} \right)^n \quad (26)$$

Based on equation (26), it is possible to calculate the strain hardening exponent (n) from the measured ratio σ_F/σ_{lys} or σ_F/σ_y . A comparison of the calculated values of n and the maximum uniform strain values (ϵ_u) is given in Table 10. Theoretically, n should equal ϵ_u ; and this was found to be the case for the recrystallized condition. For the other three conditions, n/ϵ_u was found to be 0.4 to 0.6, which is considered to be fair agreement.

Excluding strain aging effects, it is known that the strain hardening exponent (n) tends to decrease with lowering of test temperature. Therefore, the observed increase in σ_n with lowering of test temperature must be due to the overcompensating effect of the concomitant increase in the strain hardening coefficient (K). Based on equations (20) and (25A), it appears that the factors that tend to lower T_d are as follows:

- a) large σ_F value and relatively small decrease with raising of test temperature (or increased plastic straining) starting below T_d ;
- b) small σ_y value and relatively small decrease with lowering of test temperature starting above T_d ;
- c) small n value and relatively large decrease with lowering of test temperature starting above T_d .

Table 10

Comparison of Calculated Values of n and Measured Values of ϵ_u

<u>Condition</u>	<u>σ_F/σ_y^*</u>	<u>Calculated n</u>	<u>Measured ϵ_u</u>
recrystallized	1.08**	0.08	0.09
5% reduction	1.28	0.07	0.12
46% reduction	1.20	0.06	0.10
88% reduction	1.08	0.03	0.08

* based on $\epsilon_y = 0.002$

** based on σ_{lys} with $\epsilon_L = 0.036$

REFERENCES

- (1) Lement, B. S., Thomas, D. A., Weissmann, S., Owen, W. S., and Hirsch, P. B., "Substructure and Mechanical Properties of Refractory Metals", WADD-TR-61-181, (August 1961).
- (2) Lement, B. S., Thomas, D. A., Weissmann, S., Owen, W. S., and Hirsch, P. B., "Substructure and Mechanical Properties of Refractory Metals", WADD-TR-61-181, Part II (October 1, 1962).
- (3) Lement, B. S., et al., "Substructure and Mechanical Properties of Refractory Metals", Contract No. AF33(657)-8424, Progress Report No. 1 (August 15, 1962).
- (4) Thomas, G. Transmission Electron Microscopy of Metals, John Wiley & Sons, Inc. (1962).
- (5) Barrett, C. S., Structure of Metals, McGraw-Hill Book Co., Inc. (1943).
- (6) Semchyshen, M. and Timmons, G. A., "Preferred Orientation of Arc-Cast Molybdenum Sheet", Trans. AIME, 194 (1952) 279.
- (7) Tsien, L. C. and Chow, Y. S., "Glide of Single Crystals of Molybdenum", Proc. Roy. Soc. London, 163A (1937) 19.
- (8) Chen, N. K. and Maddin, R., "Plasticity of Molybdenum Single Crystals", Trans. AIME, 191 (1951) 937.
- (9) Greninger, A. B., discussion to paper by Barrett, C. S., et al, "Slip, Twinning, and Cleavage in Iron and Silicon-Ferrite", Trans. ASM, 25 (1937) 702.
- (10) Johnson, A. A., "The Ductile-Brittle Transition in Body-centered Cubic Transition Metals", Phil. Mag., 7 (1962) 177.
- (11) Hu, H., "Annealing of Silicon-Iron Single Crystals", pres. at AIME Symposium on "Recovery and Recrystallization of Metals", February 1962, New York. Interscience Publishers (in press).
- (12) Despujols, J. and Warren, B. E., "X-ray Study of Cold Work in Molybdenum", J. Appl. Phys., 29 (1958) 195.
- (13) Warren, B. E., "X-ray Study of Deformed Metals", Prog. in Met. Phys., 8 (1959) 147.
- (14) Petch, N. J., "The Cleavage Strength of Polycrystal", J. Iron & Steel Inst., 174 (1953) 25.

- (15) Armstrong, R., Codd, I., Douthwaite, R. M., and Petch, N. J., "The Plastic Deformation of Polycrystalline Aggregates", *Phil. Mag.* 7 (1962) 45.
- (16) Ault, R. T., and Spretnak, J. W., "Initial Yielding and Fracture in Notched Sheet Molybdenum", ASD-TDR-62-223 (1962).
- (17) Wronski, A. S., and Johnson, A. A., "The Deformation and Fracture Properties of Polycrystalline Molybdenum", *Phil. Mag.* 7 (1962) 213.
- (18) Johnson, A. A., "On the Determination of the Yield Stress Parameters σ_I and k_y from a Single Stress-Strain Curve", *Acta Met.*, 10 (1962) 975.
- (19) Rosenfield, A. R., private communication (cited by Owen and Hull⁽²⁰⁾).
- (20) Owen, W. S. and Hull, D., "The Fracture Transitions in Refractory Metals", AIME Symposium on Refractory Metals, Chicago, 1962, awaiting publication.
- (21) Cottrell, A. H., "Theory of Brittle Fracture in Steel and Similar Metals", *Trans. AIME*, 212 (1958) 192.
- (22) Bechtold, J. H., "Effects of Temperature on the Flow and Fracture Characteristics of Molybdenum", *Trans. AIME* 197 (1953) 1469.
- (23) Zener, C. and Holomon, J. H., "Effect of Strain Rate on the Plastic Flow of Steels", *J. Appl. Phys.*, 15 (1944) 22.
- (24) Bridgeman, P. W., "The Stress Distribution at the Neck of a Tension Specimen", *Trans. ASM*, 32 (1944) 553.
- (25) Aronofsky, A., "Evaluation of Stress Distribution in the Symmetrical Neck of Flat Tensile Bars", *J. Appl. Mech.*, 18 (1951) 75.

V. FIBERING IN REFRACTORY METALS - Work carried out at Massachusetts Institute of Technology by D. A. Thomas, M. F. Comerford, E. S. Meieran, J. F. Peck, and F. T. J. Smith.

A. Scope

This report covers several aspects of substructure and mechanical properties of body-centered cubic metals that have been drawn into wire and have thereby developed highly elongated (fibered) grains. Transmission electron microscopy was the principal technique used for studying substructure in W-P4 tungsten wire and in worked W-P5 single crystals. Correlations were established between the substructures and the mechanical properties reported previously^(1,2). Light microscopy together with dislocation etch-pit techniques were used to study an Fe-3.2% Si alloy and obtain correlations with mechanical properties. In addition, the changes in microstructure, texture, and hardness accompanying wire drawing of columbium with three levels of interstitial purity were studied although the work was not completed.

B. Transmission Electron Microscope Study of Substructure in Tungsten Wire

With the aid of a technique developed for preparing transmission electron microscopy specimens from wires⁽³⁾, the substructure in as-received and annealed W-P4 tungsten and in groove-rolled W-P5 tungsten single crystals was studied.

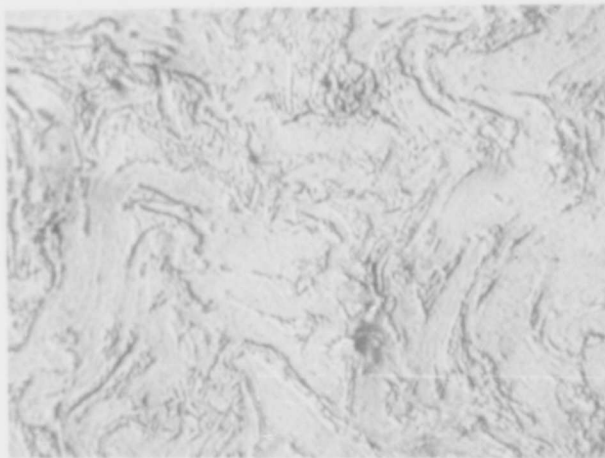
1. Structure of As-Drawn Wire

As determined by light microscopy, the microstructure of W-P4 tungsten wire (Fig. 29a) consists of elongated fibers in the longitudinal section, ranging between 1 and 10 microns wide. As reported by Peck and Thomas⁽⁴⁾, the grains are in fact ribbon-like rather than fiber-like. This is indicated by the microstructure of the transverse section (Fig. 29b). The development of this grain shape has been explained on the basis that the orientation of slip systems in [110] textured b. c. c. wires should lead to ribbons that are wide in (001) and narrow in (1 $\bar{1}$ 0) planes parallel to the [110] wire axis⁽⁴⁾. The present work confirms these predictions and provides detailed observations of the substructure of the grains as well.

Figs. 30, 31 and 32 are examples of the structures found in longitudinal sections of as-drawn W-P4 wire. The microstructure is characterized by a variable fiber width ranging from less than 0.3 micron to well over 5 microns. There is an extensive cell structure present which is somewhat elongated in the drawing direction. Also, most of the dislocations present seem to be located at the fiber and cell boundaries rather than inside the cells, as is particularly evident in Fig. 32. The fiber boundaries are very sharp, and straight, and parallel to [110]; whereas the cell boundaries are less distinct and are somewhat irregular. The cell size varies from about 0.1 micron, which is the width of some of the fibers, to about 1 micron in the wider fibers. However, not every fiber contains a well defined cell structure.



(a)



(b)

Fig. 29 - Light micrographs of as-drawn tungsten wire: (a) longitudinal section (2000X), (b) transverse section (2000X).

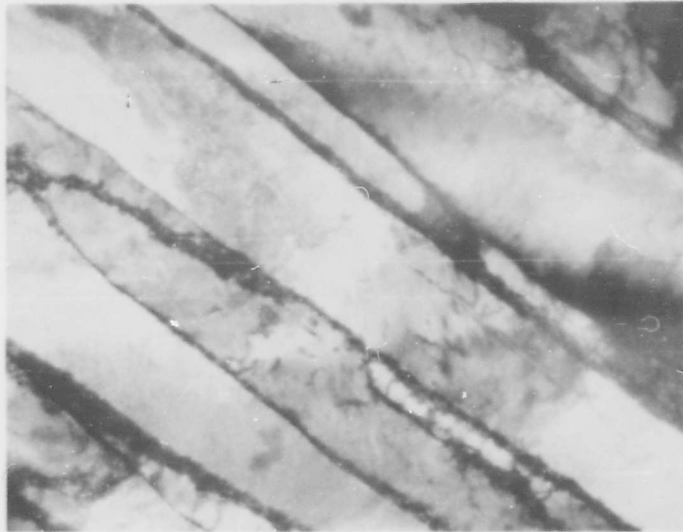


Fig. 30 - Transmission electron micrograph of longitudinal section of as-drawn tungsten wire, (40,000X).

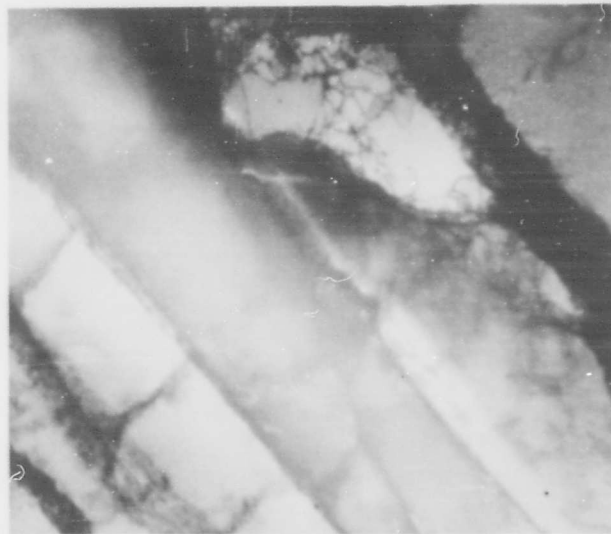


Fig. 31 - As-drawn tungsten wire, second area, (40,000X).



Fig. 32 - As-drawn tungsten wire, third area
(40,000X).

Selected area electron diffraction was used to determine the crystallographic orientations of the fibers and the misorientations between fibers or cells. For as-drawn wire, two different cases were found. The most common case is illustrated in Fig. 33. There are more spots appearing on the diffraction patterns made with the largest than with the smallest aperture. The spots index to several orientations not including (100). Consequently, the very narrow fibers of Fig. 33 are of differing orientations, mainly (110) and (111).

Another case is that of an area which gives about the same diffraction patterns even though different apertures are used. Fig. 34 is the diffraction pattern made with the largest aperture (which covers the entire area of Fig. 34 and shows (100) within a few degrees. This means that the fiber seen in the photograph has but one orientation, (100), even though there are many cell boundaries visible. The same is true for the area in Fig. 32. This is a convincing check of the prediction that wide fibers are parallel to (100).

The question of whether the fiber boundaries are actually original grain boundaries can not be answered directly because the original grain size and the total reduction in making wire are not known. Since measurements on iron⁽⁴⁾ and molybdenum⁽²⁾ indicate that many deformation bands form during heavy working and subsequently become fibered, it is probable that many of the fiber boundaries in W-P4 wire are not original grain boundaries.

Fig. 35 summarizes schematically the shape, substructure, and orientation of a typical fiber in as-drawn wire. The fibers are bent to maintain continuity with neighboring fibers, as is evident in Fig. 29b, and they are also probably twisted somewhat along their length. This is discussed in connection with the "striation" and "check mark" substructures detected in one of the cells in Fig. 35.

2. Platelet Substructure

Two unusual contrast effects were observed in many fibers: a) the "striations" in Fig. 36, which are always normal to $\langle 110 \rangle$; and b) the "check mark" patterns in Fig. 37, which lie on (110) planes and the edges of which lie in $\langle 111 \rangle$ directions. It appears that both effects are caused by a substructure of slightly misoriented thin platelets, seen either edge-on or face-on. It was not found possible to account for a number of the observations of the contrast effects on the basis that they are due to etching artefacts that occur during preparation of the transmission microscopy specimens.

The most significant experiments in interpreting the contrast effects were made on W-P5 single crystal UC-34, which had an initial orientation near the middle of the unit stereographic triangle and was groove rolled about 60% reduction in area at 800°C. Sections for transmission electron microscopy were cut longitudinally, transversely, and at 45° + 10° to the rod axis. Fig. 38 shows a transverse section of the groove-rolled crystal. The plane of the foil is (110), as shown by electron diffraction, which means that the major axis of the

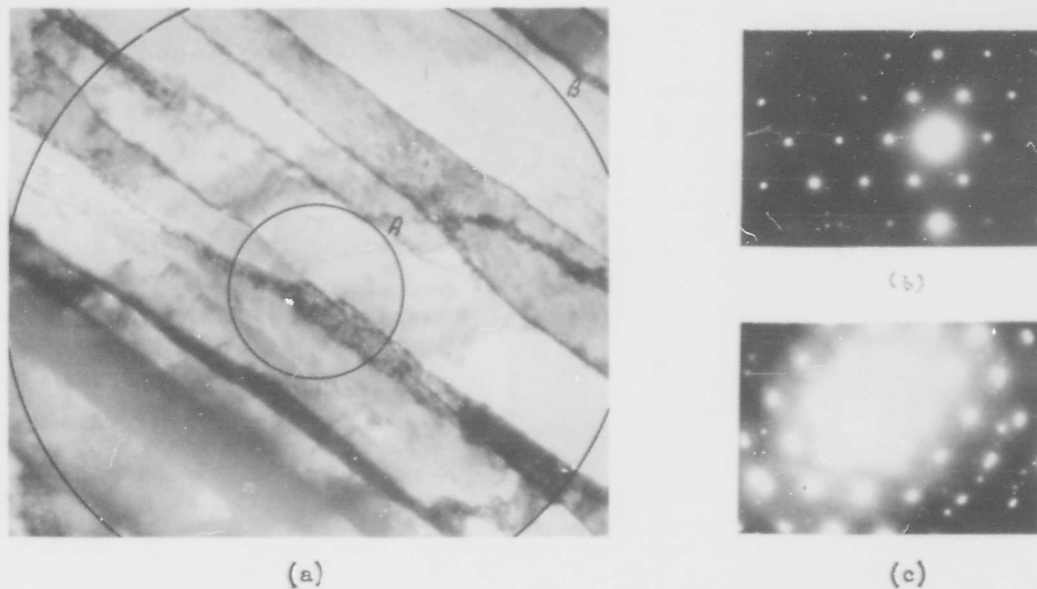


Fig. 33 - As-drawn tungsten wire: (a) electron micrograph (40,000X),
 (b) selected area electron diffraction pattern from area A,
 (c) selected area electron diffraction pattern from area B.

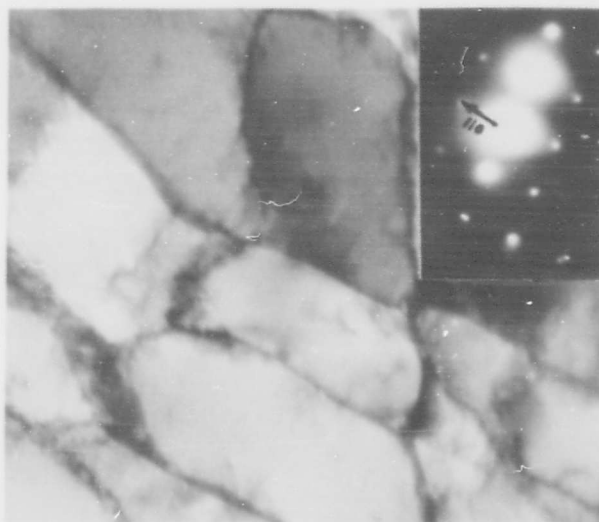


Fig. 34 - Tungsten wire annealed at 900°C for 10 min. Electron micrograph (40,000X) with corresponding electron diffraction pattern.

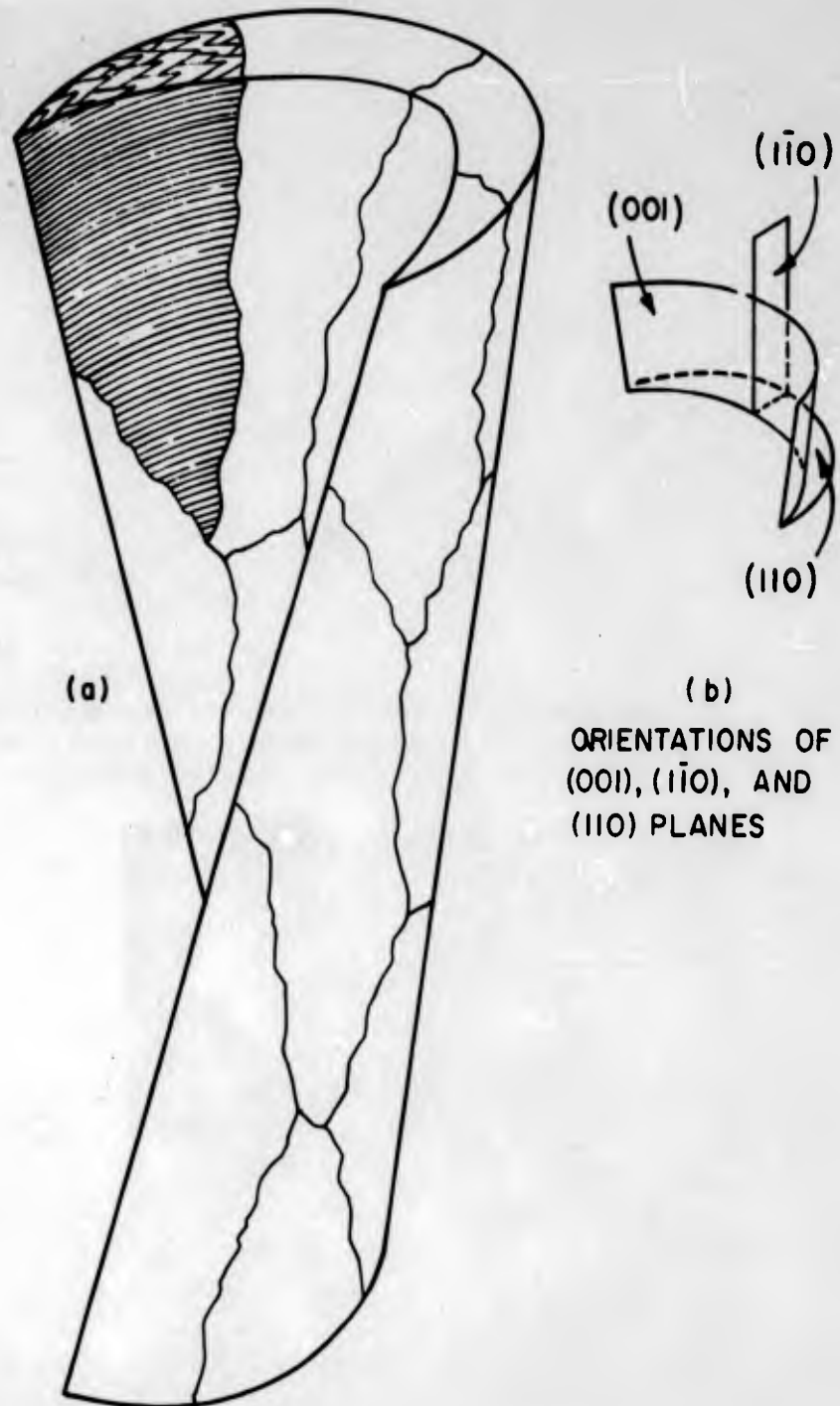


Fig. 35 - Schematic diagram of bent and twisted fiber containing cell structure. Striations and check marks appear in one of the cells.

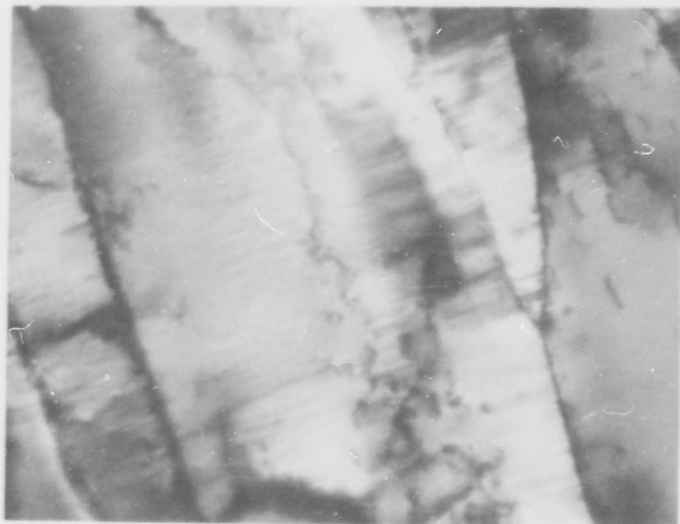


Fig. 36 - As-drawn tungsten wire (56,000X).



Fig. 37 - As drawn tungsten wire (96,000X).

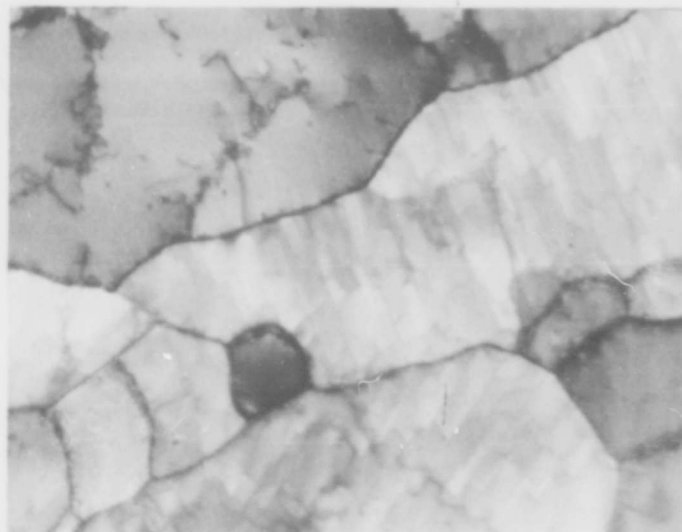


Fig. 38 - Crystal UC-34, transverse sections (40,000X).

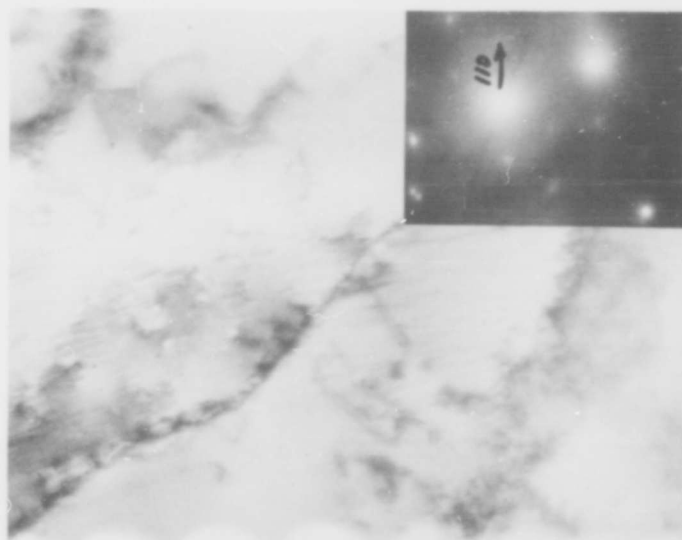


Fig. 39 - Crystal UC-34, longitudinal section, electron micrograph (80,000X) with corresponding electron diffraction pattern.

crystal has rotated to $[110]$ during deformation. The extensive subgrain structure has many check marks present, all lying on (110) and running in $[1\bar{1}1]$ and $[1\bar{1}\bar{1}]$ directions, but no striations are visible. A longitudinal section (Fig. 39) shows striations normal to $[110]$ and parallel to $[1\bar{1}1]$, but no check marks. Since both sections came from adjacent regions of the same crystal, it is reasonable to assume that both effects are due to the same cause. The 45° sections offer a check on this. Fig. 40a is a 45° section, and Fig. 40b shows the foil surface to be slightly misoriented from a (111) plane. Since the section was about 45° from (110) , the plane is probably (111) . The striations, of which Fig. 40 shows an example, have two orientations as found by selected area electron diffraction. One orientation has a trace on (111) parallel to $[1\bar{1}0]$, which is commensurate with platelets on (110) . The other orientation has a trace parallel to $[11\bar{2}]$, and indicates platelets on $(1\bar{1}0)$. Hence all sections of the single crystal (longitudinal, transverse, and 45°) are in concurrence with thin platelets on $\{110\}$ planes.

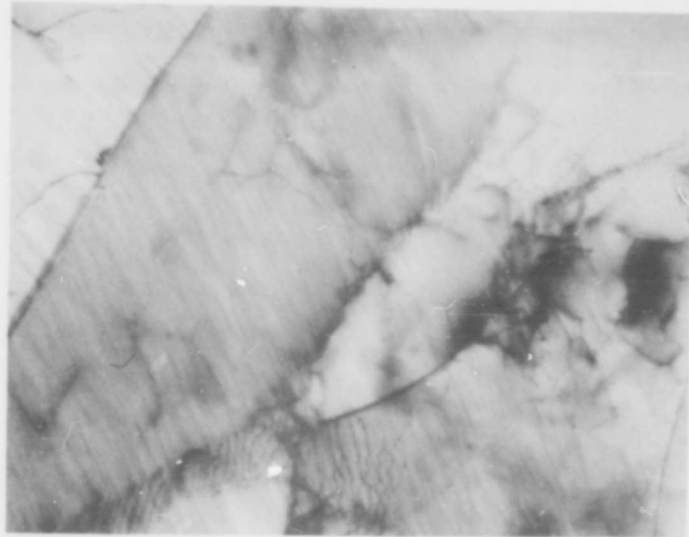
A striking feature of the striations is their separation, only about 150 \AA . Because of this, streaking of the diffraction spots in reciprocal space would be expected. The streaking is a geometrical effect due to the relaxation of the Laue condition in the thin direction of the diffracting block⁽⁵⁾ ($[110]$ in the case of the platelets), and appears in reciprocal space as shown in Fig. 41. As indicated, a foil plane parallel to $(\bar{1}11)$ should contain streaks; whereas a foil plane parallel to (110) should contain faint extra spots from the intersections of the streaks with (110) . Fig. 39 is an example of the former, with diffraction streaks normal to the striations; and Fig. 42 (another crystal) is an example of the latter and indicates streaks normal to the specimen foil. The faint extra spots are in the exact position indicated in Fig. 41. As was observed, they would be expected to shift slightly if the foil were slightly misoriented from (110) .

Tilting in the electron microscope of critically oriented specimens was found to eliminate striation contrast. This is illustrated in Fig. 43, for a 45° section. As the specimen tilts, the striations start to disappear at an end of one subgrain, while the adjacent subgrain is very light and shows no striations. As tilting progresses, the striations in the first subgrain completely disappear and the subgrain becomes bright. This is accompanied by the appearance of striations in the second subgrain and it gets darker as more and more intensity is diffracted out of the primary beam.

From this sequence of pictures, a rough estimate of platelet misorientation can be made. The amount of tilting from Fig. 43a to b is about 2° . The striations started to disappear at one end of one subgrain, and continued to disappear across the grain to the other end. Hence the misorientation across the length of the subgrain is about 2° , and occurs over a distance of about 1 micron. The misorientation was calculated as follows:

$$2^\circ \times \frac{60 \text{ min.}}{\text{deg.}} \times \frac{1}{10^4 \text{ \AA}} = 1.2 \times 10^{-2} \frac{\text{min.}}{\text{\AA}}$$

If the platelets are assumed to be 150 \AA wide and perfect within, the misorientation of $1.2 \times 10^{-2} \times 150 = 1.8 \text{ min.}$ must occur across the platelet boundary.



(a)

(iii)



(b)

Fig. 40 - Crystal UC-34, 45° section: (a) electron micrograph (72,000X), (b) electron diffraction pattern.

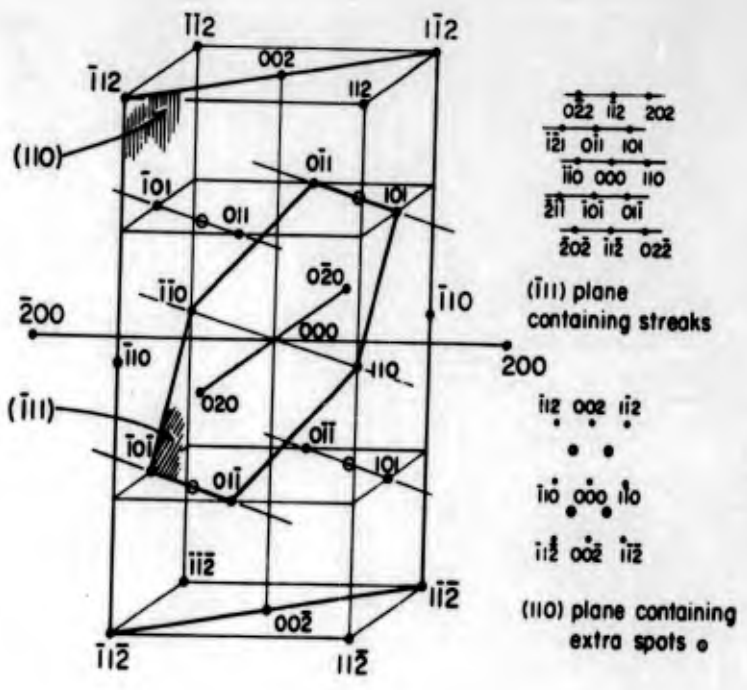


Fig. 41 - Geometry of streaks in reciprocal space, showing intersection of streaks with ($\bar{1}\bar{1}\bar{1}$) plane and (110) plane.

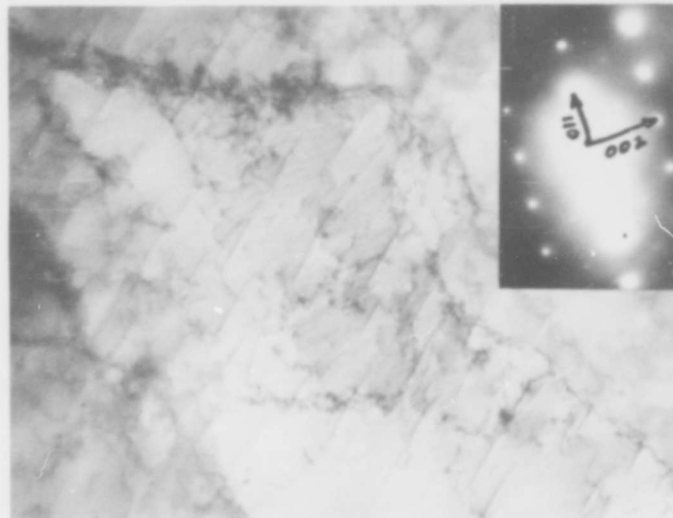
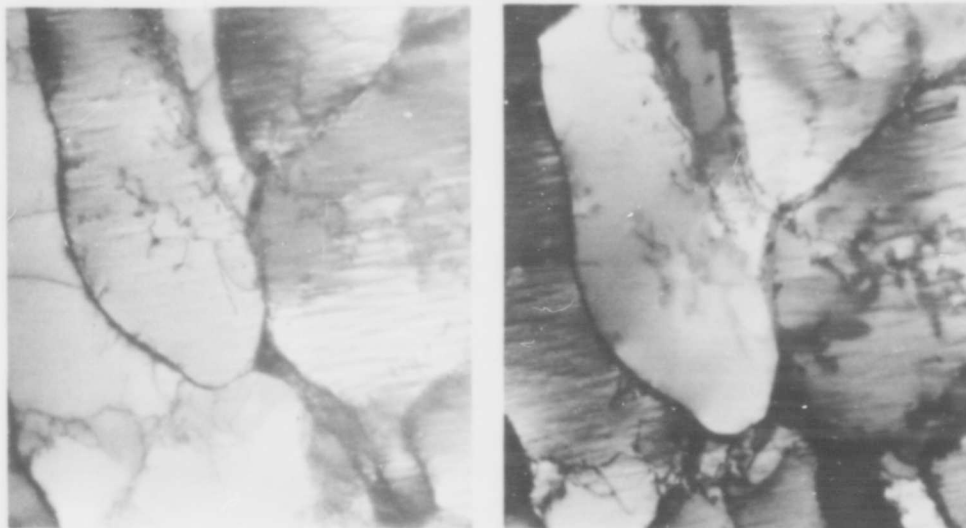


Fig. 42 - Crystal UC-44, transverse section, electron micrograph (40,000X) with corresponding electron diffraction pattern.



(a)

(b)

Fig. 43 - Crystal UC-34, 45° section. The specimen was tilted about 2° in the microscope between (a) and (b), resulting in changes in striation contrast.

Thus the platelets are apparently twisted about [110] by about 1.8 min. of arc from each other.

The check mark patterns appear to be dislocation arrays, principally in (110) planes, that give rise to the twist misorientation between platelets. However, they are not stable arrays of screw dislocations because simple crossed grids or hexagonal networks would occur. They are probably part of a more complex dislocation pattern, possibly three-dimensional rather than planar, that produces the lattice twist. This dislocation configuration is remarkably stable, as it was found to remain practically unchanged after annealing groove-rolled single crystals as high as 1500°C.

Another way of calculating the amount of twist is by the formula $\theta = b/D$, where b is the Burgers vector and D is the dislocation spacing. If the edges of the check marks are assumed to be dislocations, the spacing between them as measured on an electron micrograph is about 1000 Å. The Burgers vector magnitude is $3.16 \times \frac{\sqrt{3}}{2}$ Å for tungsten, so the twist is

$$3.16 \frac{\sqrt{3}}{2} \times \frac{1}{1000} \times \frac{57.3^\circ}{\text{rad.}} \times \frac{60 \text{ min.}}{\text{deg.}} \approx 9 \text{ minutes of arc}$$

If this amount of twist is accommodated by the thickness of the foil (about 700 Å or about five platelet thicknesses), there would be 1.8 minutes of arc misorientation per platelet. Although this is perhaps fortuitously the same as the magnitude of the twist misorientation obtained by specimen tilting, the agreement lends support to the twist boundary interpretation.

The platelets are probably formed by the bending and twisting of the metal grains during drawing or groove rolling. Bending is observed in the light micrographs of both the wires and single crystals, and the fiber twisting shown schematically in Fig. 35 can be accommodated by the platelet structure. The dislocation configurations would be expected to have long-range stress fields associated with them. This may contribute to the high work hardening of b. c. c. metals at high strains⁽⁴⁾ and to the resulting high strength of b. c. c. wires.

3. Annealing Effects

Specimens previously used for mechanical property studies^(1,2) were examined for substructure changes by transmission electron microscopy. Dislocations were observed to move at a temperature of about 800°C, with some being annihilated and others being attracted into boundaries. At about 1100°C, dislocations interact to form networks; and the number and perfection of the networks increases with higher annealing temperature. Above 1500°C, the dislocation density continues to decrease; but the dislocation networks remain even after annealing at 2000°C.

The more striking structural changes during annealing involve boundary migration and polygonization. As shown in Figs. 30 and 31, the wires initially have a variable fiber width from the ribbonlike shape of the grains.

The fiber widths become more uniform upon annealing at 800 to 1000°C (Fig. 44). Upon annealing above 1000°C, the fiber widths increase and the fibers break up (Fig. 45).

Fig. 46 is a graph of average spacing between longitudinal boundaries determined by measuring numerous micrographs, versus annealing temperature for both 10 and 30-minute annealing times. This spacing parameter is considered equal to the fiber width in the thin direction i. e. the thickness of the ribbon-like fiber. Each curve shows a slight dip in the region of 900 to 1000°C, which probably results from a polygonization process in which new longitudinal boundaries form parallel to the fiber boundaries and thereby decrease the strain energy within the bent fibers. The fiber widths become more uniform upon annealing at 1000°C because these extra longitudinal boundaries divide the wide (001) planes of the fibers into equal segments.

The principal mechanism of fiber coarsening appears to be strain induced boundary migration, similar to that reported by Koo in rolled tungsten⁽⁶⁾. This is suggested by the appearance of some regions near boundaries that are lighter in contrast than the interiors of the fibers, which indicates that fiber boundaries had migrated through these regions and left them more perfect than the original fiber interiors.

Fig. 47 is a graph of average fiber width versus annealing time for each annealing temperature, and shows curves representative of recovery. The formation of an essentially equiaxed grain structure in the wire by annealing at about 1500°C (Fig. 48) is apparently due to a recovery process. Remnants of the fibered structure were found in many regions of wires annealed at 1500°C.

Concurrent with the formation of the new longitudinal boundaries on annealing at 900 or 1000°C is the appearance of transverse boundaries as shown in Fig. 49. These boundaries separate the fiber into segments, similar in appearance to bamboo. Hence the migrating fiber boundary is usually restricted to a segment between two transverse boundaries. Thus one of the segments may grow during annealing, while neighboring segments remain the same size. This is evident in the light micrograph of a wire annealed at 1200°C for 10 minutes (Fig. 50).

4. Relationship Between Structures and Properties

Obtaining a quantitative relationship between the structures of the drawn and annealed tungsten wires and their mechanical properties is made difficult because of the number and complexity of the reactions occurring during annealing. For example, the rearrangement of dislocations during annealing undoubtedly has an effect on strength but cannot at this time be separated from other phenomena. Since accurate measurements of dislocation density in the tungsten wires was found to be extremely difficult, it has not been possible to determine whether the same relationship exists between flow stress and dislocation density as in the case of deformed iron⁽⁷⁾.



Fig. 44 - Tungsten wire annealed at 1000°C for 10 min. (40,000X).

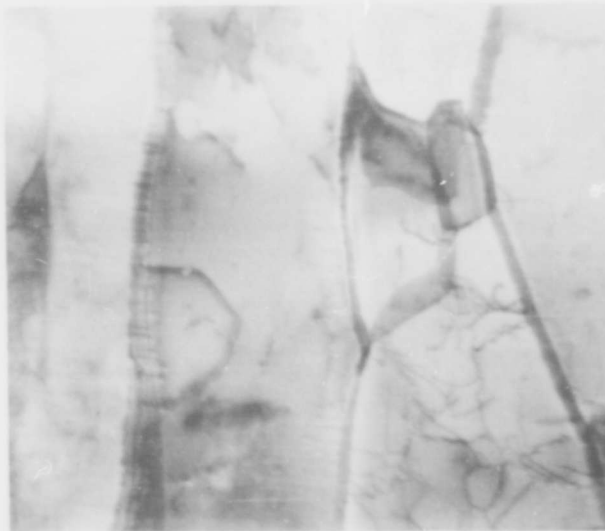


Fig. 45 - Tungsten wire annealed at 1200°C for 10 min. (44,000X).

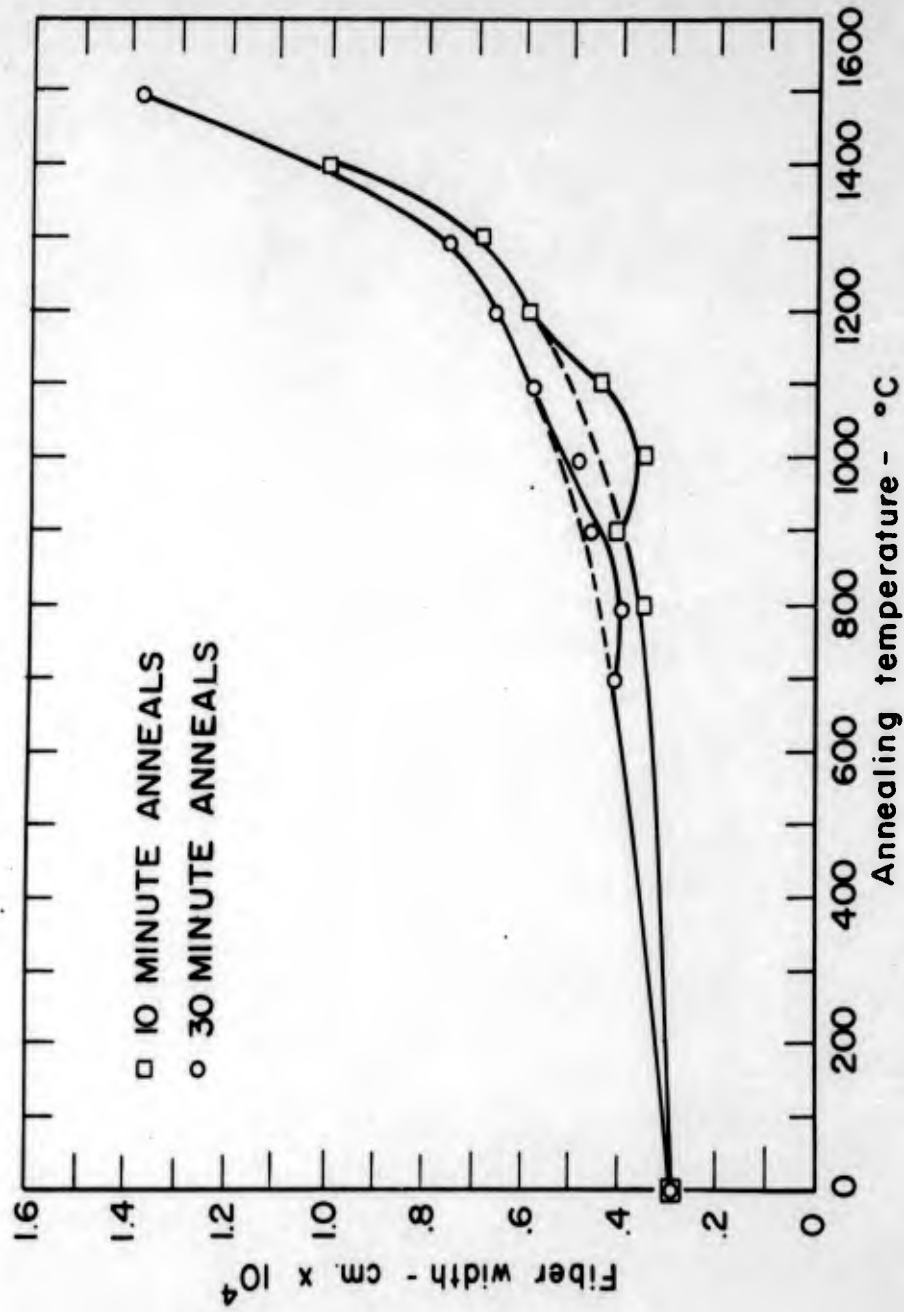


Fig. 46 - Fiber width vs. annealing temperature for 10 and 30-minute anneals.

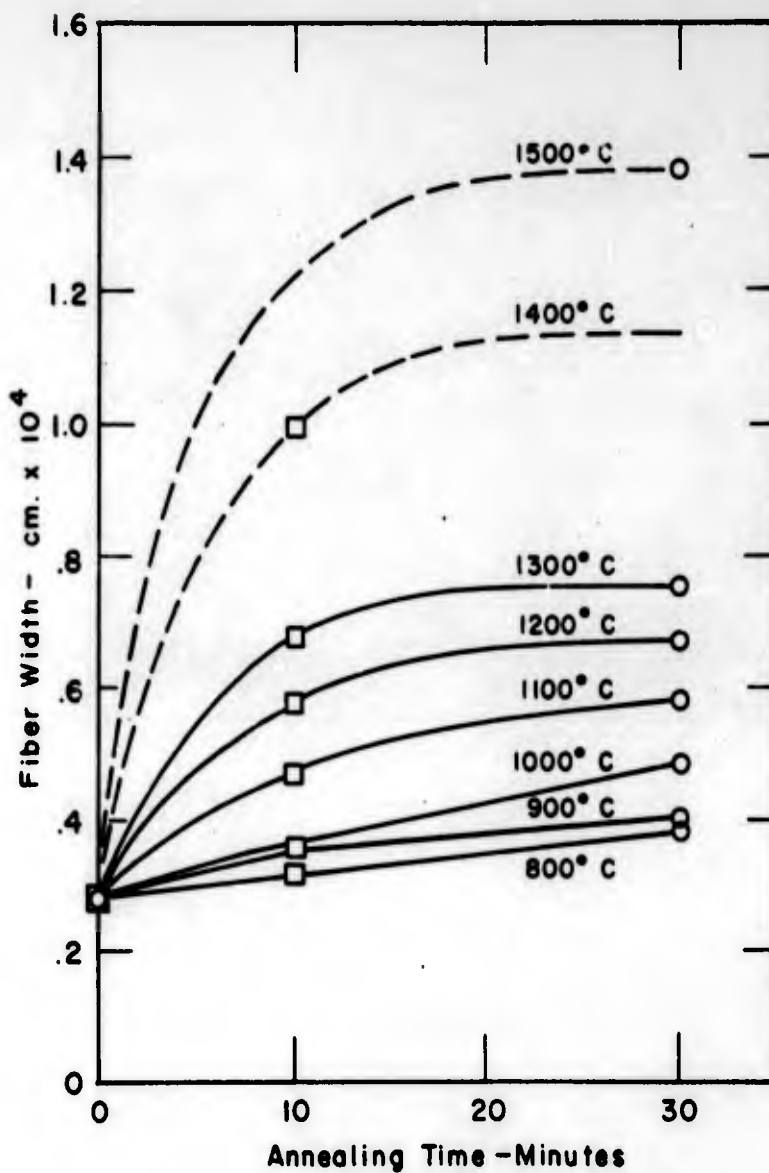


Fig. 47 - Fiber width vs. annealing time at constant temperature.



Fig. 48 - Tungsten wire annealed at 1500°C for 30 min. (40,000X).



Fig. 49 - Tungsten wire annealed at 900°C for 10 min. (40,000X).

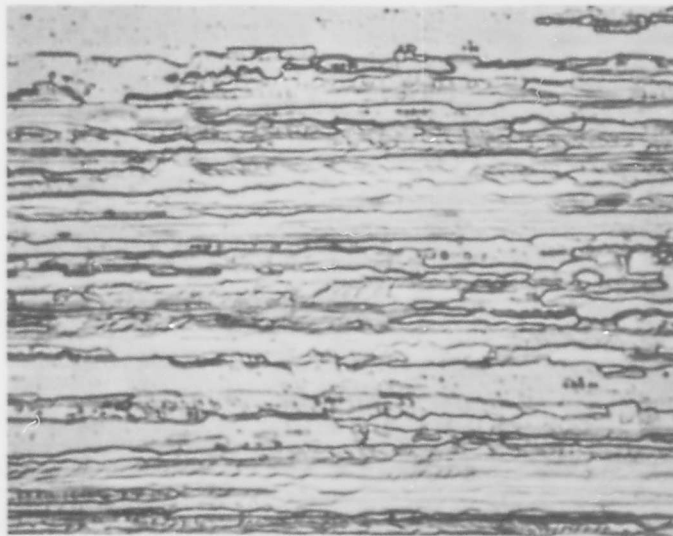


Fig. 50 - Optical micrograph of tungsten wire annealed at 1200°C for 10 min. (2000X).

Empirically, the Petch equation has proved useful in relating flow stress to grain size:

$$\sigma_f = \sigma_o + k_f d^{-1/2}$$

where σ_f is the flow stress and d for the tungsten wires was assumed to be the average fiber width. Much flow stress data for the 10 and 30-minute annealed tungsten wire has been accumulated^(1,2) and is plotted in Fig. 51 versus the inverse square root of the average fiber widths as measured in the transmission electron photomicrographs. Almost all of the points fall on a straight line. The two points that do not fall on this line correspond to wires annealed about 900 or 1000°C, which is in the region where the average fiber width is a minimum due to polygonization.

The value of the slope is 8×10^7 cgs. which checks with the value of 6×10^7 as given by the Rosenfield⁽⁸⁾ relation, $k_y/G = 5 \times 10^{-5}$, where G is the shear modulus. This agreement is probably fortuitous, since it is not known whether the slope actually represents k_f or k_y and correction should be made for shear stress and semi-grain size.

Cracks were occasionally observed at fiber boundaries by means of transmission electron microscopy. These cracks may have resulted from stresses involved in specimen thinning and observation, rather than originally being present in the bulk material. It thus appears that the grain boundaries are weaker than the grain interiors in tungsten wire, which is in agreement with the observations that fractures in tungsten wires tend to follow the fiber boundaries⁽²⁾. This suggests that the decrease in ductility of tungsten wires annealed between 800 and 1000°C is due to grain boundary failure, for this is the annealing temperature range where transverse boundaries normal to the wire axis first appear. Their weakness may be due to impurity segregation.

C. Substructure and Mechanical Properties of an Fe-Si Alloy

An Fe-3.2 wt. % Si alloy, containing 0.016 wt. % carbon, was drawn into 0.035 inch wire with final reductions in area of 31, 66, and 87%. This alloy is considered to be a body-centered cubic solid solution that is particularly suitable for substructure determination by dislocation etch-pitting techniques. The substructures and properties of this material which results from working and annealing are believed to have features that are in common with the refractory metals.

1. Mechanical Properties

The tensile properties for all drawing reductions and after annealing in hydrogen at temperatures up to 1000°C have been reported previously⁽²⁾. The tensile stress-strain curves in Fig. 52 which are representative of the results, show the occurrence of a slight strengthening effect at about 300°C, followed by softening with the eventual occurrence of discontinuous yielding at 700°C. Although extensive softening occurs at 600°C, recrystallization does not take place until 700°C and coincides with the appearance of the sharp yield. As discussed later, the initial softening is accompanied by substructural changes.

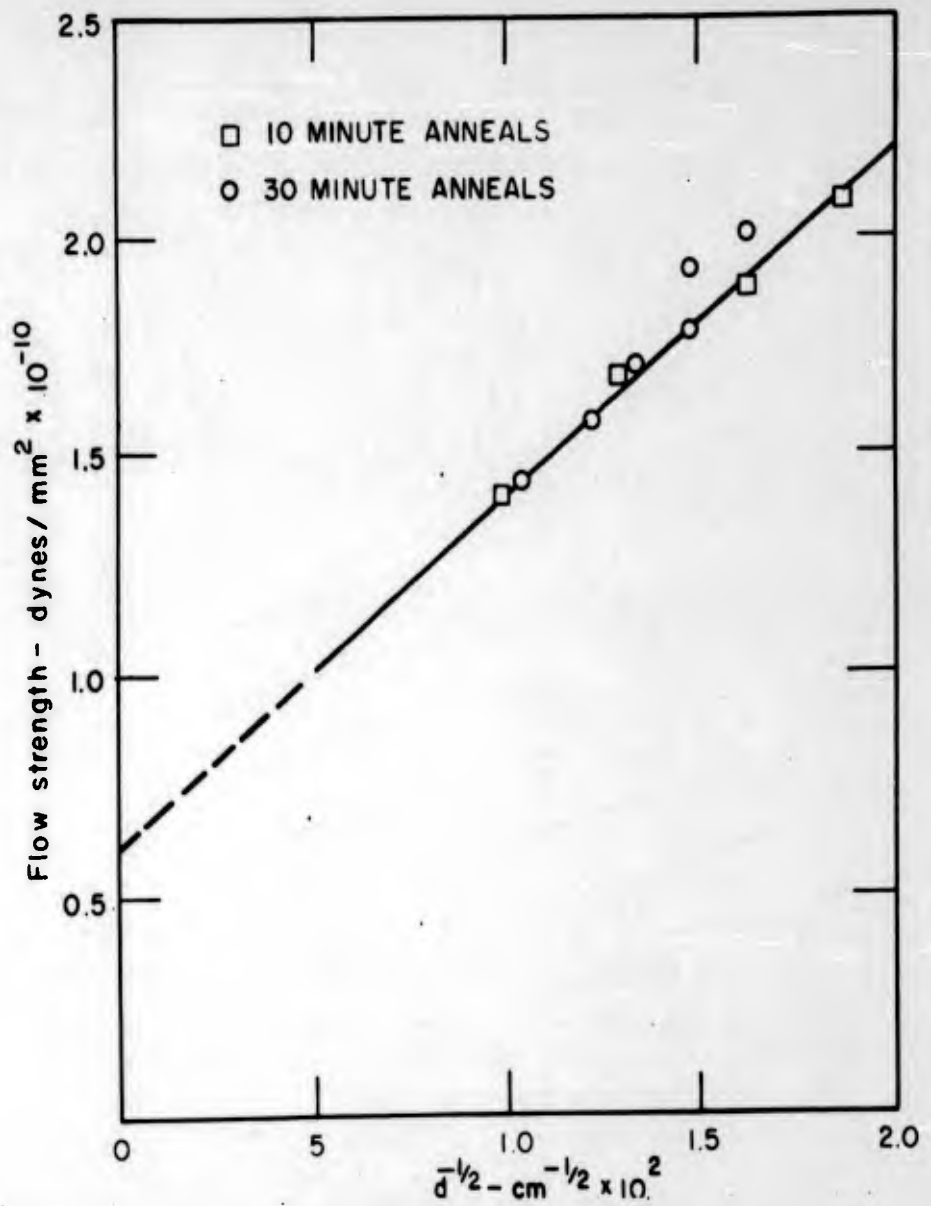


Fig. 51 - Flow stress vs. inverse square root of fiber widths.

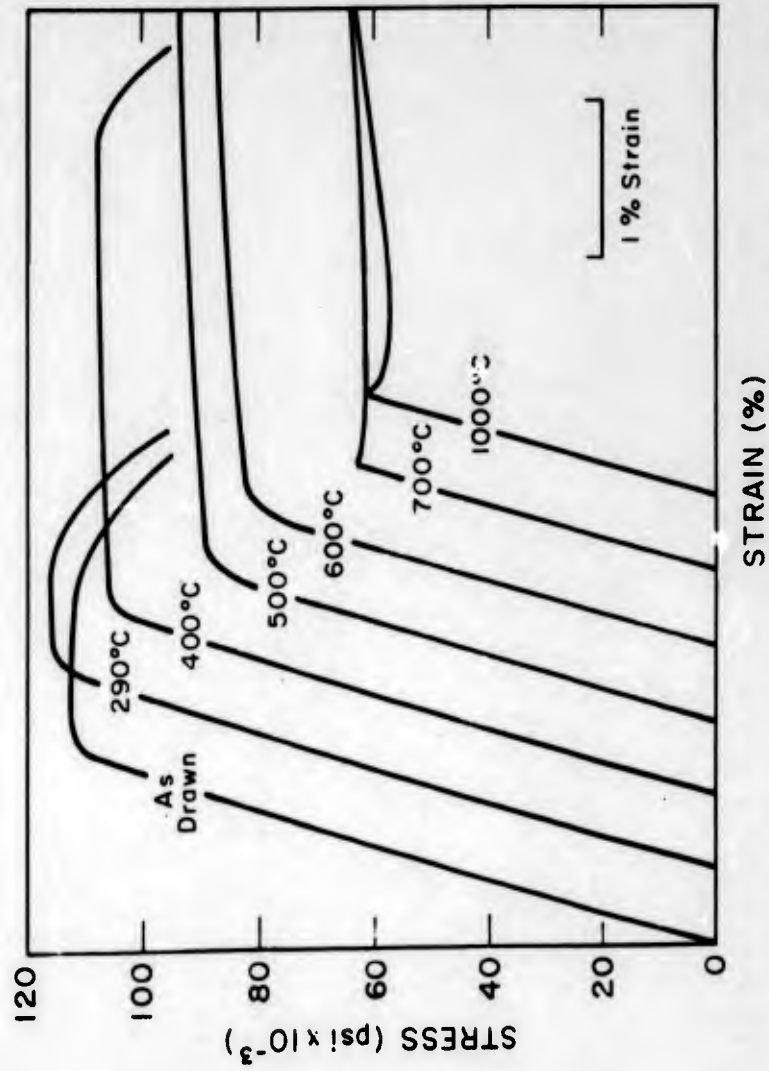


Fig. 52 - Representative engineering stress-strain relationships for Fe-Si wire cold drawn 31% and annealed for 30 minutes at temperatures indicated.

The kinetics of the annealing processes were investigated by means of hardness tests on isothermal series of annealed specimens. Preliminary tests established that hardness and tensile tests gave similar indications of softening. The complexity of the annealing process in this alloy is well illustrated by Fig. 53, which shows the isothermal time dependence of the diamond pyramid hardness of wire drawn to 66% reduction of area. For convenience in plotting, the normalized values are shown. The curves for 250°C and 300°C show significant age hardening that reaches a peak in about ten minutes. The reaction at 250°C appears slightly more rapid, although this distinction is not clear cut; otherwise the two curves are much alike. At 400°C an aging peak is reached after about one minute, and at 500°C averaging occurs almost instantly. At both these temperatures, the rate of softening is rapid and substantial softening occurs, especially at 500°C. A period of only about thirty minutes at 600°C was sufficient to achieve almost full softening.

In Fig. 54, the same data are shown plotted as a fraction of residual hardening, (1-f), where f is the fractional recovered hardness,

$$f = \frac{H_D - H}{H_D - H_0}$$

where H_D is the hardness as-drawn, H is the hardness at a given time and temperature, and H_0 is the hardness after full softening was achieved. Portions of the 400°C and 500°C curves are linear with the logarithm of time and so is the early part of the 600°C curve. There is a change in the character of the annealing kinetics that occurs during aging at 600°C. The wire undergoes a transition stage in less than ten minutes, which correlates well with metallographic observations of recrystallization as discussed in the next section.

Portions of the softening range (after aging had reached a maximum) can be treated as distinct entities for purposes of calculation. The straight portions of the curves were assumed to fit an equation that is linear with respect to the logarithm of time:

$$x = b - a \ln t \quad (1)$$

where $x = (1-f)$ is the residual fraction of unrecovered property and a and b are constants which can be evaluated for a given temperature from Fig. 54. Titchener and Bever(9) have pointed out that the differential form of Eq. 1 is not a rate in the thermodynamic sense because the instantaneous rate should depend on the state of the system. Consequently, the decremental rate which they proposed,

$$-\frac{dx}{dt} = a \exp\left(-\frac{b}{a}\right) \exp\left(\frac{x}{a}\right), \quad (2)$$

was put into an Arrhenius type equation and activation energies calculated for various values of x. Since the actual shapes of the curves of (1-f) versus log t are not known beyond the limits of Fig. 54, it was felt that there was no real

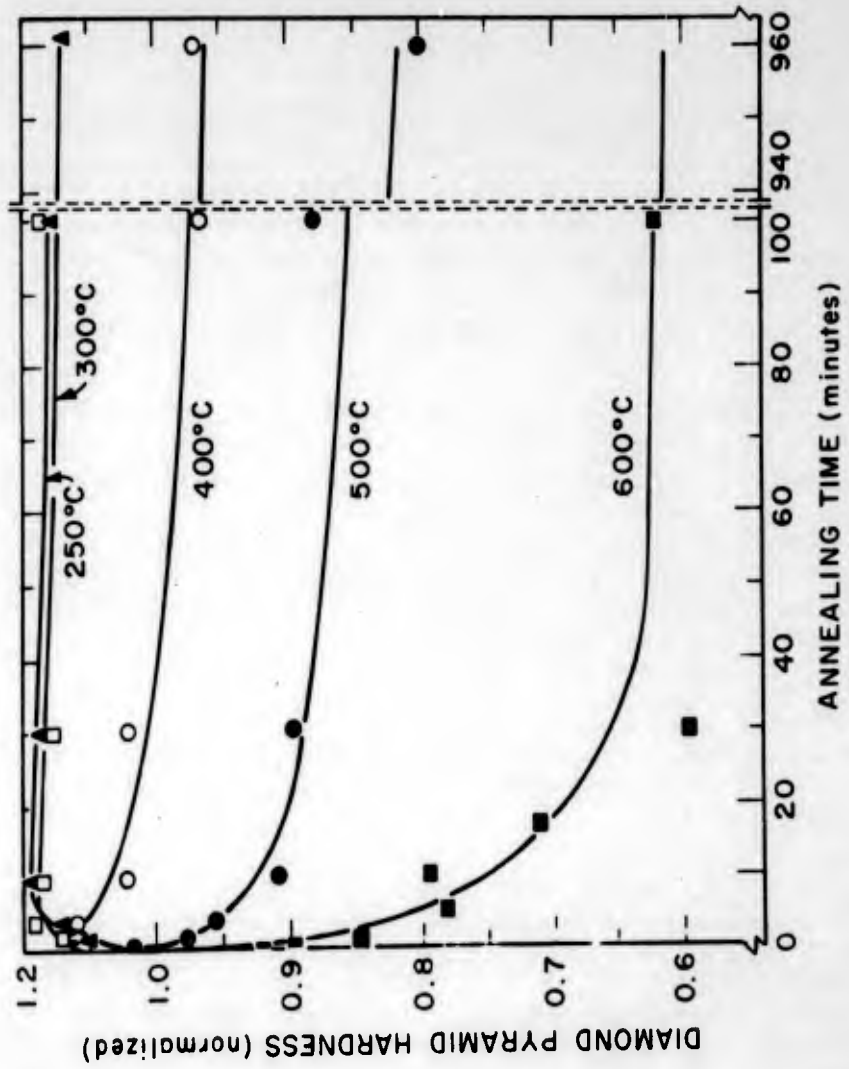


Fig. 53 - Diamond pyramid hardness as a function of annealing time for Fe-Si wire cold drawn 66%.

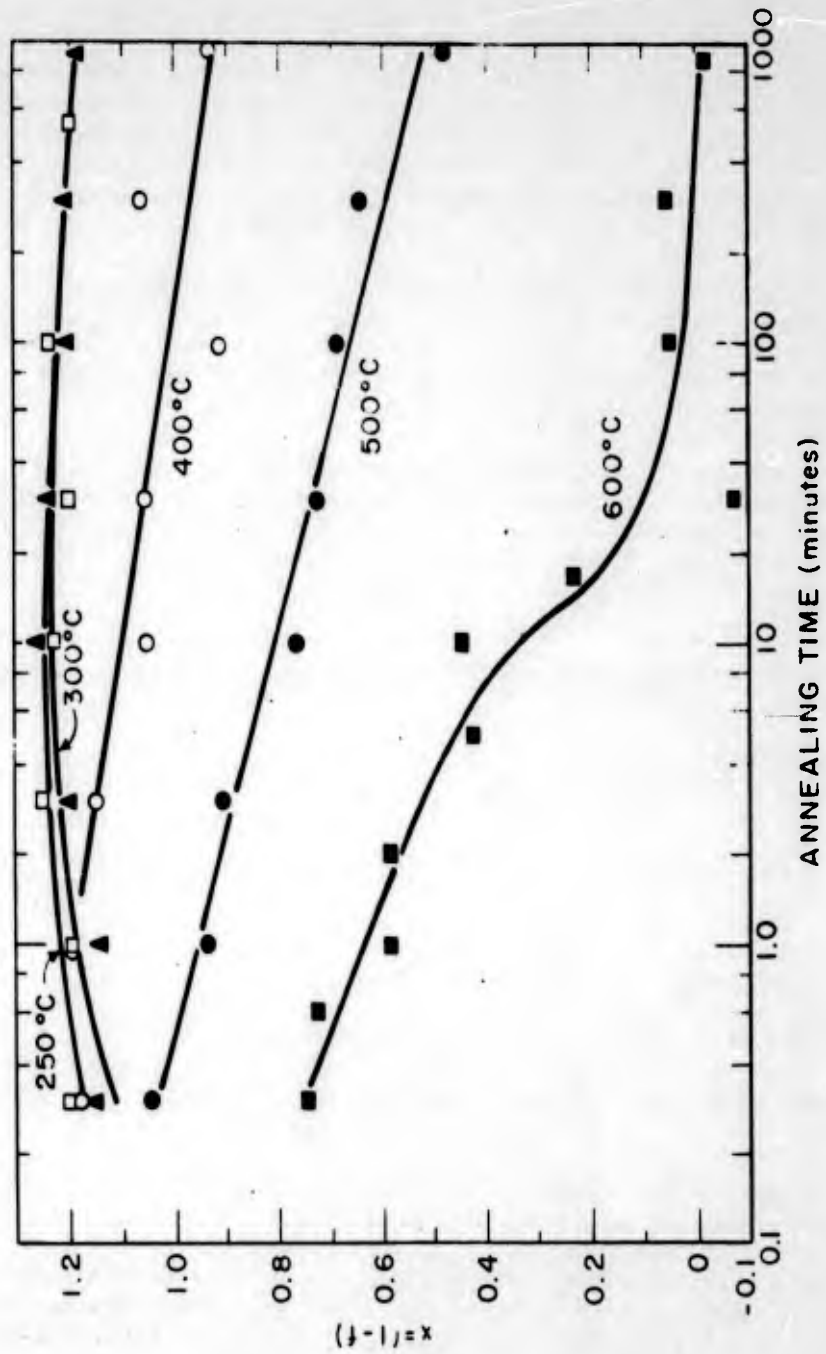


Fig. 54 - Residual fraction of hardness, $(1-f)$, of cold drawn Fe-Si wire as a function of annealing time.

justification for obtaining three-point Arrhenius curves by extrapolation of the data to longer or shorter times. Values of activation energy obtained are shown in Table 11. These values are higher than corresponding values obtained previously for the activation energy for recovery in zone-refined iron⁽¹⁰⁾. The latter approached a maximum (for complete recovery) of about 67,000 cal/mol, which is consistent with self diffusion in iron. It is not certain that the behavior of lightly deformed zone-refined iron should be directly comparable to that of the present iron-silicon alloy, but self diffusion might be a reasonable limiting factor to expect in either case. However, higher values could be encountered in the iron-silicon alloy if impurities served to stabilize partially recovered structures. This sort of stabilization might, for example, occur if carbon precipitated preferentially in sub-boundaries, thereby inhibiting further growth of the subgrains.

Although few of the data are suitable for determination of the activation energy of the initial hardness increase, approximate values are in the range 17,000 to 31,000 cal/mol. These values are consistent with the supposition that interstitial diffusion plays a role and that strain aging is responsible for the hardness increase.

Strain aging in body-centered cubic metals is usually accompanied by a drop in stress when yielding begins i. e. discontinuous yielding. The yield drop is generally attributed to the release of pinned dislocations and to a subsequent avalanche of slip. Since discontinuous yielding was not observed during recovery, this indicates that not all of the dislocations are pinned similar to the occurrence of an upper yield point.

Possible hypotheses that would explain the observed strengthening effect are as follows:

a) Dislocations are locked to such a high degree because of complex distributions that an avalanche cannot occur.

b) Fresh dislocations can be generated easily even in the highly worked material.

c) Locking is incomplete and therefore the existing dislocations can be put into motion easily.

With regard to a), discontinuous yielding has been observed in iron-carbon alloys^(11,12) after plastic straining to about 20%. Thus it is doubtful whether complex dislocation distributions per se preclude the recurrence of the upper yield point.

In line with b), the generation of fresh dislocations may occur at local inhomogeneities such as precipitated particles. Leslie⁽¹³⁾ has shown in an iron-silicon steel that an unidentified, metastable carbide (not Fe_3C) can precipitate within the matrix away from existing dislocations and may provide sites for the generation of fresh dislocations. However, these precipitates were usually not observed in this alloy below about 400°C. At approximately

Table 11

Activation Energies for Recovery in Fe-Si
Based on Equal Fractions of Recovered Hardness

<u>Fraction Recovered</u>	<u>Activation Energy (cal/mol)</u>	
	<u>400°C - 500°C</u>	<u>500°C - 600°C</u>
0	56,100	-----
0.1	66,700	54,500
0.2	-----	61,700
0.3	-----	69,000
0.4	-----	76,000
0.5	-----	83,200

600°C, the metastable carbide was found to give way to grain boundary precipitation of cementite. Therefore, the generation of new dislocations at precipitates is not expected to play a major role in attenuating the upper yield point below about 400°C. For this reason, the hypothesis of b) does not appear likely.

By a process of elimination, partial (or nonuniform) locking seems to be the most reasonable explanation for a strength increase after aging without the occurrence of discontinuous yielding. Hahn⁽¹⁴⁾ recently extended the Johnston-Gilman⁽¹⁵⁾ model of yielding to body-centered cubic metals. According to this model, yielding occurs primarily by the rapid generation of new dislocations rather than by the unpinning of existing ones. Based on this concept, the yield drop is smaller as pre-existing, unpinned dislocations are increased; and it may become non-existent. This concept may also account for the relatively small yield drop (usually much less than 5%) in the recrystallized iron-silicon. Since, however, the present experimental work was not designed to make a critical study of yield behavior, it cannot distinguish unambiguously between a dislocation multiplication mechanism and a dislocation unlocking mechanism for discontinuous yielding.

Although recovered structures exhibit no yield points, the subboundaries etched distinctly only after annealing at 500°C or higher. This indicates that carbon atoms segregate at the boundaries of relatively perfect cells, but are unable to completely prevent dislocations from leaving these boundaries in response to an applied stress. Electron microscope observations have, in fact, shown that cell walls in recovered iron do dissociate upon restraining. However, this must hold true only for fine scale polygonization. At higher temperatures, after recrystallization is initiated, the size of the polygonized cells increases and subboundaries become better defined. Concurrently, the carbon concentration in the subboundaries would be expected to increase as the total subboundary area decreases. As a consequence, easy liberation of dislocations from the subboundaries must stop. It is difficult to explain in any other way the profound influence that partial recrystallization exerts on the yield behavior. The fact that there is no significant increase in the yield drop when the volume recrystallized increases from about 50 to 100% implies that if recrystallization could be suppressed, discontinuous yielding would still occur in stable, polygonized structures.

2. Metallography

The most detailed study of the structural changes accompanying recovery and recrystallization was made of wire reduced 66% in area. The Morris electrolyte⁽¹⁶⁾ was used for electroetching at 8 volts and for times of 30 to 120 sec. After electroetching, it was necessary to rinse each specimen thoroughly in successive baths of glacial acetic acid, water, and ethyl alcohol in order to prevent staining.

No combination of etching variables was capable of bringing out general structural features of the cold-worked wire other than grain boundaries. Upon annealing, the flow pattern becomes evident and subsequently sharpens.

One minute at 500°C is sufficient to begin formation of a dark-etching type of substructure. Although this substructure is very fine, Fig. 55 shows clearly that it is associated in some way with a diagonally oriented banding that is often observed.

Severe boundary distortion was found to accompany the deformation and it becomes more striking in appearance as annealing progresses. The large steps associated with the coarse diagonal substructure of Fig. 56 are extremely persistent.

A temperature of 600°C results in the appearance in microstructures of clumps or lines of coarse subcells, which are believed to be newly formed recrystallization sites. The etching response of these cells is usually different from that of the matrix. They were found to be virtually unattacked and to present a specular surface that is quite different from the rough surface of the deformed grains.

The formation of these entities within prior grains is the dominant mode of structural change during short anneals at 600°C. In this connection, the importance of the diagonal bands, or lamellae, and of the accompanying grain boundary serrations is clearly demonstrated by Fig. 57. The thin lamellae are especially potent sites for nucleation. If these are deformation bands with an orientation that differs from but is related to that of the adjacent interlamellar material, this is in line with the theory advanced by Cahn⁽¹⁷⁾. However, subsequent observations yielded contradictory evidence; and it should be re-emphasized that Figs. 57a and b represent short time anneals at the low temperature end of the recrystallization range.

In the previous section, the recurrence of discontinuous yielding and the hardness drop at 600°C are presumed to be indicative of recrystallization. Such is, in fact, the case; but it should be noted from Fig. 58 that only partial recrystallization occurs after 30 minutes. Even 810 minutes is not long enough to remove every unrecrystallized vestige metal. For these relatively long times, it is apparent from Fig. 58 that high angle grain boundaries are the main sources of recrystallization nuclei. In a majority of cases, subsequent growth seems to proceed with about equal facility into both grains adjoining a given nucleation site (Fig. 58b). Less common were instances in which the migrating interface is contained within a single grain.

Three important points seem to emerge from the foregoing description. The first is that sites for recrystallization nucleation are not unique, at least in this alloy, but rather depend on time and temperature. At temperatures low in the recrystallization range, especially in the early stages, nucleation at internal sites such as deformation bands is preferred. Initiation of recrystallization at prior grain boundaries is almost nonexistent. On the other hand, the latter sites dominate after longer periods of time or when recrystallization is very rapid such as at high temperatures. The second point is that even though the recrystallized material may not occupy a major fraction of the total volume it can exert a profound influence on the stress-strain curve. The third point is that since the rate of increase of recrystallized volume decreases steadily with time, it appears that substructure develops concurrently with recrystallization and slows down the rate of migration of recrystallization boundaries.



Fig. 55 - Fe-3.2% Si, drawn 66% reduction in area. Annealed at 500°C for 1 min. Fine scale substructure (dark) and diagonal subboundaries (315X).

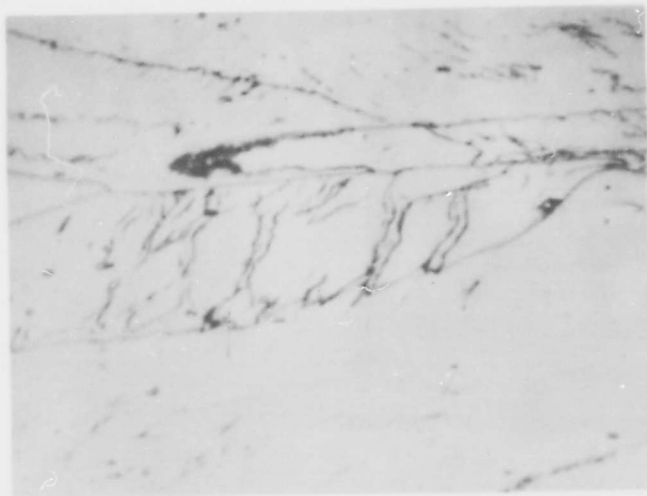
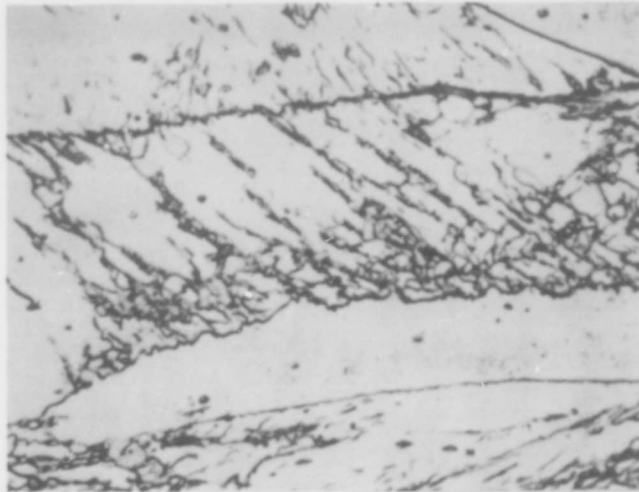
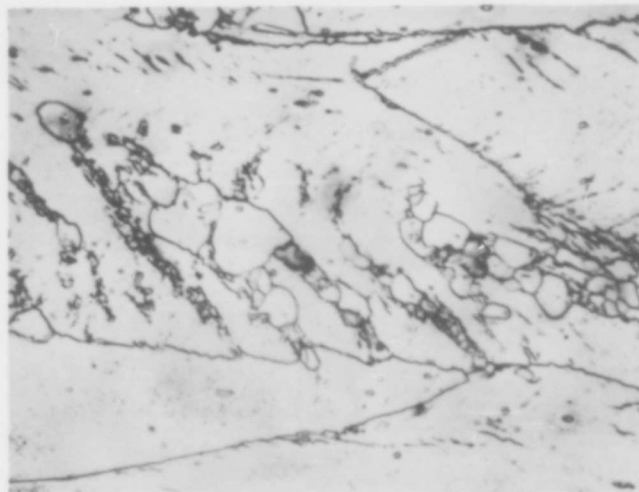


Fig. 56 - Fe-3.2% Si, drawn 66%. Annealed at 500°C for 30 min. Diagonal bands and grain boundary steps (1500X).

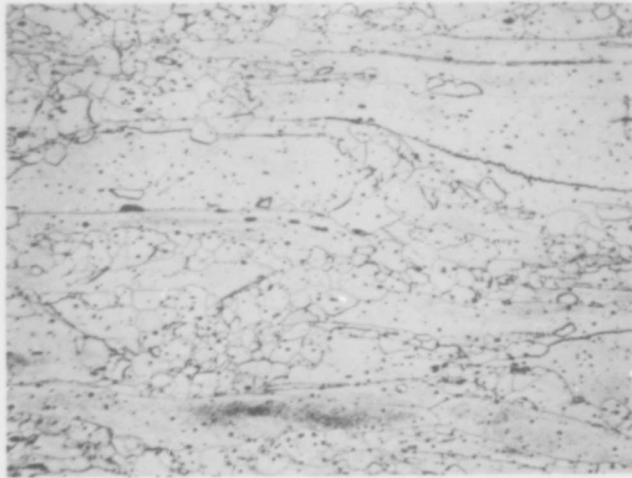


(a)

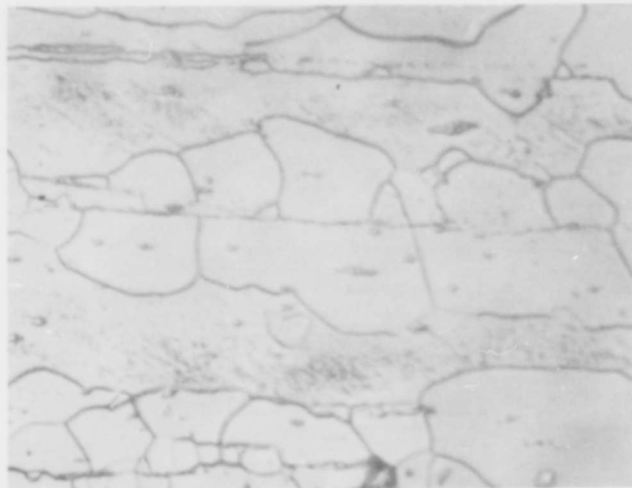


(b)

Fig. 57 - Fe-3.2% Si, drawn 66% and annealed at 600°C. Nucleation of recrystallization: (a) annealed 2 min. (1500X), (b) annealed 5 min. (1000X).



(a)



(b)

Fig. 58 - Fe-3.2% Si, drawn 66% and annealed at 600°C for 30 min. (a) 315X, (b) 1650X.

Substantial recrystallization was achieved rapidly at 700°C. Fig. 59 is a striking example of unrecrystallized portions of the specimen which have been encroached upon by the recrystallized material nucleated first at grain boundaries and growing inward toward the centers of adjoining deformed grains. Recovered but unrecrystallized areas etch very darkly, and the pattern of the substructure which caused this is clearly defined in Figs. 59 and 60.

The large number of boundaries which appear in Fig. 59 seems to rule out prior grain boundaries as the sole source of recrystallization nucleation, although they were the primary source (refer to Fig. 58b). Some new grains were able to form wholly within unrecrystallized grains, but mainly in areas contiguous to the existing recrystallized grains. This may be another manifestation of grain boundary nucleation with the interface playing the boundary role.

Cahn's hypothesis⁽¹⁷⁾ that nucleation occurs at sites which deviate from the matrix texture (i. e., deformation bands) appears to be borne out early in the recrystallization process, but grain boundary nucleation dominates when recrystallization occurs rapidly. The "ledge" theory⁽¹⁸⁾ of recrystallization was not verified by microstructural observations in the present study. However, since the large steps in many of the boundaries are undoubtedly stabilized by carbon atoms, the theory cannot be ruled out as applying to purer materials. Polygonization as such does not appear to be a source of recrystallization nuclei, and the metallographic observations indicate that polygonized cells may be very stable barriers to the growth of recrystallized grains.

D. Structures and Properties of Columbium Wires

An intensive study of the hardness, texture, and microstructure of three purities of drawn columbium wire was carried out. Hardness data from rolled columbium and drawn nickel were also obtained to show differences in their properties.

1. Texture of Drawn Wires

Wires of Cb-E1 (150 ppm total interstitial content) and Cb-E4 (450 ppm oxygen content) were drawn in 22 steps from 0.108 inch diameter to 0.015 inch diameter (reduction in area 98%, true strain 3.8). The recrystallized 0.108 inch diameter starting material has a well defined $\langle 110 \rangle$ fiber texture. Cb-E1 and Cb-E4 were also drawn in two steps to 0.093 inch diameter, lightly etched, and then recrystallized to obtain a random texture. These random textured wires were then drawn in 20 steps to 0.015 inch diameter. Columbium containing 50 ppm of interstitial impurities (called Cb-50, and supplied by National Research Corp.) was also drawn from 0.108 to 0.015 inch diameter. The wire textures of these five groups of drawn wires were determined by a photographic method, with diffraction rings recorded while the wire was rotated about its axis.

The Cb-E1 with the strong initial $\langle 110 \rangle$ fiber texture was found to lose its texture as the deformation progresses (Fig. 61). This figure is a composite of one side of the $\{110\}$ diffraction rings, one for each reduction in each

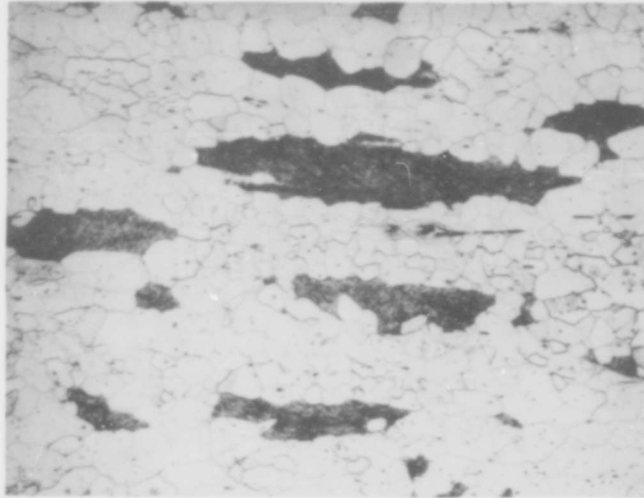


Fig. 59 - Fe-3.2% Si, drawn 66% and annealed at 700°C for 30 sec. (315X).

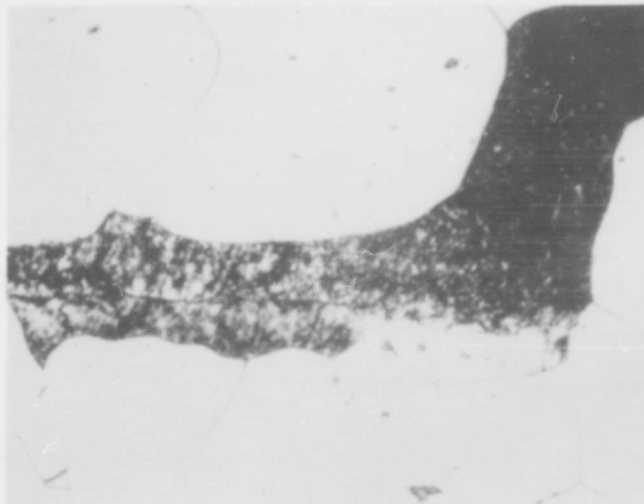


Fig. 60 - Fe-3.2% Si, drawn 66% and annealed at 700°C for 1 min. Prior grain boundary and substructure in unrecrystallized area (1650X).

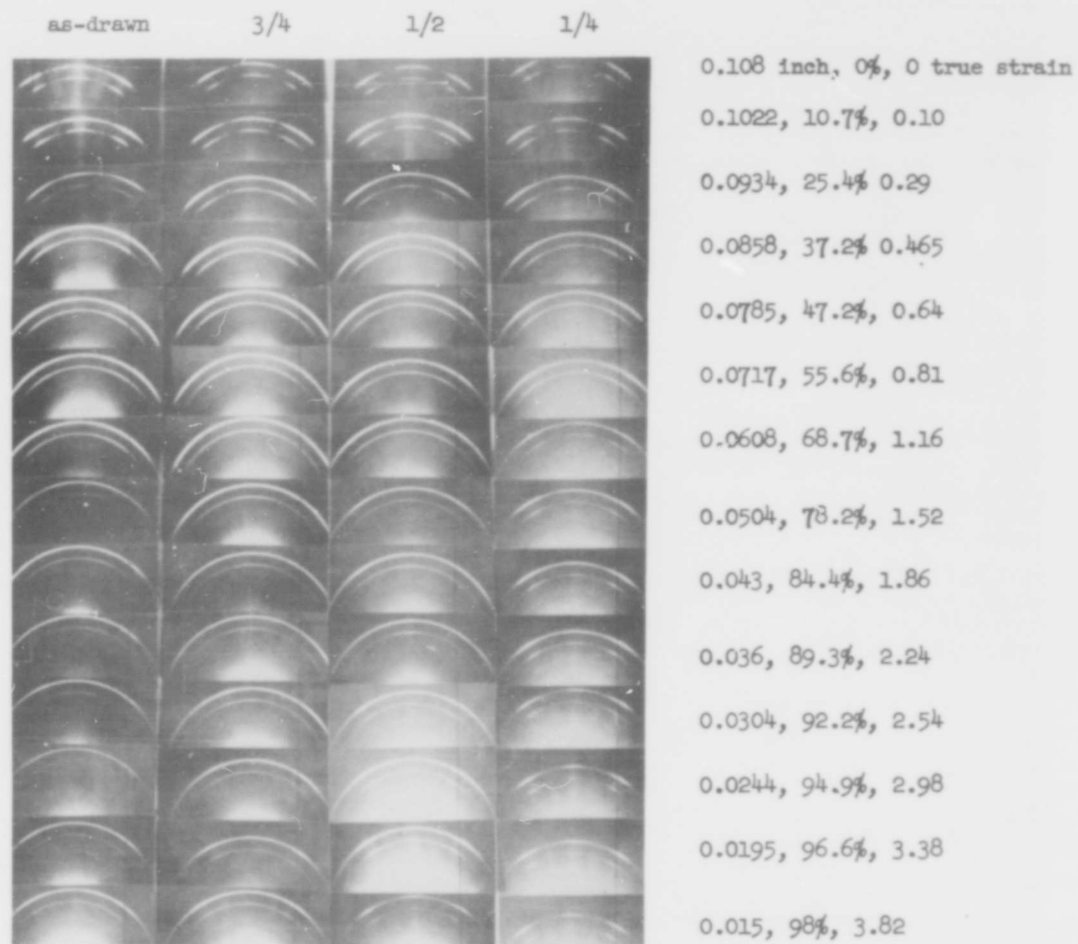


Fig. 61 - Drawing texture of Cb-EI wires with initial $\langle 110 \rangle$ fiber texture. Vertical columns show 110 diffraction rings of as-drawn wire and wire after chemical milling to 3/4, 1/2, and 1/4 diameter. Horizontal rows are labelled by the appropriate wire diameter, reduction in area, and true strain.

vertical row, and one vertical row for each part of the diameter of the wire examined. Proceeding from left to right, the four vertical rows are diffraction rings taken from the wire surface, and after chemical milling to $3/4$, $1/2$, and $1/4$ of the original diameters. When a $\langle 110 \rangle$ fiber texture is present, the half ring tends to divide into three spots. Thus it is easily seen that the original $\langle 110 \rangle$ fiber texture is destroyed when the wires are drawn to 37% reduction in area, and does not reappear to any significant extent in the outer part of the wire radius after further reduction. However, some vestige of the original texture does remain in the inner part of the wire, and becomes prominent again by 78% reduction, increasing in perfection with further reduction. The texture of Cb-E4 with a strong initial $\langle 110 \rangle$ fiber texture drawn with the same schedule of dies behaves similar to the Cb-E1.

The Cb-E1 drawn from material with an initially random texture develops the texture shown in Fig. 62 which is a composite of the 110 diffraction rings of this material. The texture first develops in the inner part of the wire, and becomes significant after 78% reduction in area. The middle part of the radius of the wire develops a significant texture at 84% reduction, whereas the outer part of the wire radius does not develop a texture. The texture of the Cb-E4 wire drawn from material with a random texture behaved similarly.

Cb-50 with a random initial texture behaves similar to the Cb-E1 with a random initial texture, although the inner part of the Cb-50 wire develops a significant texture at a slightly smaller reduction.

The cylindrical wire texture mentioned by Leber⁽¹⁹⁾ ($\{100\}$ planes parallel to the wire surface in addition to $\langle 110 \rangle$ directions parallel to the wire axis) was not found to any extent in these wires. However, the cylindrical texture was found in a swaging experiment to be discussed later. This is in agreement with later work by Leber⁽²⁰⁾ in which he found that the cylindrical texture is present to a much greater extent in swaged wires than in drawn wires.

Recrystallization textures were also determined for samples of Cb-E4 drawn from 0.108 to 0.046 inch in diameter in nine steps. Samples at each stage of reduction were recrystallized at 2250°F for 3 hours in a vacuum of 10^{-5} mm of Hg, after a light surface etch. The recrystallization texture was found to become essentially random at 25% reduction. This was the way the random Cb-E1 material referred to previously was obtained.

2. Hardness of Drawn Wires

Diamond pyramid microhardness values were obtained for each stage of reduction, using the average of a diametral traverse across a transverse section. Fig. 63 shows the variation of the microhardness of drawn Cb-E1, Cb-E4, and drawn nickel (99.95% purity) with reduction in area. The hardness of the recrystallized 0.108 inch diameter Cb-E1 (DPH 75) is considerably lower than that of the Cb-E4 (DPH 108) because of the lower oxygen content. The columbium from which these wires were drawn possess the strong initial $\langle 110 \rangle$ texture. The difference between the work hardening behavior of columbium (b. c. c.) and nickel (f. c. c.) is vividly illustrated. The hardness of the nickel levels off, while

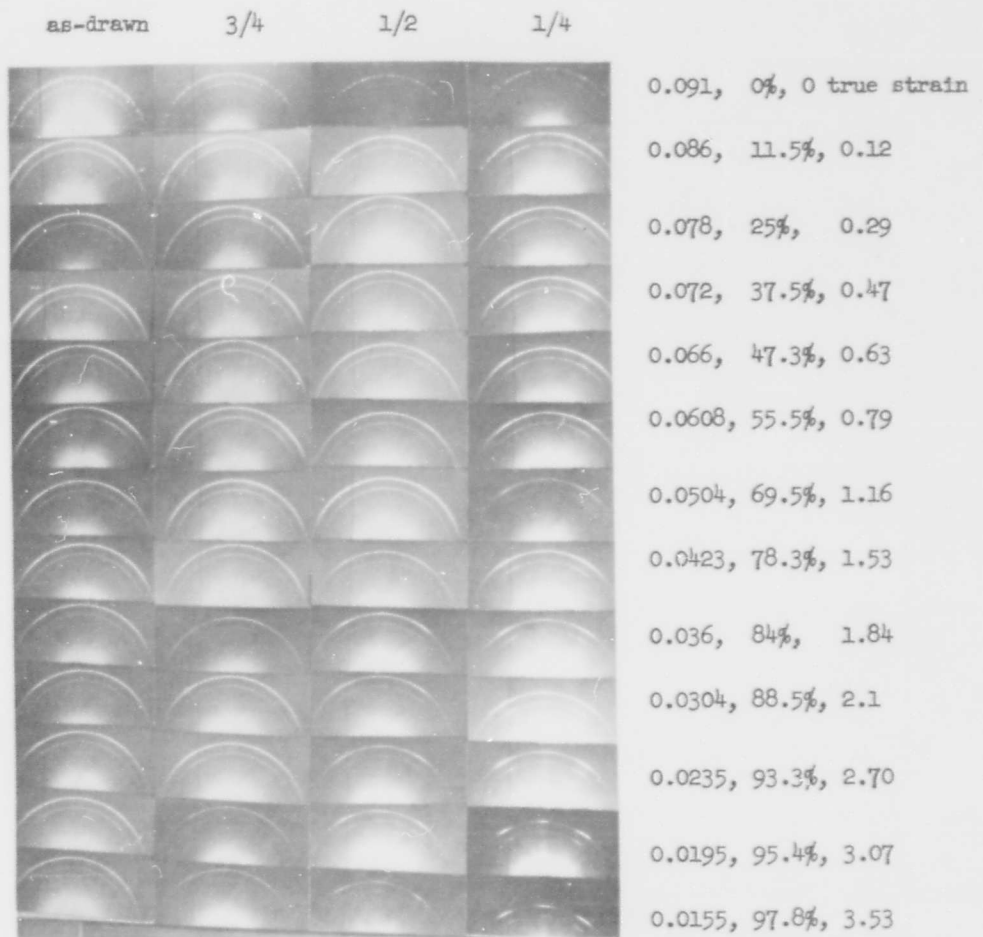


Fig. 62 - Drawing texture of Cb-EI wires with random texture. Vertical columns show 110 diffraction rings of as-drawn wire and wire after chemical milling to 3/4, 1/2, and 1/4 diameter. Horizontal rows are labelled by the appropriate wire diameter, reduction in area, and true strain.

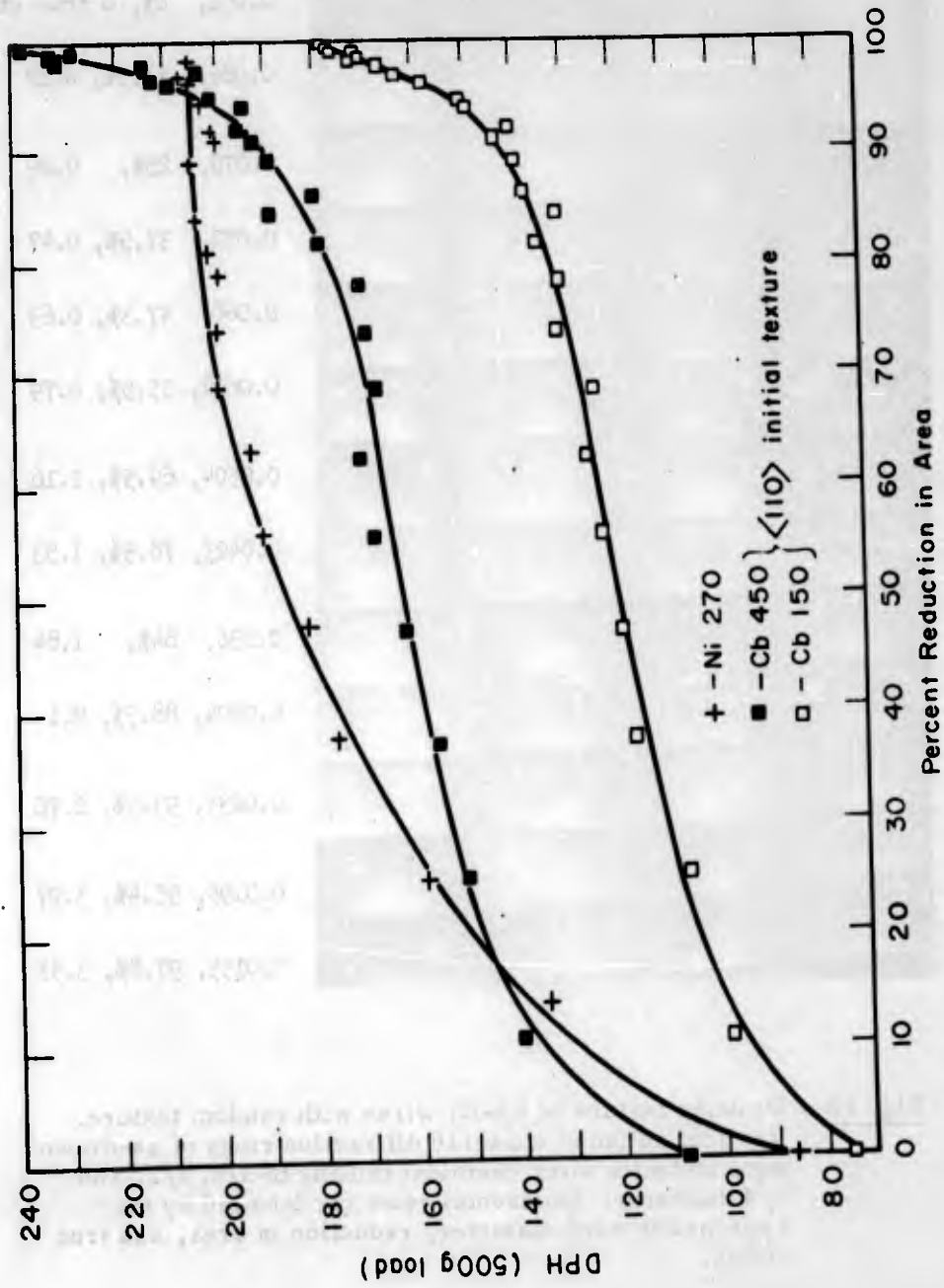


Fig. 63 - Microhardness of drawn Ni and Cb.

the columbium starts to level off but then increases sharply at reductions in area greater than 80%. The behavior of nickel is not an isolated case, since the hardness of a drawn f. c. c. alloy of gold and silver also approaches a limiting hardness. Many b. c. c. metals exhibit the behavior of columbium, including iron(4, 24).

Fig. 64 utilizes the same hardness data presented in Fig. 63, replotted versus true strain. The difference in the behavior of nickel and columbium is still apparent. The nickel approaches a limiting hardness after a sharp initial increase, whereas the columbium shows an initial increase in hardness followed by an approximately level region and then a linear increase. The curves for the two purities of columbium are similar although the less pure Cb-E4 has a higher initial hardness. It appears that as the impurity content increases, the various parts of the curve occur at lower reductions. However, the slopes of the linear portions of the curves for both purities of columbium are approximately the same.

Fig. 65 shows the hardness of three purities of drawn columbium versus true strain. These wires were drawn from material with an initially random texture. The hardness of rolled columbium (300 ppm of interstitial impurities) is also shown; however, no curve is drawn through the data points in order to avoid confusion. The hardness curves of columbium drawn from wire with an initially random texture are very similar to those of columbium with an initial $\langle 110 \rangle$ texture. The effect of impurity content is also the same, and the hardness curve of the very pure Cb-50 is in line with the effect of increasing impurity content based on Cb-E1 and Cb-E4. The rolled columbium also increases in hardness at high reductions.

3. Microstructures of Drawn Wires

The microstructure of the recrystallized Cb-E1 which has a pronounced initial $\langle 110 \rangle$ texture, is composed of equiaxed grains (Fig. 66). The first indication of deformation in the microstructure of wire drawn from this material came in the second drawing step (25% reduction in area) when deformation bands appeared. Fig. 67 shows that the grains become noticeably elliptical and slightly curved at 55% reduction. At 78% reduction, the grains are very curved (Fig. 68). Both Figs. 67 and 68 give the general impression that most of the grains tend to become elliptical. Fig. 69 shows the very marked curvature at 98% reduction. The texture is very pronounced at the center, which causes the lack of etching contrast there.

Cb-E1 drawn from starting material with a random texture again shows the first signs of deformation in the microstructure at 25% reduction. Also, the grains started to become elliptical or curved at 55% reduction (Fig. 70), are definitely curved at 78% reduction, and are very curved at 88% reduction (Fig. 71). The microstructural changes of Cb-E4 drawn according to the same schedules as the Cb-E1 described above are similar to the latter.

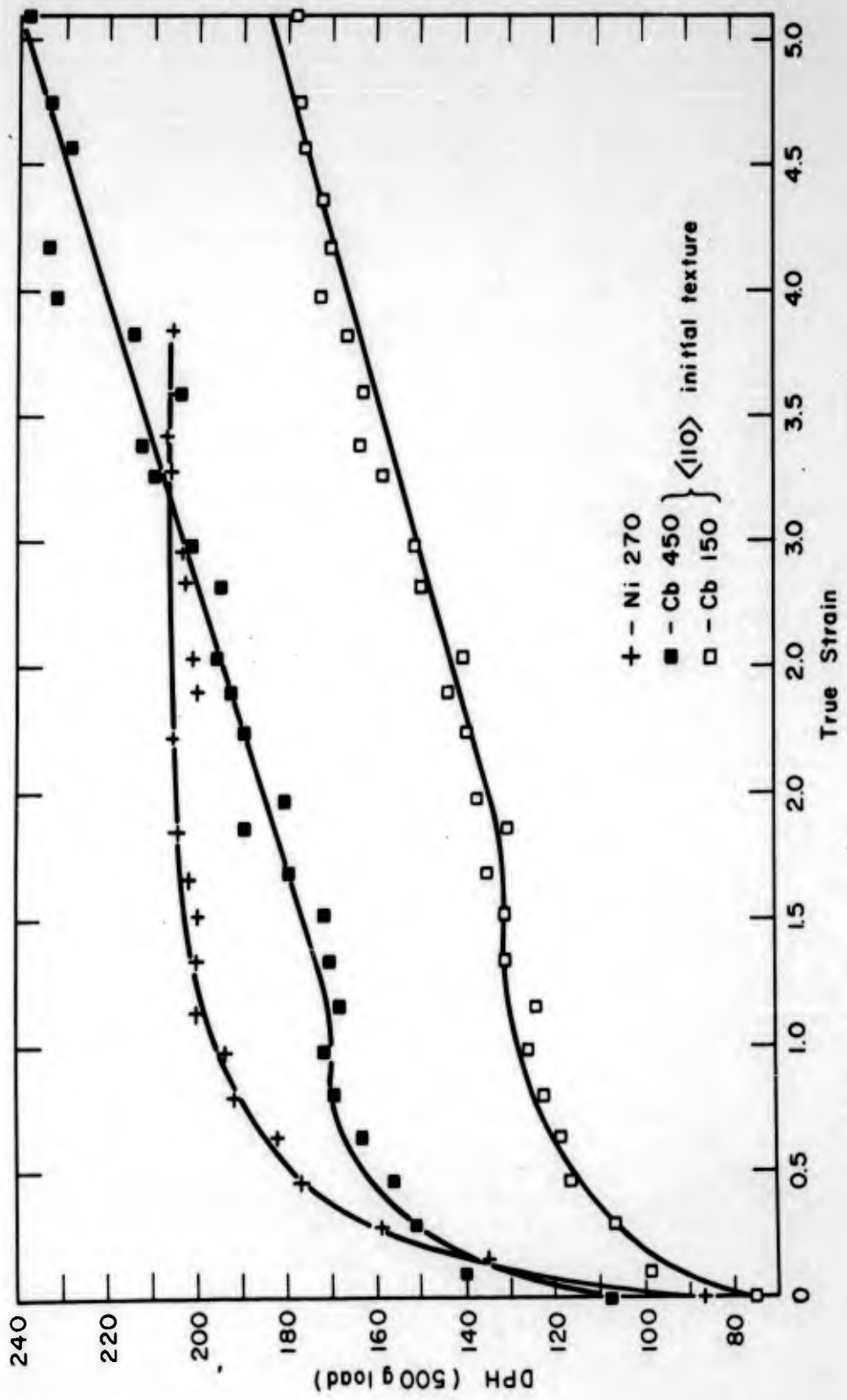


Fig. 64 - Microhardness of drawn Cb and Ni.

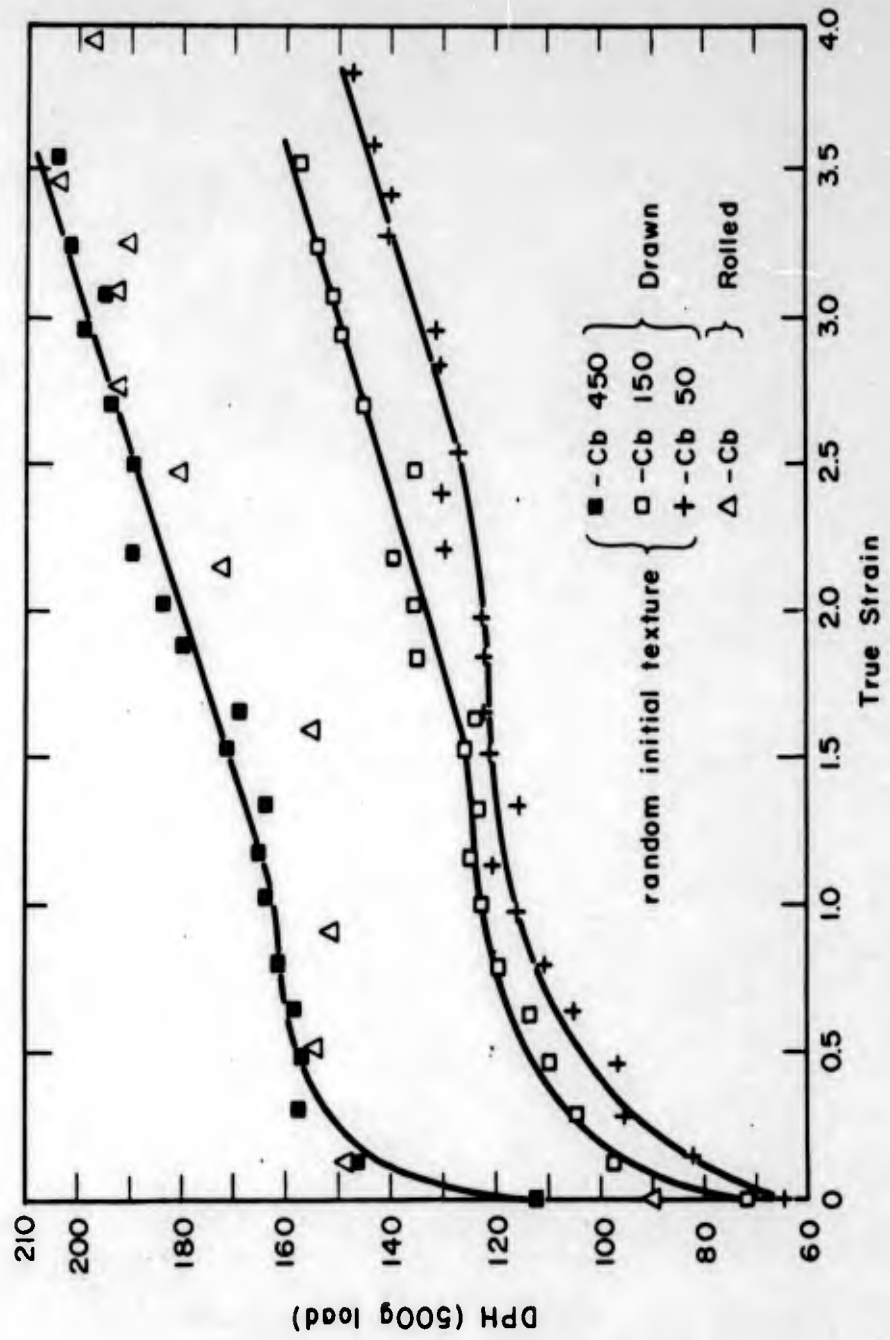


Fig. 65 - Microhardness of drawn and rolled Cb.

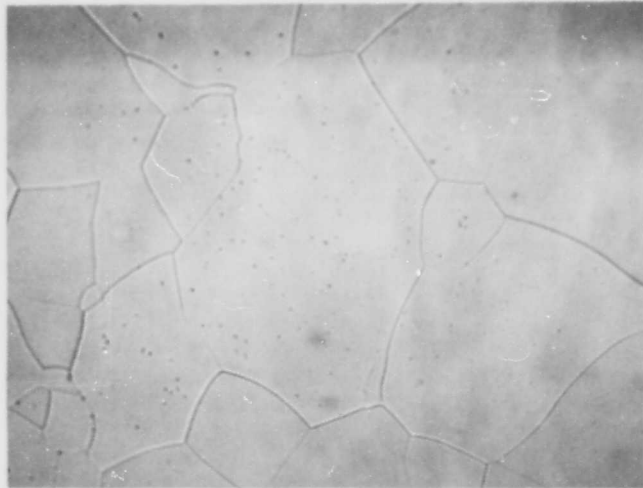


Fig. 66 - Columbium wire Cb-E1. As recrystallized.
Transverse section (500X).



Fig. 67 - Columbium wire Cb-E1. Drawn 55.6%
reduction in area, true strain 0.81.
Transverse section (250X).



Fig. 68 - Columbium wire Cb-E1. Drawn 78.2% reduction in area, true strain 1.52. Transverse section (250X).

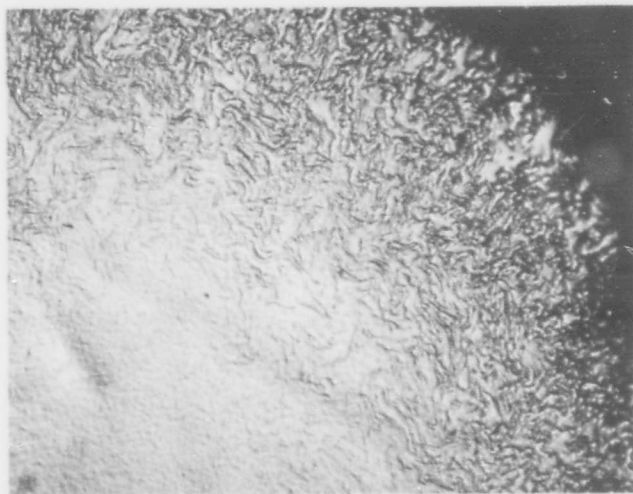


Fig. 69 - Columbium wire Cb-E1. Drawn 97.8% reduction in area, true strain 3.82. Transverse section (500X).

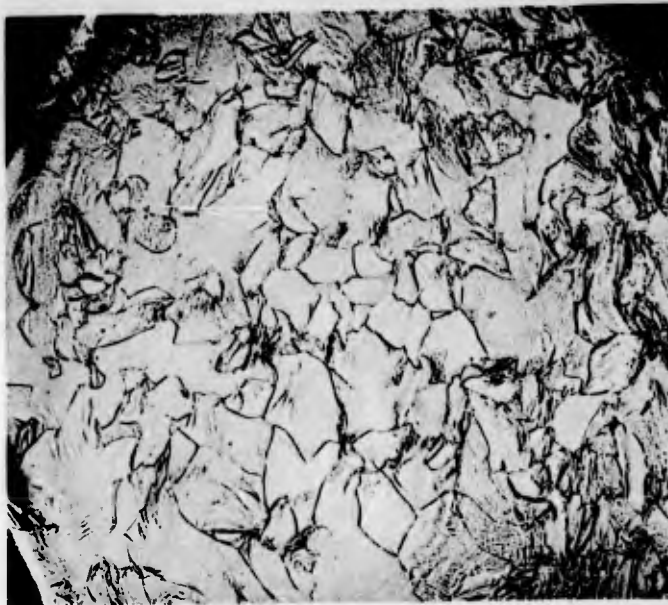


Fig. 70 - Columbium wire Cb-E1. Drawn 55.5% reduction in area, true strain 0.79, from random texture material. Transverse section (100X).

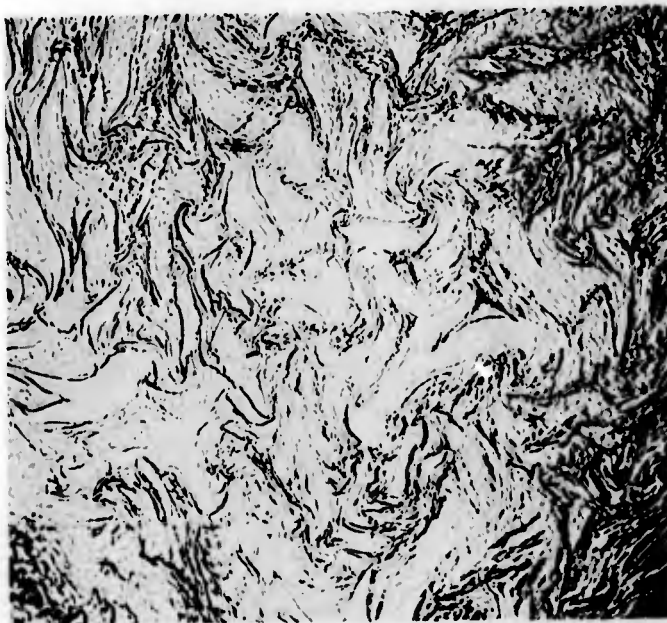


Fig. 71 - Columbium wire Cb-E1. Drawn 88.5% reduction in area, true strain 2.18, from random texture material. Transverse section (250X).

4. Microstructures and Textures in Swaging

Cb-E4 was swaged in 6 steps from 0.108 inch diameter to 0.034 inch diameter. The microstructure, texture, and hardness at each stage of reduction were determined. The deformation was found to be concentrated at the center of the wire, even at the first stage of reduction. Fig. 72a, a photomicrograph of the edge of Cb-E4 swaged to 29% reduction, and Fig. 72b, a photomicrograph of the center of the same specimen, illustrate the difference between these locations. At the third stage of reduction (66%), the spiral nebula structure shown in Fig. 73 appears.

The texture studies show that the initial $\langle 110 \rangle$ annealing texture is destroyed in the core at the same stage that the grains are shown by microscopic examination to be severely deformed. The texture does not reform in the core, even at the final reduction (true strain 2.3, reduction in area 90%). The exterior shell of the wire tends to retain the initial $\langle 110 \rangle$ texture, even in the smallest wire. When the spiral nebula structure appears, the cylindrical texture occurs in the exterior shell. This is to be expected from the microstructure, since the grains are elongated parallel to the wire surface, as well as in the direction parallel to the wire axis. Thus the deformation is similar to rolling, and the (100) plane that tends to be parallel to the rolling surface should be parallel to the swaged wire surface.

The hardness of the swaged Cb-E4 shows an initial marked increase and then a linear increase. There are not enough points to decide whether there is a tendency to level. As deformation increases, the difference in the hardness at the center and the edge increases.

5. Discussion of Results

The origin of the curved grains found in transverse sections of drawn columbium or iron wires has been previously explained^(1,4). When a grain has a $\langle 110 \rangle$ direction approximately parallel to the wire axis, only two slip directions are available, which causes the grain to deform in only one dimension in a transverse section and therefore become elliptical. The grains are forced to curve to maintain grain boundary continuity. A square in a transverse section of the original annealed wire should become a rectangle with sides that have a two to one ratio for a 50% reduction in area. The microstructures of columbium drawn 55% reduction (Figs. 67 and 70) do show a tendency toward an elliptical grain shape. Of course, there are ellipses of many major to minor axis ratios, since the grains adjacent to any particular one can cause a departure from the idealized axial ratio. Also, grains which deviate from having $\langle 110 \rangle$ exactly parallel to the wire axis will tend to have an axial ratio less than the ideal. Since the wire drawn from an initially random texture has only a relatively small fraction of its grains with $\langle 110 \rangle$ orientation compared to wire with an initial $\langle 110 \rangle$ texture, the initially random wires should have a smaller fraction of grains that tend to become elliptical. Measurement of the axial ratios of about 100 grains in the samples of Figs. 67 and 70 shows that a majority of the grains in the initially random sample have axial ratios between 1 and 1.8, while a majority of the grains in the initially textured wire have axial ratios between 1.4 and 2.6. These results are consistent with the ideal axial ratio of about two expected for 55% reduction of $\langle 110 \rangle$ oriented grains, as in the initially textured wire.



(a)



(b)

Fig. 72 - Columbium wire Cb-E4. Swaged 29.5% reduction in area, true strain 0.35. Transverse section: (a) at edge of section, (b) at center of section (500X).

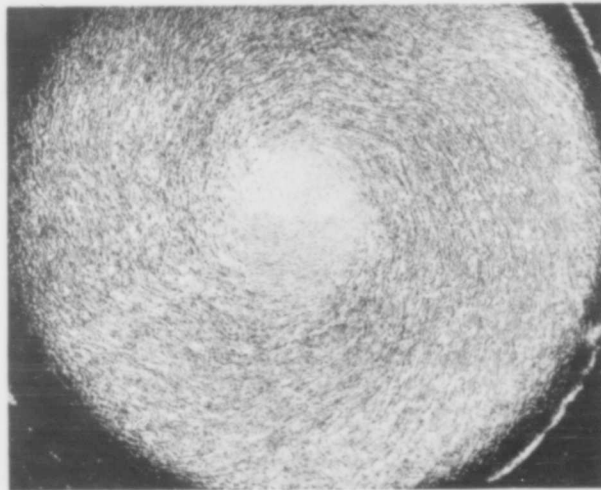


Fig. 73 - Columbium wire Cb-E4. Swaged 66.5% reduction in area, true strain 1.07. Transverse section (75X).

The removal of the strong $\langle 110 \rangle$ initial texture of Cb-E1 and Cb-E4 wires by intermediate wire-drawing reductions is apparently a new finding. Increased randomness with increasing deformation is counter to the usual conception of texture development during cold working. The phenomenon almost certainly results from lattice rotations associated with the deformation bands first observed easily by metallography at 25% reduction. In view of recent research by Cullity and co-workers^(21, 22), it is likely that some degree of control over mechanical properties of wires can be exercised by texture control, so the present findings provide a basis for further work in this direction.

The simultaneous appearance of deformation bands at 25% reduction and a random texture in wires recrystallized after such drawing is also significant. The deformation-band boundaries should have a spectrum of orientations, which could be the sites of recrystallization nuclei of the numerous orientations necessary for the production of a random texture. Work on an Fe-Si alloy by Walter and Koch⁽²³⁾ supports this idea. They found that Fe-Si crystals rolled to 70% reduction in thickness had deformation bands, that the bands had no cell structure, that the deformation band boundaries were composed of cells, and that these cells were recrystallization nuclei. However, in this case, these nuclei developed a recrystallization texture. It seems possible that, in other cases, the cells that grow may not fall within a narrow range of orientations, and give rise to a random texture.

Peck and Thomas⁽⁴⁾ proposed that the increase in hardness at high reductions of drawn b. c. c. metals may be connected with the curving of the grains in transverse section, since the two slip directions normal to the wire axis are activated when the grains curve. This is probably not the sole reason for this behavior, since rolled columbium which does not have curved grains exhibits a similar increase in hardness at high reductions (Fig. 65). The drawn wire of comparable purity starts the terminal linear hardness increase sooner than the sheet, which might be ascribed to the hardening effect of the curving grains, since the grains do show some curvature at the onset of the terminal hardness increase. Also, the wire drawn from initially textured material has a slightly but consistently higher hardness than that drawn from randomly textured material. Since a larger fraction of the grains curve in the initially textured columbium, this additional hardness increment might be due to the hardening effect of the greater number of curved grains. The reasons why f. c. c. metals work harden differently from b. c. c. metals, particularly at very high strains, remain unknown.

REFERENCES

- (1) Lement, B. S., et al, "Substructure and Mechanical Properties of Refractory Metals," WADD Technical Report 61-181, Part I, (1961).
- (2) Lement, B. S., et al, "Substructure and Mechanical Properties of Refractory Metals," WADD Technical Report 61-181, Part II, (1962).
- (3) Meieran, E. S., and Thomas, D. A., "Preparation of Wires for Examination by Transmission Electron Microscopy," Trans. AIME, 227 (1963) 284.
- (4) Peck, J. F. and Thomas, D. A., "A Study of Fibrous Tungsten and Iron," Trans. AIME, 221 (1961) 1240.
- (5) Thomas, G., Transmission Electron Microscopy of Metals, John Wiley and Sons, (1962).
- (6) Koo, R. C., "Recovery in Cold-worked Tungsten," J. Less-Common Metals, 3 (1961) 412.
- (7) Keh, A. S., "Dislocation Arrangement in Alpha Iron During Deformation and Recovery," Direct Observations of Imperfections in Crystals, Interscience Publishing Co., (1962) 213.
- (8) Rosenfield, A. R., AIME Refractory Metals Conference, Chicago (April 1962).
- (9) Titchener, A. L., and Bever, M. B., "The Stored Energy of Cold Work," Progress in Metal Physics, 7, Pergamon Press, London (1958).
- (10) Michalak, J. T., and Paxton, H. W., "Some Recovery Characteristics of Zone-Melted Iron, Trans. AIME, 221 (1961) 850.
- (11) Brittain, J. O. and Bronisz, S. E., "Stress Induced Strain Aging," Trans. AIME, 218 (1960) 289.
- (12) Parker, E. R. and Washburn, J., "Effects of Impurities and Imperfections on Mechanical Properties," Impurities and Imperfections, ASM, Cleveland (1955).
- (13) Leslie, W. C., "The Quench-Aging of Low-Carbon Iron and Iron-Manganese Alloys: An Electron Transmission Study," Acta. Met., 9 (1961) 1004.
- (14) Hahn, G. T., "A Model for Yielding with Special Reference to the Yield-Point Phenomena of Iron and Related B. C. C. Metals," Acta Met., 10 (1962) 727.
- (15) Johnston, W. G. and Gilman, J. J., "Dislocation Velocities, Dislocation Densities, and Plastic Flow in Lithium Fluoride Crystals", J. Appl. Phys., 30 (1959) 129.
- (16) Morris, C. E., "Electropolishing of Steels in Chrome-Acetic Acid Electrolyte", Met. Prog., 56 (1949) 696.
- (17) Cahn, R. W., "A New Theory of Recrystallization Nuclei", Proc. Phys. Soc., 63 (1950) 323.

REFERENCES (Continued)

- (18) Davies, P. W., Greenough, A. P., and Wilshire, B., "The Ledge Theory of Recrystallization in Polycrystalline Metals", *Phil. Mag.*, 6 (1961) 795.
- (19) Leber, S., "Cylindrical Textures in Tungsten and Other Body-Centered Cubic Metals," *Trans. ASM*, 53 (1961) 697.
- (20) Leber, S., "Discussion of paper by J. F. Peck, and D. A. Thomas," *Trans. AIME*, 224, (1962) 624.
- (21) Sree Harsha, K. S. and Cullity, B. D., "Effect of Initial Orientation on the Deformation Texture and Tensile and Torsional Properties of Copper and Aluminum Wires," *Trans. AIME*, 224 (1962) 1189.
- (22) Bhandary, V. S. and Cullity, B. D., "Texture and Mechanical Properties of Iron Wire Recrystallized in a Magnetic Field," *Trans. AIME*, 224 (1962) 1194.
- (23) Walter, J. L. and Koch, E. F., "Electron Microscope Study of the Structures of Cold-Rolled and Annealed (100) [001] Crystals of High-Purity Silicon-Iron," *Acta Met.*, 10 (1962) 1059.
- (24) Pfeil, L. B., "The Changes in Tensile Strength Due to Aging of Cold-Drawn Iron and Steel", *J. Iron and Steel Inst.*, 118 (1928) 167.

VI. X-RAY BACK-REFLECTION DIVERGENT BEAM STRAIN ANALYSES OF TANTALUM AND TUNGSTEN SINGLE CRYSTALS - Work carried out at Rutgers, The State University by S. Weissmann, N. Hosokawa and G. Padawer

A. Yielding of Tantalum Single Crystals

1. Scope

The aim of this investigation was the elucidation of the yield phenomena in zone-refined tantalum (Ta-E5) crystals deformed in compression. An attempt was made to explain the yield phenomena on the basis of the results obtained from complete strain analyses carried out for the pre-yield or micro-strain stage, for the discontinuous yielding stage, and for the regular strain hardening stage. The strain analyses are based on data obtained by the x-ray back-reflection divergent beam method. Since the underlying principles of both the x-ray method and the strain analysis have been discussed previously⁽¹⁾, they are not repeated here. In essence, the strain analysis as carried out with the aid of a digital computer describes the strain distribution for each deformation stage in terms of the three principal strains: the maximum strain ϵ_1 , the intermediate strain ϵ_2 , and the minimum strain ϵ_3 . Since these principal strains describe completely the strain ellipsoid, normal as well as shearing strains in any other direction can be computed. In the present work, the principal strains were used to compute the distribution of strains in the various slip planes for each deformation stage and to relate the changes of the strain distribution to the yield phenomena.

2. Experimental Procedure

Single crystal specimens of a triangular prismatic shape were prepared from initially cylindrical specimens having a diameter of about 6 mm and a height of about 10 mm by cutting with a Servomet spark-erosion machine. The specimens were subsequently etched to remove any lattice distortion introduced by the cutting operation. The reason for shaping the crystals into triangular prisms is the convenience which this shape affords for sampling the strain distribution in a great many different directions. Crystals of this shape can be irradiated by the x-ray beam on four different faces (three prismatic and one basal plane), and consequently the variations of the lattice spacings of many (hkl) reflections can be conveniently studied.

Specimens having an (012) orientation were deformed in compression at room temperature in the Instron machine. Teflon sheets were interposed to protect the basal planes of the prismatic crystals from harmful direct contact with the compression heads of the Instron machine. After subjecting the specimens to various amounts of compression, the changes in lattice spacings ($\frac{\Delta d}{d}$) of the various (hkl) reflections corresponding to the different compression stages were determined by the x-ray method. These values were used as the raw data for the computer strain analyses⁽¹⁾.

Subsequent to the x-ray studies, these specimens were investigated by transmission electron microscopy. For this purpose, the specimens were thinned first by means of the Servomet spark grinder and subsequently by chemical polishing in a solution containing 50% concentrated HNO_3 and 50% HF (48% conc.) until transparency was achieved with respect to the electron beam.

3. Results

3.1 Effect of Compression on the Principal Strains

A plot of the critical resolved shear stress vs. strain of the tantalum crystals deformed in compression at room temperature is shown in Fig. 74. Only the data from the divergent beam patterns corresponding to the compression stages A (or B) and C (0.077%, 0.097% and 1.44% strain respectively) were utilized for the strain analysis. The x-ray patterns corresponding to the compression stages of D (or E) were not suitable for precision measurements because the deformation was excessive and caused the patterns to broaden as well as to break up into fragments.

It is important to note that the compression stage A ($\epsilon = 0.077\%$) or B ($\epsilon = 0.097\%$) correspond to deformation that occurs before discontinuous yielding. Therefore, they are regarded as a stage pertaining to the pre-yield or microstrain region. Discontinuous yielding started somewhere between B and C.

Complete strain analyses were carried out on specimens corresponding to A, B and C, and the magnitude and directions of the principal strains obtained are listed in Table 12. These strains are listed in the order of their absolute values, and their directions are given in terms of the (hkl) planes to which the principal strains are perpendicular. The change in directions of the principal strains with increased compression is best visualized on the stereographic projection of Fig. 75. The [012] compression axis, which coincides with the orientation axis of the crystal, lies in the center of this projection.

It is noteworthy that the maximum principal strain ϵ_1 is positive for the pre-yield region, indicating lattice expansion. On discontinuous yielding, the sign of ϵ_1 changes to a negative value, indicating lattice contraction.

The consistency of the data of the strain analysis can be checked on the basis that the volume change resulting from deformation is negligibly small, and therefore the sum of the magnitudes of the principal strains should be zero. The last column of Table 12 indeed shows that the $\Sigma\epsilon$ values are very small, falling well within the limits of experimental error.

3.2 Effect of Compression on the Distribution of Shearing Strains In Slip Planes

To determine the active slip systems for the crystal deformed with [012] orientation, the maximum resolved shear stresses were computed. Table 13 gives the result of this computation. The symbols φ and λ represent

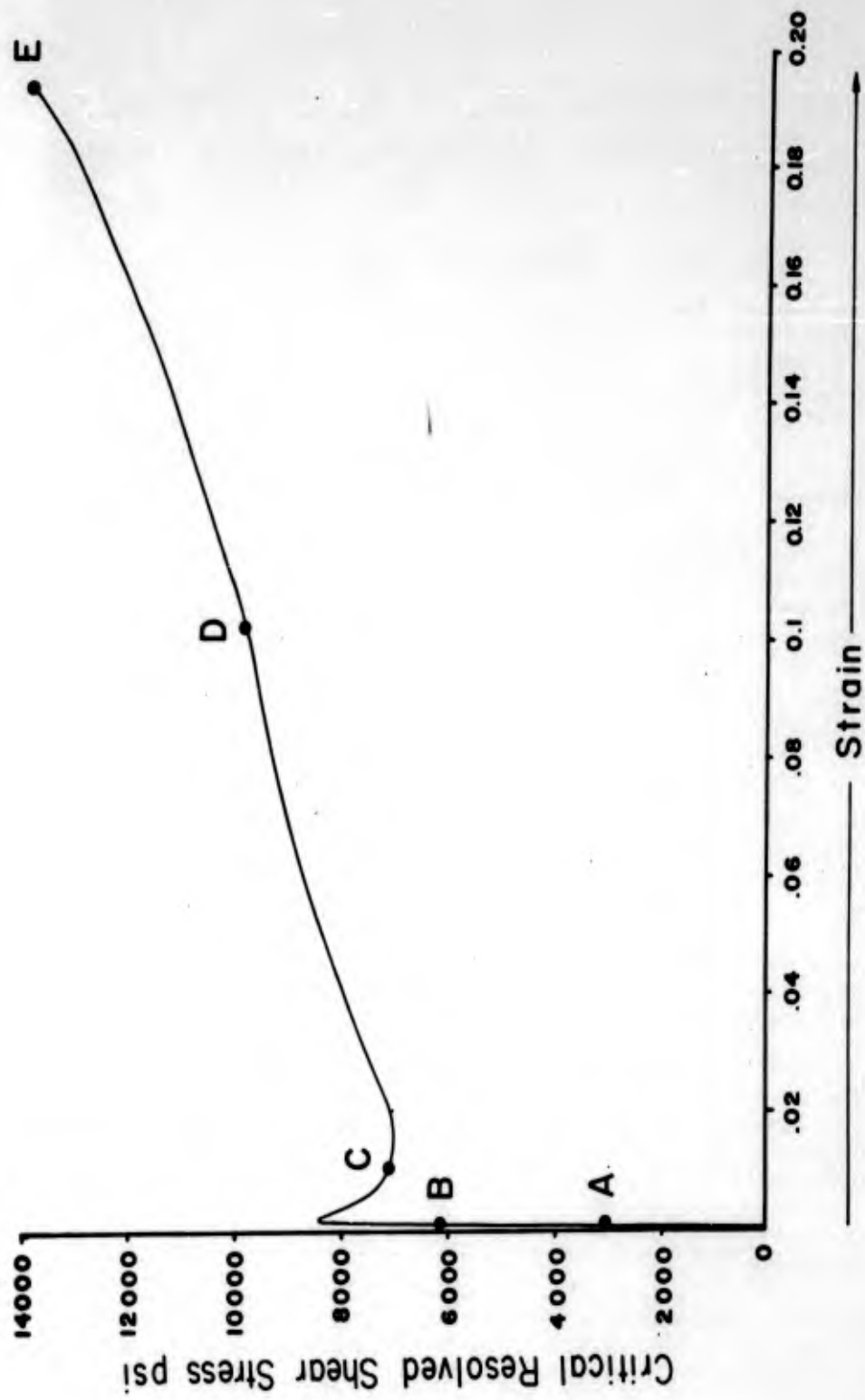
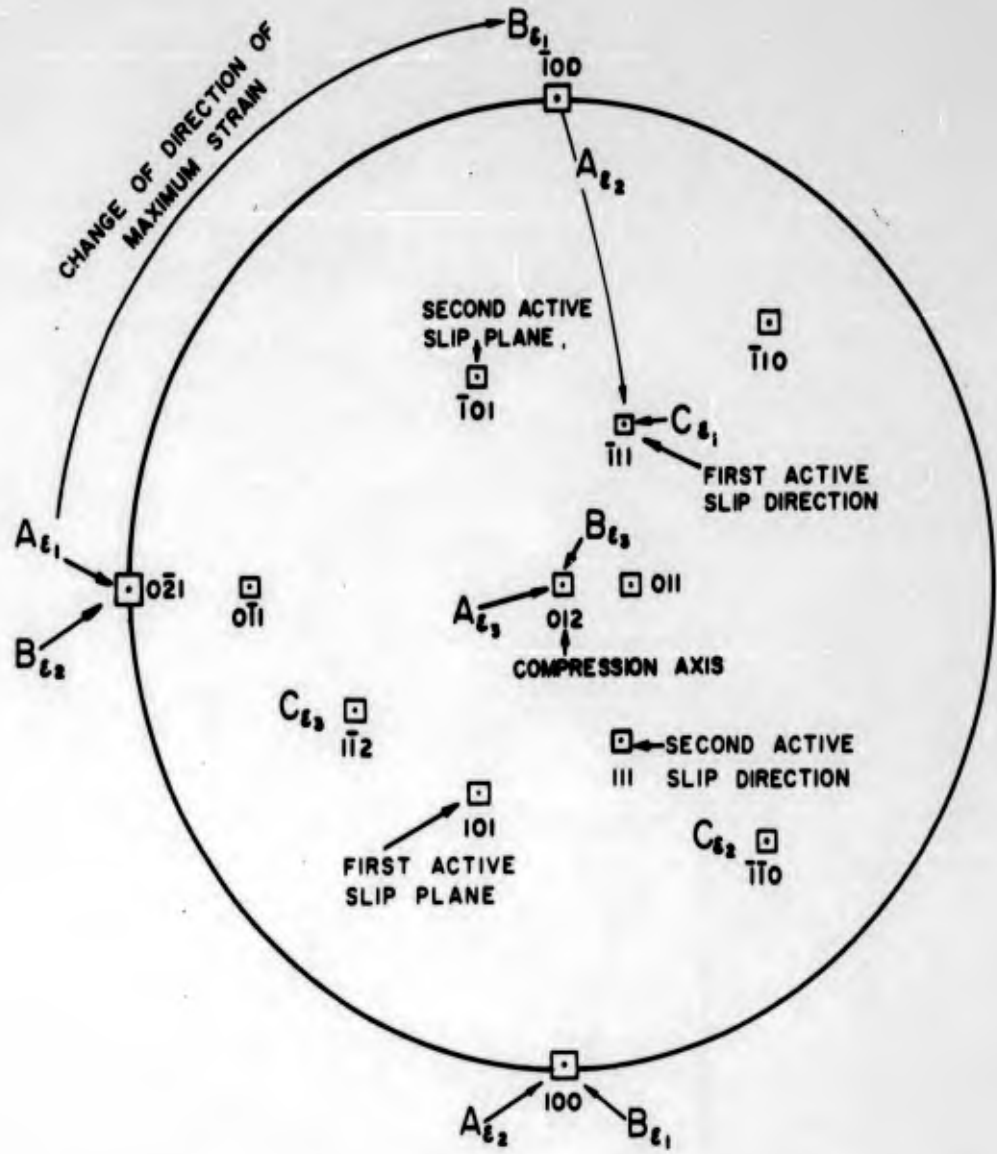


Fig. 74 - Stress-Strain curve of Ta crystal.

Table 12

Effect Of Compression On The Principal Strains In Zone Refined
Tantalum Crystal

Position On $\sigma - \epsilon$ Curve	% Compression	ϵ_1 (max.) (HKL) %	ϵ_2 (interm.) (HKL) %	ϵ_3 (min.) (HKL) %	$\sum \epsilon$ %		
A	0.077	0.31	0 $\bar{2}$ 1	100	-0.11	012	0.02
B	0.097	0.41	100	0 $\bar{2}$ 1	-0.02	012	0.02
C	1.44	-0.49	$\bar{1}$ 11	$\bar{1}\bar{1}$ 0	0.18	1 $\bar{1}$ 2	0.04



A = 0.077% COMPRESSION	ϵ_1 = MAXIMUM STRAIN
B = 0.097% "	ϵ_2 = INTERMEDIATE "
C = 1.44% "	ϵ_3 = MINIMUM "

Fig. 75 - Effect of compression on the principal strains in zone-refined tantalum crystal.

Table 13

Computation Of Maximum Resolved Shear Stress Of Zone-Refined Ta
Single Crystal Deformed by Compression

Compression Axis [012]

<u>Slip Plane</u>	<u>Slip Direction</u>	<u>cos ψ cos λ</u>	<u>Active Slip Planes</u>
(110)	[1 $\bar{1}$ 1]	0.0816	
(110)	[1 $\bar{1}$ $\bar{1}$]	-0.2449	
(1 $\bar{1}$ 0)	[111]	-0.2449	
(1 $\bar{1}$ 0)	[11 $\bar{1}$]	0.0816	
(101)	[11 $\bar{1}$]	-0.1633	
(101)	[1 $\bar{1}$ $\bar{1}$]	-0.4899	First active slip plane
(10 $\bar{1}$)	[111]	-0.4899	Second active slip plane
(10 $\bar{1}$)	[1 $\bar{1}$ 1]	-0.1633	
(011)	[11 $\bar{1}$]	-0.2449	
(011)	[$\bar{1}$ 1 $\bar{1}$]	-0.2449	
(01 $\bar{1}$)	[111]	-0.2449	
(01 $\bar{1}$)	[$\bar{1}$ 11]	-0.2449	

λ = angle of slip direction with compression axis

ψ = angle of plane normal with compression axis

the angles subtended by the slip direction and the plane normal to the compression axis, respectively. It appears that two slip systems become operative as a result of compression, namely the (101) [111] and (10 $\bar{1}$) [$\bar{1}\bar{1}\bar{1}$].

The distribution of shear strains in all slip planes, including that of the active slip planes, was computed from the principal strains ϵ_1 , ϵ_2 and ϵ_3 , using the following relation⁽¹⁾:

$$S = 2\epsilon_1(\lambda\alpha) + \epsilon_2(\gamma\beta) + \epsilon_3(\mu\gamma)$$

where S is the shear strain in the plane in a particular direction under consideration having the direction cosines α , β , γ with respect to ϵ_1 , ϵ_2 , ϵ_3 ; and λ , γ , μ are the direction cosines of the normal of the plane with respect to ϵ_1 , ϵ_2 , ϵ_3 .

Table 14 gives as a function of deformation the magnitude and sign of the shear strains in the (101) slip plane as computed for various directions. The complete distribution of shear strains in the (101) slip plane is graphically depicted in Fig. 76. Similarly, Table 15 gives the magnitude and sign of the shear strains in the (10 $\bar{1}$) slip plane and Fig. 77 gives the graphical representation of the complete strain distribution.

Of particular interest is the strain dependence in the slip direction. Referring to Table 14 and Fig. 76 for the first active slip system, (101) [111], the magnitude of the strain increases from 0.010% to 0.292% as the compression is increased from 0.077% to 0.097%; and subsequently decreases to zero as the compression is further increased to 1.44%. From Fig. 74 it appears that this decline is associated with discontinuous yielding which starts at a compressive strain 0.097% and 1.44%. On the other hand, the magnitude of the strain in the second active slip system, (10 $\bar{1}$) [$\bar{1}\bar{1}\bar{1}$], increases continuously from 0.010% to 0.446% as the compression is increased from 0.077% to 1.44% (Table 15 and Fig. 77).

A transmission electron micrograph taken of the specimen after 1.44% compression is shown in Fig. 78a. With the aid of selected area diffraction (Fig. 78b), it was possible to identify the slip traces left by the active (110) slip planes on the surface of the foil having a (11 $\bar{3}$) orientation.

4. Discussion

The yield phenomenon in body-centered cubic metals is explained by Cottrell⁽²⁾ in terms of immobilization of dislocations by impurity atoms. Cottrell's theory is based on iron-carbon alloys, containing carbon in solid solution. According to Cottrell, discontinuous yielding occurs when the stress is sufficient to unpin the dislocations. The sudden release leads to a process in which the internal barriers can be overcome

Although the possible effect of impurities on the yield phenomena in zone-refined tantalum (E5) crystals cannot be excluded, it appears on the basis of the present investigation that the impurity content is not primarily responsible for the observed phenomena. The results of this work strongly suggest that discontinuous yielding is associated with the following phenomena:

Table 14

Computation Of Shear Strains In (101) Slip Plane Of Zone-Refined
Tantalum Crystal from Principal Strains

Active Slip System	Strain Direction [hkl]	Angle of Strain Direction	Compression		
			0.077%	0.097%	1.44%
	010	0	-0.238	0.198	0.062
	13 $\bar{1}$	25°14'	-0.278	0.392	0.076
	12 $\bar{1}$	35°16'	-0.284	0.450	0.078
	11 $\bar{1}$	54°44'	-0.264	0.522	0.074
	21 $\bar{2}$	70°32'	-0.224	0.538	0.072
	10 $\bar{1}$	90°	-0.154	0.500	0.046
	21 $\bar{2}$	109°28'	-0.066	0.404	0.022
First active slip system	11 $\bar{1}$	125°16'	0.010	0.292	0
	12 $\bar{1}$	144°44'	0.106	0.106	-0.026
	13 $\bar{1}$	154°46'	0.150	0.036	-0.038
	0 $\bar{1}$ 0	180°	0.238	-0.198	-0.062
	$\bar{1}$ 31	205°14'	0.278	-0.392	-0.076
	$\bar{1}$ 21	215°16'	0.284	-0.450	-0.078
	$\bar{1}$ 11	234°44'	0.264	-0.522	-0.074
	2 $\bar{1}$ 2	250°32'	0.224	-0.538	-0.072
	$\bar{1}$ 01	270°	0.154	-0.500	-0.046
	212	289°28'	0.066	-0.404	-0.022
	$\bar{1}$ 11	305°16'	-0.010	-0.292	0
	$\bar{1}$ 21	324°44'	-0.106	-0.106	0.026
	$\bar{1}$ 31	334°46'	-0.150	-0.036	0.038

Let $\epsilon_1, \epsilon_2, \epsilon_3$ be the three principal strains, λ, ν, μ and α, β, γ the direction cosines of the normal strain and of the direction in the plane, respectively, then the shear strain $S = 2[\epsilon_1(\lambda\alpha) + \epsilon_2(\nu\beta) + \epsilon_3(\mu\gamma)]$.

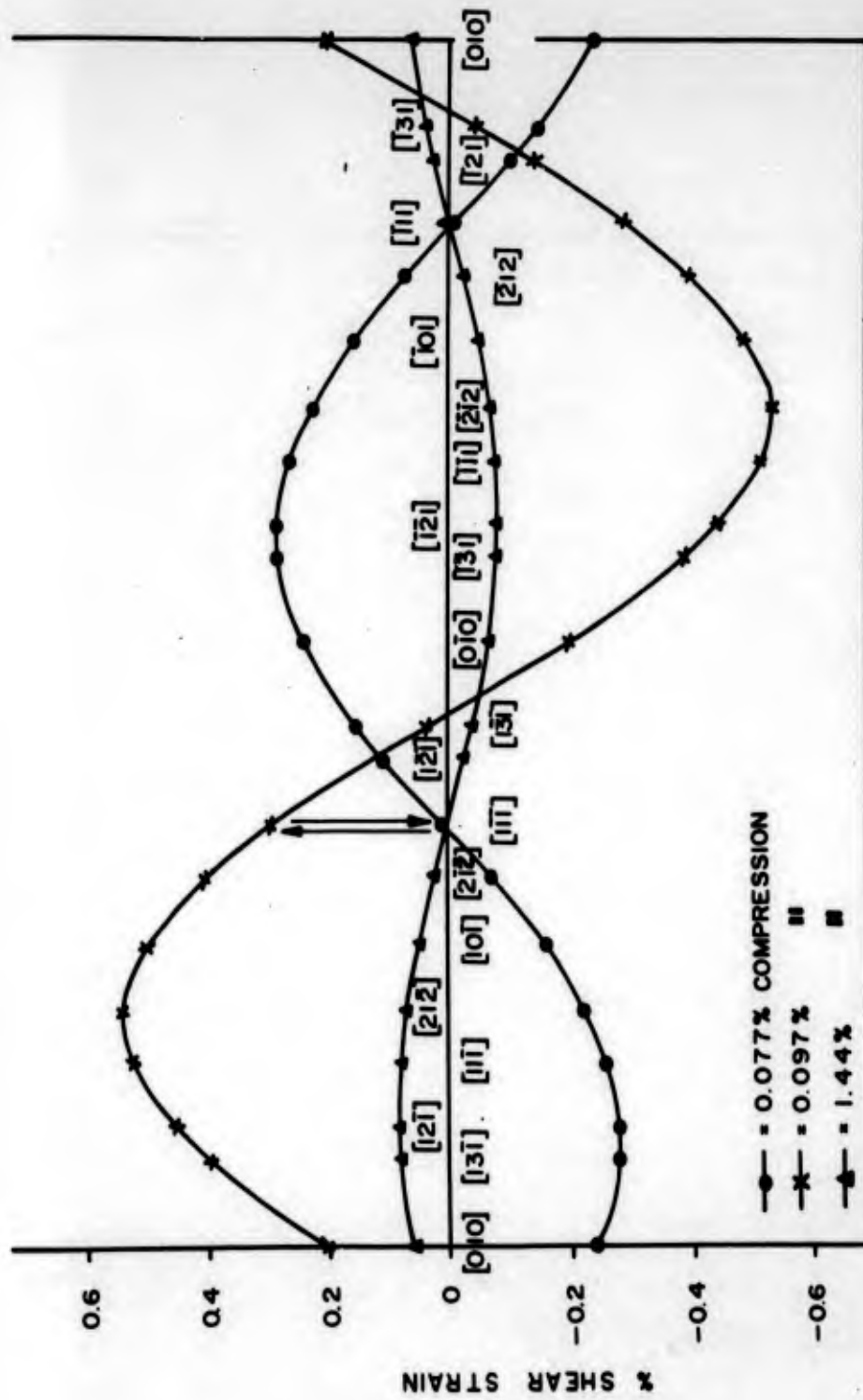


Fig. 76 - Dependence of shear strain upon direction on (101) slip plane.

Table 15

Computation Of Shear Strain In (10 $\bar{1}$) Slip Plane Of Zone-Refined
Tantalum Crystal From Principal Strains

Active Slip System	Strain Direction [khl]	Angle of Strain Direction	Compression		
			0.077%	0.097%	1.44%
	010	0	0.238	-0.198	0.696
	131	25°14'	0.150	0.034	0.648
	121	35°16'	0.104	0.126	0.592
Second active slip system	111	54°44'	0.010	0.294	0.446
	212	70°32'	-0.066	0.404	0.274
	101	90°	-0.154	0.500	0.046
	2 $\bar{1}$ 2	109°28'	-0.224	0.538	-0.190
	1 $\bar{1}$ 1	125°16'	-0.264	0.522	-0.364
	1 $\bar{2}$ 1	144°44'	-0.284	0.450	-0.540
	1 $\bar{3}$ 1	154°46'	-0.280	0.390	-0.610
	0 $\bar{1}$ 0	180°	-0.238	0.198	-0.696
	13 $\bar{1}$	205°14'	-0.150	-0.034	-0.648
	12 $\bar{1}$	215°16'	-0.104	-0.126	-0.592
	11 $\bar{1}$	234°44'	-0.010	-0.294	-0.446
	21 $\bar{2}$	250°32'	0.066	-0.404	-0.274
	10 $\bar{1}$	270°	0.154	-0.500	-0.046
	21 $\bar{2}$	289°28'	0.224	-0.538	0.190
	11 $\bar{1}$	305°16'	0.264	-0.522	0.364
12 $\bar{1}$	324°44'	0.284	-0.450	0.540	
13 $\bar{1}$	334°46'	0.280	-0.390	0.610	

Let $\epsilon_1, \epsilon_2, \epsilon_3$ be the three principal strains, λ, ν, μ and α, β, γ the direction cosines of the normal strain and of the direction in the plane, respectively, then the shear strain $S = 2[\epsilon_1(\lambda\alpha) + \epsilon_2(\nu\beta) + \epsilon_3(\mu\gamma)]$.

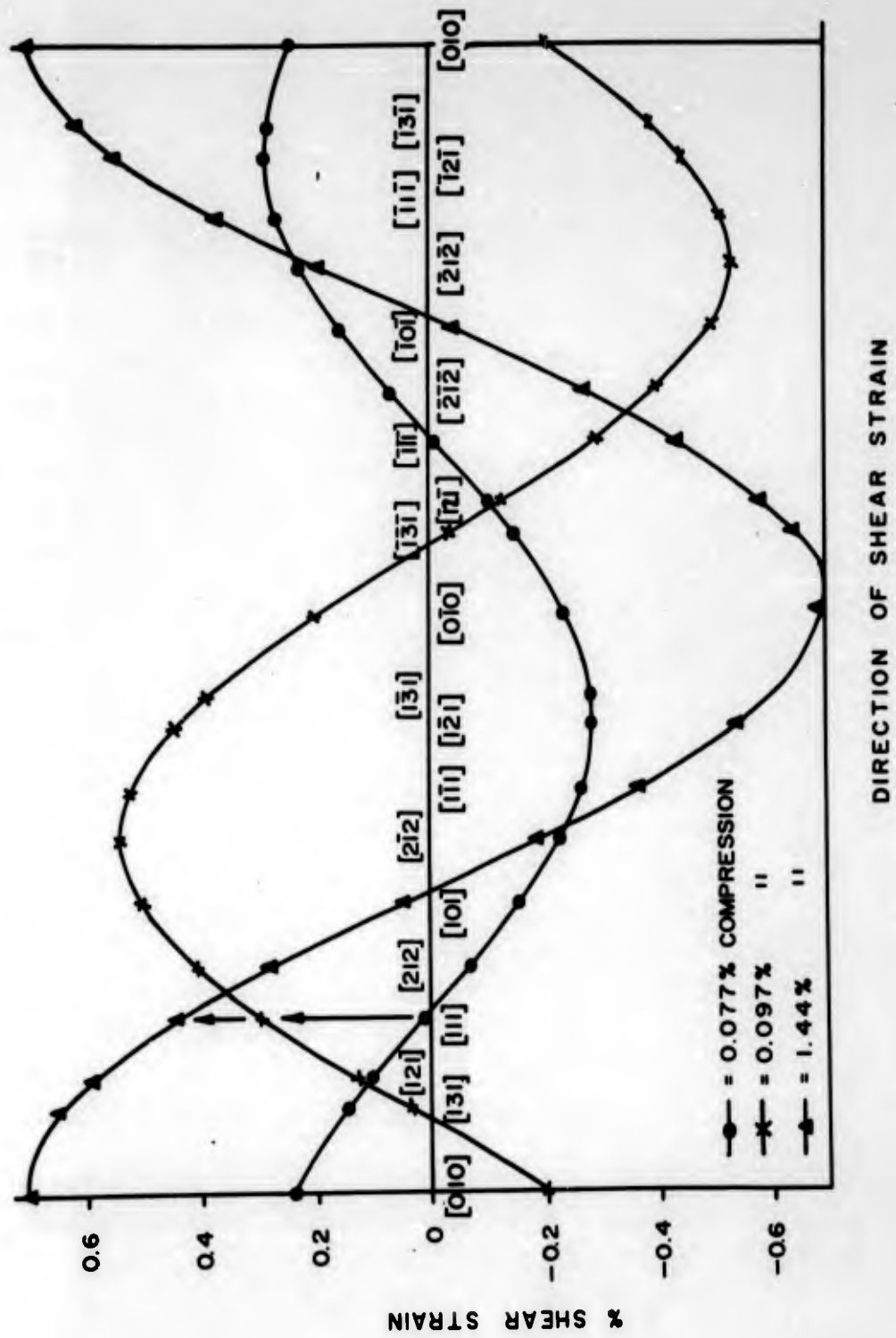
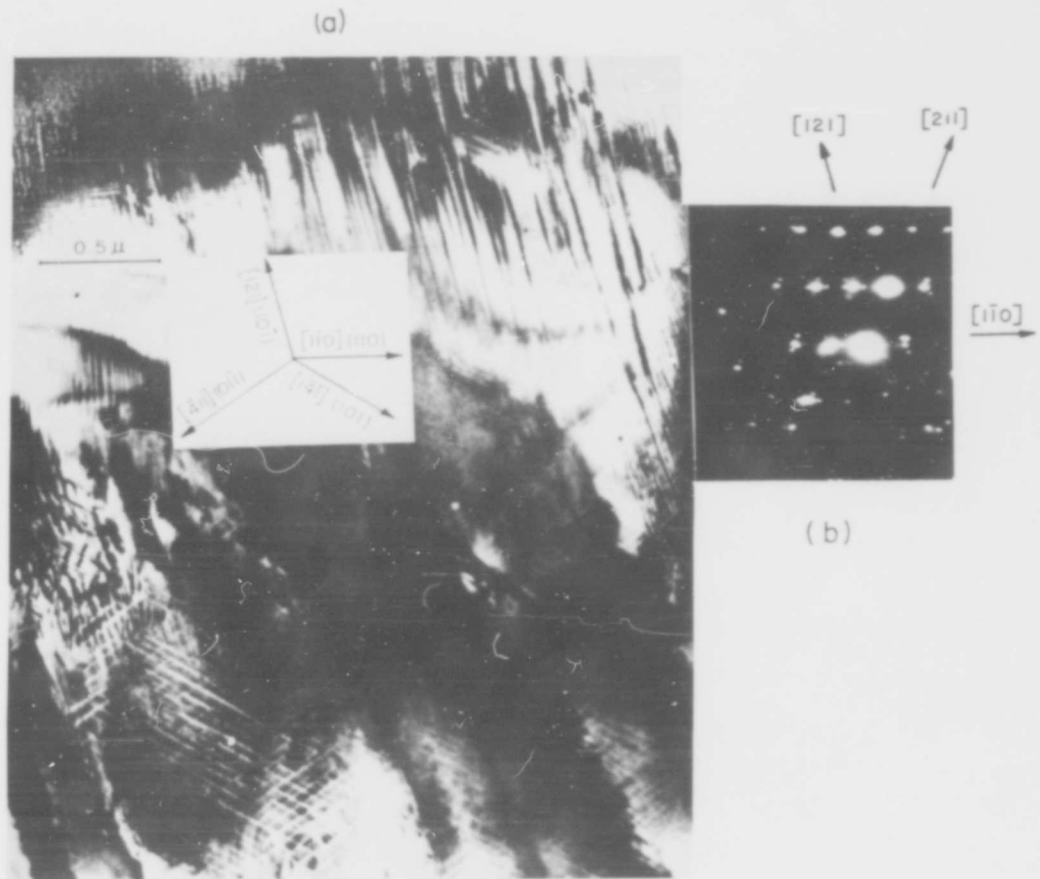


Fig. 77 - Dependence of shear strain upon direction on (101) slip plane.



(a) THE ORIENTATION OF THE FOIL IS $(11\bar{3})$. THE ACTIVE $\{110\}$ SLIP PLANES AND THE DIRECTIONS OF THEIR INTERSECTION WITH THE FOIL ARE MARKED.
 (b) SELECTED AREA DIFFRACTION.

Fig. 78 - Dislocation structure in tantalum after yielding.

- a) strain accumulation on two different slip systems in the pre-yield or microstrain stage,
- b) strain relaxation on the first active slip system and concurrent build-up of strain on the second active slip system, the yield drop being associated with the strain relaxation on the first active slip system.

For body-centered cubic metals, it is well established that under the influence of an applied stress, screw dislocations will from time to time cross-glide off their primary glide plane onto a secondary plane⁽³⁾. The dislocation structure formed is characterized by dislocation junctions, superjogs, pinched-off dislocation loops and dislocation tangles; all of which are expected to create a long-range stress field affecting other slip systems. Conversely, it can be assumed that the strain field is temporarily relaxed through the action of another slip system, so that internal barriers formed on the primary slip system are overcome and circumvented by cross-slip activated by the long-range stress field of the secondary slip system. Impurity atoms may, of course, influence the strain distribution in the slip plane by pinning the dislocations as postulated by Cottrell⁽²⁾. However, this pinning effect is believed to have an indirect effect on yielding.

In support of the concepts on yielding developed in this investigation, it is noteworthy that recent metallographic studies of zone-refined tantalum crystals by Rose et al⁽⁴⁾ have shown a marked orientation dependence of both slip activity and yield phenomena. For example, it was found that single crystals of (111) and (100) orientations do not exhibit discontinuous yielding, whereas the (110) orientation does.

B. Strain Analysis Associated with Ductile-Brittle Transition of Tungsten Crystals

1. Scope

The use of strain analyses based on x-ray divergent beam data appears to offer a fruitful approach for studying the mechanism of ductile-brittle transition in refractory metals. If the strain distribution for various slip planes can be determined as a function of deformation and temperature it is possible that a better understanding of the relation of slip interaction processes and the ductile-brittle transition would result. In line with this objective, a preliminary study was made of single crystals deformed in compression at two temperatures by means of the x-ray divergent beam method.

2. Experimental Procedure

Several compression specimens were prepared from a 10-inch long, 0.2 inch diameter single tungsten crystal (W-E5), using the Servomet spark cutter to attain a near triangular prism shape with side dimensions of 0.15 inch and a height of 0.5 inch. The specimens were subsequently electropolished to remove any lattice distortion introduced by the shaping operation.

Compression of the specimens was carried out on the Instron machine at -195°C and at 185°C . The x-ray divergent beam patterns obtained from the undeformed crystals served as standards for the strain analysis of the deformed specimens.

3. Preliminary Results of the X-Ray Study

Fig. 79 shows a back-reflection divergent beam pattern of the specimen compressed 0.48% at -195°C by a stress of 118 psi. A subsequent increase of only 10% in stress resulted in brittle fracture. With the exception of slight dilatations of one or two ellipses, the diffraction pattern of Fig. 79 is exceedingly sharp and does not exhibit any break-up of the line pattern into segments. No appreciable broadening of the $K\alpha_1$ and $K\alpha_2$ lines occurred, and consequently the $K\alpha$ doublet pattern is distinctly resolved.

Fig. 80 shows a divergent beam pattern of the specimen compressed 7.8% at 185°C by a stress of 90 psi. In contrast to Fig. 79 the pattern of Fig. 80 exhibits strong distortions for virtually every ellipse, i. e. for every set of reflecting (hkl) planes. The pattern is blurred, contains displaced line segments and the $K\alpha$ doublet is totally unresolved. At 185°C , considerable plastic deformation occurred and the strain introduced is distributed over many slip planes.

Based on these preliminary results, it appears that as the deformation temperature is decreased, the number different slip planes decreases. Whether this occurs continuously or discontinuously remains to be determined.

C. Improvement of the Precision of the Strain Analysis

1. Scope

Since the strain analysis is based on $\frac{\Delta d}{d}$ values measured by the x-ray divergent beam method, the precision that can be achieved by the analysis depends primarily on the precision with which the $\frac{\Delta d}{d}$ values can be measured. Consequently it was considered highly desirable to improve the precision of these measurements.

2. Precision of X-Ray Measurements

Referring to Fig. 81 it can be seen that each ellipse of the divergent beam pattern corresponds to a reflection from a definite (hkl) set of planes. Based on the film distance from the x-ray source (a), the specimen distance to the x-ray source (b), and measurements of the major axis of the ellipse, the spacing of the corresponding (hkl) reflection can be obtained⁽⁵⁾. Precise determination of these d-spacings is greatly dependent on the accurate determination of the parameters a and b. Two methods have been developed to accomplish this: a) internal calibration and b) multiple exposure.

According to the first method, a thin quartz crystal is placed in front of the test crystal for the purpose of internal calibration. Thus patterns of both the quartz and the test crystal are simultaneously recorded on the film. In this way, the lattice parameter of the quartz crystal, which is known very accurately, can

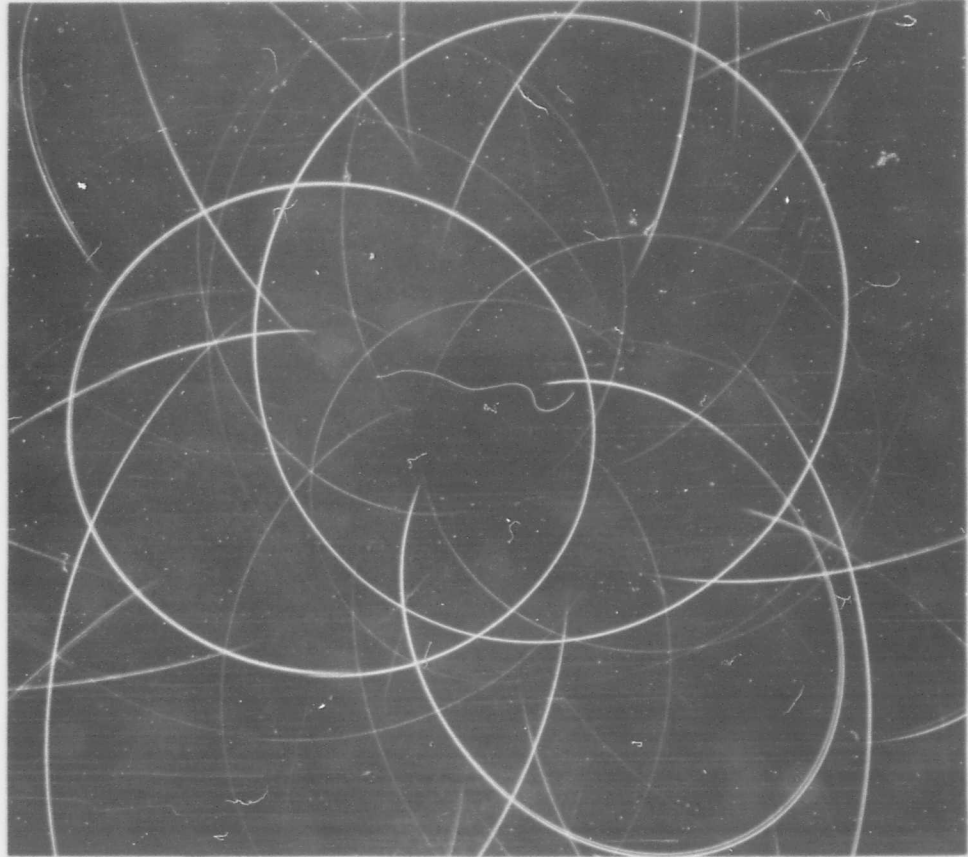


Fig. 79 - Divergent beam pattern of tungsten crystal compressed at -195°C
($\epsilon = 0.48\%$).

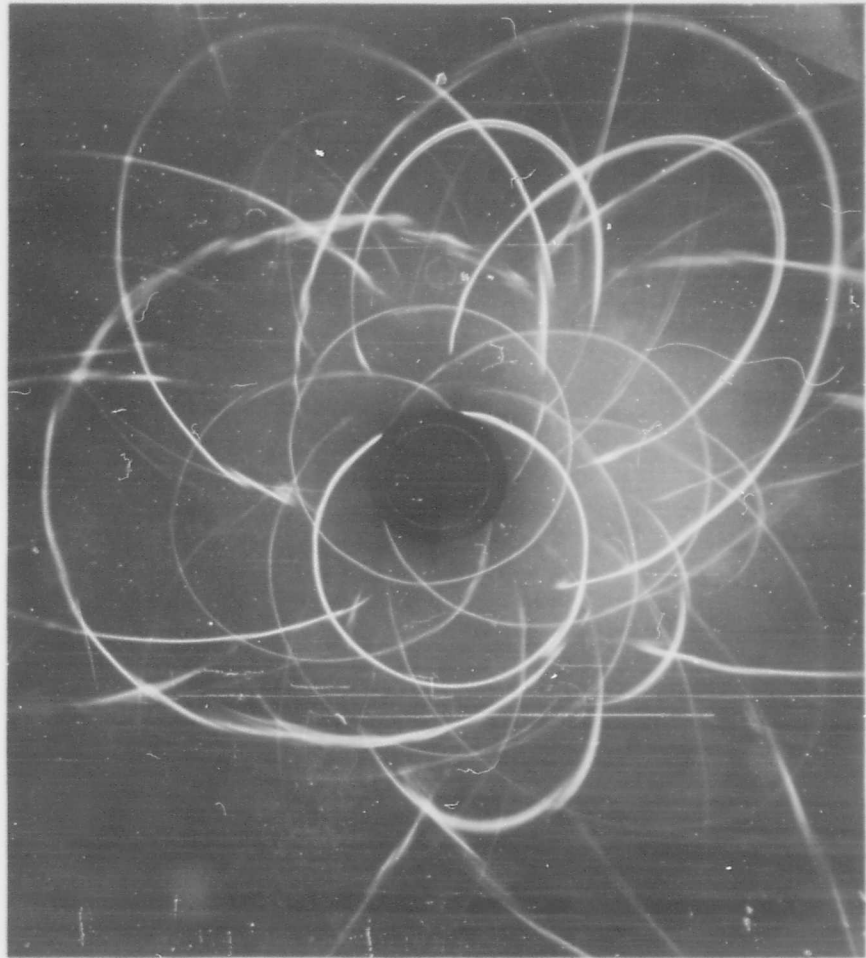


Fig. 80 - Divergent beam pattern of tungsten crystal compressed at 185°C
($\epsilon = 7.8\%$).

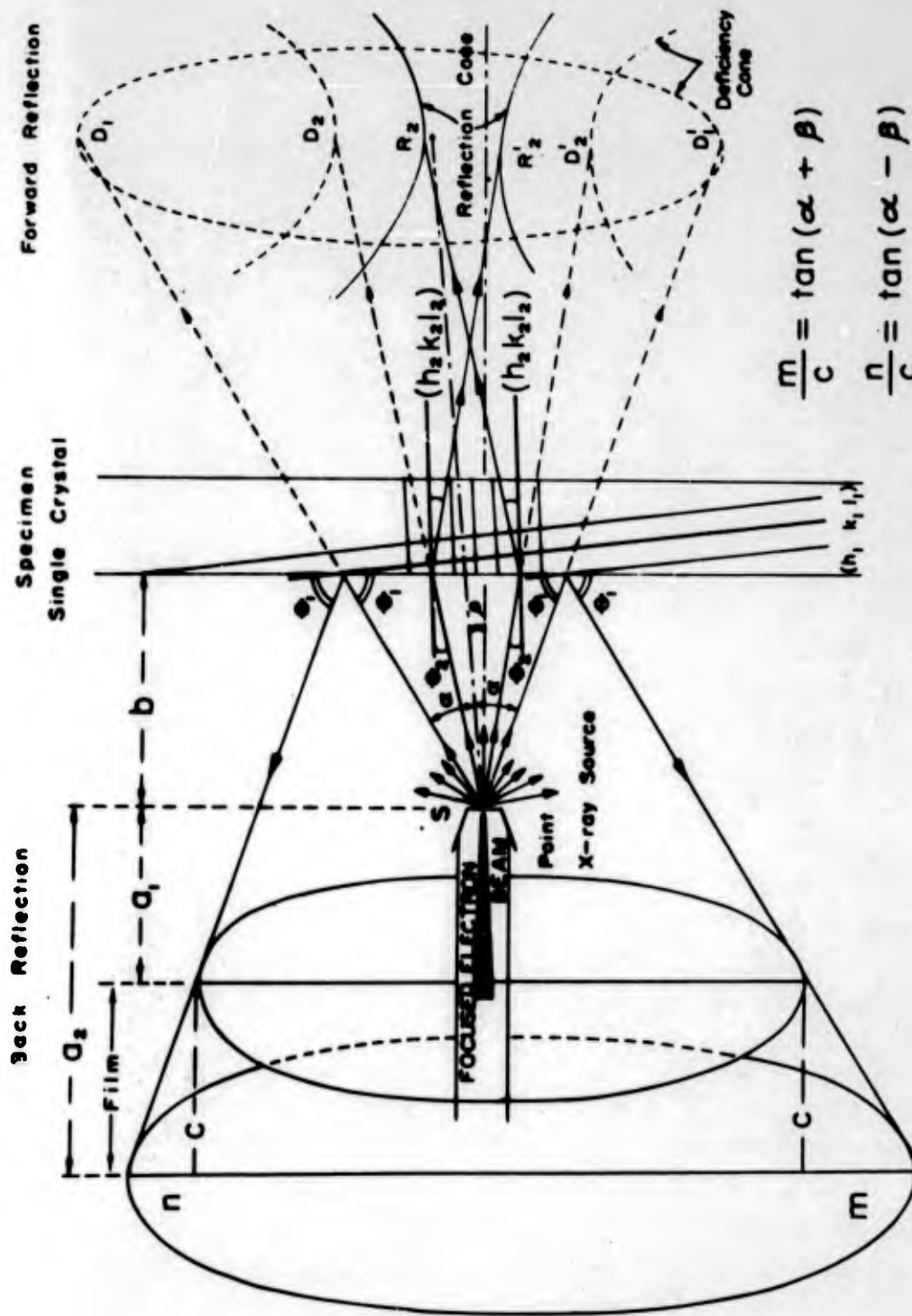


Fig. 81 - Schematic representation of the generation of pseudo-kossel patterns by the divergent beam method.

be used for the precise determination of the specimen-to-film distance ($a + b$). Application of this method leads to a precision of strain measurement of ± 0.0002 (strain units).

Recently, the multiple exposure method was developed, which is simpler and gives the same degree of precision. In this method, the divergent beam patterns are recorded on the same film at different specimen-to-film distances as shown in Fig. 8; and the diffraction angle θ of the (hkl) reflection is directly determined from the precisely known distances between consecutive film positions. Defining β as the angle between the optical axis of the capillary x-ray tube and the normal of the diffracting (hkl) planes, α as equal to $90^\circ - \theta$, m and n as the distances of the corresponding points on the elliptical pattern recorded at film positions a_2 and a_1 respectively, and c as equal to $a_2 - a_1$; then the following relationships hold:

$$m/c = \tan(\alpha + \beta) \quad (1)$$

$$n/c = \tan(\alpha - \beta) \quad (2)$$

From these two equations α and therefore θ and $d(hkl)$ can be determined directly if m and n are known. The latter parameters are directly obtained from measurements of the different film positions, which can be determined with great accuracy by the use of precision spacers. By this method, the difficulty in measuring a and b values can be avoided.

References

- (1) Imura, T., Weissmann, S., and Slade, J. J., Jr., "A Study of Age-Hardening of Al-3.85% Cu by the Divergent X-Ray Beam Method," *Acta Cryst.*, 15 (1962) 786.
- (2) Cottrell, A. H., "Plastic Deformation of Metals," Report of Conference held in Pittsburgh, Pa., by Carn. Inst. Techn. and O. N. R., Washington (1950).
- (3) Keh, A. S., and Weissmann, S., "Deformation Substructure in Body-Centered Cubic Metals," Symposium on Electron Microscopy and Strength of Crystals held in Berkeley, Cal., (1961) Interscience Publishers (in press).
- (4) Ferriss, D. P., Rose, R. M., and Wulff, J., "Deformation of Tantalum Single Crystals," *Trans. AIME*, 224 (1962) 975; "Yielding and Plastic Flow in Single Crystals of Tungsten," *ibid.*, 981.
- (5) Lement, B. S., et al., "Substructure and Mechanical Properties of Refractory Metals," WADD Technical Report 61-181, Part II (1962).

VII. YIELD PHENOMENA IN REFRACTORY METALS - Work carried out at the University of Liverpool by W. S. Owen, D. Hull, C. L. Formby, I. D. McIvor and A. R. Rosenfield.

A. Scope

The primary objective was to determine the mechanism by which yielding and flow occurs in refractory metals. The work is conveniently subdivided into the following studies:

- a) Dislocation-interstitial binding energies.
- b) The strain-aging of a dilute tantalum-oxygen alloy.
- c) The variation of flow stress with dislocation density in tantalum.

B. Dislocation-Interstitial Binding Energies

1. Introduction

According to Friedel⁽¹⁾, the binding energy W_M between a dislocation and an interstitial atom is

$$W_M = G(c) - G_0(c) \quad (1)$$

where $G_0(c)$ is the free-energy per interstitial atom dissolved in a perfect lattice and $G(c)$ the corresponding free-energy when the lattice contains dislocations. In general, there are two ways of measuring W_M : either the solubility of the interstitial element may be measured as a function of temperature and dislocation density⁽²⁾, or the yield drop may be measured as a function of temperature for a specimen of known interstitial content and dislocation density. The latter method depends upon the assumption that the equilibrium concentration of interstitial atoms at a dislocation line varies with temperature according to the relation⁽³⁾

$$C = C_0 \exp(-W_M/kT) \quad (2)$$

where C_0 is the concentration when there is no segregation. Above some temperature T_b , C falls below the saturation value C_m at which the Petch locking parameter k_y is just greater than zero. Thus for $k_y = 0$,

$$W_M = k T_b \ln (C_0/C_m) \quad (3)$$

The value of C_m is somewhat uncertain as it depends on the precise model which is assumed for the unpinning of a dislocation line under the action of an applied shear stress. Estimates vary between 0.07 and 1.0. Fortunately, the value of W_M determined by this method is quite insensitive to variations in the value adopted for C_m .

Usually T_b has been determined by finding the temperature at which the discontinuous yield disappears in tensile tests carried out at successively higher temperatures. However, the conditions existing during tests at elevated

temperatures do not satisfy the requirements of equation 3 and the values of W_M deduced from them are erroneous. Yield points are observed at low temperatures because dislocations can move under the influence of an applied stress faster than interstitial atoms can diffuse. As the testing temperature is raised, the temperature dependence of the dislocation velocity is less than that of the diffusivity and at a particular temperature (and strain rate) the impurity atoms move with about the same velocity as the dislocations, producing the blue-brittleness (serrated yielding) phenomenon. This fact has been used to calculate the activation energy for interstitial diffusion⁽⁴⁾. The discontinuous yield point disappears at a temperature just above the blue-brittleness temperature because the interstitial atoms become sufficiently mobile to be dragged along with the moving dislocations. Therefore, the disappearance of a yield drop does not indicate the absence of segregated interstitial atoms.

The temperature T_b for iron-carbon alloys is widely quoted as 700°K ⁽⁵⁾, but this was obtained from the high temperature tensile tests of Boulanger⁽⁶⁾ and consequently the value of W_M deduced from it is incorrect. To determine T_b it is necessary to carry out all the tensile tests at a temperature below the blue-brittleness temperature. Thus, a series of specimens must be quenched from successively higher annealing temperatures at a rate sufficient to freeze-in the interstitial distribution. The experimental difficulties are considerable since it is necessary to ensure a) that there is no contamination of the specimen during the annealing and quenching, and b) that either the dislocation density is unaffected by the annealing or that the density corresponding to each annealing temperature is known. However, a number of determinations of W_M for different systems have been reported. This information with the limited data available from measurements of solubility as a function of dislocation density are given in Table 16. When calculating W_M from T_b as determined by the quenching method, the usual practice is to take C_m as one atom per atomic plane intersecting the dislocation.

2. Experimental

The value of W_M for tantalum-oxygen shown in Table 16 was determined experimentally by the quenching method. The apparatus and experimental procedure are described in the previous summary report⁽⁷⁾. The technique was improved by replacing the tap used to isolate the vacuum pumps from the quenching liquid by a water trap. Larger capacity vacuum pumps were substituted for those used originally. In the present series of experiments, the pressure was less than 10^{-5} mm Hg (as measured by an ionization gauge) at all times during the outgassing and annealing of the specimen.

All specimens were annealed at 1300°K to establish a constant grain size and dislocation density. One specimen was cooled slowly to room temperature. The others were cooled to selected temperatures below 1300°K , held for a few minutes and then quenched in brine. All the specimens were held for 15 minutes at room temperature before testing.

The variation of k_y , obtained from the room temperature stress-strain curves by the extrapolation method⁽²²⁾, with quenching temperature for Ta-E2 (50 ppm oxygen) is shown in Fig. 82. The value of k_y decreases from the value of the slowly-cooled specimen to a minimum at 1000°K . Specimens

Table 16

Measured and Calculated Binding Energies

<u>System</u>	<u>Reference</u>	<u>W_M(Measured)</u> e. v.	<u>W_{M1}(Calculated)</u> e. v.	<u>W_{M2}(Calculated)</u> e. v.
Fe-C	(23)	0.80*	0.76	0
Fe-N	(24) (19)	0.73* 0.71*		
Fe-(C,N) average	(52)	0.85*		
Ta-O	(25)	0.54	0.44	+0.10

* Average value for Fe-systems is 0.76 ± 0.08 e. v.

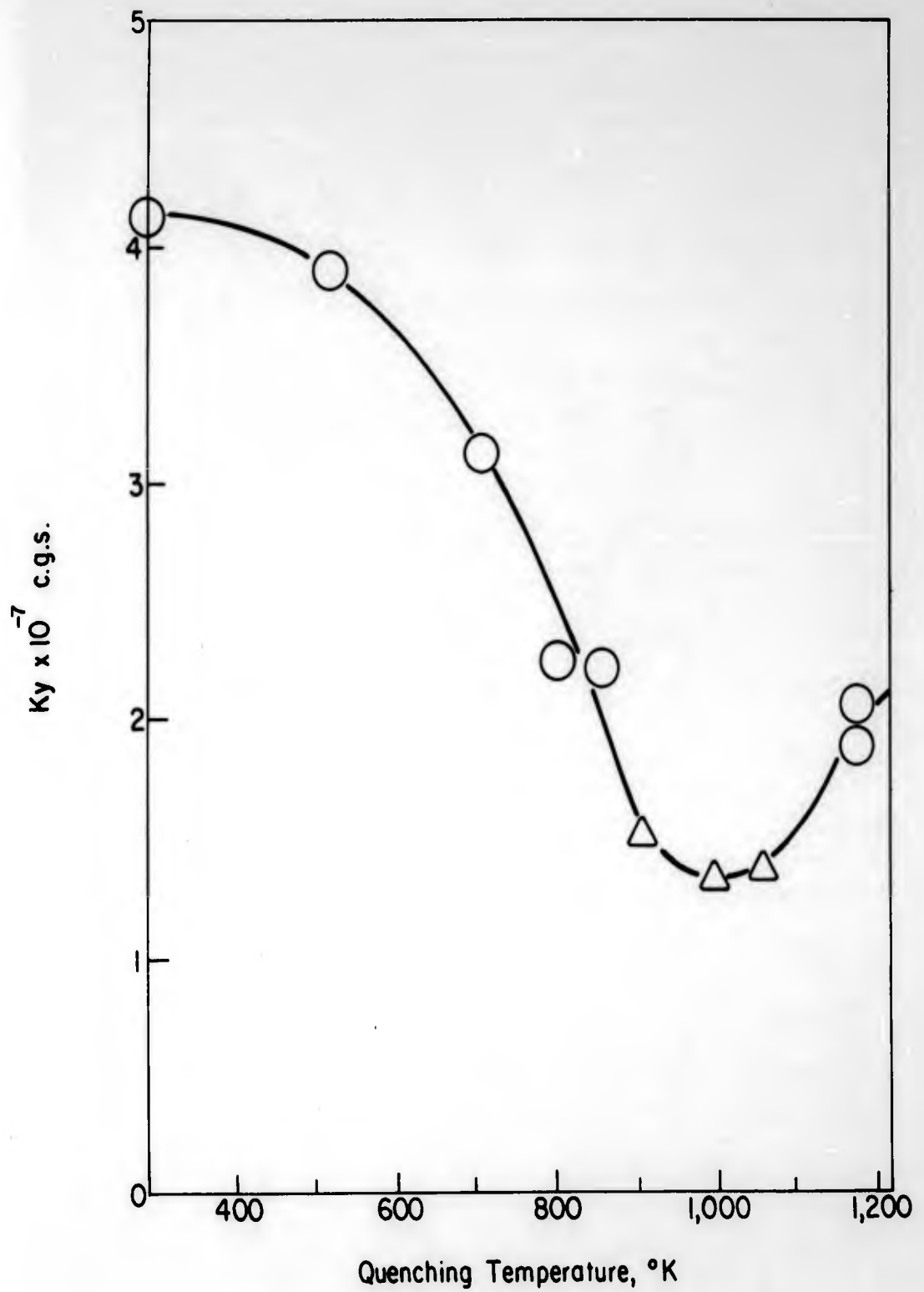


Fig. 82 - Ta-E2 annealed 1300°K . Variation of k_y with quenching temperature.

quenched from temperatures between 900° and 1100°K did not exhibit a discontinuous yield or a Luders plateau, but the value of σ_i obtained by extrapolation of the work-hardening portion of the stress-strain curve is less than the proportional limit. The small positive values of k_y obtained from these data are shown as triangular points in Fig. 82. T_b was taken as the minimum temperature (1000°K) and W_M is 0.54 e.v. (Table 16). On quenching from temperatures above 1100°K, k_y was found to increase. Initially, this was thought to be due to contamination of the specimen during the period immediately after the closure of the isolation tap when the chamber pressure increased, but the effect persisted after the apparatus was modified to eliminate the pressure rise. Although it seems improbable, the anomalous increase in k_y may be due to contamination by the quenching medium.

A parallel series of experiments were carried out using Ta-E1 (150 ppm oxygen) and the general features of the results are similar to those for Ta-E2. In this series, the minimum value of k_y was only about half that of the slowly cooled specimen. It was concluded that the higher oxygen content of Ta-E1 accentuated the small effect due to the segregation of oxygen atoms to the dislocations either during the quench or during the 15-minute holding period at room temperature. This view was supported by the results of experiments with specimens of Ta-E2 (lower oxygen content) with a high dislocation density obtained by an initial anneal at 1100°K which is below the recrystallization temperature of this material. After quenching from 1000°K (the temperature for minimum k_y in Ta-E2), it was found that the extrapolated value of σ_i coincides with the proportional limit and k_y is zero. The minimum value of k_y for the Ta-E1 series occurs at 1100°K, giving the same value of W_M as that obtained from the Ta-E2 series.

3. Discussion

The binding energy W_M has two components, W_{M1} due to strain and W_{M2} due to electronic interaction between the dislocation and the interstitial atom. These energies are usually considered to be additive⁽¹⁾:

$$W_M = W_{M1} + W_{M2} \quad (4)$$

The electronic contribution to the binding energy in the iron-carbon and iron-nitrogen systems is zero because the carbon atom is not ionized, but in systems with appreciable solubility the electronic effect is probably significant. The heterogeneous strain field around an edge dislocation produces an electric dipole⁽²⁾ because electrons flow from the compressed region above the slip plane to the dilated region below. Thus, a net negative charge is created below the extra plane, which attracts positively charged ions but repels ions which carry a negative charge.

In general, the elastic-strain interaction energy is

$$W_{M1} = A/R \quad (5)$$

where A is an interaction parameter which varies with the elastic constants, the lattice parameter of the solvent, and the extent of the dilation of the lattice by the interstitial atom; and R is the distance between the interstitial atom and the geometric center of the dislocation. A can be estimated from the Cottrell-Bilby model⁽⁸⁾ or from refinements of this model due to Cochardt⁽⁹⁾.

The dilation caused by a carbon atom in an iron lattice can be estimated from the measured lattice parameter change of the martensite lattice with carbon content⁽⁸⁾. Similar calculations can be made from the lattice parameter change with increasing interstitial content for those alloy systems, such as tantalum-oxygen, which do not form martensite but which have appreciable solubility. It is usual to assume that R is one Burgers vector. The calculated values of W_{M1} are compared with the experimental values of W_M in Table 16. In iron-carbon alloys W_M and W_{M1} are identical, confirming the prediction that the interaction in these alloys is entirely due to elastic strain. However, in the tantalum-oxygen case, W_M is slightly greater than W_{M1} . Unfortunately, the value is very dependent upon the assumptions made of A . Thus, although estimates of this type are inevitably very crude, there appears to be grounds for suggesting that in tantalum-oxygen, and probably in similar alloys, there is a significant electronic contribution to the dislocation-solute interaction energy.

C. The Strain-Aging of a Dilute Tantalum-Oxygen Alloy

1. Introduction

Strain-aging in iron-carbon and iron-nitrogen alloys has been studied extensively⁽¹⁰⁾. The kinetics of the removal of the interstitial solute from solution appear to agree with the predictions of the Cottrell-Bilby⁽⁸⁾ model or a variation of it proposed by Harper⁽¹¹⁾. Solute segregates to the dislocations under the influence of the elastic strain field of the dislocation, and the rate of depletion of the solute can be measured by following the change in electrical resistivity⁽¹²⁾ or internal friction⁽¹³⁾.

On reloading a prestrained specimen, plastic flow starts at σ_p (Fig. 83); but after aging the re-loaded specimens yield discontinuously at a higher stress σ_y . The aging index $\Delta\sigma = \sigma_y - \sigma_p$ reflects the extent to which

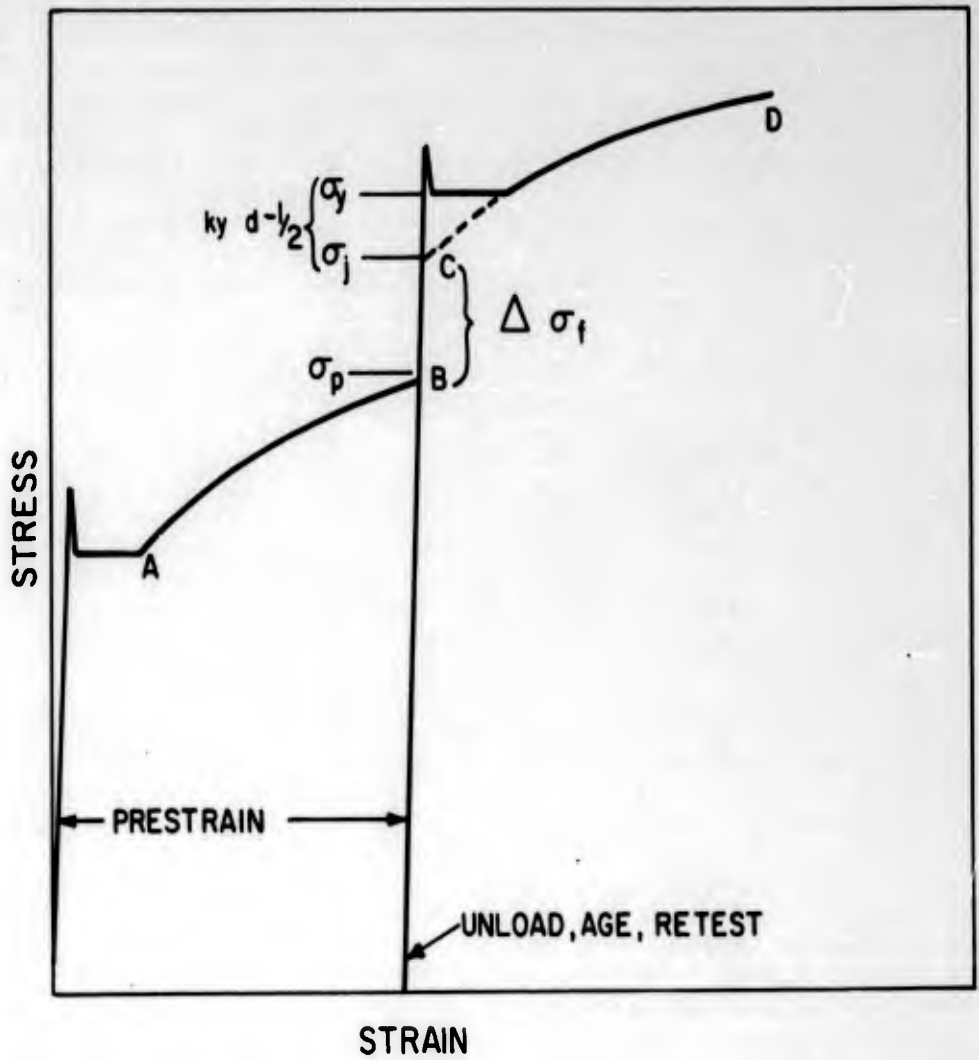


Fig. 83 - Schematic stress-strain curve for a prestrain, age and retest sequence.

the yield has returned. Until recently it was usual to assume that $\Delta\sigma$ is a result solely of the pinning of dislocations by the segregated solute atoms, i. e. σ_p and σ_j coincide and the strain hardening curves AB and CD are continuous. Thomas and Leak⁽¹³⁾ found the variation with aging time of $\Delta\sigma$ and the rate of depletion of solute as measured by internal friction to be parallel, which appeared to confirm these assumptions. However, similar work by Lautenschlager and Brittain⁽¹⁴⁾ failed to confirm the parallel kinetics of the segregation of solute and the increase in $\Delta\sigma$. A detailed study by Wilson and Russell⁽¹⁵⁾ of the change of $\Delta\sigma$ with aging reveals the reason for the latter result. Although during the early part of aging the increase in $(\sigma_y - \sigma_j)$ is parallel to the increase in $\Delta\sigma$, $(\sigma_y - \sigma_j)$ eventually reaches a saturation value; and the subsequent change is due to increasing σ_j . They concluded that the increase in σ_j is due to long-range lattice strains produced by solute atom clusters or precipitates. A small increase in σ_j , attributed to the Snoek effect, was also observed at a very early stage of aging⁽¹⁶⁾.

The Cottrell-Bilby concept of the discontinuous yield, the unpinning of segregate locked dislocations, appears to describe adequately the behavior of alloys in which there is only weak pinning⁽¹⁷⁾. However, it is clear that the existing dislocations become immobilized quite early in the aging process, and then yielding occurs by the generation of new dislocations from grain boundaries or some other source⁽¹⁸⁾. Thus, the assumption that the aging index, $\Delta\sigma$, is a continuous function of the extent of solute segregation does not seem to be warranted.

Neither the kinetic nor the yield-point aspects of strain-aging in b. c. c. metals other than iron have received much attention. Tantalum-oxygen appears to be a particularly suitable alloy to study. Oxygen is highly soluble in tantalum (the solubility limit at 500°C being about 2000 ppm) so that in dilute alloys no precipitates are formed and the possibility of a change in σ_j by dislocation-precipitate interaction is excluded. Since ordered tantalum oxides based on the tantalum lattice⁽¹⁹⁾ form in concentrated alloys, there seems little possibility of oxygen clusters forming in the dilute alloys. Studies of the decrease of the discontinuous yield on quenching from successively higher annealing temperatures have shown that the dislocation-oxygen binding energy in tantalum is at least as great as that for dislocation-carbon interaction in iron⁽²⁰⁾. At the usual aging temperatures, diffusion of oxygen in tantalum is slower than carbon or nitrogen⁽²¹⁾ in iron. Consequently aging proceeds relatively slowly, enabling the early stages to be examined more easily. However, oxygen diffuses much more rapidly than the other interstitial impurities likely to be present in tantalum, and therefore aging by carbon or nitrogen is unlikely to interfere⁽²¹⁾.

2. Experimental

Cold-drawn 0.030 inch diameter wire specimens were annealed for 6 minutes at 1050°C in a vacuum better than 10^{-5} mm Hg (baked glass apparatus with a negligible leak rate) to establish a grain size of $d^{-1/2} = 5.0 + 0.5 \text{ mm}^{-1/2}$, where $2d$ is the mean grain diameter. After this treatment the tantalum (alloy Ta-E1) was found to contain 149 ppm oxygen, 28 ppm carbon and 6 ppm nitrogen. All specimens were prestrained 10% in tension at either 293°, 232° or 195°K,

and all were aged at $100 \pm 1^\circ\text{C}$. Tensile testing was carried out at either 293° , 232° or 195°K in a Polyani machine at a strain rate of $4.5 \times 10^{-4} \text{ sec}^{-1}$. The stress measurements are accurate to within 1% and a strain of 2×10^{-4} could be detected(22).

For each combination of prestrain and test temperature, $\Delta\sigma$ was determined as a function of aging time. Wilson and Russell(15) found $(\sigma_y - \sigma_j)$ by employing the Petch(23) relationship:

$$\sigma_y = \sigma_i + k_y d^{-1/2} \quad (7)$$

where k_y is the locking parameter given by the variation of σ_y with $d^{-1/2}$. σ_j can be identified with σ_i (24) and

$$\sigma_y - \sigma_j = k_y d^{-1/2} \quad (8)$$

In the present experiments, σ_j , and hence k_y , was found by the logarithmic extrapolation method(22). The post-Lüder's strain-hardening curve is fitted to

$$\sigma = K \epsilon^n \quad (9)$$

where K is a strength constant, ϵ the total strain, and n the strain-hardening index. In these experiments, the linear $\log \sigma$ versus $\log \epsilon$ plot was extrapolated to the prestrain, ϵ_p . It has been demonstrated experimentally, that for an alloy with approximately the same content as that used in the present series of experiments there is excellent agreement between the values of k_y and σ_j obtained by the two methods(22). The change in σ_j with aging time was expressed as $\Delta\sigma_f = \sigma_j - \sigma_p$. When the prestrain and test temperatures were different, σ_p at the test temperature was taken to be the value of σ_j at very short aging times.

3. Results and Discussion

The strain-hardening index n at different testing temperatures is plotted as a function of aging time in Fig. 84. For specimens prestrained and tested at the same temperature, n passes through a minimum value after about ten minutes aging. The effect is small but probably greater than the experimental error. Data for specimens prestrained and tested at different temperatures are also plotted. Although increased scatter was encountered, there is no indication that n is affected by the prestrain temperature.

The initial decrease in n has not been reported previously, but Szkopiak(25) has found that in columbium after short aging times there is a decrease in total elongation, and since n is equal to the true strain at the maximum engineering stress it would seem that n was decreasing with aging time. Wilson and Russell(12) found that in iron-carbon alloys n increases with aging time to a maximum value; but the effect is small, the maximum increase being about 0.05. Although n for tantalum-oxygen aged at 100°C increases with aging times greater than 10 minutes, the value does not rise above the value for the

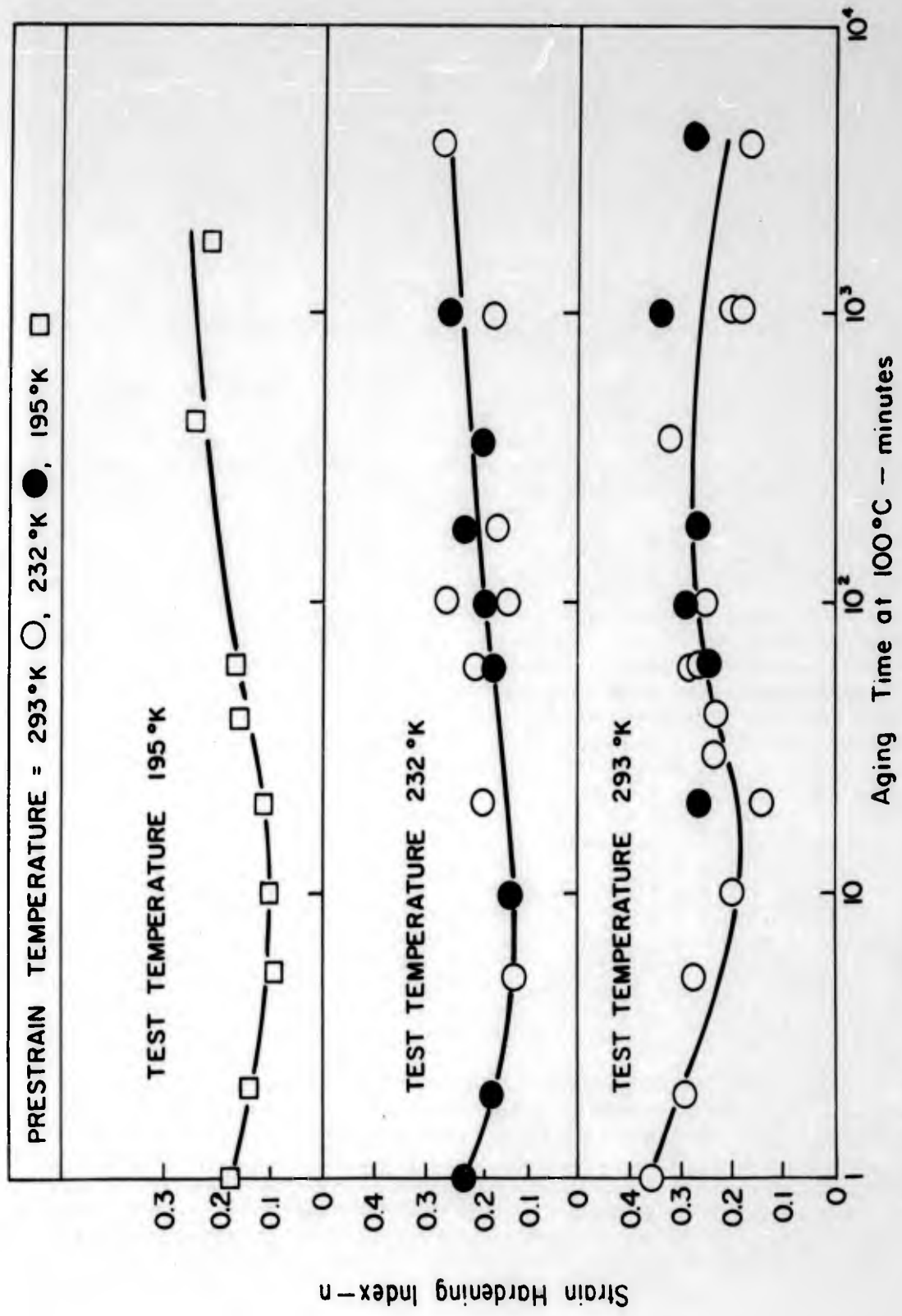


Fig. 84 - Strain-hardening index as a function of aging time.

unaged specimen in 5×10^3 minutes and there is no clear evidence of a maximum. In the absence of any generally accepted quantitative theory of strain-hardening in b.c.c. metals, speculation about possible mechanisms producing the small variation of n with aging time is not warranted.

When specimens are prestrained and tested at the same temperature, k_y starts to increase after about 60 minutes aging and then quickly reaches a plateau value (Figs. 85, 86 and 87). At the lowest testing temperature, σ_j increases before there is any detectable change in k_y ; but at the highest temperature, the two effects are initiated at about the same aging time. The maximum value of σ_j is not reached after 5×10^3 minutes aging, and the changes in σ_j and k_y are not parallel. The parameter k_y reaches the plateau value at each testing temperature after about the same aging time, but the time required for $\Delta\sigma_f$ to attain 1.0 Kg mm^{-2} decreases with testing temperature. Testing at 293°K , $\Delta\sigma_f$ attains this value several hours after k_y has reached the plateau; at 252°K , the k_y plateau and $\Delta\sigma_f = 1.0 \text{ Kg mm}^{-2}$ are achieved by aging for about the same time; and at 195°K , $\Delta\sigma_f$ reaches 1.0 Kg mm^{-2} after aging for a time which results in only a very small change in k_y . Thus, changes in σ_j and k_y are not related. This contrasts with the aging behavior of iron-carbon alloys, in which σ_j remains unchanged until after k_y has reached its maximum value⁽¹⁶⁾. It was found that k_y produced by aging tantalum-oxygen for the longest time used in these experiments appears to be weakly temperature dependent, the value being about 50% higher at 195° than at 293°K . However, the experimental scatter is too great to allow the dependence to be established quantitatively. The discontinuous yield in this material after slow cooling from the annealing temperature corresponds to a k_y value at 293°K about 7 times larger than that attained by aging for 5×10^3 minutes at 100°C , but the percentage variation with testing temperature is about the same⁽²²⁾.

When prestrained and tested at different temperatures the change in $\Delta\sigma_f$ with aging time at 100°C is strikingly different from that observed when the prestrain and test temperatures are the same. The results of prestraining at 232°K and testing at 293°K are compared with those obtained when the temperatures are reversed (Figs. 88 and 89). In neither case was $\Delta\sigma_f$ after aging for 5×10^3 minutes found to be as large as at the same test temperature in the first series of experiments. On testing at 293°K , prestraining at a lower temperature (232°K) causes the start of the increase in $\Delta\sigma_f$ to occur at shorter aging time than for specimens prestrained at 293°K (Fig. 86). When the test temperature is 232°K , prestraining at a higher temperature (293°K) produces the same effect in a more exaggerated form (Fig. 89). However, although $\Delta\sigma_f$ is markedly affected by the choice of prestrain and aging temperature, k_y is insensitive to these variables, i. e. the aging time at which k_y starts to increase and the plateau value being independent of the prestrain temperature.

Figs. 90a and 90b show the difference in dislocation density on straining Ta-E4 (an alloy of similar in composition to Ta-E1) 7 - 7.5% at 293°K and 240°K . The only important effect relative to the segregation concept is the difference in dislocation density. Even at the lowest prestrain temperature (195°K), the dislocation density after straining 10 percent is about $2 \times 10^{10} \text{ cm}^{-2}$, requiring an oxygen concentration of only 11 ppm for segregation of one atom per atom plane intersecting the dislocation line. The oxygen content of alloy Ta-E1 is greatly

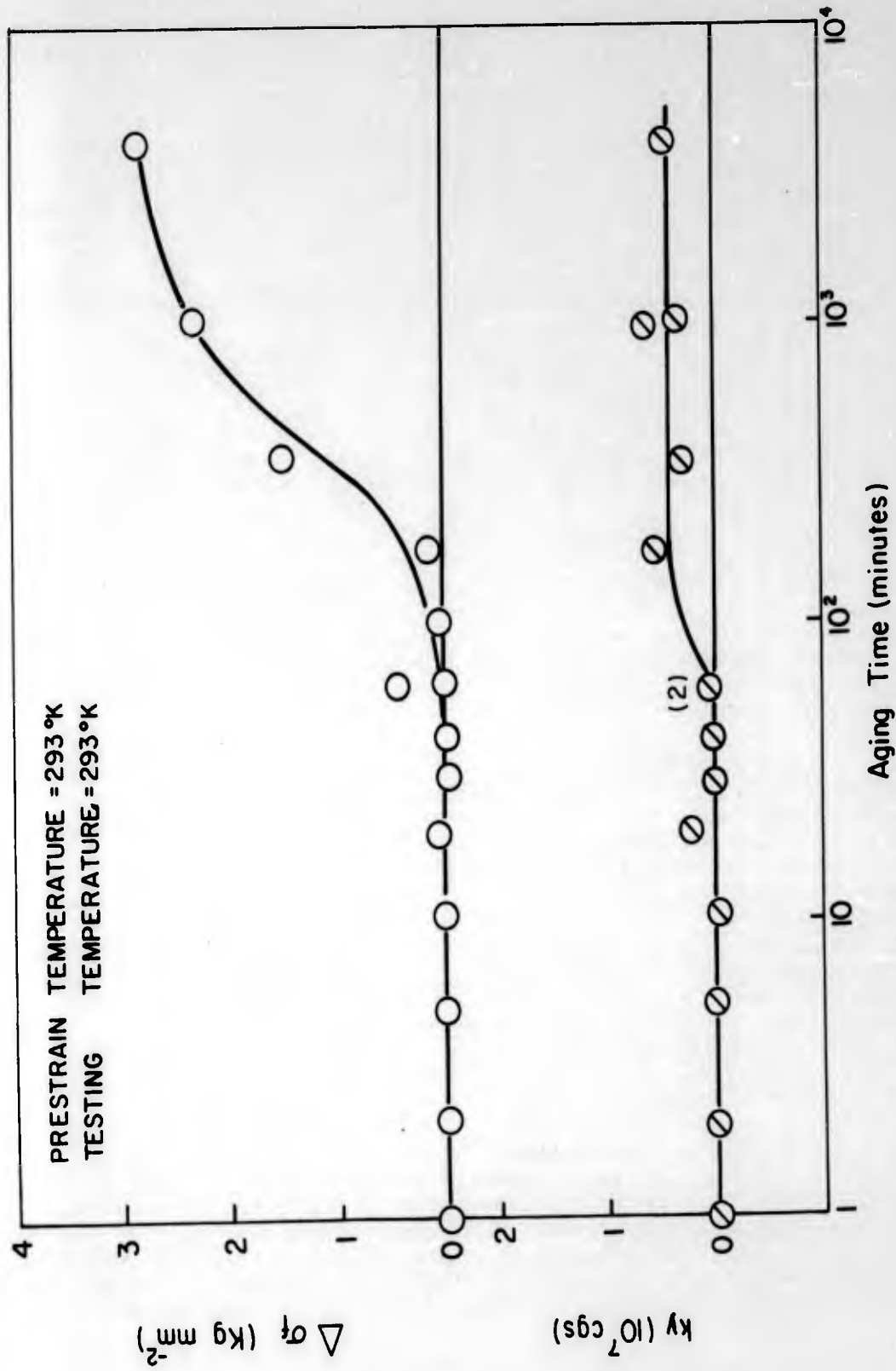


Fig. 85 - $\Delta\sigma_f$ and k_y as a function of aging time at 100°C. Prestrained and tested at 293°K.

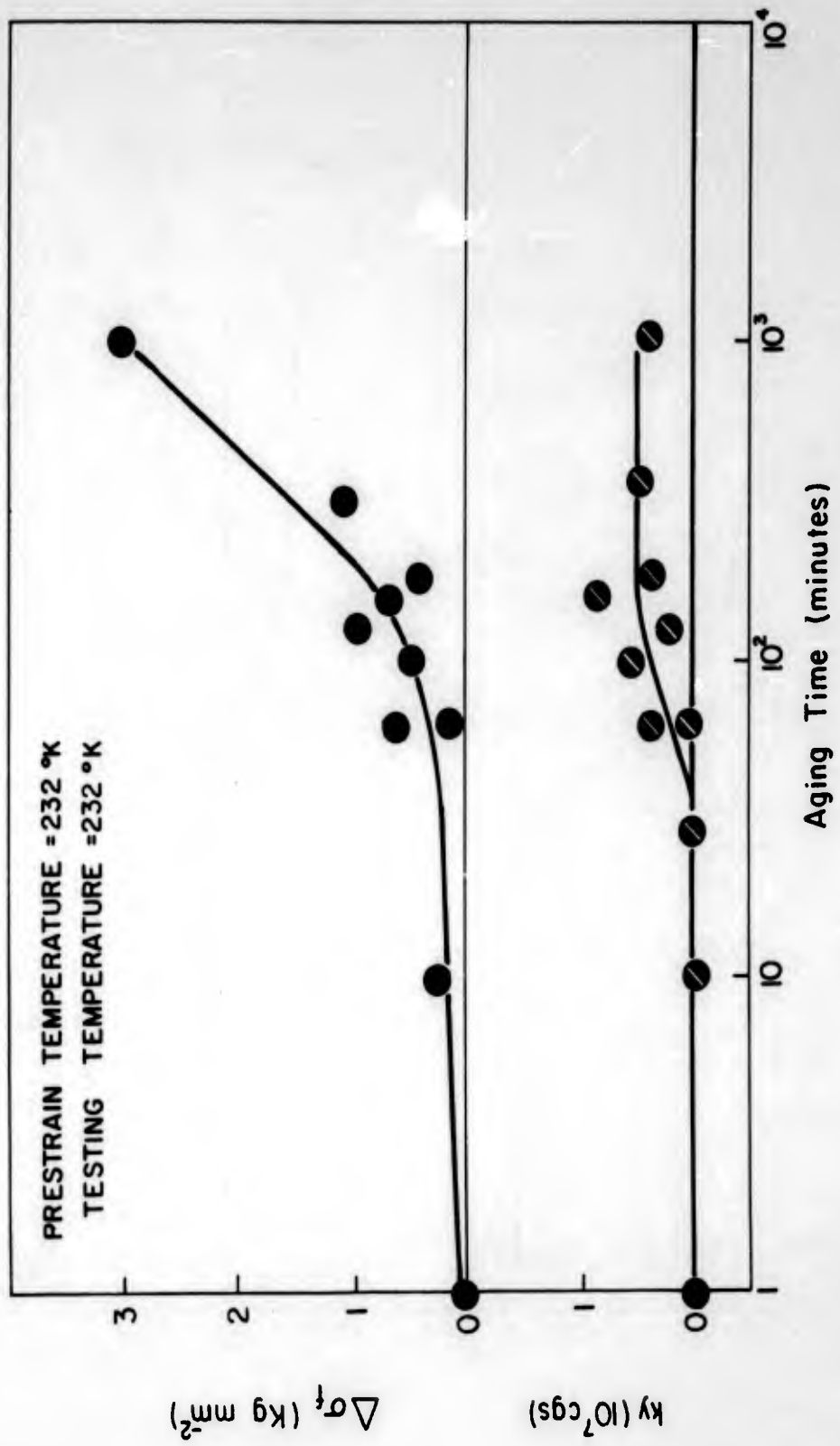


Fig. 86 - σ_f and k_y as a function of aging time at 100°C. Prestrained and tested at 232°K.

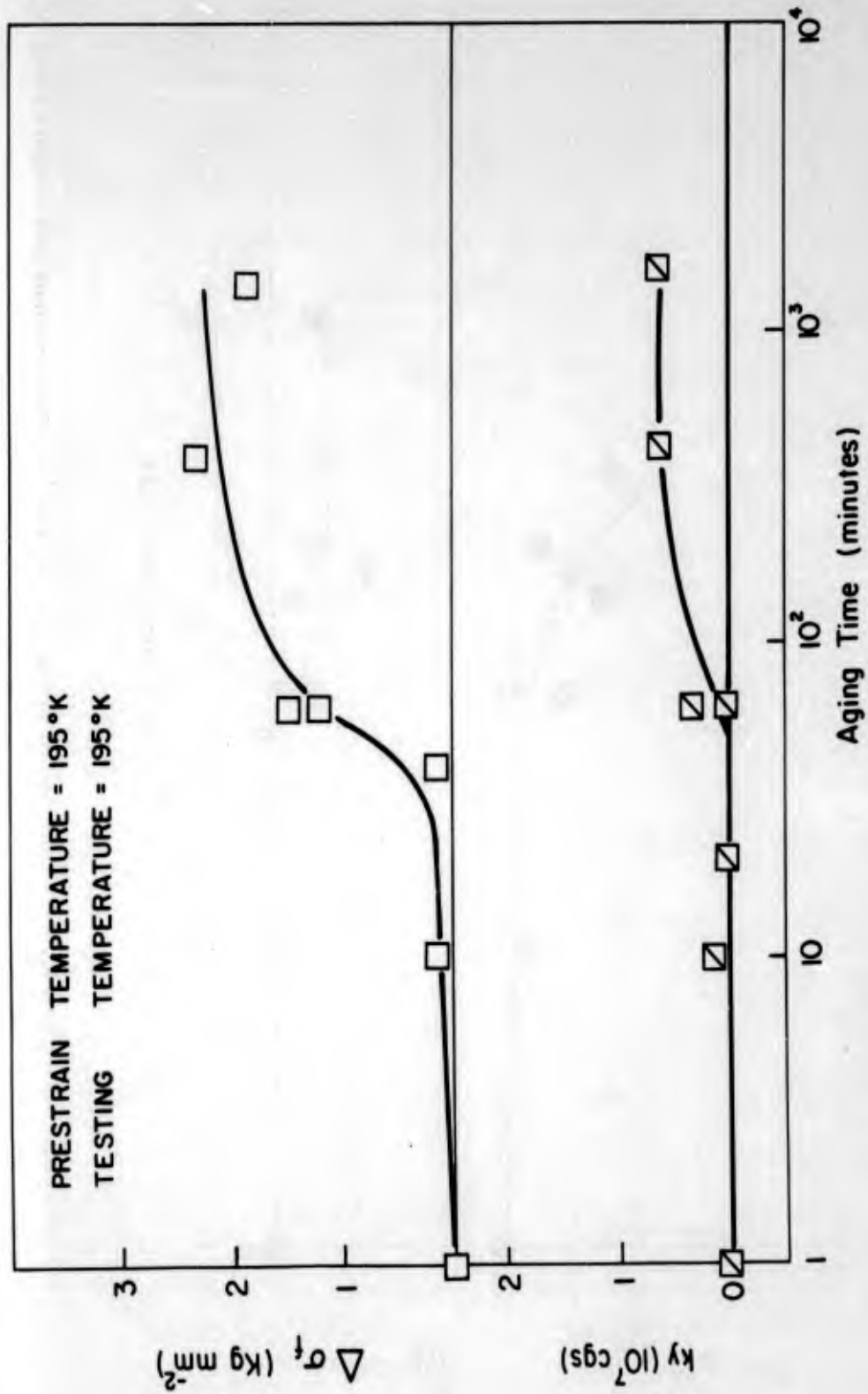


Fig. 87 - $\Delta\sigma_f$ and k_y as a function of aging time at 100°C. Prestrained and tested at 195°K.

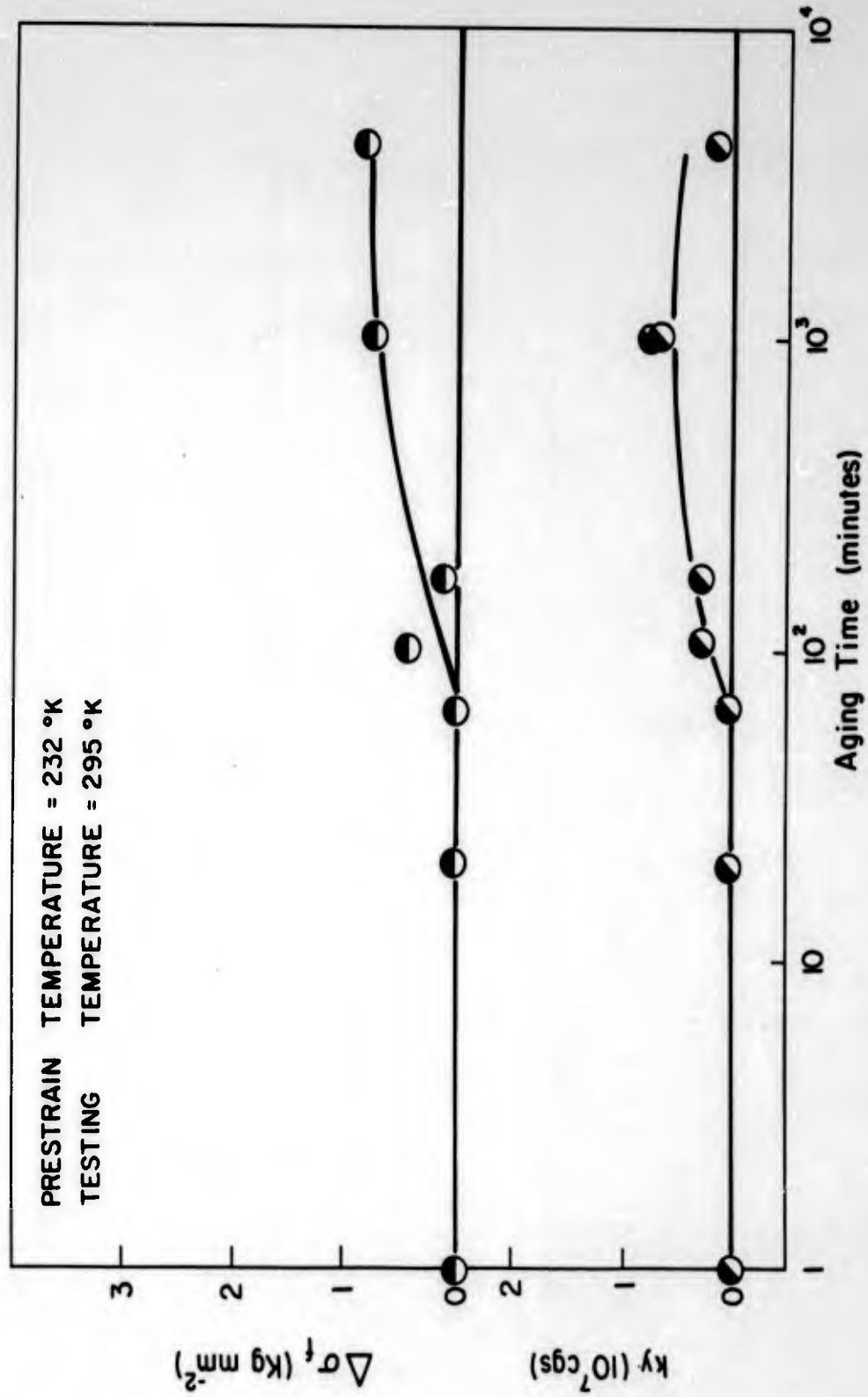


Fig. 88 - σ_f and k_y as a function of aging time at 100°C. Prestrained 293°K, tested 295°K.

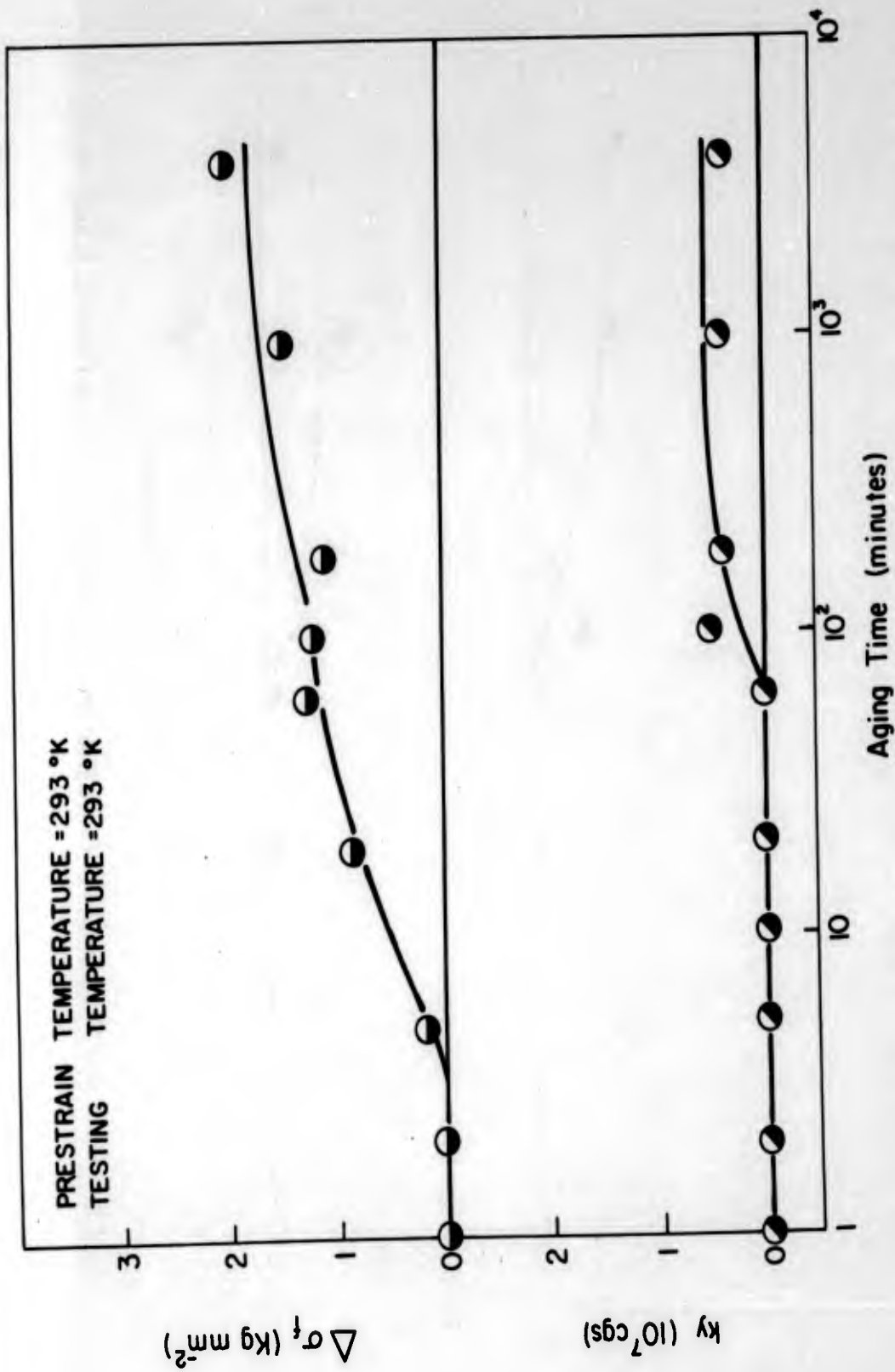


Fig. 89 - $\Delta\sigma_f$ and k_y as a function of aging time at 100°C. Prestrained 293°K, tested 232°K.

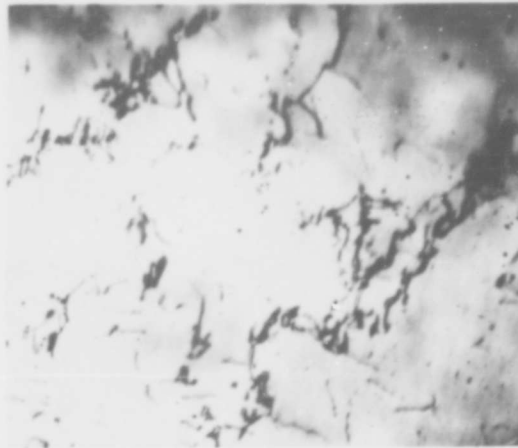


Fig. 90a - Tantalum-oxygen alloy (Ta-E4) annealed 1750°C, deformed 7.5 percent at 293°K (X40,000).



Fig. 90b - Tantalum-oxygen alloy (Ta-E4) annealed 1750°C, deformed 7.0 percent at 240°K (X40,000).

in excess of this and, consequently there is no shortage of oxygen atoms available for dislocation pinning. The small value of k_y as compared with that in the annealed alloy even after prolonged aging at 100°C is remarkable. The slow rate of diffusion of oxygen in tantalum at 100°C suggests that insufficient segregation has occurred to give complete locking. The amount of segregation of oxygen atoms to dislocations can be estimated from the Cottrell-Bilby equation⁽¹⁰⁾

$$\frac{n(t)}{n_0} = 3 \left(\frac{\pi}{2} \right)^{1/3} L \left(\frac{ADt}{kT} \right)^{2/3} \quad (4)$$

where $n(t)$ is the concentration of impurity atoms segregating to dislocations in time t , n_0 is the original concentration of impurity atoms, L is the total length of dislocation line per unit volume, A is an interaction parameter estimated to be 2.7×10^{-20} dyne cm^2 for tantalum-oxygen⁽²⁰⁾, D is the diffusivity of oxygen in tantalum, k is Boltzmann's constant, and T is the aging temperature. Taking a value of L of 2×10^{11} cm^{-2} , the fraction of available dislocation sites occupied by oxygen atoms at $t = 60$ minutes (when k_y begins to rise) is about 2 1/2%. Even after the longest aging times employed (5×10^3 minutes), less than half of the available sites are occupied. With such weak pinning it seems reasonable to assume that yielding occurs by unpinning of the dislocations, and not by the generation of dislocations from new sources as in the iron-carbon case. In the aged tantalum-oxygen alloy, there will be substantial lengths of dislocation lines free of impurity atoms and the unpinning will require less thermal energy than if the dislocations were more strongly pinned⁽²⁶⁾. Thus, a small temperature dependence of k_y would be expected.

Wilson and Russell⁽¹⁵⁾ found an increase in $\Delta\sigma_f$ of about 1.5 Kg mm^{-2} at 293°K after aging iron-carbon at 20°C for only a short time, which they attributed to the Snoek effect. No evidence of a corresponding change in tantalum-oxygen was found, although an increase in $\Delta\sigma_f$ of this magnitude could have been detected easily in the present experiments. For a Snoek effect to occur, each interstitial atom involved must make at least one jump into neighbouring vacant interstitial sites. This jump time is 1.5 times the relaxation time associated with the relevant internal friction peak⁽²¹⁾. The jump time at 293°K for carbon in iron is about 0.6 seconds, but for oxygen in tantalum is about 468 minutes. Thus, for the temperatures and strain rates used in the present experiments, the Snoek effect cannot occur in tantalum-oxygen alloys.

The other major difference between strain-aging iron carbon at 60°C and tantalum-oxygen at 100°C is in the increase in $\Delta\sigma_f$ with aging time, prestrain and test temperature relative to the increase in k_y . The effects which have been proposed to explain the increase in $\Delta\sigma_f$ in iron-carbon alloys cannot explain the phenomenon in tantalum-oxygen. Most of these explanations can be eliminated because in tantalum-oxygen $\Delta\sigma_f$ starts to increase either at about the same time as k_y or, in some cases, long before there is any evidence of the return of the discontinuous yield. Clearly, there can be no precipitates on dislocations under these conditions. Furthermore the oxygen content of the alloy is small compared with the solubility limit, and therefore precipitation within the lattice is also improbable. Carbide precipitates have been observed in iron

after aging treatments which would produce an increase in $\Delta\sigma_f$ ⁽¹⁰⁾; but although alloy Ta-E1 has been examined extensively by thin-film electron microscopy, no evidence of precipitation has been found after any combination of straining and thermal treatments. Thus, it is concluded that the change in $\Delta\sigma_f$ is not due to precipitate hardening. Strengthening by the formation of oxygen clusters is improbable because the tendency in the tantalum-oxygen system is to form ordered structures, nor is it likely that lattice clusters would form before dislocation atmospheres. The suggestion by Keh and Leslie⁽²⁷⁾ that hardening can occur by the pinning of forest dislocations which increases their resistance to the passage of glide dislocations can also be eliminated since the increase in $\Delta\sigma_f$ can be found before any pinning occurs as indicated by an increase in k_y .

The variation of $\Delta\sigma_f$ is a function of prestrain temperature and aging time, and so it is probably the result of the movement of some kind of point defect to a location where it can interact with glide dislocations. However, it is unlikely that the evidence from mechanical tests alone will provide the information from which the nature and behavior of these point defects can be deduced. Parallel studies of the kinetics of strain aging and of internal friction effects taking into account the spectrum of relaxation peaks observed in tantalum-oxygen alloys⁽²⁸⁾ will be required. Of course, any explanation of the mechanism by which $\Delta\sigma_f$ changes with mechanical and thermal treatment should take into account the unusual effects observed when prestraining is carried out at temperatures either above or below the testing temperature.

D. The Variation of Flow Stress with Substructure in Tantalum

1. Introduction

It has been shown⁽²²⁾ that the yield stress and associated parameters of polycrystalline tantalum are dependent on temperature, grain size, impurity content, and initial substructure. This is not surprising since these variables affect the stress required to move dislocations and the rate at which dislocations multiply. There is no straight forward connection between the same variables and the work hardening behavior. The present study was undertaken a) to determine the effect of temperature, grain size, and substructure on the change in dislocation density and distribution with plastic strain, and b) to relate these changes to the change in flow stress with strain.

Different initial substructures were obtained by suitable thermal treatments of severely cold worked material. In a previous study⁽²⁹⁾ it was found that after 90 percent reduction at 20°C the dislocation density in tantalum was greater than $3 \times 10^{11} \text{ cm}^{-2}$. The dislocations were difficult to resolve and no cell structure was observed. When the cold worked material was annealed at successively higher temperatures, four main effects were observed:

a) After 30 minutes at 900°C the dislocation density dropped to $9 \times 10^{10} \text{ cm}^{-2}$ due to the rearrangement and the annihilation of some of the dislocations.

b) Annealing between 900° and 1200°C produced subboundary networks which were very regular at the higher temperatures in this range.

c) At higher annealing temperatures, the spacing of dislocations in the networks increased corresponding to a decrease in the angular misorientation across the boundary; and there was a small decrease in the average dislocation density.

d) No networks were found in specimens annealed at still higher temperatures (about 1700°C) and there was a marked decrease in the average dislocation density. The processes involved overlap somewhat and the annealing temperature at which each effect is observed varies appreciably with the purity of the tantalum. For the alloy used in the present study, the effects occurred at the lowest temperatures.

2. Experimental Details

A tantalum alloy containing 3 ppm carbon 12 ppm nitrogen and 147 ppm oxygen was used. This alloy is referred to in previous work^(22, 29) as Ta-E4. The solubility of carbon and nitrogen in tantalum is small but probably in excess of the amount present. Since the solubility of oxygen is greater than 1600 ppm, all the impurities are presumed to be in solid solution.

As detailed in Table 17, a series of mechanical and thermal treatments was used to produce specimens with different grain size and substructure. All of the thermal treatments were carried out in a vacuum of less than 10⁻⁶ mm Hg. The experiments were arranged in three series designed to reveal:

a) the effect of initial dislocation arrangement in specimens with a constant grain size,

b) the effect of grain size for a given initial dislocation arrangement, e.g. random low density or subboundary networks,

c) the effect of temperature for a given grain size and dislocation distribution.

Tensile tests were made on sheet specimens 0.01 cm thick, 0.3 cm wide and with a gage length 2.0 cm. The strain rate was 0.017 mm⁻¹. After straining the specimens were thinned⁽²⁹⁾ and examined in the electron microscope. The dislocation density (N) was measured using a line intersection method⁽³⁰⁾ involving the following relation:

$$N = \frac{1}{t} \left[\frac{n_1}{L_1} + \frac{n_2}{L_2} \right] \quad (5)$$

where t is the thickness of the foil, n₁ the number of dislocations cut by a line of length L₁, and n₂ the number of dislocations cut by a line of length L₂ normal to L₁.

Table 17

Details of Specimen Preparation, Grain Size, Dislocation Density and Distribution

	Ta(1)	Ta(2)	Ta(3)	Ta(4)	Ta(5)
Thermal - Mechanical Treatment	Cold-worked 90% Annealed 1750°C for 6 mins.	Cold-worked 90% Annealed 1750°C for 6 mins. Cold-worked 12% Annealed 1000°C for 1 hour.	Cold-worked 90% Annealed 1750°C for 6 mins. Cold-worked 12% Annealed 800°C for 1/2 hour.	Cold-worked 90% Annealed 1200°C for 1 hour.	Cold-worked 90% Annealed 900°C for 1 hour.
Grain Size, $d^{-1/2}$ mm ^{-1/2}	3.9	3.9	3.9	4.5	7.7
Initial Dislocation density (N_i), cm ⁻²	1.0×10^9	1.6×10^{10}	4.0×10^{10}	1.6×10^9	2.0×10^{10}
Initial Dislocation Arrangement	Random Low Density	Networks	Random High Density	Random	Networks
Test Temperature	240°K, 293°K	293°K	293°K	293°K	293°K

3. Change in Substructure on Deforming Annealed Foils in Tension

The sequence of changes in the substructure on deforming annealed specimens in tension is similar to that observed in iron^(30,31,32) but there are differences in detail. Five specimen conditions, Ta(1) to Ta(5) for which information is given in Table 17, were deformed at 293°K. Ta(1) was also deformed at 240°K. The changes in substructure are as follows:

a) Ta(1) at 293°K - Before deformation the dislocations were randomly distributed within the grains. After the Lüders strain (about 3%), a few irregular dislocations are present, particularly close to the grain boundaries. As the strain is increased, irregular tangles of dislocations are produced throughout the specimen; and there is an increasing number of dislocations associated with the grain boundaries (Figs. 91, 92, and 93). The tangles surround regions of crystal relatively free from dislocations, but the well defined cell structure observed in iron deformed at 20°C is not produced.

b) Ta(1) at 240°K - In the early stages of deformation, a few long straight dislocations were observed. With increasing strain, the distribution becomes similar to that observed in Ta(1) at 293°K except that the tangling is less pronounced (Fig. 94).

c) Ta(2) at 293°K - Before deformation most of the dislocations were in regular networks forming low angle boundaries (Fig. 95). During the Lüder's strain (about 1.8%) some of the networks begin to break up (Fig. 96), particularly those with widely spaced dislocations, and many long dislocations are observed. As the strain is increased, more networks break up and the dislocations become fairly uniformly distributed with some tangling. Even after 8.5% strain some finely spaced networks still remain (Fig. 97).

d) Ta(3) at 293°K - The initial dislocation density was high and the dislocations were randomly distributed (Fig. 98). This structure represents the arrangement of dislocations prior to the formation of low angle boundaries during annealing. In the early stages of deformation, the dislocations become more tangled and small dislocation-free regions are formed. This is not pronounced, and after 10% strain the distribution is nearly homogeneous.

e) Ta(4) at 293°K - Similar to Ta(1) at 293°K.

f) Ta(5) at 293°K - Apart from the difference in the grain size, the initial substructure was the same as Ta(2), and the changes in dislocation distribution with strain are also similar.

Several sources of dislocation multiplication have been identified. Many dislocations are formed when a dislocation network disintegrates. The way this occurs is not clear. It was observed in all the specimens that as the deformation increased the grain boundaries become thicker and more fuzzy, due to dislocations either accumulating at or being generated from the boundary. It is unlikely that these dislocations are formed by the blocking of a slip band because where this occurs the new dislocations are readily identified.

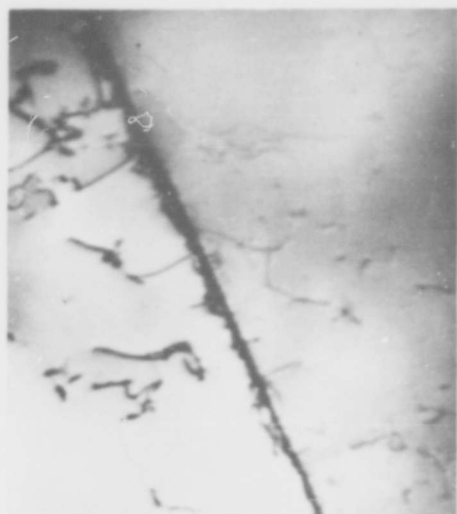


Fig. 91 - Ta(1) strained 4.3% at 293°K
Dislocations associated with
grain boundary.

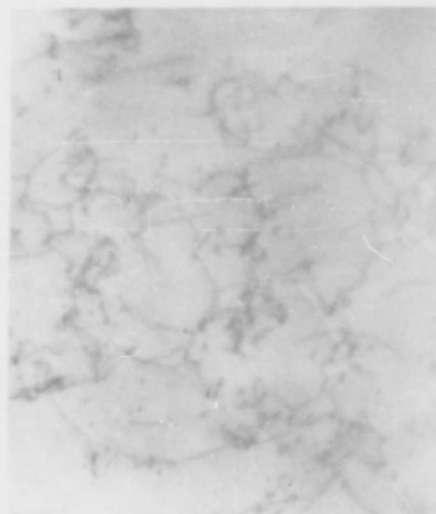


Fig. 92 - Ta(1) strained 6.2% at 293°K
Small dislocation tangles.



Fig. 93 - Ta(1) strained 9.9% at 293°K
Ill defined cell structure.



Fig. 94 - Ta(1) strained 6.9% at 240°K.



Fig. 95 - Initial substructure in Ta(2). Extensive dislocation networks forming sub-boundaries.

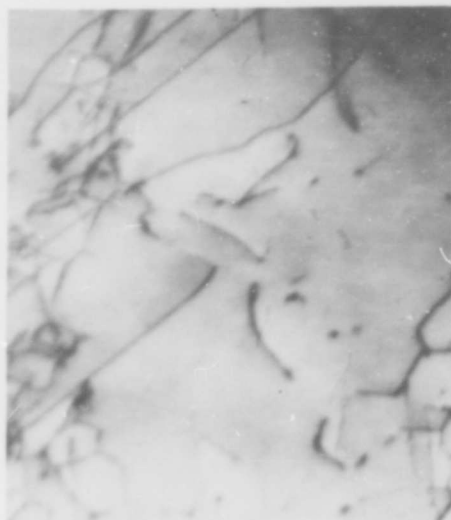


Fig. 96 - Ta(2) after Lüder's strain. A dislocation network on the left hand side has started to break down.



Fig. 97 - Ta(2) strained at 293°K. Extensive dislocation networks still remaining after 8.5% strain.

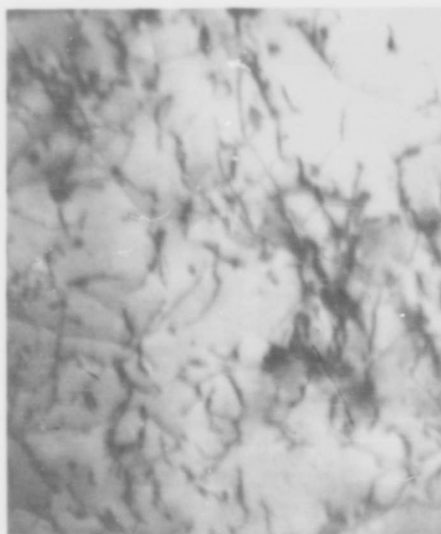


Fig. 98 - Initial substructure in Ta(3).

4. Variation of Flow Stress with Dislocation Density

The stress-strain curves for all the different types of specimens listed in Table 17 are shown in Fig. 99. As with all polycrystalline tantalum alloys tested in this and other investigations, the logarithm of the true stress varies linearly with the logarithm of the true strain (ϵ) for values greater than the Luders strain. Thus, the strain hardening curve is accurately represented by

$$\sigma_f = K\epsilon^n \quad (6)$$

where K is the strength constant and n the strain hardening index. Values of the flow stress at zero plastic strain σ_{f_0} were obtained by logarithmic extrapolation of the strain hardening curve to the intersection with the elastic line^(22, 33, 24). Values of the lower yield stress σ_y , σ_{f_0} and n are listed in Table 18. Changing the initial substructure (compare Ta(1), Ta(2) and Ta(3)) produces only a very small difference in the yield stress at 293°K, but the difference in σ_{f_0} is appreciable. Clearly, σ_{f_0} and n are affected by the initial substructure. Many determinations of σ_i , which is equivalent to σ_{f_0} ⁽²⁴⁾, have been made on other materials using the Petch extrapolation which depends upon

$$\sigma_y = \sigma_i + k_y d^{-1/2} \quad (7)$$

where $2d$ is the grain diameter and k_y a locking parameter. This method cannot be used to study the effect of substructure on yield parameters because of the practical difficulty of maintaining a constant dislocation arrangement and density in a series of specimens with an appreciable range of grain size. When the grain size is established by annealing cold worked tantalum at successively higher temperatures, the Petch method measures some average value of σ_i which is higher than σ_{f_0} measured by extrapolation of the strain hardening curve⁽²²⁾. In iron specimens, the variation in substructure with annealing temperature is not marked and there is good agreement between σ_i by the Petch method and σ_{f_0} by extrapolation of the strain hardening curve⁽³³⁾.

Following Keh and Weissmann⁽³⁰⁾, the flow stress was plotted (Fig. 100) as a function of \sqrt{N} , where N is the average dislocation density. All the tantalum specimens were found to obey approximately the empirical relationship:

$$\sigma_f = \sigma_0 + \alpha Gb \sqrt{N} \quad (8)$$

where σ_0 and α are constants, G is the shear modulus and b the Burgers vector. A relationship of this type is predicted by several theories of strain hardening, but the models on which the theories are based are related to specific distributions of dislocations. The application of a theory relating to one crystal structure to another structure has limited value. To interpret equation 7 an assumption is necessary about the appropriate value of N to use. For the results plotted in Fig. 100 the average dislocation density is used. However, if for example, the dislocations are arranged in dense tangles with large regions free from dislocations, the stress σ_f may well be determined by the density of dislocations in the tangles. This difficulty may be overcome by assuming that the

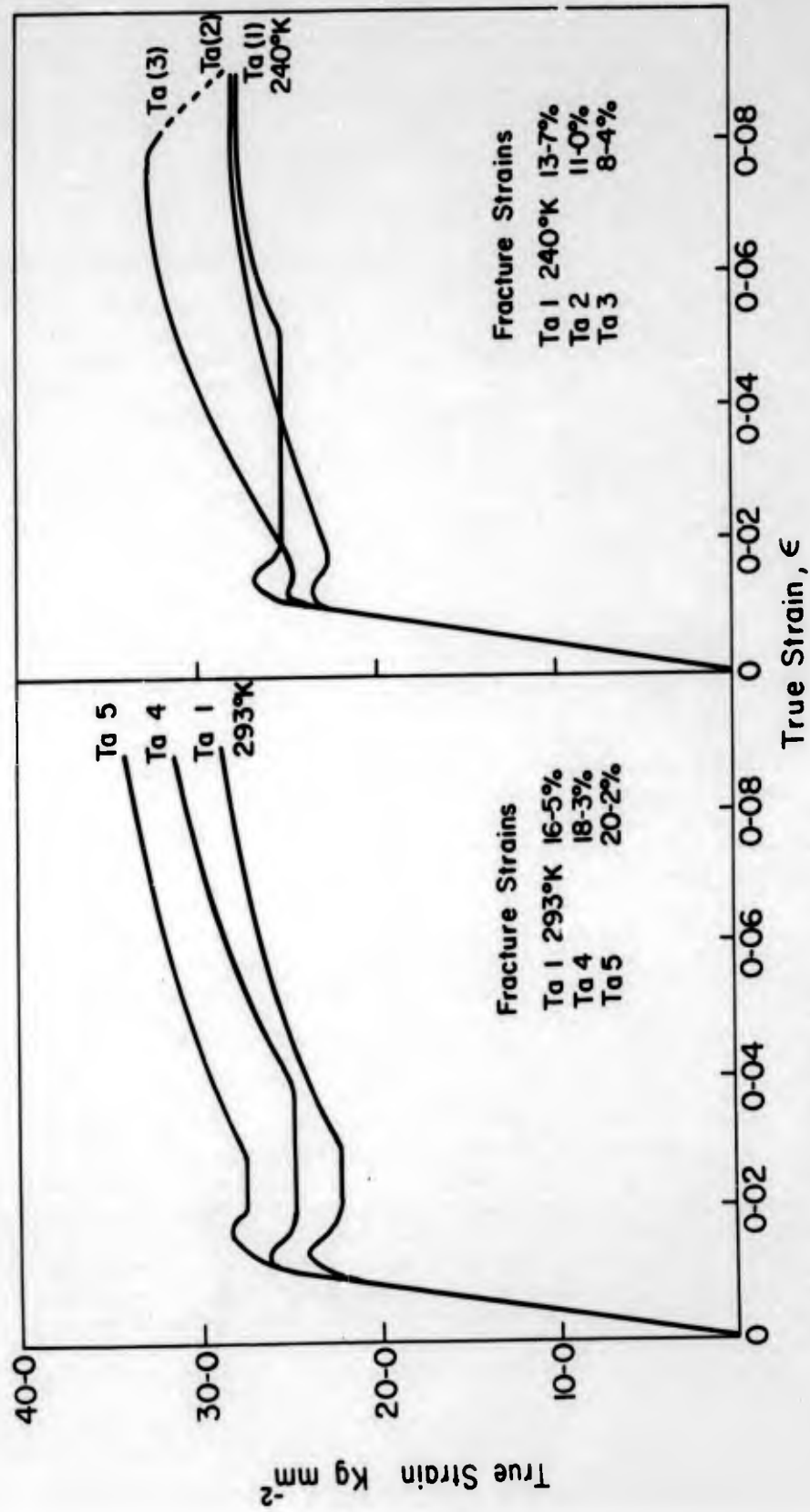


Fig. 99 - Experimental stress-strain curves.

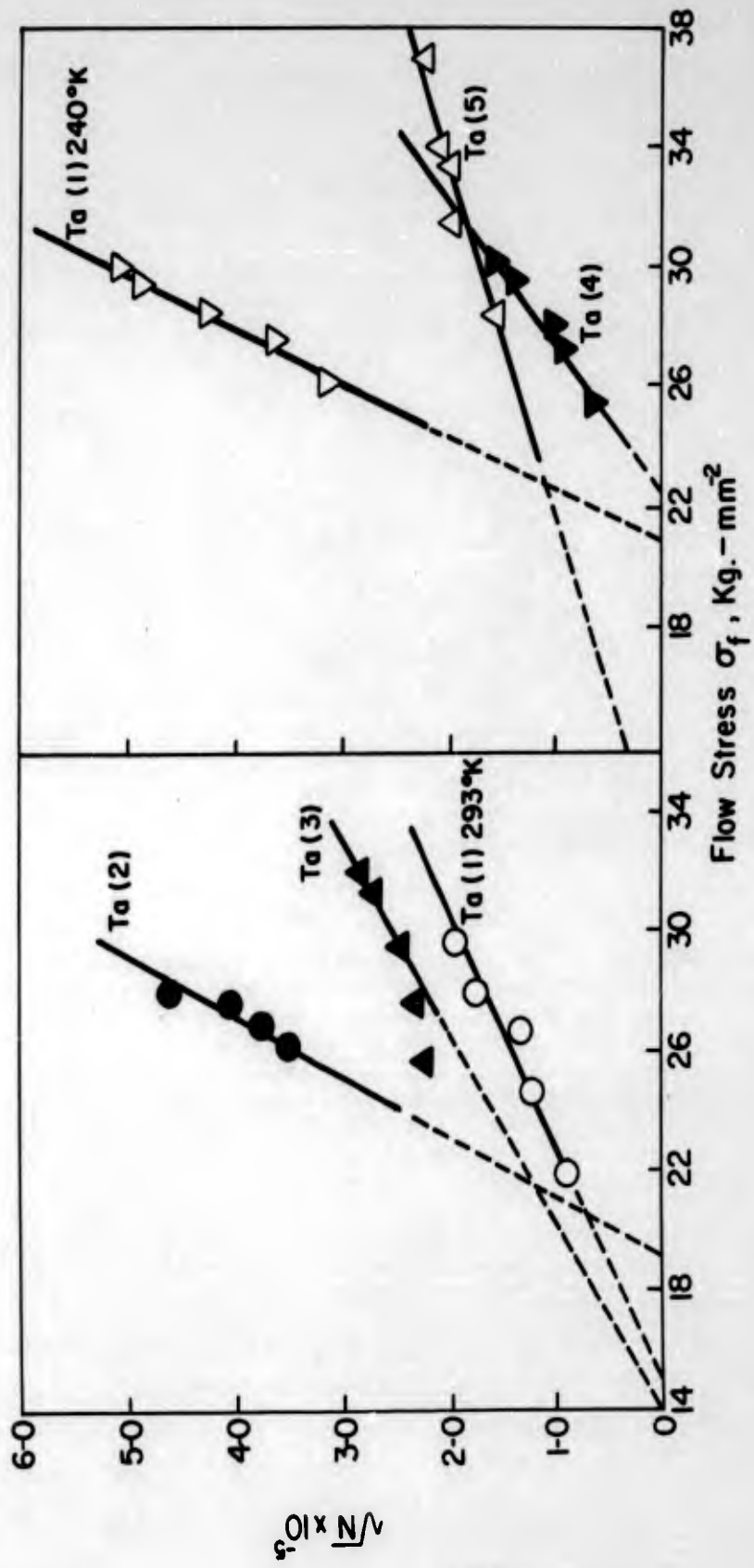


Fig. 100 - Dislocation density as a function of flow stress according to equation (8).

ratio of the density of the dislocations in the tangles (N_f) to the average dislocation density (N) is independent of strain; for example $N_f/N = 5$, see reference 30.

The value of σ_0 (equation 8) can be determined by extrapolation, since σ_0 is the stress to move dislocations in the absence of other dislocations ($N = 0$). In the present results, σ_0 was found to vary between 14.0 and 22.7 Kg mm^{-2} for specimens with differing substructures. Since no other variables have been introduced, it would be expected that σ_0 would be independent of initial substructures and the different values of σ_0 imply that this approach is not satisfactory. However, equation 8 is a useful empirical representation of the results. It can be used with some confidence to determine the flow stress at zero strain as an alternative to extrapolation of the stress-strain curve. The symbol σ_{f_0} is the stress corresponding to the initial dislocation density N_i . Values of σ_{f_0} determined by this method are given in Table 4 and, in general, they compare favorably with those determined from the stress-strain curve.

A different approach is to consider the change in the average dislocation density with strain (Figs. 101 and 102). The results can be represented by a simple power relationship (Fig. 103);

$$N = C\epsilon^a \quad (9)$$

The value of the constants C and a are given in Table 19. A similar result has been found in iron and mild steel⁽²⁴⁾. Hahn⁽³⁴⁾ replaces the total strain ϵ by the plastic strain ϵ_p ; but as the elastic strain is small compared with ϵ over the range of experimental measurements, the substitution does not make a significant difference. From the relationship

$$\epsilon = N_m b l \quad (10)$$

where N_m is the number of moving dislocations and l is the slip distance, each increment of strain is proportional to the product of the number of moving dislocations and the slip distance. For Ta(1) and Ta(2) deformed at 293°K, a is nearly unity which indicates that the product $N_m l$ is a constant. If the difference in slip distance is assumed to be small, the ratio of moving to static dislocations should be independent of initial substructure. Thus, the fraction of dislocations moving can be assumed to be independent of strain only if the slip distance is independent of the average dislocation density. For Ta(1) deformed at 240°K, the situation is quite different since the strain varies approximately as the square root of the dislocation density. Thus the product $(N_m/N) l$ should vary with strain. Without exact knowledge of the change in slip distance with strain and temperature, no deduction can be made about the effect of these variables on the fraction of dislocations moving.

If equations 6 and 10 are judged to be a correct representation of the data, then eliminating gives

$$\sigma_f = KC \frac{a-n}{n} N^{\frac{n}{a}} \quad (11)$$

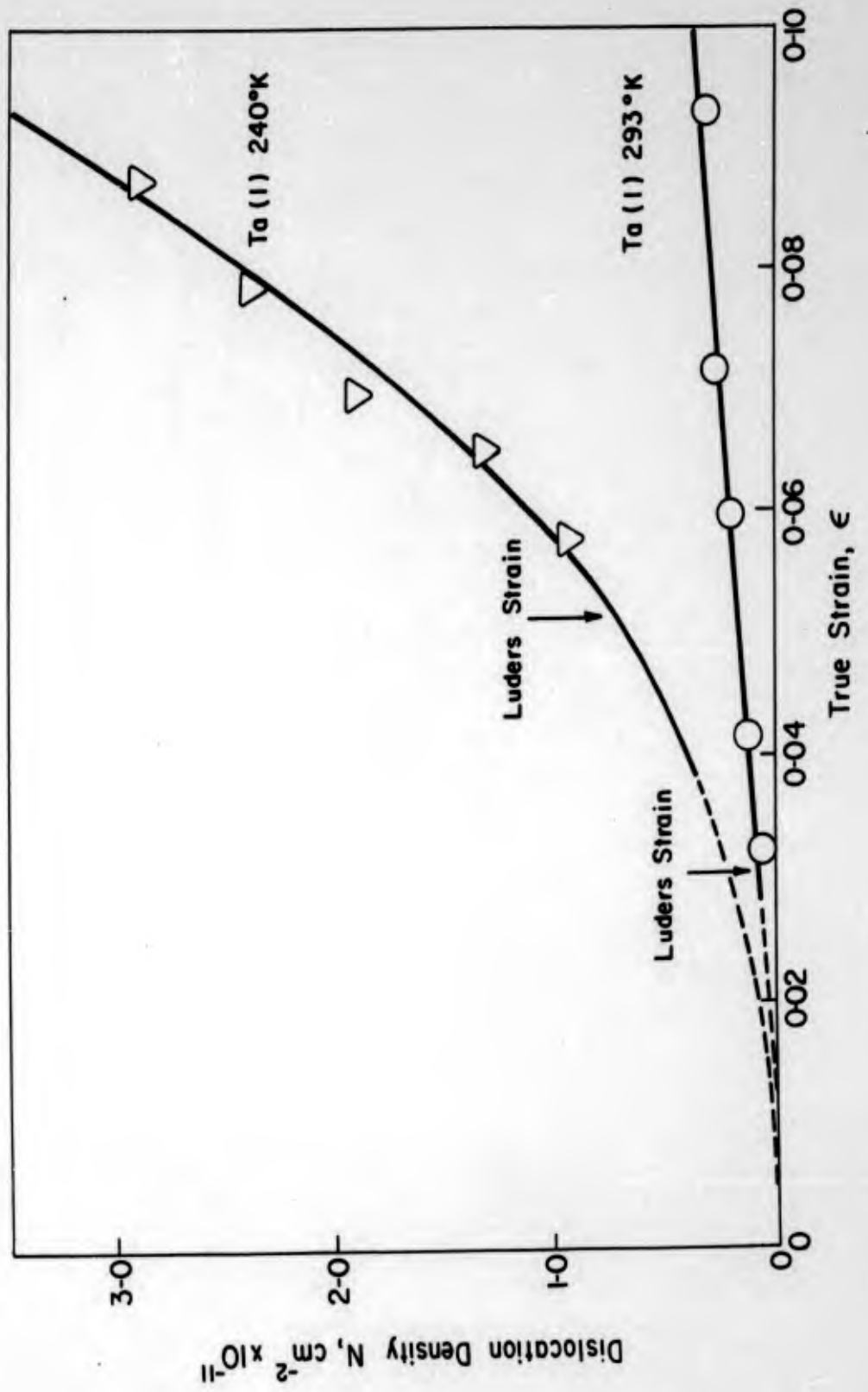


Fig. 101 - Variation of dislocation density with strain.

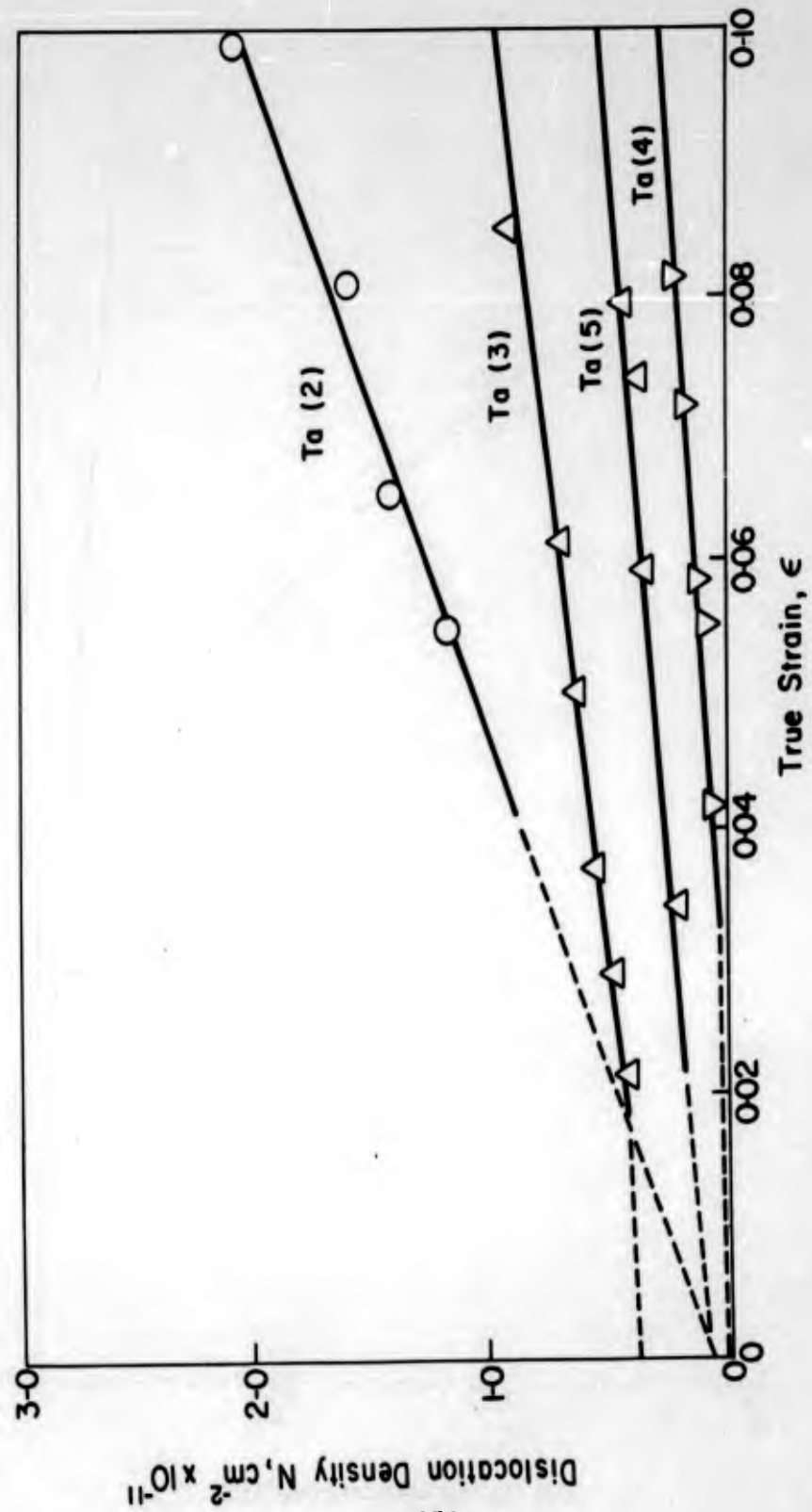


Fig. 102 - Variation of dislocation density with strain.

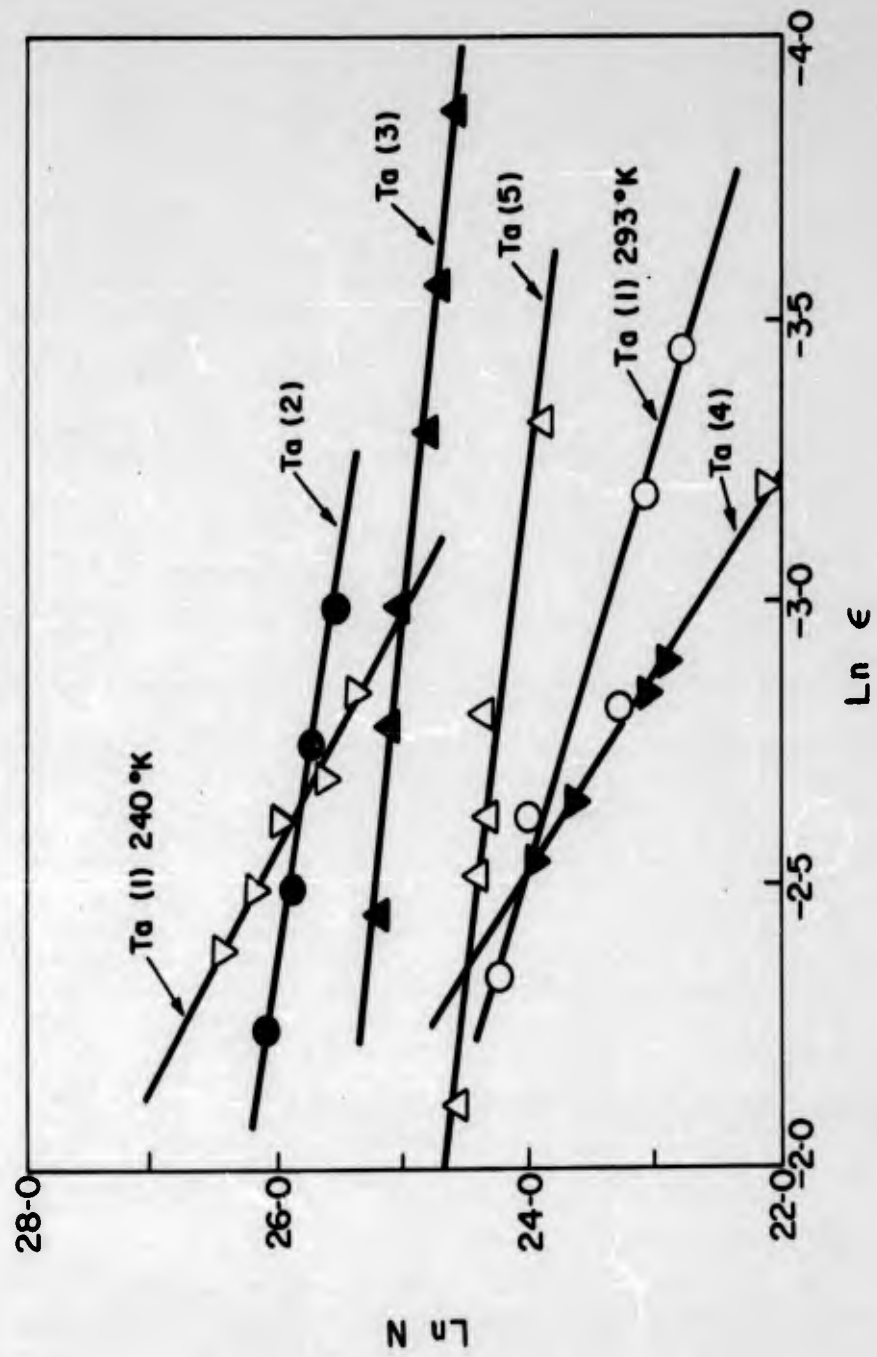


Fig. 103 - Variation of dislocation density with strain according to equation 9.

It is not surprising that the experimental results fit this relationship since σ_f , N and ϵ represent interrelated data. The values of $\frac{n}{a}$ are given in Table 19. Since $\frac{n}{a} = 0.5$, equation 11 is not compatible with equation 8 and the flow stress is not proportional to the average spacing between dislocations. The best agreement is shown by Ta(3) which has a high initial dislocation density.

The most striking finding that emphasizes the importance of dislocation distribution on the flow stress is the relation between $\left(\frac{\partial \sigma_f}{\partial \epsilon}\right)_\epsilon$ and $\left(\frac{\partial N}{\partial \epsilon}\right)_\epsilon$. It follows from equation 6 and a combination of equations 9 and 10 that $\frac{\partial \sigma}{\partial \epsilon}$ is related directly to $\frac{\partial N}{\partial t}$. However, comparisons of Ta(1) deformed at 293° and 240°K and of Ta(1), Ta(2) and Ta(3) deformed at 293°K show that large values of $\left(\frac{\partial \sigma}{\partial \epsilon}\right)_\epsilon = 0.06$ correspond to relatively low values of $\frac{\partial N}{\partial \epsilon}$ for $\epsilon = 0.06$ and vice versa (Table 18). The results for Ta(1) at 293° and 240°K can be accounted for by a small difference in the distribution of dislocations. At 240°K the dislocations are more uniformly distributed than at 293°K and $\left(\frac{\partial \sigma}{\partial \epsilon}\right)_{293} > \left(\frac{\partial \sigma}{\partial \epsilon}\right)_{240}$, $\left(\frac{\partial N}{\partial \epsilon}\right)_{293} < \left(\frac{\partial N}{\partial \epsilon}\right)_{240}$. This implies that when the dislocations are uniformly distributed, the multiplication rate is higher and the average slip length is smaller than for less uniform distributions. A higher increase in the density of dislocations is required to produce a given increase in σ_f . This suggests that the average dislocation density cannot be related directly to σ_f . The results are consistent with the suggestion that σ_f is determined by the density of dislocations in the tangled regions. Thus, although N may be small, the density in the tangles may be large, and the rate of multiplication in the tangles and the free slip length determines the work hardening rate.

The effect of grain size on the change of N with strain is not clear. The difference in grain size between Ta(1) and Ta(4) is too small to produce significant differences in behavior (Table 18). For Ta(2) and Ta(5) the difference in grain size is larger. This is responsible for the increase in the yield stress, work hardening parameter n , and work hardening rate, as well as for the decrease in $\frac{\partial N}{\partial \epsilon}$. Since $\frac{\partial N}{\partial \epsilon}$ is smaller in specimens with a larger total grain boundary area, the decrease indicates that whereas grain boundaries may be sources of dislocations they do not control the rate of multiplication.

5. The Significance of σ_0

In the equation used by Keh and Weissmann (equation 8), $\sigma_f = \sigma_0$ when $N = 0$ and σ_0 might be considered to be the Peierls stress. However, σ_0 defined in this way varies over a wide range when the initial substructure is changed (Fig.100 and Table 17). Equation 13 is also unsatisfactory because neither of the equations from which it is derived (equations 6 and 9) take account of the Peierls stress. However, the fact that these equations appear to be a good representation of the experimental data suggests that the Peierls stress is small compared with σ_f .

Table 18

Flow Stress and Work Hardening Parameters

	Strain Hardening Index n	Lower Yield Stress σ_y , Kg-mm ⁻²	σ_{f0} -2 Kg-mm ⁻²	$\frac{\partial \sigma_f}{\partial \epsilon}$ at $\epsilon = 0.060$ Kg-mm ⁻²	$\frac{\partial N}{\partial \epsilon}$ at $\epsilon = 0.060$ cm ⁻²
Ta (1) 293°K	0.25	22.2	14.7	106.0	4.0×10^{11}
Ta (1) 240°K	0.12	25.4	19.6	51.8	4.2×10^{12}
Ta (1) 293°K	0.25	22.2	14.7	106.0	4.0×10^{11}
Ta (2) 293°K	0.13	22.6	19.8	57.4	1.4×10^{12}
Ta (3) 293°K	0.21	24.4	23.3	110.2	5.9×10^{11}
Ta (1) 293°K	0.25	22.2	14.7	106.0	4.0×10^{11}
Ta (4) 293°K	0.22	25.1	19.4	102.0	5.6×10^{11}
Ta (2) 293°K	0.13	22.6	19.8	57.4	1.4×10^{12}
Ta (5) 293°K	0.19	27.6	23.2	90.6	4.8×10^{11}

In the absence of a firmly-based equation relating the flow stress and the average dislocation density, an attempt to assess the Peierls stress by a more circuitous route appears justified. Previously, σ_{f_0} has been defined as the point satisfying simultaneously equation 6 and the elastic equation

$$\sigma = E\epsilon \quad (12)$$

where E is Young's modulus (Fig. 22) and

$$\sigma_{f_0} = \left[K \frac{1}{1-n} \right] \left[\frac{n}{E^{n-1}} \right] \quad (13)$$

However, if it is assumed that σ_{f_0} is the sum of the Peierls stress σ_0 and the stress σ_s required to move a dislocation through the annealed-in substructure, the relation between the elastic line and the strain-hardening curve may be as represented in Fig. 104. ϵ_0 is the strain introduced into the specimen by building up the dislocation density from zero to N_i . Hypothetically, if this is done without any dislocation interaction, the stress required would be σ_0 . Then, σ_{f_0} , now defined as the stress at which the elastic line (equation 8) is tangential to the strain-hardening curve

$$\sigma_f - \sigma_0 = K (\epsilon - \epsilon_0)^n \quad (14)$$

becomes

$$\sigma_{f_0} = \sigma_0 + K \frac{1}{1-n} \frac{n}{E^{n-1}} \frac{n}{1-n} \quad (15)$$

Experimentally the stresses σ_f and strains ϵ can be measured only at strains larger than the Lüders strain. In these circumstances, if it is assumed that $\sigma_f \gg \sigma_0$ and $\epsilon \gg \epsilon_0$ equation 14 reduces to equation 6 and n and K can be determined experimentally. Equation 14 fits the strain hardening curve very closely, suggesting that at large strains this approximation is reasonable. The second term on the right-hand side of equation 15 differs from the right-hand side of equation 13 only by the factor $n^{n/1-n}$. For tantalum tested at 293°K, n has values between 0.1 and 0.3 depending upon the initial substructure

and $n^{n/1-n}$ varies between 0.77 and 0.60. Probably the least ambiguous method of determining σ_{f_0} experimentally is from the data in Fig. 91, taking σ_{f_0} as the stress corresponding to N_i . Since the value from equation 13 (that is logarithmic extrapolation of the stress-strain curve) agrees fairly well with this value, the

decrease due to $n^{n/1-n}$ must be approximately compensated by the introduction of σ_0 into equation 15. That is, between about 60 and 75% of σ_{f_0} at 293°K is due to dislocation interaction.

Values of σ_0 from the tantalum data obtained by taking σ_{f_0} from the plots of σ_f versus \sqrt{N} , and n and K from the application of equation 6 at large values of ϵ are given in Table 19. Although the values of σ_0 calculated from

Table 19
Calculated Parameters (c.g.s. units)

	Ta(1) 293°K	Ta(1) 240°K	Ta(2)	Ta(3)	Ta(4)	Ta(5)
α (equation 8)	0.34	0.07	0.08	0.30	0.14	0.47
δ_o (N = O equation 8)	14.8	21.4	18.9	14.0	22.7	11.0
q_{fo} (N = N _i equation 8)	17.3	21.9	21.5	24.0	24.1	25.0
C (equation 9)	7.9×10^{11}	7.9×10^{13}	1.4×10^{12}	3.2×10^{11}	3.6×10^{13}	1.7×10^{11}
^a (equation 9)	1.2	2.2	0.80	0.45	2.96	0.6
n/a (equation 11)	0.20	0.08	0.11	0.42	0.09	0.19
σ_o (equation 15)	7.2	6.5	7.0	8.6	11.3	9.5

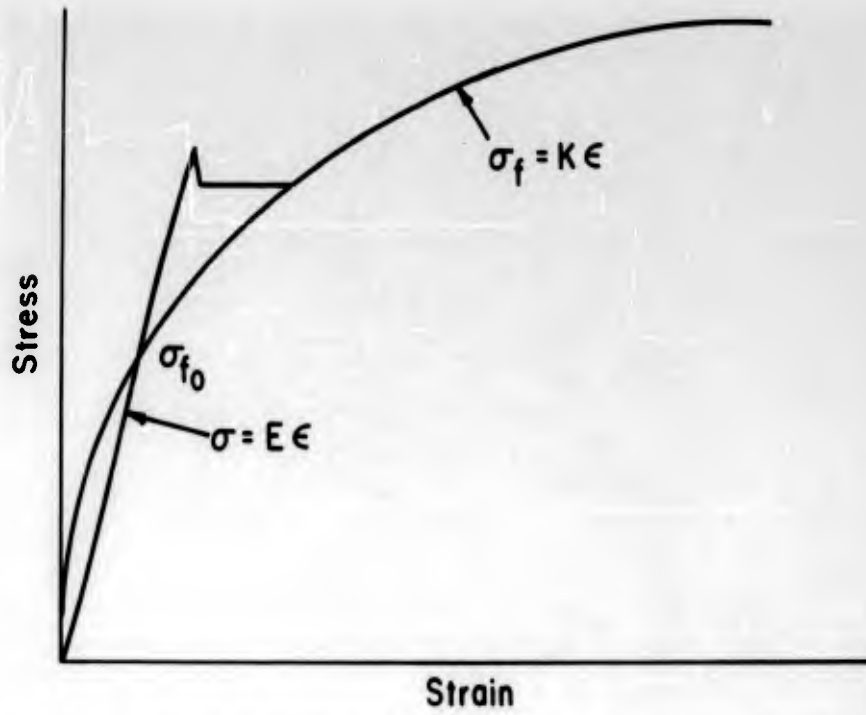


Fig. 104a - Definition of σ_{f0} according to equations 6 and 12.

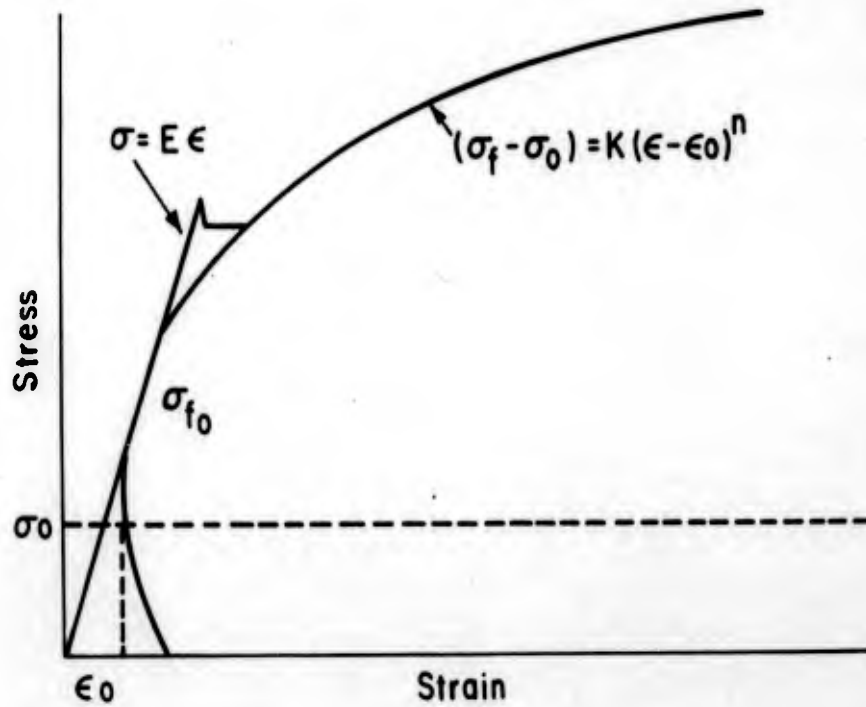


Fig. 104b - Definition of σ_{f0} taking account of Peierls stress and initial dislocation density.

data for different grain size and initial dislocation density show some scatter (σ_0 varies between 6.5 and 11.3 Kg mm⁻², average 8.4 Kg mm⁻²), the average value is in reasonable agreement with the value deduced by Conrad⁽³⁵⁾ for the variation of the yield stress of tantalum with temperature.

REFERENCES

- (1) Friedel, J., Les Dislocations, Gauthier-Villars (1956).
- (2) Darken, L.S., "Some Observations on Atoms and Imperfections," Trans. ASM, 54 (1961) 601.
- (3) Cottrell, A.H., Report on Strength of Solids, Phys. Soc. London (1948).
- (4) Cottrell, A.H., "A Note on the Portevin-Le Chatelier Effect," Phil. Mag., 44 (1953) 829.
- (5) Mott, N.F., "Mechanical Strength and Creep in Metals," Imperfections in Nearly Perfect Crystals, ed. W. Shockley, John Wiley and Sons (1952).
- (6) Boulanger, Ch., "Contribution to the Study of Plastic Deformation of Iron and Soft Steels," Rev. Met., 47 (1950) 547.
- (7) Lement, B.S., et al, "Substructure and Mechanical Properties of Refractory Metals," WADD Technical Report 61-181, Part II, (1962).
- (8) Cottrell, A.H., and Bilby, B.A., "Dislocation Theory of Yielding and Strain Aging of Iron," Proc. Phys. Soc., A62 (1949) 49.
- (9) Cocharadt, A., Schoeck, G., and Wiedersich, H., "Interactions Between Dislocation and Interstitial Atoms in Body-Centered Cubic Metals," Acta Met., 3 (1955) 533.
- (10) Keh, A.S., and Leslie, W.C., Progress in Materials Science, 10, Pergamon Press, London (to be published).
- (11) Harper, S., "Precipitation of Carbon and Nitrogen in Cold-Worked Alpha-Iron," Phys. Rev., 83 (1951) 709.
- (12) Wilson, D.V., and Russell, B., "The Contribution of Precipitation to Strain Aging in Low Carbon Steels," Acta Met., 8 (1960) 468.
- (13) Thomas, W.R., and Leak, G.M., "The Strain Aging of Alpha-Iron," J. Iron and Steel Inst., 200 (1962) 229.
- (14) Lautenschlager, E., and Brittain, J.O., "The Influence of the Temperature of Deformation on Strain Aging of Alpha-Iron," Trans. AIME, 224 (1962) 48.
- (15) Wilson, D.V., and Russell, B., "The Contribution to Atmosphere Locking to the Strain Aging of Low Carbon Steels," Acta Met., 8 (1960) 36.
- (16) Wilson, D.V., and Russell, B., "Steel Induced Ordering and Strain Aging in Low Carbon Steels," Acta Met., 7 (1959) 628.
- (17) Reid, C.N., and Owen, W.S., "The Thermal Activation of Yielding in Low-Carbon Iron," J. Iron and Steel Inst., 200 (1962) 229.
- (18) Fisher, R.M., private communication.
- (19) Pawel, R.E., Cathcart, J.V., and Campbell, J.J., "Oxide Platelet Formation in Tantalum Single Crystals," Acta Met., 10 (1962) 149.

REFERENCES (Continued)

- (20) Formby, C. L. , private communication.
- (21) Powers, R. W. , and Doyle, M. V. , "Diffusion of Interstitial Solutes in the Group V Transition Metals," J. Appl. Phys., 30 (1959) 514.
- (22) Gilbert, A., Hull, D., Owen, W.S., and Reid, C.N., "The Yielding of Polycrystalline Tantalum," J. Less Common Metals, 4(1962) 399.
- (23) Petch, N.J., "The Cleavage Strength of Polycrystals," J. Iron and Steel Inst., 174 (1953) 25.
- (24) Rosenfield, A.R., J. Inst. of Met. (to be published).
- (25) Szkopiak, Z.C., Battersea College Interim Report CON/RIS/18405(A), (Jan. 1961).
- (26) Lothe, J., "The Effect of Temperature on Dislocations with Condensed Impurity Atmospheres. Theory of Dislocation Motion and Dislocation Break-Away," Acta Met., 10 (1962) 663.
- (27) Keh, A.S., and Leslie, W.C., "Structure and Properties of Engineering Materials," Interscience Publishers (to be published).
- (28) Chambers, R., private communication.
- (29) Hull, D., McIvor, I., and Owen, W.S., "The Distribution of Dislocations in Annealed Tantalum," J. Less Common Metals, 4 (1962) 409.
- (30) Keh, A.S., and Weissmann, S., Conference on the Impact of Transmission Electron Microscopy on the theories of Strength of Crystals, Berkeley, Calif. (1961).
- (31) Carrington, W., Hale, K.F., and McLean, D., "Arrangement of Dislocations in Iron," Proc. Roy. Soc., 259 A (1960) 203.
- (32) Brandon, D.G., and Nutting, J., "Dislocations of Alpha-Iron," J. Iron and Steel Inst., 196 (1960) 160.
- (33) Mogford, I., and Hull, D., "Effect of Temperature and Neutron Irradiation in Yield and Work Hardening in Iron," J. Iron and Steel Inst., 201 (1963) 55.
- (34) Hahn, G. T., "A Model for Yielding with Special Reference to the Yield-Point Phenomena of Iron and Related B. C. C. Metals," Acta Met. 10 (1962) 727.
- (35) Conrad, H., Nat. Phys. Lab. Symposium (Jan. 1963).

VIII. A TRANSMISSION ELECTRON MICROSCOPY STUDY OF DEFECTS IN COLUMBIUM AND TANTALUM - Work carried out at the University of Cambridge (England) by T. E. Mitchell, R. A. Foxall and P. B. Hirsch.

A. Introduction

The purpose of this investigation was to examine the relationship between the mechanical properties of single crystals of b.c.c. metals and their dislocation structures as observed by transmission electron microscopy. Since the electron microscopy results did not progress far enough to permit definite conclusions, this report is concerned mainly with the results of mechanical tests. These were directed towards measuring the temperature dependence and strain-rate dependence of the flow stress in order to study thermally-activated processes occurring in b.c.c. metals.

B. Experimental Techniques

Single crystals of tantalum and columbium were grown in an electron-beam zone-refiner constructed in this laboratory. Six zone passes were normally made and the final vacuum was better than 5×10^{-6} torr. Crystals of 1/8 inch diameter were grown for tensile testing and crystals of 1/4 inch diameter for electron microscopy experiments. Since the as-grown crystals were usually rather uneven in cross-section along their length, it was necessary to machine a uniform gauge length on them by means of a lathing attachment on the spark-cutting machine supplied by Metals Research Ltd. The slight damage caused by the spark-eroding was afterwards removed by chemical polishing.

Specimens were deformed in tension in an Instron table model machine at temperatures between 77°K and 473°K . Temperature cycling experiments were performed by deforming at one temperature to a particular strain, changing the temperature and measuring the new flow stress at the same strain. Strain-rate cycling experiments were also performed by instantaneously changing the strain-rate by a factor of ten (from $\sim 5 \times 10^{-5}$ to $\sim 5 \times 10^{-4}$ sec.^{-1}) and measuring the accompanying increase of flow stress ($\Delta\sigma$).

Crystals for electron-microscope studies were deformed to various strains at selected temperatures and then sectioned along different crystallographic planes (including the slip-plane) by spark-cutting and planing techniques. Thin specimens for examination in the electron microscope were then obtained by chemical polishing in HF/HNO_3 solutions.

C. Mechanical Test Results

1. Slip systems

The slip direction of b.c.c. single crystals is $[111]$ and the slip plane is usually (110) . It is sometimes considered to be (211) or (321) depending on the test temperature and initial orientation, although it is possible that slip on these high index planes is composed of alternate slip on close-packed

(110) planes⁽¹⁾. The slip direction has been investigated by following the path of the tensile axis during deformation by back-reflection X-ray techniques. For example, crystals oriented within the standard [001]-[101]-[111] stereographic triangle slip towards the [111] direction. When the tensile axis meets the [001]-[101] symmetry line, slip in the [111] direction should become equally probable and a resultant motion of the tensile axis towards [101] should occur. However, it has been observed that in tantalum and columbium crystals the tensile axis "overshoots" the [001]-[101] symmetry line by 3 to 4 degrees at room temperature before tending to move towards [101]. This "overshoot" indicates that hardening on the secondary systems is greater than that on the initial primary slip system, as occurs in f.c.c. alloy crystals⁽²⁾.

2. Initial flow stress

B.c.c. crystals are characterized by their very high initial flow stress (critical resolved shear stress), which are 2 or more orders of magnitude higher than in pure f.c.c. metal crystals. Yield points occur for impure b.c.c. crystals and also to a certain extent for pure crystals, depending on orientation⁽¹⁾. No definite yield points were observed in the present investigation. Values of the initial flow stress (τ_0) are plotted against temperature between 77 and 473°K in Fig. 105 for tantalum and columbium crystals. The stresses quoted are shear stresses resolved on the most highly stressed (110)[111] slip system. For tantalum the steep rise of τ_0 at low temperatures extrapolates to value $\sim 40 \text{ kg/mm}^2$ at 0°K. For columbium there are not sufficient low temperature data for such an extrapolation. Above room temperature, Fig. 105 shows that the curves tend to level off and it appears that τ_0 becomes constant above about 500°K for tantalum and above about 450°K for columbium. The temperature variation of τ_0 is usually explained in terms of two contributions to the flow stress, τ_s and τ_g ; where τ_s is the thermally activated component which disappears at temperatures higher than those quoted above and is responsible for the increase of τ_0 at low temperatures, and τ_g is a "long-range" stress which is largely independent of temperature.

3. Shear stress-shear strain curves

Shear stress-shear strain curves of b.c.c. single crystals are characterized by the fact that the work-hardening rate decreases continuously with increasing strain, in contrast to f.c.c. crystals which show three distinct stages of work-hardening. In tantalum crystals deformed at room temperature, a short linear hardening region was observed at the beginning of the stress-strain curve. The hardening rate (θ) is about 6 kg/mm^2 , which corresponds to about $G/1000$, where G is the shear modulus. This is smaller than the stage II work-hardening rate in f.c.c. metals, ($\theta \cong G/300$). The explanation of this difference may be that cross-slip is easy in b.c.c. metals because of their high stacking-fault energy. However, it was observed in tantalum crystals that θ tends to increase with increasing temperature in agreement with the observations of Mordike⁽³⁾ in compression tests of tantalum crystals. Further experiments are in progress to examine this effect.

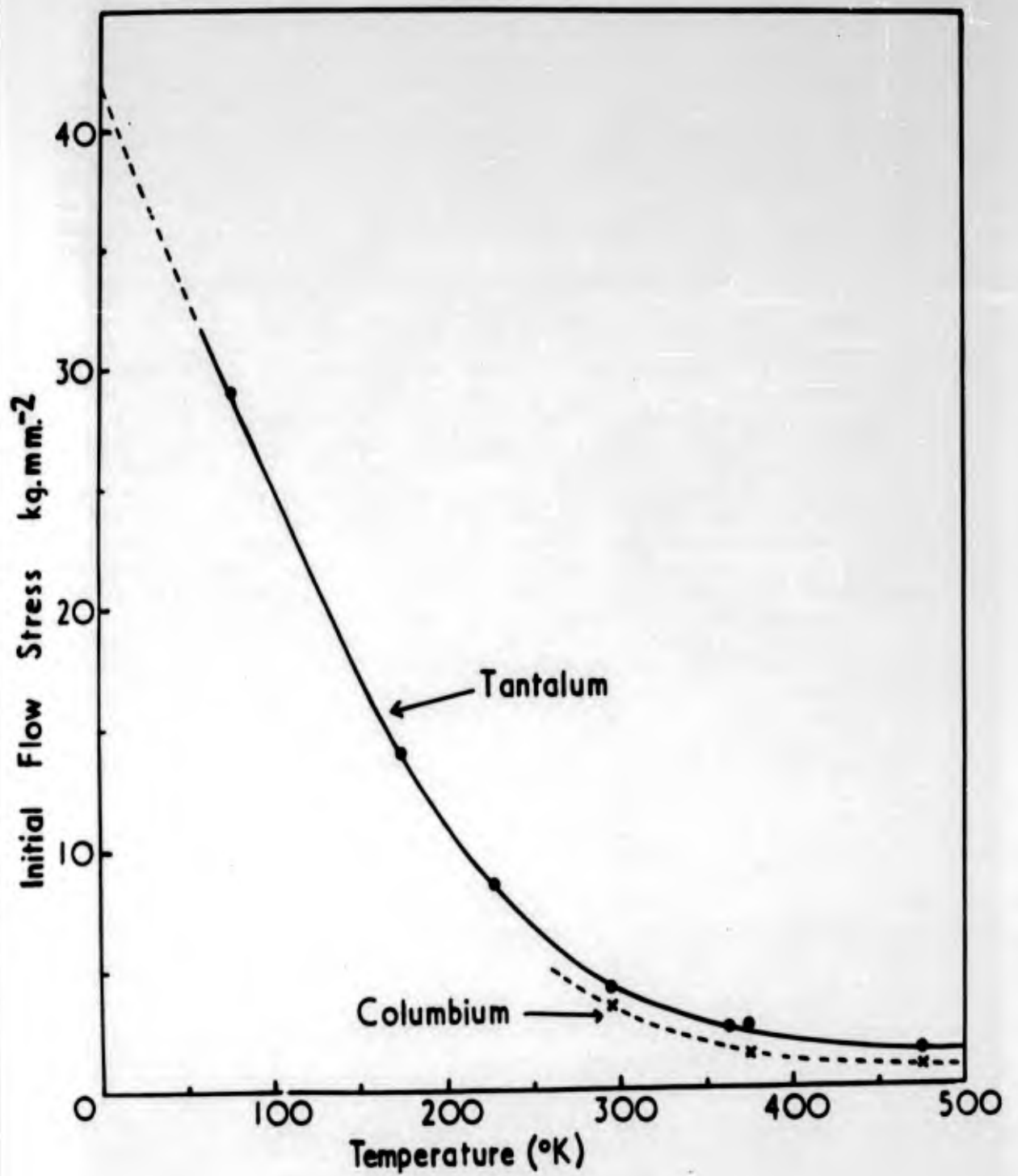


Fig. 105 - Temperature dependence of τ_0 for single crystals of tantalum and columbium.

4. The temperature dependence of the flow stress

A typical shear stress-shear strain curve obtained during a temperature cycling experiment on a tantalum crystal is shown in Fig. 106. The two test temperatures employed were 295°K and 473°K. Room temperature was used as the base temperature in all cases, and it was found that $\tau_T - \tau_{295}$ was independent of prestrain or decreased slightly with strain. This should be compared with f.c.c. metals in which the change of flow stress increases in proportion to the flow stress at one temperature (the Cottrell-Stokes⁽⁴⁾ law).

The variation of $\tau_T - \tau_{295}$ with temperature for tantalum crystals is shown in Fig. 107. For comparison the variation of $\tau_T - \tau_{295}$, using values of the initial flow stress, is also shown in Fig. 107. The temperature dependences of the reversible flow stress and the initial flow stress were found to be essentially the same. It therefore appears that the movement of dislocations are controlled by the same mechanism throughout the stress-strain curve. It is also deduced that τ_s is approximately the same at all strains for a given temperature, and therefore movement of dislocations is probably controlled by a "frictional" type of mechanism that is independent of the dislocation density. It was also noted that $\tau_s = 0$ in tantalum crystals above about 500°K (Fig. 107).

5. Strain rate dependence of the flow stress

Changing the strain-rate provides essentially the same information as changing the temperature, since $\Delta\tau$ is proportional to τ_s at a given temperature according to Thornton, Mitchell and Hirsch⁽⁵⁾. Curves of $\Delta\tau$ against τ for strain rate changes of a factor of ten are shown in Fig. 108 for tantalum single crystals deformed at 228°, 295°, 373° and 473°K. At all temperatures, $\Delta\tau$ was found to be independent of stress, in agreement with the temperature cycling results. Fig. 108 also shows that $\Delta\tau$ increases with decreasing temperature down to 228°K. However, $\Delta\tau$ was observed to decrease below this temperature in agreement with the results of Mordike⁽³⁾. The limited results obtained so far on columbium show that this metal behaves in much the same way as tantalum.

To compare the strain-rate ($\dot{\epsilon}$) dependence of the flow stress with the temperature dependence, the following proportionality was derived:

$$\frac{1}{T} \frac{\Delta\tau}{\ln(\dot{\epsilon}_1/\dot{\epsilon}_2)} = \frac{1}{T} \left[\frac{\partial\tau}{\partial \ln \dot{\epsilon}} \right]_T \quad (1)$$

where the inverse temperature term compensates for the larger thermal fluctuations at higher temperatures. The term indicative of the strain-rate sensitivity of the flow stress, $\frac{1}{T} \left[\frac{\partial\tau}{\partial \ln \dot{\epsilon}} \right]_T$, is plotted against temperature in Fig.

109. This curve is qualitatively the same as the temperature dependence of the flow stress in Fig. 106.

6. Activation energy calculations

The effective activation energy for the deformation of metals can be calculated in the following way. The strain-rate can be written

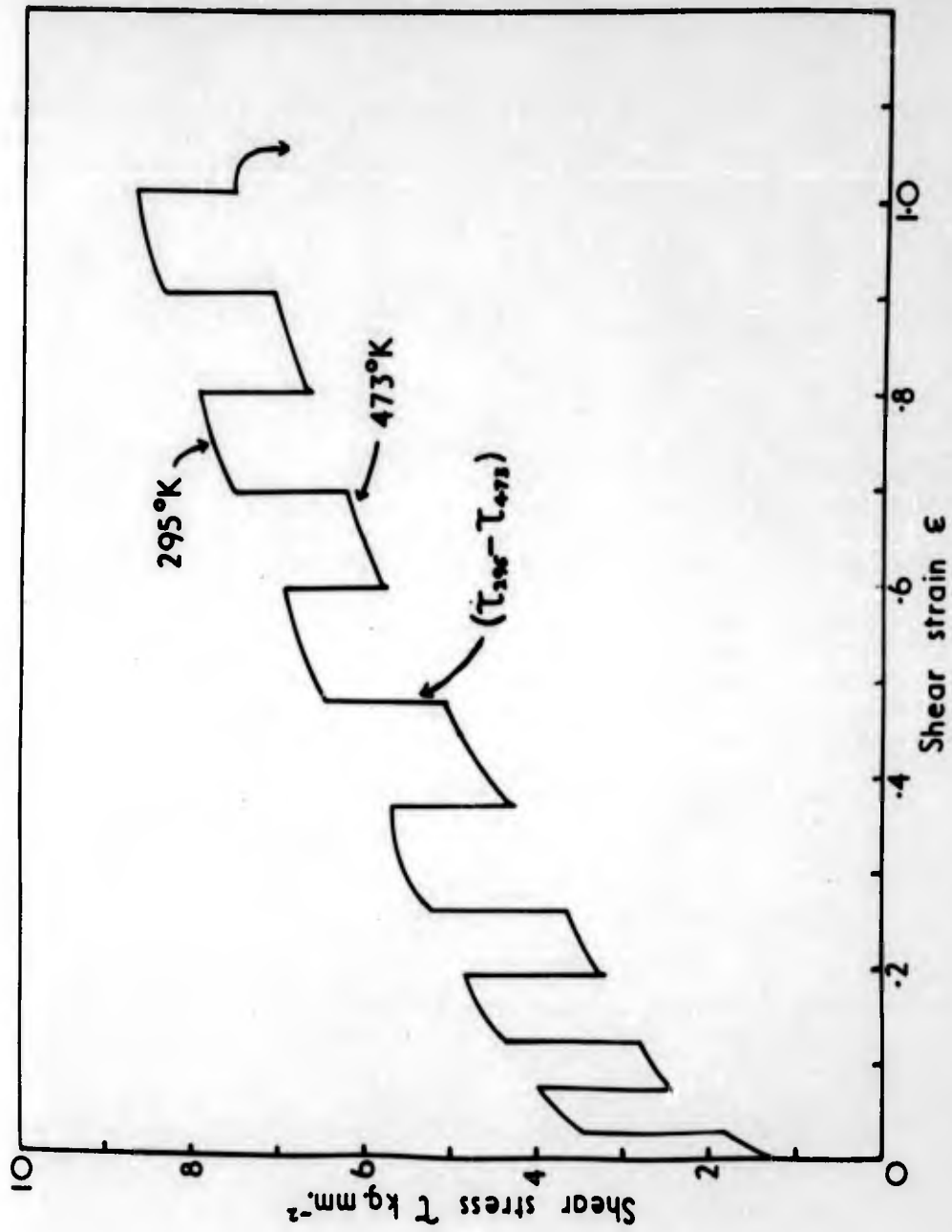


Fig. 106 - Temperature cycling experiment on a Tantalum crystal.

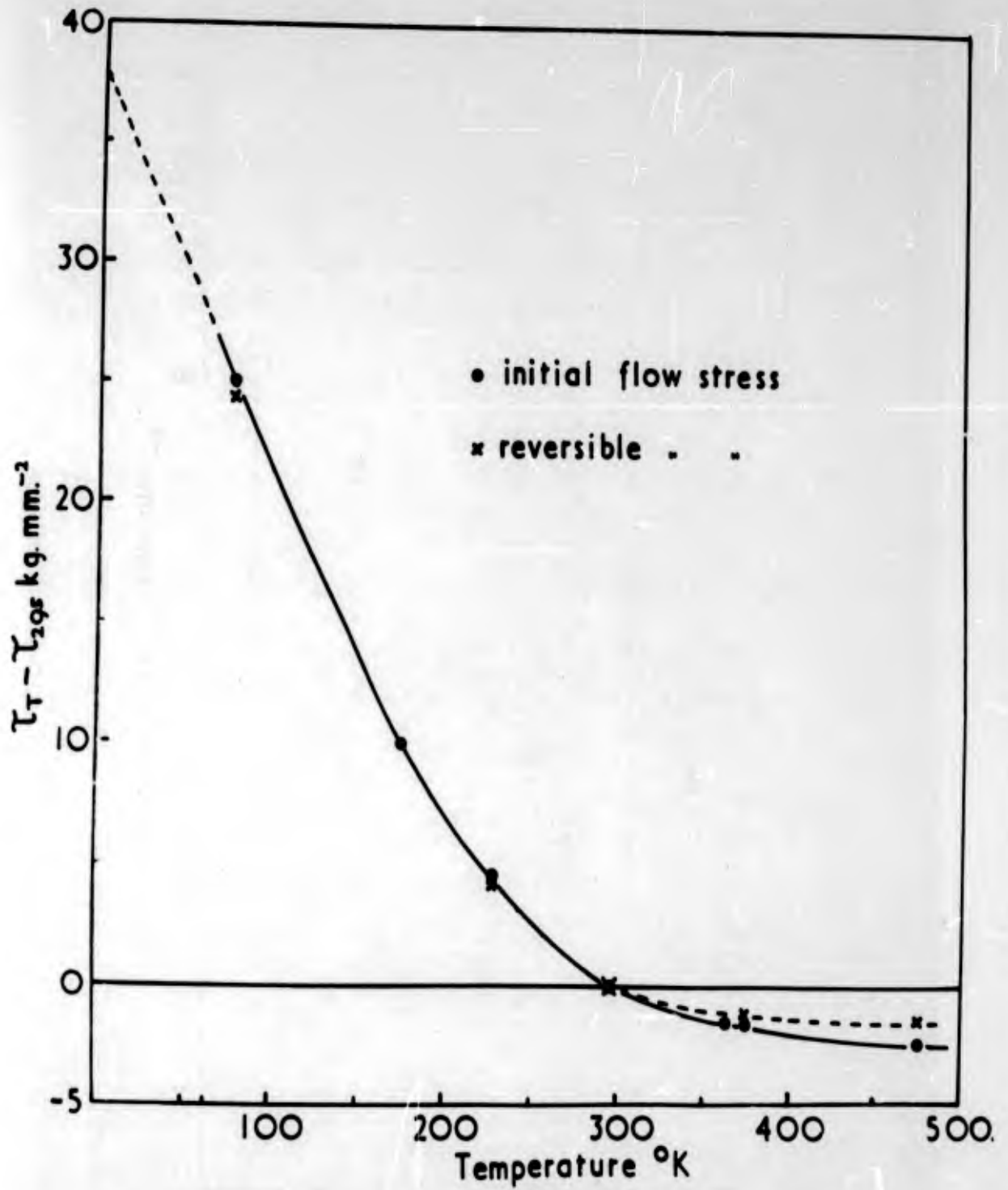


Fig. 107 - Temperature dependence of flow stress for tantalum single crystals.

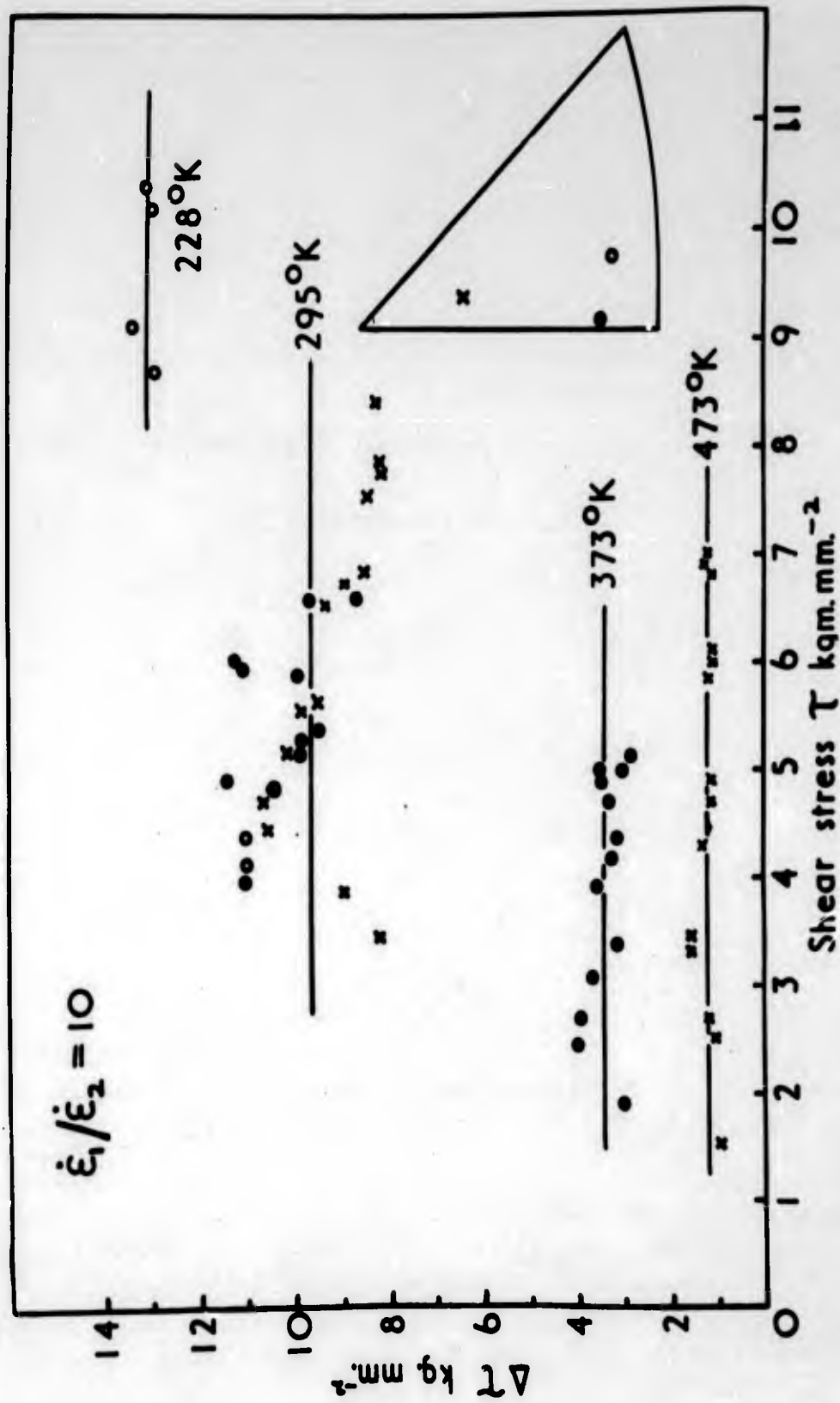


Fig. 108 - ΔT vs. τ curves for tantalum single crystals.

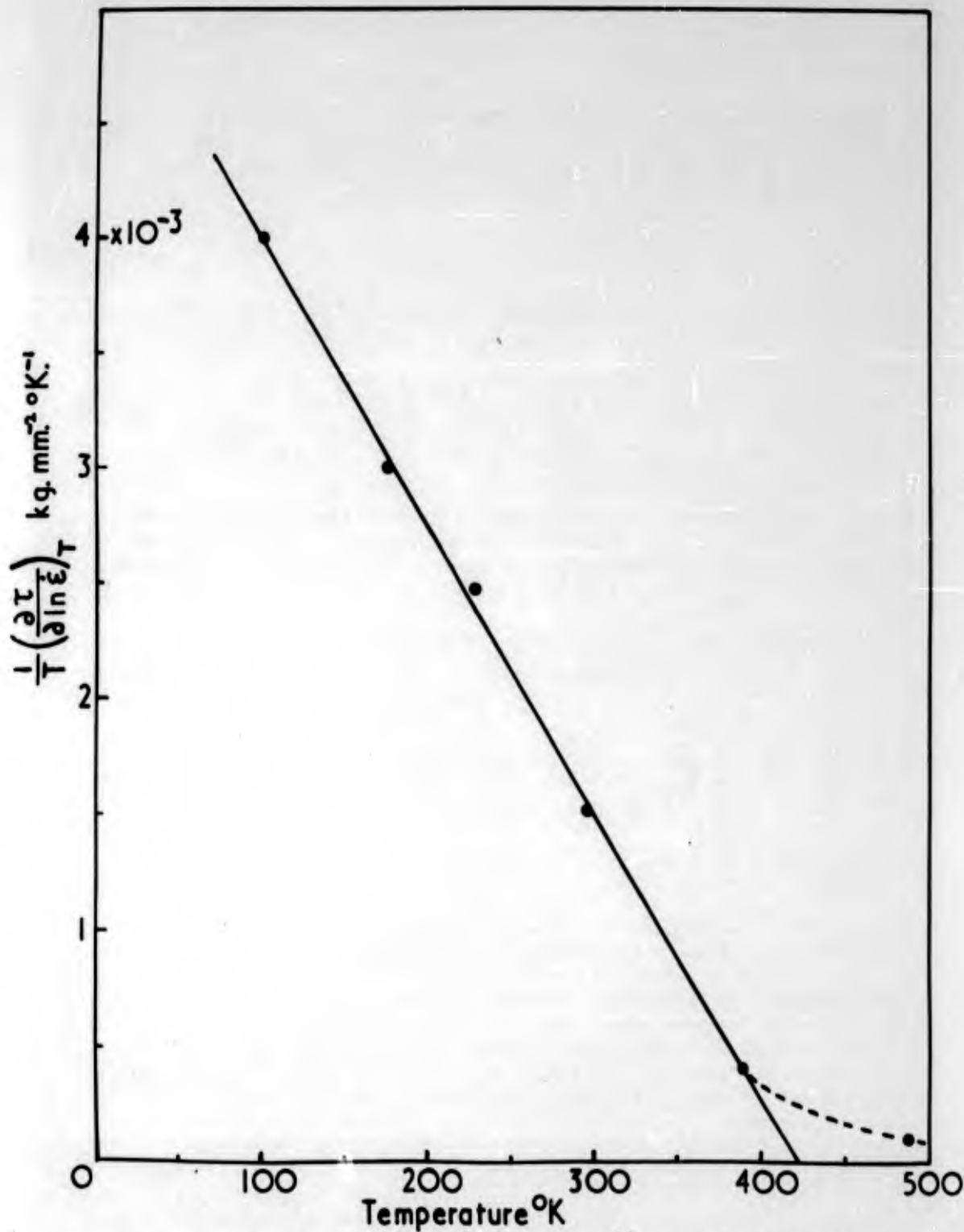


Fig. 109 - Temperature dependence of term indicative of strain-rate sensitivity of flow stress for tantalum single crystals.

$$\dot{\epsilon} = NAb \nu \exp (-H/kT) \quad (2)$$

where H is the activation energy, N is the density of activation sites, A is the area swept out by a dislocation element after activation, b is the Burgers vector and ν is the frequency of oscillation of a dislocation line. If it is assumed that H is a function of temperature and that

$$H = H(T, \tau_s) \quad (3)$$

then it can be shown from equations (2) and (3) that^(6,7)

$$H = -kT \left[\left(\frac{\partial \tau_s}{\partial T} \right) \dot{\epsilon} / \frac{1}{T} \left(\frac{\partial \tau}{\partial \ln \dot{\epsilon}} \right)_T \right] \quad (4)$$

Hence, using equation (4), H can be derived from the temperature and strain-rate dependence of the flow stress in Figs. 106 and 109. H is plotted against temperature in Fig. 110 for tantalum single crystals. It was found that H increases linearly with temperature at low temperatures, as expected from equation (1) since

$$H = kT \ln (NAb\nu/\dot{\epsilon}) \quad (5)$$

From the slope of the curve in Fig. 110, it was calculated that $\ln NAb\nu \approx 30$ or $NAb\nu \approx 10^{13} \text{ sec.}^{-1}$ using the experimental value of the strain-rate $\dot{\epsilon} = 5 \times 10^{-5} \text{ sec.}^{-1}$. Fig. 110 also shows that H tends to level off at about 450° to 500°K when $\tau_s = 0$. This constant value of the activation energy, H_0 , is that required to completely overcome a dislocation barrier without the aid of stress. For tantalum H_0 was found $\approx 1.5 \text{ e.v.}$, which agrees well with the value (1.6 e.v.) obtained by Conrad⁽⁸⁾.

A detailed discussion of these results is premature since experiments are still in progress to obtain data over a wide range of temperature and strain-rates (particularly for columbium). However, it seems fairly certain that the only mechanism that will explain the experimental results satisfactorily is the Peierls force. Other mechanisms such as dislocation-impurity reactions, dislocation-dislocation reactions, the movement of jogs on gliding dislocations and cross-slip have various draw-backs as discussed by Conrad⁽⁸⁾. A possible mechanism for a strong Peierls force in b.c.c. metals is discussed in the next section.

D. Peierls force in b.c.c. metals

The minimum energy configuration of a dislocation is determined by minimization of the misfit and elastic strain energies. In the b.c.c. system, screw dislocations with Burgers vector $1/2[111]$ have threefold symmetry, and therefore the possibility exists that the misfit may be spread along three planes.

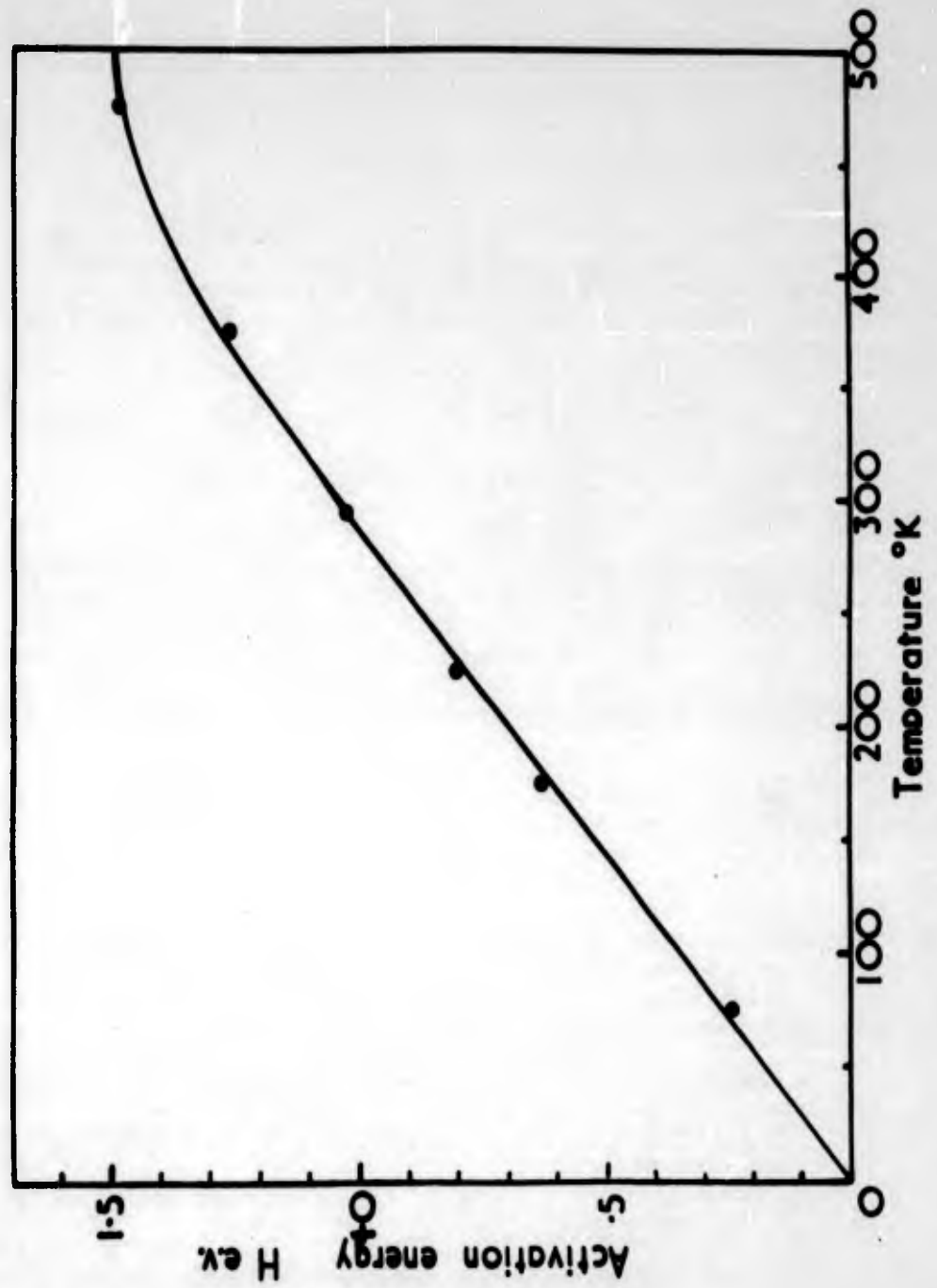
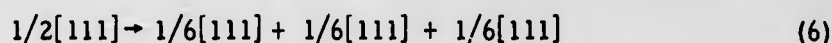


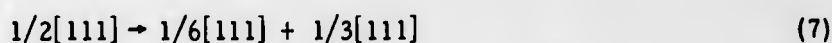
Fig. 110 - Activation energy vs. temperature for tantalum single crystals.

The conditions under which this may occur may be illustrated by the following example:-

A dislocation on a (211) plane in b.c.c. lattice can in principle disassociate according to the following reaction:



However, the stacking faults between the first and second dislocation, and between the second and third one are of different character. One of these faults corresponds to a twinning shear, the other to a structure not observed. It is therefore usually assumed that dissociation occurs only according to the following reaction:



the fault being of a twin type, the energy of the other fault being too large for further dissociation to be appreciable.

It is possible, however, for the dislocation to dissociate along three intersecting (211) planes forming twin type faults, the reaction being now described by equation (6). Such a dissociation is favored if the energy of the second type of fault is large. The dissociation could also take place on three intersecting (110) planes. The important point is that the screw dislocations could dissociate along three planes because of their three-fold symmetry in this lattice.

If such a dissociation occurs, a constriction must be formed before the dislocation can advance. This will lead to a temperature dependent frictional lattice stress, i.e. a Peierls stress. Some calculations are now under way to examine the conditions under which such a lattice frictional term might be important in b.c.c. metals. It is of interest to note that constrictions can occur as soon as the initial flow stress is reached and the Peierls stress can be overcome. Thus, cross-slip can always occur during plastic deformation; which explains why a prominent linear hardening region (such as occurs in f.c.c. single crystals) is never observed in b.c.c. metals.

It should be noted that this mechanism applies only to screw dislocations. The mobility of edge dislocations must be limited by some other Peierls mechanism. The observed flow stress may be controlled by the mobility of both edge and screw dislocations.

E. Electron microscopy

No significant results have yet been obtained in the sectioning experiments on tantalum and columbium single crystals after deformation. It is hoped to study the nature of dipoles and tangles of dislocations as observed by Low and Turkalo⁽⁹⁾ in silicon-iron single crystals.

As described previously⁽¹⁰⁾, observations on fatigued columbium and tantalum using an electron microscope heating stage were completed. These experiments establish quite firmly that direct observation of the annealing-out of dislocation loops in these metals cannot be accomplished by electron microscopy. This is because of the heavy contamination which rapidly occurs as specimens are heated in the relatively poor vacuum ($\sim 10^{-4}$ torr) of the microscope column. Hence, it has not been possible to comment further on the low activation energy values that have been found for the annealing-out of dislocation loops in columbium and tantalum.

REFERENCES

- (1) Ferriss, D. P., Rose, R. M., and Wulff, J., "Deformation of Tantalum Single Crystals", *Trans. AIME*, 224 (1962) 975.
- (2) Piercy, G. R., Cahn, R. W., and Cottrell, A. H., "A Study of Primary and Conjugate Slip in Crystals of Alpha-Brass", *Acta Met.*, 3 (1955) 331.
- (3) Mordike, B. L., "Plastic Deformation of Zone Refined Tantalum Single Crystals", *Z. Metallk.*, 55 (1962) 586.
- (4) Cottrell, A. H., and Stokes, R. J., "Effects of Temperature on the Plastic Properties of Aluminum Crystals", *Proc. Roy. Soc.*, A233 (1955) 17.
- (5) Thornton, P. R., Mitchell, T. E., and Hirsch, P. B., "The Strain Rate Dependency of the Flow Stress of Copper Single Crystals", *Phil. Mag.*, 7 (1962) 337.
- (6) Mitchell, T. E., Ph. D. Thesis, University of Cambridge (1962).
- (7) Conrad, H., and Wiedersich, H., "Activation Energy for Deformation of Metals at Low Temperature", *Acta Met.*, 8 (1960) 128.
- (8) Conrad, H., "Symposium on the Relation Between Structure and Properties of Metals", National Physical Laboratory (1963).
- (9) Low, J. R., and Turkalo, A. M., "Slip Band Structure and Dislocation Multiplication in Silicon-Iron Crystals", *Acta Met.*, 10 (1962) 215.
- (10) Lement, B. S., et al., "Substructure and Mechanical Properties of Refractory Metals," WADD Technical Report 61-181, Part II (1962).

Appendix A
List of Publications

The reports and papers (published, awaiting publication, or to be submitted) that have resulted at least partly from the work accomplished on this program are listed below:

1. Lement, B. S. et al., "Substructure and Mechanical Properties of Refractory Metals", Contract No. AF33(616)6838, Progress Report No. 1 (April 30, 1960).
2. Lement, B. S. et al., "Substructure and Mechanical Properties of Refractory Metals", Contract No. AF33(616)-6838, Progress Report No. 2 (October 31, 1960).
3. Lement, B. S., Thomas, D. A., Weissman, S., Owen, W. S., and Hirsch, P. B., "Substructure and Mechanical Properties of Refractory Metals", WADD T.R. 61-181, (August 1961).
4. Lement, B. S. et al., "Substructure and Mechanical Properties of Refractory Metals", Contract No. AF33(616)6838, Progress Report No. 3 (November 15, 1961).
5. Lement, B. S., Thomas, D. A., Weissman, S., Owen, W. S., and Hirsch, P. B., "Substructure and Mechanical Properties of Refractory Metals", WADD TR-61-181, Part 2, (October 1, 1962).
6. Lement, B. S., et al., "Substructure and Mechanical Properties of Refractory Metals", Contract No. AF33(657)-8424, Progress Report No. 1 (August 15, 1962).
7. Lement, B. S. and Perlmutter, L., "Mechanical Properties Attainable by Alloying of Refractory Metals", *Journal of the Less-Common Metals*, 2 (April-August 1960) 253.
8. Weissman, Sigmund, Passmore, Edmund, and Allen, Steven, "Changes in Mechanical Properties and Dislocation Structure During Recovery Annealing of Tungsten," to be submitted.
9. Cohen, Morris, Weissman, S., and Lement, B. S., "Substructure in Refractory Metals", AIME Chicago Section Presentation, (April 12-13, 1962).
10. Thomas, David, A. and Peck, J. F., "A Study of Fibrous Tungsten and Iron," *Trans. AIME*, 221 (December 1961) 1240.
11. Weissmann, S., "Substructure and Dislocation Networks in Tungsten", submitted as Chapter in Imperfections in Crystals, Interscience Publishers, Inc. (1962).

12. Weissmann, S. and Imura, T., Discussion to chapter on Tungsten and Tungsten-Base Alloys, in Refractory Metals and Alloys, Interscience Publishers (1961), 349.
13. Keh, A. and Weissmann, S., Dislocation Structure in B. C. C. Metals, Prec. 1961, Submitted to International Conference on Impact of Electron Microscopy on Strength on Crystals, Interscience Publishers (1962).
14. Gilbert, A., Hull, D., Owen, W. S., and Reid, C. N., "Yield of Polycrystalline Tantalum", J. Less Common Met. October 1962, p. 399.
15. Hull, D., McIvor, I. D., and Owen, W. S., "Substructure of Annealed Polycrystalline Tantalum", J. Less Common Met. 4 (1962) 399.
16. Segall, R. L., "Annealing Twins and Stacking Faults in Niobium", Acta Met., 9 (October 1961) 975.
17. Owen, W. S. and Hull, D., "The Fracture Transitions in Refractory Metals", A.I.M.E. Symposium on Refractory Metals, Chicago, 1962, awaiting publication.
18. Owen, W. S., and Rosenfield, A. R., "The Stable/Unstable Plastic Flow Transition Temperature in Annealed Tantalum," J. Institute of Metals, 91 (1962) 117.
19. Rosenfield, A. R., "The Significance of σ_i ", J. Inst. Met., 91 (1962) 104.
20. Hull, D., McIvor, I. D., and Owen, W. D., "Variation of Flow Stress in Tantalum," N.P.L. Conference, January 1963, awaiting publication.
21. Rosenfield, A. R., and Owen, W. S., "The Strain Aging of a Dilute Tantalum-Oxygen Alloy," A.I.M.E., September 1962, awaiting publication.
22. Hull, D. and Owen, W. S., "The Interaction of Interstitial Solute and Substructure in Refractory Metals," A.G.A.R.D. Conference, Oslo, June 1962, awaiting publication.
23. Rosenfield, A.R. and Owen, W. S., "Strain Aging in B. C. C. Metals," ASD Symposium, Florida, December 1962, awaiting publication.
24. Owen, W.S., "The Variation of Flow Stress with Dislocation Density in Tantalum", ASD Symposium, Florida, December 1962, awaiting publication.

25. Lement, B. S., "Effect of Substructure on Fracture on Tungsten and Molybdenum", Discussion at ASD Conference, Florida, December 1962, awaiting publication.
26. Weissmann, S., "The Observations and Measurement of Substructures in Crystals by X-ray Techniques", ASD Symposium, Florida, December 1962, awaiting publication.
27. Weissmann, S. and Hosokawa, N., "Yielding of Tantalum Single Crystal", to be published in Proceedings of International Symposium on "Structure and Properties of Materials", Melbourne, May 1963.
28. Meieran, E. S., "Use of the Reciprocal Lattice for the Development of a New Pole Figure Technique," Rev. Sci. Inst. 33, 319 (1962).
29. Meieran, E. S. and Thomas, D.A., "Preparation of Wires for Examination by Transmission Electron Microscopy," Trans. AIME 227, 284 (1963).
30. Meieran, E. S. and Thomas, D.A., "A Transmission Electron Microscopy Study of Deformed and Annealed Tungsten Wire," in preparation.
31. Meieran, E. S., Kaplow, R., and Thomas, D.A., "A Twist Substructure in Deformed Tungsten Wire," in preparation.
32. Meieran, E. S. and Richman, M. H., "An Analytical Method for Calculating Electron Diffraction Patterns Containing Twin Reflections," to be published in Trans. AIME.
33. Comerford, M. F. and Thomas, D.A., "Substructure and Mechanical Properties of Deformed and Annealed Iron-3% Silicon," in preparation.
34. Passmore, E. M., Andersson, C. A., and Lement, B. S., "The Effect of Deformation and Recovery on the Ductile-Brittle Transition in Tungsten Wire," in preparation.

Appendix B

Fabrication of Experimental Materials

(Tables B-1 to B-11)

Table B-1

Interstitial Contents of Fabricated Experimental Materials

<u>Item</u>	<u>Form</u>	<u>or Diameter</u> <u>rolls</u>	<u>Interstitial Content in ppm.</u>			
			<u>C</u>	<u>N</u>	<u>O</u>	<u>H</u>
Mo-E1-E-1	strip	30	32	-	22	-
Mo-E1-E-2	strip	30	34	-	20	-
Mo-E1-F-1	strip	30	13	4	23	0.8
Mo-E1-H-7	strip	30	42	-	31	-
Mo-E1-H-1	strip	30	53	-	17	-
Mo-E1-TA	rod	230	33	15	5.5	-
Mo-E1-T ₁ B	rod	230	27	10	6	-
Mo-E2-C-1	strip	30	44	-	15	-
Mo-E2-E-1	strip	30	75	3	46	-
Mo-E2-H-1	strip	30	40	-	13	-
Mo-E2-H-8	strip	30	36	-	65	-
Mo-E2-1*	rod	230	38	5	381	1.0
Mo-E2-1	rod	230	49	-	2.5	-
Mo-E2-1	rod	230	56	-	2.1	-
Mo-E2-2	rod	230	54	-	3.3	-
Mo-E2-2	rod	230	59	-	17	-
Mo-E3-E-1	strip	30	-	7	18	-
Mo-E3-E-1	strip	30	-	8	26	-
Mo-E3-F-2	strip	30	12	7	29	0.1
Mo-E3-H-4	strip	30	-	14	12	-
Mo-E3-H-8	strip	30	-	15	13	-
Mo-E3-T ₂ A	rod	230	15	17	8.3	-
Mo-E3-T ₂ C	rod	230	24	8	5.0	-
Ta-E1-W2-.067	wire	30	6	-	24	5
Ta-E2-W0-.030	wire	30	63	-	50	27
Ta-E2-W1-.030	wire	30	62	-	96	-
Ta-E2-W1-.072	wire	30	67	-	48	-
Ta-E3-W0-.030	wire	30	-	19	220	21
Ta-E3-W1-.030	wire	30	-	26	240	-
Ta-E3-W1-.072	wire	30	-	20	70	-
Ta-E4-W0-.030	wire	30	-	-	65	25
Ta-E4-W1-.030	wire	30	-	-	50	-
Ta-E4-W1-.072	wire	30	-	-	52	-
Ta-E5-W0-.030	wire	30	29	9	41	6
Ta-E5-W1-.030	wire	30	28	6	167	3

*Specimen probably not representative

Table B-1 (cont'd)

<u>Item</u>	<u>Form</u>	<u>or Diameter</u> <u>mils</u>	<u>Interstitial Content in ppm.</u>			
			<u>C</u>	<u>N</u>	<u>O</u>	<u>H</u>
Ta-E1-S1-.030	strip	30	10	18	46	2
Ta-E1-S1-.150	strip	30	8	17	40	125
Ta-E2-S1-.030	strip	30	70	-	72	-
Ta-E2-S1-.150	strip	30	67	-	-	-
Ta-E3-S1-.030	strip	30	-	103	39	-
Ta-E3-S1-.150	strip	30	-	65	-	-
Ta-E4-S1-.030	strip	30	-	-	132	-
Ta-E4-S1-.150	strip	30	-	-	150	-
Ta-E6-Q	rod	125	3	15	2	-
Cb-E1-W0-.030	wire	30	15	79	128	8
Cb-E1-W1-.030	wire	30	27	50	140	4
Cb-E1-W1-.072	wire	30	12	80	161	9
Cb-E4-W0-.030	wire	30	-	-	687	17
Cb-E4-W1-.030	wire	30	-	-	767	-
Cb-E4-W1-.072	wire	30	-	-	628	-
Cb-E5-W0-.030	wire	30	90	35	91	5
Cb-E5-W1-.030	wire	30	45	50	550	9
Cb-E1-S1-.030	strip	30	23	46	130	2
Cb-E1-S1-.150	strip	30	20	90	184	65
Cb-E4-S1-.030	strip	30	-	-	626	-
Cb-E4-S1-.150	strip	30	-	-	694	-
Cb-E6-L	rod	125	3	27	25	.3

Table B-2
Results of Fabrication of Tantalum and Columbium Experimental
Materials to 30-mil Wire

<u>Item</u>	<u>Condition</u>	<u>Amount feet</u>
Ta-E1-W0	80% R.A.	59
Ta-E1-W1-.030 to .067	0-80% R.A.	870
Ta-E1-W2-.030	recryst.	174
Ta-E1-W2-.0303 to .067	2-80% R.A.	1315
Ta-E2-W0	90% R.A.	222
Ta-E2-W1-.030	recryst.	126
Ta-E2-W1-.0333 to .072	2-80% R.A.	731
Ta-E3-W0	90% R.A.	228
Ta-E3-W1-.030	recryst.	134
Ta-E3-W1-.0333 to .072	2-80% R.A.	714
Ta-E4-W0	90% R.A.	238
Ta-E4-W1-.030	as recryst.	119
Ta-E4-W1-.0333 to .072	2-80%	740
Ta-E5-W0	80% R.A.	60.4
Ta-E5-W1	as recryst.	59
Cb-E1-W0	70% R.A.	150
Cb-E1-W1-.030	as recryst.	170
Cb-E1-W1-.0333 to .072	2-80% R.A.	1216
Cb-E4-W0	77% R.A.	170
Cb-E4-W1-.030	as recryst.	218
Cb-E4-W1-.0333 to .072	2-80% R.A.	1250
Cb-E5-W0	80% R.A.	76.1
Cb-E5-W1	as recryst.	44

Table B-3

Results of Fabrication of Tungsten and Molybdenum Experimental
Materials to Wire

<u>Item</u>	<u>Condition</u>	<u>Size mils</u>	<u>Fabricated Amount feet</u>
W-E5			16 (total)
crystal UC 33	rolled at 800°C	61 sq. 95 sq.	
crystal UC 34	rolled at 800°C	85 sq.	
crystal UC 35	rolled at 800°C	85 sq.	
crystal UC 41	rolled at 800°C	95 sq.	
crystal UC 44	rolled at 800°C	100 sq.	
crystal UC 46	rolled at 800°C	100 sq.	
crystal UC 47	rolled at 800°C	108 sq.	
crystal UC 48	rolled at 800°C	116 sq.	
crystal UC 52	rolled at 800°C	108 sq.	
crystal UC 53	rolled at 800°C	116 sq. 118 sq.	
W-E1 (S-154 T)	swaged to 0.275 in.		4
W-E1 (S-167, N, T)	swaged to 0.275 in.		16
Mo-E1	as-swaged rod	250	22
Mo-E2	as-swaged rod	250	8
Mo-E3	as-swaged rod	250	11.5
	recrystallized at 1625°C and reduced 75% at 400°C	30	100
Mo-E5			25 (total)
crystal Mo-32	recrystallized at 1000°C and reduced 76% at 400°C	30	
crystal Mo-33	recrystallized at 1000°C and reduced 76% at 400°C	30	
crystal Mo-34	recrystallized at 1000°C and reduced 76% at 400°C	30	
crystal Mo-35	recrystallized at 1000°C and reduced 76% at 400°C	30	
crystal Mo-36	recrystallized at 1000°C and reduced 76% at 400°C	30	
crystal Mo-41	recrystallized at 1100°C and reduced 76% at 400°C	30	
crystal Mo-43	recrystallized at 1100°C and reduced 96% at 400°C	30	
crystal Mo-44	recrystallized at 1100°C and reduced 96% at 400°C	30	
crystal Mo-46	recrystallized at 1100°C and reduced 96% at 400°C	30	

Table B-4

Results of Fabrication of Tantalum and Columbium
Experimental Materials to Strip

<u>Item</u>	<u>Fabricated Amount</u> <u>feet</u>
Ta-E1-S0	6.6
Ta-E1-S1-.030 to .150	57
Ta-E2-S0	12.1
Ta-E2-S1-.005	7.8
Ta-E2-S1-.030 to .150	47.5
Ta-E3-S0	12.8
Ta-E3-S1-.005	5.0
Ta-E3-S1-.030 to .150	57.5
Ta-E4-S0	8.1
Ta-E4-S1-.005	7.3
Ta-E4-S1-.030 to .150	50
Ta-E5-S0	12.7
Ta-E5-S1	12.1
Cb-E1-S0	7.9
Cb-E1-S1-.005	2.2
Cb-E1-S1-.030 to .150	55
Cb-E4-S0	3.7
Cb-E4-S1-.005	5.2
Cb-E4-S1-.030 to .150	45
Cb-E5-S0	15.1
Cb-E5-S1	6.5

Table B-5

Results of Fabrication of Tungsten and Molybdenum Experimental
Materials to Strip

Item	Condition	Thickness mils	Width inch	Fabricated Amount feet
W-E1-H (S - 152, N, C)	recrystallized at 1450°C and reduced 87% at 1300 to 1000°C	38	1-3/8	2.3
W-E1-C (S - 157)	hot rolled 75% at 1400°C and reduced 70% at 1100°C	40	1-3/4	3.5
W-E1-D (S - 157)	recrystallized at 1450°C and reduced 39% at 1300 to 1000°C	37	2-1/4	0.8
W-E2-C (S - 168 N)	hot rolled 58% at 1400°C and reduced 70% at 1300 to 1100°C	40	1-7/8	1.7
W-E2-H (S - 168 C)	recrystallized at 1450°C and reduced 84% at 1300 to 1000°C	40	1-5/8	1.4
W-E2-H (S - 154 N)	recrystallized at 1450°C and reduced 91% at 1300 to 1000°C	33	1-3/4	0.8
Mo-E5	2.4 total
crystal Mo-25	reduced 92% at 400°C	8	7/16	-
crystal Mo-42	recrystallized at 1100°C and reduced 55% at 400°C	12	1/2	-
crystal Mo-45	recrystallized at 1100°C and reduced 55% at 400°C	11	1/2	-
Mo-E1				
Mo-E1-C	recrystallized at 1200°C and reduced 5% at 1250 to 1000°C	44	1-3/4	1.6
Mo-E1-D	recrystallized at 1200°C and reduced 40% at 1250 to 900°C	39	1-3/4	3.1
Mo-E1-E	recrystallized at 1200°C and reduced 46% at 1250 to 400°C	35	1-3/4	3

Table B-5 (Continued)

Item	Condition	Thickness mils	Width inch	Fabricated Amount feet
Mo-E1-F	recrystallized at 1200°C and reduced 58% at 1250 to 400°C	32	1-3/4	1.1
Mo-E1-G	recrystallized at 1200°C and reduced 68% at 1250 to 400°C	32	1-3/4	4.5
Mo-E1-H	recrystallized at 1200°C and reduced 88% at 1000 to 400°C	32	1-5/8	8.7
Mo-E2-B	recrystallized at 1200°C and reduced 96% at 1250 to 400°C	8	1-3/4	2
Mo-E2-C	recrystallized at 1200°C	33	1-1/2	1.1
Mo-E2-D	recrystallized at 1200°C and reduced 40% at 1250 to 900°C	30	1-5/8	1.3
Mo-E2-E	recrystallized at 1200°C and reduced 46% at 1250 to 400°C	31	1-1/2	4.1
Mo-E2-F	recrystallized at 1200°C and reduced 58% at 1250 to 400°C	30	1-1/2	5
Mo-E2-G	recrystallized at 1200°C and reduced 68% at 1000 to 400°C	29	1-5/8	5.1
Mo-E2-H	recrystallized at 1200°C and reduced 88% at 1600 to 400°C	31	1-5/8	8.1
Mo-E3-B	recrystallized at 1200°C and reduced 96% at 1200 to 400°C	10	1-3/4	5.4
Mo-E3-D	recrystallized at 1200°C and reduced 40% at 1250 to 900°C	38	1-3/4	2
Mo-E3-E	recrystallized at 1200°C and reduced 46% at 1250 to 400°C	35	1-3/4	1.8
Mo-E3-F	recrystallized at 1200°C and reduced 58% at 1250 to 400°C	32	1-3/4	3.4
Mo-E3-G	recrystallized at 1200°C and reduced 68% at 1250 to 400°C	33	1-3/4	3.1
Mo-E3-H	recrystallized at 1200°C and reduced 86% at 1000 to 400°C	32	1-5/8	9.5
Mo-E4-C	hot rolled 64% at 1250°C and reduced 86% at 900 to 600°C	35	1-5/8	1.2
Mo-E4-E	recrystallized at 1300°C and reduced 50% at 900 to 600°C	30	2	1.1

Table B-6

Fabrication Schedule of Single Crystal Molybdenum Experimental
Materials to Wire and Strip

A. Wire

1. As received crystal.
2. Grind to 0.185 inch diameter x length.
3. Electropolish to 0.180 inch diameter x length.
4. Roll in diamond shaped grooves to 0.064 inch square (84% reduction at 10% per pass) at 400°C.
5. Electropolish.
6. Recrystallize as desired.
7. Roll in diamond shaped grooves to 0.052 inch square (34% reduction at 10% per pass) at 400°C.
8. Swage to 0.0355 inch diameter (63% reduction at 10% per pass) at 400°C.
9. Centerless grind to 0.0305 inch diameter.
10. Electropolish to .030 inch diameter.

Total reduction in area - 96% (76% after recrystallization)

Notes:

The major change in the original fabrication schedule is the insertion of a centerless grinding operation when it was found that proper dimensional control could not be maintained during electropolishing from 0.035 inch. Material yields after the various operations varied considerably. Initial conditioning of the as received crystals resulted in an average loss in weight of approximately 50%. Based on the weight after conditioning, no significant losses occurred during rolling to 0.064 inch square (99% recovery). After recrystallization, however, substantial losses were encountered (including sampling and final grinding) and recoveries ranged from 0-65%.

Recrystallization was accomplished by annealing in hydrogen for times up to one hour and temperatures up to 1160°C. It was found necessary to redetermine the recrystallization temperature for each crystal since none were recrystallized after annealing for one-half hour at 1000°C, the treatment found earlier to cause complete recrystallization. Crystals Mo-23, 32, 33, 34, 35 and 36 were recrystallized after one hour at 1000°C; crystal 41 recrystallized after an additional one-half hour anneal at 1100°C and crystal 29 recrystallized only after an additional one hour anneal at 1160°C.

Table B-6 (continued)

B. Strip

1. As received crystal.
2. Grind to 0.150 inch thick by length.
3. Electropolish to 0.145 inch thick by length.
4. Cross roll at 400°C (50% reduction in two passes).
5. Long roll at 400°C to 0.010 inch thick by length at 25% per pass.
6. Electropolish.

Total reduction in height 92% (50-60% after recrystallization)

Notes:

The major change in the original fabrication schedule was the substitution of two cross-roll passes for the single 50% reduction used in step 4. This change was necessitated by the greater length of the crystals used here over the small pieces used earlier. Since the crystals could not be electropolished uniformly, they were shipped after cleaning at the final rolled sizes of 8, 12 and 11 mils respectively. The material yields were poor with recoveries amounting to about 30%.

Recrystallization was accomplished by annealing in hydrogen for times up to one hour and temperatures up to 1160°C. Again it was found necessary to redetermine the recrystallization temperature of both crystals (Mo-42 and Mo-45) since neither was found to be recrystallized after annealing for one-half hour at 1000°C. Mo-42 recrystallized only after an additional anneal of one-half hour at 1100°C and Mo-45 only after an additional anneal of one hour at 1160°C. There was some doubt that recrystallization of Mo-45 was complete, even after this drastic treatment.

Table B-7

Fabrication Schedule for Single Crystal Tungsten Experimental
Materials to Wire

1. As received crystal.
2. Grind to 0.185 inch diameter by length.
3. Electropolish to 0.180 inch diameter by length.
4. Roll in diamond shaped grooves to .064 inch square (84% reduction at 10% per pass) at 800°C.
5. Electropolish and sample for recrystallization study to be made by ManLabs.
6. Recrystallize as instructed.
7. Roll in diamond shaped grooves to .052 inch square (34% reduction at 10% per pass) at 800°C.
8. Swage to .0355 inch diameter (63% reduction at 10% per pass) at 800°C.
9. Polish to .030 inch diameter.

Total reduction in area - 96% (76% after recrystallization)

Notes:

The main changes made in the original schedule are the substitution of rolling for swaging down to 0.050 inch square and the elimination of the cladding. An additional change was innovated because of the greater length of the starting crystals. Since groove rolling is essentially a batch process at these sizes, it was necessary to cut the crystals for convenience in heating and handling, after they had been extended to a certain length. The practice chosen was to cut the crystals in thirds after 50% reduction in area. This yielded samples short enough (6-7 inches) for convenient handling during rolling, and also long enough at 0.052 inch to be entered into the continuous swaging machine. The crystals were, however, only rolled at 800°C, at which time the rolls required re-surfacing.

Table B-8

Fabrication Schedule for Mo-E4 Strip Bar

A. Mo-E4 (S-169)

1. Cut off nose and tail ends, macroetch, and photograph.
2. Billet machined and hand conditioned. See Table B-10-A.
3. Cut billet into 2 sections as shown below:

Nose End	<u>S-169-N</u> <u>6-1/2"</u>	<u>S-169-T</u> <u>4-1/2"</u>	Tail End
----------	---------------------------------	---------------------------------	----------

4. Break all sharp edges.
5. Forging in argon atmosphere.

<u>Identity</u>	<u>Item</u>	<u>Forge Temp. °C</u>	<u>Forged Size</u>
S-169-N	CDE	1450	1-3/4" x 5-5/8" x 3/4"
S-169-T	H	1450	Cracked during forging (scrap)

Table B-9

Fabrication Schedule for Mo-E4 Strip

A. Mo-E4 (S-169)

<u>Item</u>	<u>Starting Thickness, In.</u>	<u>Final Thickness, In.</u>	<u>Rolling Temp., °C</u>	<u>% Reduction</u>
D	0.720	0.254	1250	65
E	0.720	0.254	1250	65
	0.254	0.078	1000	69
	Conditioned and recrystallized - 1300°C (1 hour)			
	0.070	0.041	900	41
	0.039	0.033	600	15
	Conditioned 0.030" x 2" x 13-1/2"			
C	0.720	0.257	1250	64
	0.254	0.168	900	34
	0.164	0.039	600	76
	Conditioned 0.035" x 1-5/8" x 15-1/4"			

Table B-10

Fabrication Schedule for W-E1, W-E2, and W-E4 Wire and Strip Bars

A. W-E1 (S-158)

1. Cut off nose and tail ends, macroetch, and photograph.
2. Billet machined and hand conditioned. See Table B-10-A.
3. Cut billet into 3 sections as shown below:

Nose End	<u>S-158-N</u> <u>3-1/2"</u>	<u>S-158-C</u> <u>5"</u>	<u>S-158-T</u> <u>6-1/2"</u>	Tail End
----------	---------------------------------	-----------------------------	---------------------------------	----------

4. Break all sharp edges.
5. Forging in argon atmosphere

<u>Identity</u>	<u>Item</u>	<u>Forge Temp. °C</u>	<u>Forged Size</u>
S-158-N	C	1450	1-3/4" x 3-7/8" x 5/8"
S-158-C	H	1450	1-3/8" x 5-1/2" x 7/8"*
S-158-T	E	1450	1-1/8" x 7-3/4" x 5/8"

*Cracked-scrap.

B. W-E1 (S-152)

1. Cut off nose and tail ends, macroetch, and photograph.
2. Billet machined and hand conditioned. See Table B-10-A.
3. Cut billet into 5 sections as shown below:

Nose End	<u>S-152-N</u> <u>7-1/2"</u>	<u>S-152-N'</u> <u>6-7/8"</u>	<u>S-152-C</u> <u>3-1/2"</u>	<u>S-152-T'</u> <u>2-7/8"</u>	<u>S-152-T</u> <u>Scrap</u>	Tail End
----------	---------------------------------	----------------------------------	---------------------------------	----------------------------------	--------------------------------	----------

4. Break all sharp edges.
5. Forging in Argon Atmosphere

<u>Identity</u>	<u>Item</u>	<u>Forge Temp. °C</u>	<u>Forged Size</u>
S-152-N	DE	1450	1-3/4" x 10-1/4" x 5/8"
S-152-N'	H	1450	1-1/2" x 8" x 7/8"
S-152-C	C	1450	1-3/4" x 4-5/8" x 5/8"
S-152-T'	C	1450	1-3/4" x 3-1/2" x 11/16"

C. W-E1 (S-154)

1. Cut off nose and tail ends, macroetch, and photograph.
2. Billet machined and hand conditioned. See Table B-10-A.
3. Cut billet into 3 sections as shown below:

Nose End	<u>S-154-N</u> <u>3"</u>	<u>S-154-C</u> <u>2-1/8"</u>	<u>S-154-T</u> <u>5-3/8"</u>	Tail End
----------	-----------------------------	---------------------------------	---------------------------------	----------

4. Break all sharp edges.

Table B-10 (Cont'd)

5. Forging in argon Atmosphere

<u>Identity</u>	<u>Item</u>	<u>Forge Temp. °C</u>	<u>Forged Size</u>
S-154-N	CE	1450	1-7/8" x 3-5/16" x 11/16"
S-154-C	H	1450	1-1/2" x 2-1/2" x 7/8"
*S-154-T	Wire Bar	1400	3/4" x 8-9/16" 3/4" x 4-15/16"

* Cut in half during forging to facilitate handling.

D. W-E1 (S-157)

1. Cut off nose and tail ends, macroetch, and photograph.
2. Billet machined and hand conditioned. See Table B-10-A.
3. Cut billet into 2 sections as shown below:

<u>Nose End</u>	<u>S-157-N</u>	<u>S-157-T</u>	<u>Tail End</u>
	8"	4"	

4. Break all sharp edges.
5. Forging in argon atmosphere

<u>Identity</u>	<u>Item</u>	<u>Forge Temp. °C</u>	<u>Forged Size</u>
S-157-N	CDE	1450	1-5/8" x 11" x 11/16"
S-157-T	H	1450	1-7/16" x 4-3/4" x 7/8"

E. W-E2 (S-168)

1. Cut off nose and tail ends, macroetch, and photograph.
2. Billet machined and hand conditioned. See Table B-10-A.
3. Cut billet into 5 sections as shown below:

<u>Nose End</u>	<u>S-168-N</u>	<u>S-168-N'</u>	<u>S-168-C</u>	<u>S-168-T'</u>	<u>S-168-T</u>	<u>Tail End</u>
	3-1/2"	5-3/4"	Scrap	3-3/8"	5-3/4"	

4. Break all sharp edges.
5. Forging in argon atmosphere

<u>Identity</u>	<u>Item</u>	<u>Forge Temp. °C</u>	<u>Forged Size</u>
S-168-N	H	1450	1-7/16" x 4-1/8" x 15/16"
S-168-N'	CDE	1450	1-1/2" x 8-7/8" x 11/16"
S-168-T'	H	1450	1-5/16" x 4-1/4" x 15/16"*
S-168-T	CDE	1450	1-3/4" x 8-7/8" x 5/8"

* cracked-scrap

Table B-10 (Cont'd)

F. W-E4 (S-167)

1. Cut off nose and tail ends, macroetch, and photograph.
2. Billet machined and hand conditioned. See Table B-10-A.
3. Cut billet into 2 sections as shown below:



4. Break all sharp edges.
5. Forging in argon atmosphere

<u>Identity</u>	<u>Item</u>	<u>Forge Temp. °C</u>	<u>Forged Size</u>
S-167-N*	Wire	1400	3/4" x 9-5/16"
	Bar		3/4" x 14-1/2"
S-167-T**	Wire	1400	3/4" x 13-1/4"
	Bar		

* Cut in half during forging to facilitate handling.

** Cut in half during forging to facilitate handling, one end cracked (scrap).

G. Wire Rod Processing

1. Forged bars hand conditioned and dye penetrant inspected.
2. Bars swaged at a starting temperature of 1530°C; temperature gradually reduced to a finish temperature of 1225°C (See Table B-10-B).
3. Reduction per pass ranged from 7.2% - 28.4% depending on availability of dies.
4. Bars were given an intermediate anneal of 1510°C for 15 minutes, at approximately 45% reduction.
5. Bars were centerless ground to finished diameter.
6. See Table B-10-C.

Table B-10-A

Conditioning of Extruded Bars

<u>Identity</u>	<u>Received Wt., Lbs.</u>	<u>Conditioned Wt., Lbs.</u>	<u>Nominal Conditioned Size; Dia. and Length, In.</u>
S-158	18	10-1/2	1-1/4 x 15-1/2
S-152	24	21-1/4	1-1/4 x 21
S-154	12	11	1-1/4 x 10-3/4
S-157	15	12-1/4	1-1/4 x 12
S-168	23	19-1/2	1-3/8 x 18-3/4
S-167	22	17-1/4	1-1/4 x 18-1/2
S-169	13	7-1/2	1-1/4 x 11-1/4

Table B-10-B

Swaging Sequence

<u>Dia. Size, In.</u>	<u>Temperature, °C</u>	<u>% Reduction</u>
0.693	1530	15 (approx.)
0.668	1530	7
0.598	1530	20
0.568	1390	10
0.512	1390	19
0.488	1390	9
0.420	1390	26
0.400*	1315	9
0.372	1300	13
0.348	1300	13
0.295	1225	28
0.278	1225	10

* All bars annealed 1/4 hour at 1510°C after this step.

Table B-10-C

Conditioning of Swaged Bars

<u>Identity</u>	<u>Dia. and Length Before Swaging, In.</u>	<u>Dia. and Length After Swaging, In.</u>	<u>Ground Dia. and Length</u>	<u>Finished Wt., Lbs.</u>
S-167	23/32 x 14-1/2	0.275 x 50-3/4 0.278 x 35-1/2	0.235 x 50 0.235 x 35-1/2	1-1/2 1-1/8
S-167N	11/16 x 9-5/16	0.281 x 41-3/8	0.235 x 41-3/8	1-1/4
S-167T	23/32 x 13-1/4	0.280 x 50-1/4 0.278 x 49-5/8	0.235 x 50-1/4 0.235 x 49-5/8	1-1/2 1-3/8
S-154T	23/32 x 4-15/16	0.273 x 17-1/8	0.235 x 17-1/8	1/2
S-154T	23/32 x 8-9/16	0.274 x 30-1/8	0.235 x 30-1/8	1

Table B-11

Fabrication Schedule for W-E1 and W-E2 Strip

A. W-E1 (S-158)

<u>Item</u>	<u>Starting Thickness, In.</u>	<u>Final Thickness, In.</u>	<u>Rolling Temp., °C</u>	<u>% Reduction</u>
C	0.600	0.156	1300	74
		Split-scrap		
E	0.590	0.265	1400	55
	0.265	0.070	1100	73
	Conditioned and recrystallized - 1450°C (1 hour)			
	0.065	cracked-scrap	1000	--

B. W-E1 (S-152)

<u>Item</u>	<u>Starting Thickness, In.</u>	<u>Final Thickness, In.</u>	<u>Rolling Temp., °C</u>	<u>% Reduction</u>
D	0.597	0.263	1400	57
	0.263	0.082	1100	69
	Conditioned and recrystallized - 1450°C (1 hour)			
	0.075	cracked-scrap	1000	--
E	0.597	0.263	1400	57
	0.263	0.077	1100	71
	Conditioned and recrystallized - 1450°C (1 hour)			
	0.072	cracked-scrap	1000	--
H	0.845	0.284	1400	66
	Conditioned and recrystallized - 1450°C (1 hour)			
	0.284	0.196	1300	31
	0.196	0.167	1000	15
	0.164	0.038	1000	77
	Portions of strip cracked. Good material measures: 0.038" x 1-3/8" x 28-1/2"			
C	0.602	0.158	1400	74
	0.158	0.056	1100	65
	Conditioned			
	0.052	0.047	1000	10
		cracked-scrap		

Table B-11 (Cont'd)

<u>Item</u>	<u>Starting Thickness, In.</u>	<u>Final Thickness, In.</u>	<u>Rolling Temp., °C</u>	<u>%Reduction</u>
C	0.662	0.159	1400	76
	0.159	0.051	1100	68
	Conditioned			
	0.048	0.041	1000	15
		Cracked-scrap		
C. <u>W-E1 (S-154)</u>				
<u>Item</u>	<u>Starting Thickness, In.</u>	<u>Final Thickness, In.</u>	<u>Rolling Temp., °C</u>	<u>%Reduction</u>
C	0.650	0.267	1300	59
		Cracked-scrap		
E	0.650	0.267	1400	59
	0.267	0.085	1100	68
	Conditioned and recrystallized - 1450°C - (1 hour)			
	0.076	Cracked-scrap	1000	--
H	0.842	0.290	1400	66
	Conditioned and recrystallized - 1450°C - (1 hour)			
	0.279	0.195	1300	30
	0.195	0.154	1300	21
	Conditioned			
	0.151	0.033	1000	78
	Portions cracked. Good material measures			
	0.033" x 1-3/4" x 10"			
D. <u>W-E1 (S-157)</u>				
<u>Item</u>	<u>Starting Thickness, In.</u>	<u>Final Thickness, In.</u>	<u>Rolling Temp., °C</u>	<u>%Reduction</u>
C	0.620	0.155	1400	75
	0.155	0.054	1100	65
	Conditioned			
	0.048	--	--	--
	Holding 2 pieces - 0.048" x 1-3/4" x 22"			
	and 0.048" x 1-3/4" x 15-1/4"			
D	0.620	0.254	1400	59
	0.254	0.070	1100	72
	Conditioned and recrystallized - 1450°C - (1 hour)			
	0.064	0.051	1300	20
	0.051	0.039	1000	24
	Portions cracked. Good material measures			
	0.037" x 2-1/4" x 10-1/8"			
E	0.620	0.255	1400	59
	0.255	0.077	1100	70
	Conditioned and recrystallized - 1450°C (1 hour)			
	0.069	Cracked-scrap	1000	--

Table B-11 (Cont'd)

Item	Starting Thickness, In.	Final Thickness, In.	Rolling Temp., °C	%Reduction
H	0.845	0.290	1400	66
	Conditioned and recrystallized - 1450°C (1 hour)			
	0.281	0.199	1300	29
	0.199	0.170	1000	15
	Conditioned			
	0.167	0.042	1000	75
		Cracked-scrap		

E. W-E2(S-168)

Item	Starting Thickness, In.	Final Thickness, In.	Rolling Temp., °C	%Reduction
H	0.910	0.287	1400	68
	Conditioned and recrystallized - 1450°C (1 hour)			
	0.275	0.199	1300	28
	0.199	0.167	1000	16
	Conditioned			
	0.164	0.040	1000	76
	Holding 2 pieces - 0.040" x 1-5/8" x 15" and 0.040" x 1-5/8" x 14"			
C	0.597	0.259	1400	57
	0.259	0.160	1300	38
	0.160	0.055	1100	66
	Conditioned			
	0.052	--	--	--
	Holding 1 piece - 0.055" x 1-7/8" x 12-1/8"			
C	0.621	0.260	1400	58
	0.260	0.159	1300	39
	0.159	0.051	1100	68
	Conditioned			
	0.048	--	--	--
	Holding 1 piece - 0.048" x 1-7/8" x 5-3/4"			
D	0.621	0.260	1400	58
		split-scrap		
D	0.597	0.259	1400	57
	0.259	0.079	1100	70
	Conditioned and recrystallized - 1450°C - (1 hour)			
	0.074	Cracked-scrap	1000	--
E	0.621	0.260	1400	58
	0.260	0.079	1100	70
	Conditioned and recrystallized - 1450°C (1 hour)			
	0.074	Cracked-scrap	1000	--
E	0.597	0.259	1400	57
	0.259	0.083	1100	68
	Conditioned and recrystallized - 1450°C (1 hour)			
	0.080	Cracked-scrap	1300	--

Appendix C

Effect of Recovery on Recrystallization in Columbium

The possible effect of prior recovery-annealing on subsequent recrystallization in both relatively high-purity columbium (Cb-E1) and high-oxygen columbium (Cb-E4) wires was studied by means of metallographic examination and micro-hardness measurements.

<u>Material</u>	<u>C</u>	<u>N</u>	<u>O</u>	<u>H</u>
Cb-E1 (wire analysis)	12-27	50-80	130-160	4-9
Cb-E4 (ingot analysis)	16	76	630-770	17

The recrystallized wires were first drawn 40% reduction in area at room temperature and then recovery-annealed in vacuum for 16 hours at 300°, 500°, and 600°C.

Light microscopic examination revealed no changes as a result of recovery-annealing. However, the microhardness of both the cold drawn Cb-E1 and Cb-E4 wires was found to increase slightly with increasing recovery-annealing temperature, go through maxima at 300°C and then decrease to values slightly below those of the as-drawn wires (Fig. 1). The hardness maxima at 300°C are attributed to strain aging. As expected from the higher oxygen content, Cb-E4 wires are harder than Cb-E1 wires in both the as-drawn and recovery-annealed conditions. Although no microstructural changes were found as a result of recovery-annealing, it may be concluded from the changes in microhardness that recovery processes actually occur.

During subsequent annealing for 1/4 hour at 900°, about 25% of the fibrous microstructure transforms to recrystallized grains in the Cb-E1 wires and about 15% in the Cb-E4 wires for all prior conditions. The microhardness decreases substantially and is independent of prior recovery temperature (Fig. C-1). Consequently, it is concluded that prior recovery has no significant effect on subsequent recrystallization in the columbium wires studied.

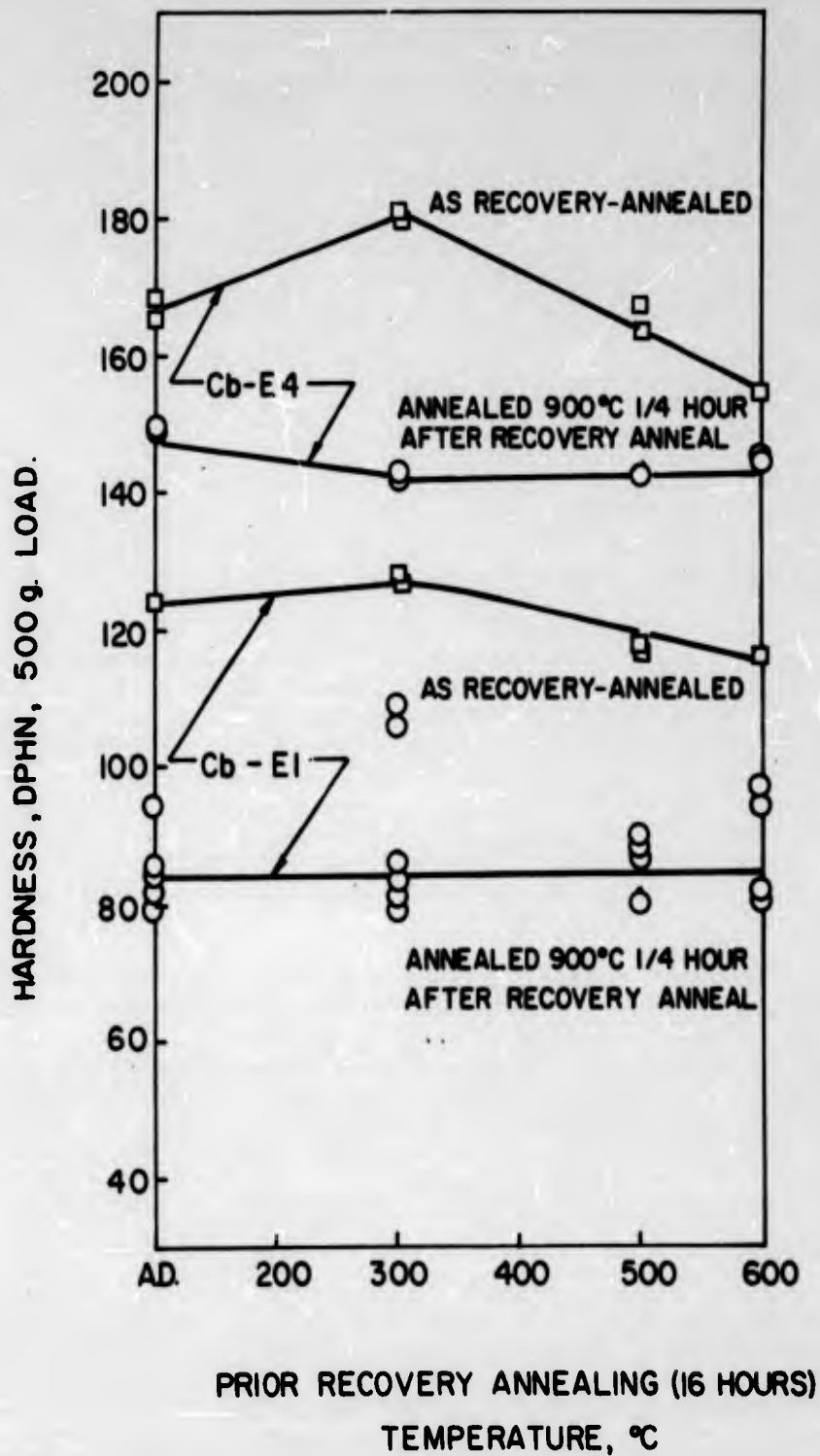


Fig. C-1- Effect of prior recovery annealing (for 16 hours) on subsequent recrystallization (900°C, 1/4 hour) on microhardness of columbium (Cb-E1 and Cb-E4) wire.

1. Refractory metals
 2. X-ray diffraction analysis
 3. Electron microscopy
- I. AFSC Project 7351, Task 735101
 - II. Contract AF33(657)-8424
 - III. ManLabs, Inc. Cambridge, Mass.
 - IV. Lement, B.S. et al.
 - V. Aval fr OTS
 - VI. In ASTIA collection

Aeronautical Systems Division, Dir/Materials And Processes, Metals & Ceramics Lab, Wright-Patterson AFB, Ohio
 Rpt No ASD-TR-61-181, Part III. SUB-STRUCTURE AND MECHANICAL PROPERTIES OF REFRACTORY METALS. Final report, Apr 63, 220 p. incl. illus., tables, refs.
 Unclassified Report

Coordinated program on W, Mo, Ta and Cb was carried out by ManLabs, M.I.T., Rutgers, U. Liverpool (Eng.) and U. Cambridge (Eng.) by means of advanced microscopic, x-ray diffraction, and mechanical testing techniques. The effective surface energy for fracture of molybdenum strip was

(over)

found to be about 3000 ergs/cm². The tensile ductility transition in molybdenum is associated with the occurrence of necking. Fiber-like grains containing a dislocation cell structure in which fine platelets occur. Discontinuous yielding in tantalum single crystals is correlated with a decrease in the shearing strain in the principal slip system to zero while that in the secondary system continues to increase. The binding energy between oxygen atoms and dislocations in tantalum is about 0.54 e.v. Dissociation of screw dislocations along three interesting symmetrically located planes may account for the strong lattice friction stress in b.c.c. metals.

1. Refractory metals
 2. X-ray diffraction analysis
 3. Electron microscopy
- I. AFSC Project 7351, Task 735101
 - II. Contract AF33(657)-8424
 - III. ManLabs, Inc. Cambridge, Mass.
 - IV. Lement, B.S. et al.
 - V. Aval fr OTS
 - VI. In ASTIA collection

Aeronautical Systems Division, Dir/Materials And Processes, Metals & Ceramics Lab, Wright-Patterson AFB, Ohio
 Rpt No ASD-TR-61-181, Part III. SUB-STRUCTURE AND MECHANICAL PROPERTIES OF REFRACTORY METALS. Final report, Apr 63, 220 p. incl. illus., tables, refs.
 Unclassified Report

Coordinated program on W, Mo, Ta and Cb was carried out by ManLabs, M.I.T., Rutgers, U. Liverpool (Eng.) and U. Cambridge (Eng.) by means of advanced microscopic, x-ray diffraction, and mechanical testing techniques. The effective surface energy for fracture of molybdenum strip was

(over)

found to be about 3000 ergs/cm². The tensile ductility transition in molybdenum is associated with the occurrence of necking. Fiber-like grains containing a dislocation cell structure in which fine platelets occur. Discontinuous yielding in tantalum single crystals is correlated with a decrease in the shearing strain in the principal slip system to zero while that in the secondary system continues to increase. The binding energy between oxygen atoms and dislocations in tantalum is about 0.54 e.v. Dissociation of screw dislocations along three interesting symmetrically located planes may account for the strong lattice friction stress in b.c.c. metals.

<p>Aeronautical Systems Division, Dir/Materials And Processes, Metals & Ceramics Lab, Wright-Patterson AFB, Ohio Rpt No ASD-TR-61-181, Part III. SUB-STRUCTURE AND MECHANICAL PROPERTIES OF REFRACTORY METALS. Final report, Apr 63, 220 p. incl. illus., tables, refs.</p> <p>Unclassified Report</p> <p>Coordinated program on W, Mo, Ta and Cb was carried out by ManLabs, M.I.T., Rutgers, U. Liverpool (Eng.) and U. Cambridge (Eng.) by means of advanced microscopic, x-ray diffraction, and mechanical testing techniques. The effective surface energy for fracture of molybdenum strip was</p> <p style="text-align: center;">(over)</p>	<p>1. Refractory metals analysis 2. X-ray diffraction 3. Electron microscopy</p> <p>I. AFSC Project 7351, Task 735101 II. Contract AF33(657)-8424 III. ManLabs, Inc. Cambridge, Mass. IV. Lement, B.S. et al. V. Aval fr OTS VI. In ASTIA collection</p>	<p>1. Refractory metals analysis 2. X-ray diffraction 3. Electron microscopy</p> <p>I. AFSC Project 7351, Task 735101 II. Contract AF33(657)-8424 III. ManLabs, Inc. Cambridge, Mass. IV. Lement, B.S. et al. V. Aval fr OTS VI. In ASTIA collection</p>	<p>1. Refractory metals analysis 2. X-ray diffraction 3. Electron microscopy</p> <p>I. AFSC Project 7351, Task 735101 II. Contract AF33(657)-8424 III. ManLabs, Inc. Cambridge, Mass. IV. Lement, B.S. et al. V. Aval fr OTS VI. In ASTIA collection</p>
<p>found to be about 3000 ergs/cm². The tensile ductility transition in molybdenum is associated with the occurrence of necking. Fiber- ing in tungsten involves formation of ribbon- like grains containing a dislocation cell structure in which fine platelets occur. Discon- tinuous yielding in tantalum single crystals is correlated with a decrease in the shearing strain in the principal slip system to zero while that in the secondary system continues to increase. The binding energy between oxygen atoms and dislocations in tantalum is about 0.54 e.v. Dissociation of screw dis- locations along three interesting symmetri- cally located planes may account for the strong lattice friction stress in b.c.c. metals.</p> <p style="text-align: center;">(over)</p>	<p>found to be about 3000 ergs/cm². The tensile ductility transition in molybdenum is asso- ciated with the occurrence of necking. Fiber- ing in tungsten involves formation of ribbon- like grains containing a dislocation cell struc- ture in which fine platelets occur. Discon- tinuous yielding in tantalum single crystals is correlated with a decrease in the shearing strain in the principal slip system to zero while that in the secondary system continues to increase. The binding energy between oxygen atoms and dislocations in tantalum is about 0.54 e.v. Dissociation of screw dis- locations along three interesting symmetri- cally located planes may account for the strong lattice friction stress in b.c.c. metals.</p> <p style="text-align: center;">(over)</p>	<p>found to be about 3000 ergs/cm². The tensile ductility transition in molybdenum is asso- ciated with the occurrence of necking. Fiber- ing in tungsten involves formation of ribbon- like grains containing a dislocation cell struc- ture in which fine platelets occur. Discon- tinuous yielding in tantalum single crystals is correlated with a decrease in the shearing strain in the principal slip system to zero while that in the secondary system continues to increase. The binding energy between oxygen atoms and dislocations in tantalum is about 0.54 e.v. Dissociation of screw dis- locations along three interesting symmetri- cally located planes may account for the strong lattice friction stress in b.c.c. metals.</p> <p style="text-align: center;">(over)</p>	<p>found to be about 3000 ergs/cm². The tensile ductility transition in molybdenum is asso- ciated with the occurrence of necking. Fiber- ing in tungsten involves formation of ribbon- like grains containing a dislocation cell struc- ture in which fine platelets occur. Discon- tinuous yielding in tantalum single crystals is correlated with a decrease in the shearing strain in the principal slip system to zero while that in the secondary system continues to increase. The binding energy between oxygen atoms and dislocations in tantalum is about 0.54 e.v. Dissociation of screw dis- locations along three interesting symmetri- cally located planes may account for the strong lattice friction stress in b.c.c. metals.</p> <p style="text-align: center;">(over)</p>

<p>Aeronautical Systems Division, Dir./Materials And Processes, Metals & Ceramics Lab, Wright-Patterson AFB, Ohio Rpt No ASD-TR-61-181, Part III. SUB-STRUCTURE AND MECHANICAL PROPERTIES OF REFRACTORY METALS. Final report, Apr 63, 220 p. incl. illus., tables, refs.</p> <p>Unclassified Report</p> <p>Coordinated program on W, Mo, Ta and Cb was carried out by ManLabs, M.I.T., Rutgers, U. Liverpool (Eng.) and U. Cambridge (Eng.) by means of advanced microscopic, x-ray diffraction, and mechanical testing techniques. The effective surface energy for fracture of molybdenum strip was</p> <p style="text-align: center;">(over)</p>	<ol style="list-style-type: none"> 1. Refractory metals 2. X-ray diffraction analysis 3. Electron microscopy <ol style="list-style-type: none"> I. AFSC Project 7351, Task 735101 II. Contract AF 33(657)-8424 III. ManLabs, Inc. Cambridge, Mass. IV. Lement, B.S. et al. V. Aval fr OTS VI. In ASTIA collection 	<p>Aeronautical Systems Division, Dir./Materials And Processes, Metals & Ceramics Lab, Wright-Patterson AFB, Ohio Rpt No ASD-TR-61-181, Part III. SUB-STRUCTURE AND MECHANICAL PROPERTIES OF REFRACTORY METALS. Final report, Apr 63, 220 p. incl. illus., tables, refs.</p> <p>Unclassified Report</p> <p>Coordinated program on W, Mo, Ta and Cb was carried out by ManLabs, M.I.T., Rutgers, U. Liverpool (Eng.) and U. Cambridge (Eng.) by means of advanced microscopic, x-ray diffraction, and mechanical testing techniques. The effective surface energy for fracture of molybdenum strip was</p> <p style="text-align: center;">(over)</p>	<ol style="list-style-type: none"> 1. Refractory metals 2. X-ray diffraction analysis 3. Electron microscopy <ol style="list-style-type: none"> I. AFSC Project 7351, Task 735101 II. Contract AF 33(657)-8424 III. ManLabs, Inc. Cambridge, Mass. IV. Lement, B.S. et al. V. Aval fr OTS VI. In ASTIA collection
<p>found to be about 3000 ergs/cm². The tensile ductility transition in molybdenum is associated with the occurrence of necking. Fiber- ing in tungsten involves formation of ribbon- like grains containing a dislocation cell structure in which fine platelets occur. Discon- tinuous yielding in tantalum single crystals is correlated with a decrease in the shearing strain in the principal slip system to zero while that in the secondary system continues to increase. The binding energy between oxygen atoms and dislocations in tantalum is about 0.54 e.v. Dissociation of screw dis- locations along three interesting symmetri- cally located planes may account for the strong lattice friction stress in b.c.c. metals.</p> <p style="text-align: center;">(over)</p>		<p>found to be about 3000 ergs/cm². The tensile ductility transition in molybdenum is asso- ciated with the occurrence of necking. Fiber- ing in tungsten involves formation of ribbon- like grains containing a dislocation cell struc- ture in which fine platelets occur. Discon- tinuous yielding in tantalum single crystals is correlated with a decrease in the shearing strain in the principal slip system to zero while that in the secondary system continues to increase. The binding energy between oxygen atoms and dislocations in tantalum is about 0.54 e.v. Dissociation of screw dis- locations along three interesting symmetri- cally located planes may account for the strong lattice friction stress in b.c.c. metals.</p> <p style="text-align: center;">(over)</p>	

Aeronautical Systems Division, Dir/Materials
And Processes, Metals & Ceramics Lab,
Wright-Patterson AFB, Ohio
Rpt No ASD-TR-61-181, Part III. SUB-
STRUCTURE AND MECHANICAL PROPER-
TIES OF REFRACTORY METALS. Final
report, Apr 63, 220 p. incl. illus., tables,
refs.

Unclassified Report

Coordinated program on W, Mo, Ta and Cb
was carried out by ManLabs, M.I.T.,
Rutgers, U. Liverpool (Eng.) and U. Cam-
bridge (Eng.) by means of advanced micro-
scopic, x-ray diffraction, and mechanical
testing techniques. The effective surface
energy for fracture of molybdenum strip was

(over)

found to be about 3000 ergs/cm². The tensile
ductility transition in molybdenum is asso-
ciated with the occurrence of necking. Fiber-
ing in tungsten involves formation of ribbon-
like grains containing a dislocation cell struc-
ture in which fine platelets occur. Discon-
tinuous yielding in tantalum single crystals
is correlated with a decrease in the shearing
strain in the principal slip system to zero
while that in the secondary system continues
to increase. The binding energy between
oxygen atoms and dislocations in tantalum is
about 0.54 e.v. Dissociation of screw dis-
locations along three interesting symmetri-
cally located planes may account for the
strong lattice friction stress in b.c.c.
metals.

1. Refractory metals
 2. X-ray diffraction analysis
 3. Electron micro-
scopy
- I. AFSC Project 7351,
Task 735101
 - II. Contract AF33(657)-
8424

III. ManLabs, Inc.
Cambridge, Mass.
IV. Lement, B.S. et al.
V. Aval fr OTS
VI. In ASTIA collection

Aeronautical Systems Division, Dir/Materials
And Processes, Metals & Ceramics Lab,
Wright-Patterson AFB, Ohio
Rpt No ASD-TR-61-181, Part III. SUB-
STRUCTURE AND MECHANICAL PROPER-
TIES OF REFRACTORY METALS. Final
report, Apr 63, 220 p. incl. illus., tables,
refs.

Unclassified Report

Coordinated program on W, Mo, Ta and Cb
was carried out by ManLabs, M.I.T.,
Rutgers, U. Liverpool (Eng.) and U. Cam-
bridge (Eng.) by means of advanced micro-
scopic, x-ray diffraction, and mechanical
testing techniques. The effective surface
energy for fracture of molybdenum strip was

(over)

found to be about 3000 ergs/cm². The tensile
ductility transition in molybdenum is asso-
ciated with the occurrence of necking. Fiber-
ing in tungsten involves formation of ribbon-
like grains containing a dislocation cell struc-
ture in which fine platelets occur. Discon-
tinuous yielding in tantalum single crystals
is correlated with a decrease in the shearing
strain in the principal slip system to zero
while that in the secondary system continues
to increase. The binding energy between
oxygen atoms and dislocations in tantalum is
about 0.54 e.v. Dissociation of screw dis-
locations along three interesting symmetri-
cally located planes may account for the
strong lattice friction stress in b.c.c.
metals.

UNCLASSIFIED

UNCLASSIFIED